REPORT DOCUMENTATION PAGE

Form Approved OMB NO. 0704-0188

1. REPORT DATE (DD-MM-YYYY)	2. REPORT TYPE	3. DATES COVERED (From - To)
13-10-2008	Final Report	1-Aug-2004 - 31-Jul-2008

4. TITLE AND SUBTITLE
Analysis and Modeling of Complex Geomorphic Systems: Technique Development, Data Collection, and Application to Rangeland Terrain

5a. CONTRACT NUMBER
W911NF-04-1-0340

5b. GRANT NUMBER

5c. PROGRAM ELEMENT NUMBER
611102

6. AUTHORS
Gregoy E. Tucker, D. Nathan Bradley

5d. PROJECT NUMBER

5e. TASK NUMBER

5f. WORK UNIT NUMBER

7. PERFORMING ORGANIZATION NAMES AND ADDRESSES
University of Colorado - Boulder
Office of Contracts and Grants
Campus Box 572, 3100 Marine Street Rm 481
Boulder, CO 80309 -0572

8. PERFORMING ORGANIZATION REPORT NUMBER

9. SPONSORING/MONITORING AGENCY NAME(S) AND ADDRESS(ES)
U.S. Army Research Office
P.O. Box 12211
Research Triangle Park, NC 27709-2211

10. SPONSOR/MONITOR'S ACRONYM(S)
ARO

11. SPONSOR/MONITOR'S REPORT NUMBER(S)
47033-EV-DRI.1

12. DISTRIBUTION AVAILIBILITY STATEMENT
Approved for Public Release; Distribution Unlimited

13. SUPPLEMENTARY NOTES
The views, opinions and/or findings contained in this report are those of the author(s) and should not contrued as an official Department of the Army position, policy or decision, unless so designated by other documentation.

14. ABSTRACT
This report describes the results of a four-year, multi-faceted investigation into the physics of sediment transport and erosion in channels and hillslopes. The project addressed two objectives: (1) develop and explore new mathematical computational tools for modeling complex land-surface systems, and in particular the applicability of stochastic transport theory and fractional calculus; and (2) use numerical modeling and field data analysis to develop a better understanding of the processes, mechanisms, and dynamics of land-surface change in semi-arid rangeland environments, with a focus on the Colorado piedmont. These two aims are interconnected in the sense that rangeland landscapes provide a template for

15. SUBJECT TERMS
geomorphology, landscape evolution, sediment transport, dispersion, random walks, fractional calculus, rangelands, erosion

16. SECURITY CLASSIFICATION OF:			17. LIMITATION OF ABSTRACT	15. NUMBER OF PAGES	19a. NAME OF RESPONSIBLE PERSON
a. REPORT	b. ABSTRACT	c. THIS PAGE			Gregory Tucker
U	U	U	SAR		19b. TELEPHONE NUMBER: 303-492-6985

Report Title

Analysis and Modeling of Complex Geomorphic Systems: Technique Development, Data Collection, and Application to Rangeland Terrain

ABSTRACT

This report describes the results of a four-year, multi-faceted investigation into the physics of sediment transport and erosion in channels and hillslopes. The project addressed two objectives: (1) develop and explore new mathematical computational tools for modeling complex land-surface systems, and in particular the applicability of stochastic transport theory and fractional calculus; and (2) use numerical modeling and field data analysis to develop a better understanding of the processes, mechanisms, and dynamics of land-surface change in semi-arid rangeland environments, with a focus on the Colorado piedmont. These two aims are interconnected in the sense that rangeland landscapes provide a template for documenting and measuring process dynamics, while mathematical and numerical models contribute to interpreting these landscapes. This report is divided into three main sections. The first focuses on the primary thrust of the project, which involves applying recent concepts in stochastic transport theory and fractional calculus to sediment transport and dispersion. Our objective was to determine what new light these methods may shed on the dynamics of geomorphic systems. The second section analyzes the interplay between rainfall, runoff, vegetation, and erosion in setting the dynamics of the ephemeral channel networks that are so common in rangeland landscapes. The third section explores the shaping of channel cross-section geometry, which turns out to play a critical role in governing flows of mass and energy across the landscape.

List of papers submitted or published that acknowledge ARO support during this reporting period. List the papers, including journal references, in the following categories:

(a) Papers published in peer-reviewed journals (N/A for none)

Tucker, G.E., Arnold, L., Bras, R.L., Flores, H., Istanbulluoglu, E., Solyom, P. (2006) Headwater channel dynamics in semiarid rangelands, Colorado high plains, USA. Geological Society of America Bulletin, v. 118, no. 7/8, p. 959-974.

Arnold, L.J., Bailey, R.M., and Tucker, G.E. (2007) Statistical treatment of fluvial dose distributions from southern Colorado arroyo deposits: Quaternary Geochronology, v. 2, p. 162-167.

Istanbulluoglu, E., Bras, R.L., Flores-Cervantes, H., and Tucker, G.E. (2005) Implications of bank failures and fluvial erosion for gully development: Field observations and modeling. Journal of Geophysical Research - Earth Surface, v. 110, no. F1, F01014, doi:10.1029/2004JF000145.

Solyom, P.B., and Tucker, G.E. (2007) The importance of the catchment area-length relationship in governing non-steady state hydrology, optimal junction angles and drainage network pattern. Geomorphology, v. 88, p. 84-108.

Wobus, C.W., Tucker, G.E., and Anderson, R.S. (2006) Self-formed bedrock channels. Geophysical Research Letters, v. 33, L18408, doi: 10.1029/2006GL027182.

Wobus, C.W., Kean, J.W., Tucker, G.E., and Anderson, R.S. (2008) Modeling the evolution of channel shape: balancing computational efficiency with hydraulic fidelity. Journal of Geophysical Research - Earth Surface, v. 113, F02004, doi:10.1029/2007JF000914.

Whittaker, A.C., Cowie, P.A., Attal, M., Tucker, G.E., and Roberts, G.P. (2007) Bedrock channel adjustment to tectonic forcing: implications for predicting river incision rates. Geology, v. 35, no. 2, p. 103-106 (doi: 10.1130/G23106A.1).

Attal, M., Tucker, G.E., Whittaker, A.C., Cowie, P.A., and Roberts, G.P. (2008) Modeling fluvial incision and transient landscape evolution: Influence of dynamic channel adjustment. Journal of Geophysical Research - Earth Surface, v. 113, F03013, doi:10.1029/2007JF000893.

Clevis, Q., Tucker, G.E., Lock, G., Lancaster, S.T., Gasparini, N.M., Desitter, A., and Bras, R.L. (2006) Geoarchaeological simulation of meandering river deposits and settlement distributions; a three-dimensional approach. Geoarchaeology, v. 21, no. 8, p. 843-874 (doi: 10.1002/gea.20142).

Number of Papers published in peer-reviewed journals: 9.00

(b) Papers published in non-peer-reviewed journals or in conference proceedings (N/A for none)

Number of Papers published in non peer-reviewed journals: 0.00

(c) Presentations

Tucker, G.E., and Bradley, D.N., Imaging rapid landscape change along the West Bijou Escarpment: Paper presented at Workshop on Studying Earth Surface Processes with High Resolution Topographic Data, Boulder, CO, June 2008.

Tucker, G.E., Using natural experiments to test models of drainage basin evolution: Invited paper presented at "Resilience and Vulnerability of Natural and Managed Hydrologic Systems: The Inaugural CUAHSI Biennial Colloquium on Hydrologic Science and Engineering" Boulder, CO, July 2008.

Bradley, D.N., and Tucker, G.E. (2007) Channel motion as a random walk: erosion probabilities and implications for sediment residence time. Paper presented at American Geophysical Union fall meeting, San Francisco, CA, December 2007.

Tucker, G.E. (2007) Theory, observation and scaling in landscape evolution. Invited lecture presented at Geological Society of London Bicentennial Conference, London, UK, September 2007.

Tucker, G.E., Arnold, L.J., Bras, R., Flores-Cervantes, H., Istanbulluoglu, E., Sólyom, P., and Winchester, V. (2007) Origins of episodicity in arroyo formation and development: evidence from the Colorado High Plains. Invited paper presented at Geological Society of America conference, Denver, CO, October 2007.

Tucker, G.E., and Bradley, D.N. (2007) Statistical modeling of sediment dispersion in drainage networks. Paper presented at ARO Terrestrial Sciences Soil Moisture / Arid Lands Research Review Meeting, Fort Carson, CO, March 2007.

Tucker, G.E., and Bradley, D.N. (2007) Landscape evolution models and challenges in formulating earth-surface transport laws. Invited talk presented at workshop on “Stochastic Transport and Emergent Scaling in Earth Surface Processes,” Incline Village, NV, November 2007.

Tucker, G.E., Bradley, D.N., and Wobus, C.W. (2007) Bed sediment dispersion and channel geometry evolution in headwater streams. Paper presented at Joint ARO-ERDC Review Meeting of ARO Terrestrial Science Program, U.S. Army Engineer Research and Development Center, Vicksburg, MS, September 2007.

Wobus, C., Tucker, G., Anderson, R., Kean, J., Small, E., and Hancock, G. (2007) The dynamics of bedrock channel adjustment: modeling the influence of sediment supply, weathering, and lithology on channel cross-sectional and longitudinal shape. Paper presented at American Geophysical Union fall meeting, San Francisco, CA, December 2007.

Bedford, D. Small, E.E., Tucker, G.E., and Pockman, W.T. (2006) Effect of soil and vegetation heterogeneity on runoff in a semi-arid grassland. Paper presented at American Geophysical Union fall meeting, San Francisco, December 2006.

Bradley, D.N., and Tucker, G.E. (2006) Gambler's ruin and the residence time distribution in fluvial sediment dispersion. Paper presented at American Geophysical Union fall meeting, San Francisco, December 2006.

Tucker, G.E. (2006) Using natural experiments to test river erosion laws. Invited keynote lecture presented at INSU/CNRS conference on “Reliefs de la Terre,” Oleron, France, October 2006.

Tucker, G.E., and Bradley, D.N. (2006) Probabilistic treatment of sub-reach-scale bed stress in long-term channel evolution models. Invited paper presented at AGU Hydrology Days conference, Fort Collins, CO, March, 2006.

Tucker, G.E., Clevis, Q., Lock, G., Lancaster, S.T., A., Gasparini, N., Desitter, and Bras, R.L. (2006) Geoarchaeological simulation of meandering river deposits. Paper presented at Geological Society of America annual meeting, Philadelphia, PA, October 2006.

Wobus, C.W., Tucker, G.E., and Anderson, R.S. (2006) Modeling the geometry of bedrock river channels. Paper presented at American Geophysical Union fall meeting, San Francisco, December 2006.

Attal, M., Tucker, G., Whittaker, A., Cowie, P., and Roberts, G. (2005) Modeling river incision across active normal faults using the Channel-Hillslope Integrated Landscape Development Model (CHILD): the case of the Central Apennines (Italy). Paper presented at American Geophysical Union fall meeting, San Francisco, December,

2005.

Bradley, D.N., and Tucker, G.E. (2005) Normal and Anomalous Dispersion in Fluvial Sediment Transport. Paper presented at American Geophysical Union fall meeting, San Francisco, December, 2005.

Bras, R.L., and Tucker, G.E. (2005) Myths about Mathematical Modeling in Hydrology and Geomorphology. Paper presented at American Geophysical Union fall meeting, San Francisco, December, 2005.

Clevis, Q., Tucker, G.E., Lock, G., Lancaster, S.T., Gasparini, N.M., and Desitter, A. (2005) Geoarchaeological simulation of meandering river deposits and settlement distributions; a three-dimensional approach. Paper presented at the 8th International Conference on Fluvial Sedimentology, Delft, Netherlands, August, 2005.

Tucker, GE, Lee Arnold, Rafael Bras, Daniel Collins, Homero Flores, Erkan Istanbulluoglu, Stephen Stokes, and Vanessa Winchester (2004) Chronology and Dynamics of Gully Development, Fort Carson and Pinon Canyon Maneuver Site, Colorado. Paper presented at Workshop on Desert Surficial Processes and Landscape Dynamics on Military Lands, Zzyzx, CA, September 2004.

Tucker, GE, Lee Arnold, Rafael Bras, Homero Flores, Erkan Istanbulluoglu, Peter Solyom, Stephen Stokes, Vanessa Winchester (2004) Dynamics of gully networks: inferences from numerical modeling and geochronology. Presentation at U.S. Army Research Office investigators' meeting, USACE Waterways Experiment Station, Vicksburg, MS, November.

Tucker, GE, Arnold, L, and Stokes, S (2004) Evidence for autogenic cyclicity in ephemeral stream cut-fill deposits. Paper presented at American Geophysical Union fall meeting, San Francisco, December.

Arnold, L, Tucker, GE, and Stokes, S (2004) Optical dating of arroyo-system deposits: insights into cut-fill cycles in the southern Colorado piedmont. Paper presented at American Geophysical Union fall meeting, San Francisco.

Number of Presentations: 23.00

Non Peer-Reviewed Conference Proceeding publications (other than abstracts):

Number of Non Peer-Reviewed Conference Proceeding publications (other than abstracts): 0

Peer-Reviewed Conference Proceeding publications (other than abstracts):

Number of Peer-Reviewed Conference Proceeding publications (other than abstracts): 0

(d) Manuscripts

Number of Manuscripts: 0.00

Number of Inventions:

Graduate Students

NAME	PERCENT_SUPPORTED
D. Nathan Bradley	0.70
FTE Equivalent:	**0.70**
Total Number:	**1**

Names of Post Doctorates

NAME	PERCENT_SUPPORTED
FTE Equivalent:	
Total Number:	

Names of Faculty Supported

NAME	PERCENT_SUPPORTED	National Academy Member
Gregory E. Tucker	0.10	No
FTE Equivalent:	**0.10**	
Total Number:	**1**	

Names of Under Graduate students supported

NAME	PERCENT_SUPPORTED
FTE Equivalent:	
Total Number:	

Student Metrics

This section only applies to graduating undergraduates supported by this agreement in this reporting period

The number of undergraduates funded by this agreement who graduated during this period:	0.00
The number of undergraduates funded by this agreement who graduated during this period with a degree in science, mathematics, engineering, or technology fields:.....	0.00
The number of undergraduates funded by your agreement who graduated during this period and will continue to pursue a graduate or Ph.D. degree in science, mathematics, engineering, or technology fields:.....	0.00
Number of graduating undergraduates who achieved a 3.5 GPA to 4.0 (4.0 max scale):	0.00
Number of graduating undergraduates funded by a DoD funded Center of Excellence grant for Education, Research and Engineering:	0.00
The number of undergraduates funded by your agreement who graduated during this period and intend to work for the Department of Defense	0.00
The number of undergraduates funded by your agreement who graduated during this period and will receive scholarships or fellowships for further studies in science, mathematics, engineering or technology fields:	0.00

Names of Personnel receiving masters degrees

NAME
Total Number:

Names of personnel receiving PHDs

NAME
Total Number:

Names of other research staff

NAME	PERCENT_SUPPORTED
FTE Equivalent:	
Total Number:	

Sub Contractors (DD882)

Inventions (DD882)

Analysis and Modeling of Complex Geomorphic Systems: Technique Development, Data Collection, and Application to Rangeland Terrain

Gregory E. Tucker and D. Nathan Bradley

October, 2008

Contents

Chapter 1

Introduction

This project report describes the results of a four-year, mutli-faceted investigation into the physics of sediment transport and erosion in channels and hillslopes. The project was motivated by a need to understand the dynamics of sediment erosion, transport, and sedimentation within drainage basins. Understanding the dynamics of land-surface systems is essential for making informed estimates of how a particular landscape will respond to a particular type of impact, as well as for understanding the transport and fate of solid-phase environmental pollutants. The processes that contribute to moving sediment across the earth's land surface represent a classic example of a complex system: there are many degrees of freedom, there are instances of emergent behavior from a large ensemble of individual particles, there are examples of strong process localization (such as concentration of mass and energy flow along branches of a river network), and nonlinearities abound.

The project has sought to address two particular objectives: (1) to develop and explore new mathematical computational tools for modeling complex land-surface systems, and in particular to investigate the applicability of stochastic transport theory and of fractional calculus; and (2) to deploy a combination of numerical modeling and field data analysis to develop a better quantitative understanding of the processes, mechanisms, and dynamics of land-surface change in semi-arid rangeland environments, with a focus on the Colorado piedmont. These two aims are interconnected in the sense that rangeland landscapes provide a template for documenting and measuring process dynamics, while mathematical and numerical models contribute to interpreting these landscapes.

This report is divided into three main sections. The first focuses on the primary thrust of the project, which involves applying recent concepts in stochastic transport theory and fractional calculus to sediment transport. These methods have

proven quite useful in the study of homologous systems, such as groundwater contaminant transport, and our objective has been to determine what new light they may shed on the dynamics of geomorphic systems. The second section analyzes the interplay between rainfall, runoff, vegetation, and erosion in setting the dynamics of the ephemeral channel networks that are so common in rangeland landscapes. The third section explores a critical element of fluvial transport systems: the shaping of channel cross-section geometry, which turns out to play a critical role in governing flows of mass and energy across the landscape.

Chapter 2

Applying Stochastic Transport Theory and Fractional Calculus to Geomorphic Systems

Classical thermodynamics provides a tremendously successful macroscopic description of flows of energy and mass resulting from molecular motion. One might imagine therefore that many other multi-particle transport systems would give rise to fairly simple, linear macroscopic behaviors similar to, for instance, Fourier's law of heat conduction. Yet research in the physical and biological sciences over the last few decades has unearthed numerous examples of systems that do not exhibit such simple emergent behaviors (e.g., West et al., 2003). This has prompted the development of new mathematical and computational methods designed to better describe and understand what have come to be called "complex dynamic systems."

Many of the geomorphic transport processes that give rise to the earth's landscapes fall into this category, exhibiting features such as strong heterogeneity, lack of separation between micro and macro scales, scale invariance, and strong nonlinearity. In allied fields in the physical sciences, phenomena with similar properties have been successfully explained and modeled using relatively new (or newly applied) concepts in stochastic dynamics, such as fractional calculus. Some examples include charge transport in semi-conductors (e.g., Scher et al., 1991), fluid transport in turbulent flows (e.g., Weeks et al., 1996), and contaminant dispersion in flowing groundwater (e.g., Berkowitz and Scher, 1995; Benson et al., 2000). These successes led us to hypothesize that new insights could be gained by applying the same concepts to geomorphic transport systems. This section describes some tests of that hypothesis.

Our investigation has focused primarily, though not exclusively, on the transport

and dispersion of sediment in rivers and streams. With the exception of the pioneering work of H.A. Einstein (1937, 1950), most current models of sediment transport are based on bulk fluxes, and therefore say nothing about the speed with which sediment moves or the manner in which it disperses over time. Yet the "virtual velocity" and dispersion characteristics of sediment are of fundamental importance to several issues, including the fate and transport of solid-phase and sediment-bound contaminants (e.g., Clark et al., 2006; Graf, 1994, 1996; Reneau et al., 2004) and the residence time properties of stored sediment (e.g., Dietrich and Dunne, 1978; Malmon et al., 2003). The problem of sediment motion and dispersion is considered to be of particular relevance to the Army because of the need to manage and mitigate solid-phase pollutants, such as munitions residues and fine sediments, on installations.

Our effort has involved several related components:

1. Develop and analyze random-walk-based models for sediment transport, with a particular emphasis on the necessary and sufficient conditions for anomalous dispersion.

2. Use a mobile/immobile transport model with Lévy flights to reinterpret results from a radioactive sand dispersion experiment by Sayre and Hubble (1965), which is one of the few comprehensive data sets on sediment dispersion.

3. Generate a new laboratory-based data set on gravel dispersion under steady, unidirectional flow, using a research flume at the U.S. Geological Survey's Geomorphology and Sediment Transport Laboratory in Golden, Colorado.

4. Conduct a field experiment in gravel dispersion using tracer stones with embedded radio-frequency Passive Integrated Transponder (PIT) tags.

5. Develop a model for long-term sediment motion through a fluvial system, including temporary storage in floodplain deposits, based on "Gambler's Ruin" or first-passage-time models, and compare these with physically based numerical models of riverine sediment erosion, transport, and deposition.

6. Explore the potential for, and consequences of, non-local behavior in hillslope sediment transport, using a particle-based model of hillslope evolution that replicates commonly observed parabolic to planar slope forms.

These efforts are described in the sections that follow.

2.1 Sediment Motion and Dispersion

2.1.1 Normal versus Anomalous Dispersion

The nature of sediment dispersion is an unsolved problem in fluvial geomorphology (Nikora et al., 2002). If one places a pile of tracer pebbles on a streambed, how fast will they spread out? The answer depends on how much variability there is in the overall, or virtual, velocity of the pebbles. A tracer's virtual velocity depends on how far it moves during an episode of motion and how long it rests between movements. For a population of tracers in a natural stream, it is unlikely that all particles will move with the same frequency and travel the same distance. Instead, there will be a distribution of virtual velocities as a result of the variability in the duration of the rests and the length of the steps of different particles. If the distribution of velocities is very broad, meaning that a high velocity is not extremely unlikely, then the pattern of spreading will be very different from the pattern that results if high velocities are unlikely.

The classic example of a dispersive process is Brownian motion, named for the botanist Robert Brown. He noticed that pollen grains in a dish of water moved continuously and randomly, no matter how long he left them to settle down. Albert Einstein showed that the pollen grains don't stop moving because they are continually colliding with individual water molecules and used a random walk to work out the mathematics (Einstein 1905, Feynman, 1963).

A normal, or Fickian, diffusive process is completely described by the velocity of the mean position of the particle cloud and rate at which particles spread out from the mean. The "rate" of spreading is the diffusivity. Fick's Law is built into the familiar Advection-Diffusion Equation (ADE). The one-dimensional ADE describes the way the concentration, C, of a cloud of particle changes in time, t, and space, x:

$$\frac{\partial C}{\partial t} = -v\frac{\partial C}{\partial x} + D\frac{\partial^2 C}{\partial x^2} \tag{2.1}$$

Fickian diffusivity is steady in time. The rate at which the particle cloud expands never changes. This is the signature of normal diffusion. In Fickian diffusion, variance grows linearly in time. Yet Fickian diffusion is only one special case of a broader class of dispersive processes in which the variance, σ^2, scales as a power function of time:

$$\sigma^2 \sim t^{\gamma}, 0 < \gamma < \ 2 \tag{2.2}$$

When $\gamma = 1$, we have Fickian dispersion and when $\gamma \neq 1$ we have anomalous, or

non-Fickian dispersion.

Anomalous dispersion appears to be common in nature. An interesting example in the geosciences is the transport of contaminants in ground water through heterogeneous media (e.g. Dentz and Tartakovsky, 2006). Other examples include anomalous diffusion of a protein tracer inside a live cell (Wachsmuth et al., 2000) and the fluctuations of stock prices (Plerou et al., 2000). The transport medium doesn't even have to be strongly heterogeneous. Benson et al. (2000) measured the dispersion of a fluid tracer in box of the most homogenous sand they could find. To their mild surprise, anomalous dispersion was observed even in this carefully controlled, nearly homogeneous experiment.

2.1.2 Previous Studies of Sediment Dispersion

There have been only a few studies on the mathematical nature of sediment dispersion. These will be discussed in some detail. Other work has focused problems related to the sediment dispersion problem. Tracer studies, inspired by Einstein's stochastic model for sediment transport have examined particle travel distance and the resting time, but only during active transport. These studies of the resting time distribution during active transport appear inadequate for predicting the long-term dispersion of sediment. Most attempts to measure the long-term distribution of storage time have relied unrealistic assumptions, but two recent studies suggest a new approach.

As a part of a Cold War era investigation of how rivers move radioactive pollution, Sayre and Hubble (1965) placed 40 pounds of fine sand labeled with radioactive iridium 192 on the bed of North Loup River in Nebraska. Iridium 192 has a half-life of about 74 days and emits gamma radiation when it decays. By measuring the intensity of gamma radiation, Sayre and Hubble were able to measure the motion of the radioactive sand for thirteen days. A re-analysis of this data set is the subject of Section 2.3 below.

In another dispersion study, Drake et al. (1988) released 125 painted grains on the bed of Duck Creek near Pinedale, Wyoming and photographed their position at 15-second intervals for 240 seconds. They plotted the longitudinal and transverse standard deviation of the particle cloud vs. time in linear space and fit square root curves to the data to calculate downstream and cross-stream diffusivities. By assuming a square root fit, they implicitly assumed normal dispersion of the tracers.

Nikora et al. (2002) reanalyzed the Duck Creek data and concluded it did not support the authors assumption of normal dispersion. They replotted the 1988 data as non-dimensional mean square displacement vs. non-dimensional time and found

that the scaling was less than linear, indicating anomalous sub-dispersion. They also videotaped 159 particle trajectories from entrainment to trapping along the bed of Balmoral Canal in New Zealand and concluded that in the very short term ($\sim$1 second), they observed anomalous super-diffusion.

In a related study, Nikora et al. (2001) develop a conceptual model for bed load sediment dispersion and support it with results from a sophisticated numerical model of particle motion in a turbulent flow. Their conceptual model divides transport into three time scales, which they call the local, intermediate, and global range. The local range is the ballistic trajectory of a particle from entrainment to a collision with the bed and is not of first order importance here. The intermediate range is the time between two significant periods of rest and is comprised of many episodes of local motion. The intermediate range may be normally diffusive, super-diffusive, or sub-diffusive. The global range of motion consists of many intermediate trajectories. They predict that the global range should be sub-diffusive and find support in the Duck Creek data. They reason that sub-diffusion at the global range is due to heavy tailed resting time distributions. As discussed below, our numerical results and the theoretical work of Weeks and Swinney (1998) show that heavy-tailed resting time distributions can lead to either sub-diffusive or super-diffusive behavior.

2.1.3 Resting Time and Residence Time

It is important to recognize that the intervals of rest a particle endures between episodes of motion occur on two very different time scales and to be specific about the terminology. The first is the time between steps during an active transport event. When the river is at flood stage and pebbles are skittering along the bed, the brief moments when they stop make up the resting time distribution. The second is the time in between transport events, which can be extremely long if particles are deeply buried or stranded high on bars or flood plains. This is referred to here as the residence time distribution.

It should be noted that opinions differ on the terminology of sediment storage. Dietrich et al. (1982), following Eriksson (1971), call this the "transit time distribution," referring to the time a particle takes to pass through a storage reservoir such as a short section of floodplain. Citing Bolin and Rodhe (1973), they use residence time to mean the average of the transit time distribution. Malmon et al. (2003) redefine transit time as the time necessary to transit the whole system but keep the definition of residence time as the expected time a particle will spend in a reservoir. Other workers adopt other definitions or are less precise in their usage. Phillips et al. (2006) do not define their usage or residence time exactly, but refer to a "mean

residence time," suggesting that their definition is different from the mean of the transit time distribution.

To avoid confusion, we will be explicit with terminology. "Residence time" will refer to the random time that a single particle spends between deposition and subsequent erosion. "Residence time distribution" refers to the probability distribution of the residence time for an ensemble of particles. Residence time is distinct from the resting time, which refers to the rest periods between steps during a transport event.

Einstein used the resting time distribution in his stochastic model of bed load transport and it has been the focus of several tracer experiments. Schmidt and Ergenzinger (1992) tracked the motion radio transmitting clasts in the Lainbach River in Germany during several transport events and found an exponential distribution of rest periods. Habersack (2001) performed a similar experiment in a large gravel bed river in New Zealand and also found an exponential distribution. Citing five other studies, he makes the extraordinary claim that "for non-braided rivers, the exponential distribution of rest periods has been proven in the laboratory and nature."

That may very well be the case, but the relevance of the resting time distribution to a long-term random walk model of sediment dispersion is limited because it does not include the time between transport events. There is another limitation too. Ferguson et al. (2002) compared the virtual velocity (travel distance divided by the duration of competent flows) of tracers measured after two years to the virtual velocity measured after eight years. He found that the velocity decreased by half because the tracers eventually found resting places where they were less easily mobilized. The radio transmitting gravel experiments were probably not long enough to observe this effect.

These experiments ignore the fact that rivers store large amounts of sediment. Dunne et al. (1998) found that on the Amazon River in Brazil, the sediment flux between the channel and long-term storage (bars, banks, and the floodplain) exceeds the downstream sediment flux. Pizzuto (1994) observed year-to-year fluctuations between deposition and erosion along the banks of the Power River over sixteen years, indicating exchange of sediment between the channel and the banks. As Church (2006) writes, the widespread notion that bed load moves dominantly as a continuous traction carpet in the deep channel appears more to be an artifact of simplified models for computation than a reality of rivers. Because of long-term sediment storage, the residence time distribution is more important than the resting time distribution for predicting the long-term dispersion of sediment.

The residence time distribution for a fluvial deposit is difficult to measure. Dating the material in a sediment reservoir can reveal the time since deposition, the sediment

age. Everitt (1968) mapped the age distribution of cottonwoods along a 34 km stretch of the Little Missouri River in North Dakota. Dietrich et al. (1982) applied Erikssons (1971) method to estimate the residence time distribution from Everitts age distribution. Somewhat mysteriously, they did not report the form of either the age distribution or the residence time distribution they calculated, saying only "the transit time function probably has an exponential form for most rivers." Because Erikssons method assumes that reservoirs are in steady state and requires an accurate estimate of the age distribution, it is probably not practical for most rivers (Dietrich et al., 1982).

Dietrich et al.'s statement about the form of the residence time distribution is justified if a sediment reservoir is defined so that all material in the reservoir has an equal probability of erosion and the probability is steady from year to year. This assumption is almost certainly incorrect in many cases. Differences in grain size, sediment cohesiveness, distance from the channel, and depth of burial all create variability in the erosion probability.

Malmon (2003) suggests that the way to get around this problem is to define sediment reservoirs as groups of particles that have an equal erosion probability. Even if that were practical, the erosion probability would vary from reservoir to reservoir. Each reservoir would have an exponential distribution of residence times but that does not necessarily lead to an overall exponential distribution. Depending on how the erosion probability varies from reservoir to reservoir, the total distribution can be much heavier-tailed than an exponential distribution (Sornette, 2004, section 14.4).

The most compelling attempt to measure the residence time distribution of sediment appears to be that by Lancaster (2006). He measured the radiocarbon ages of material in the cut bank of a channel. Because the age of eroded sediment is its residence time, the age of material that is about to be eroded should be a reasonable proxy for residence time. He found an exponential distribution in the alluvial portion of the channel and an infinite mean power law distribution in the debris flow dominated reach. Recent work by Thompson et al. (2007) is also worth noting. They measured the burial ages of fluvial sediment in Australia with optically stimulated luminescence (OSL) dating and found a strongly right-skewed distribution. While burial age is not residence time, OSL dating of grains in the cut bank, following Lancaster (2006), is a promising approach.

2.1.4 Particle Step Length

The distribution of sediment particle travel distances has received considerable attention and studies generally conclude that travel distances are right-skewed and well described by an exponential or gamma distribution. The probability of a long step from an exponential or gamma distribution is too small to violate the CLT and lead to anomalous dispersion. However, Pyrce and Ashmore (2003) concluded that the transport distance of tracers in a flume can be modeled by a Cauchy distribution with a mean equal to the bar spacing. This result is interesting because the probability of a long step from a Cauchy distribution is high enough that it results in anomalous dispersion. The Cauchy distribution is a special case of the heavy-tailed distribution that we used to model the velocity distribution of the Sayre and Hubbell tracer data, described in the next section. The preliminary results from our tracer experiments (described below) also suggest that sediment grain travel distance is better described by a heavy-tailed distribution than by an exponential or gamma distribution.

2.2 Sediment Motion as a Continuous-Time Random Walk

Anomalous dispersion has received considerable attention since Montroll and Weiss (1965) developed the mathematical tools to describe it. The Continuous Time Random Walk (CTRW) framework casts the motion of a particle as a random walk with rests between steps. Probability Density Functions (PDFs) describe the step length and the duration of rests. This is essentially the same as H.A. Einstein's stochastic model of sediment transport. The CTRW framework can model the entire range of dispersive phenomena. Weeks et al. (1996) studied the diffusion properties in a CTRW model with power-law tails on the hop-length and resting-time distributions, and derived a phase diagram relating these tails to the nature of the dispersion process (normal, sub-, or super-diffusion).

We have explored a particle-based numerical simulation of unidirectional CTRWs as an analogy for sediment motion. Exploration of the CTRW parameter space in this model is shown in Figure 2.1, along with the analytical prediction for unbounded distributions from Weeks and Swinney (1998). As predicted, if the both PDFs of motion have tails that are thin enough (an exponent greater than 3), the motion is Fickian. If particle step length and the resting time are distributed as an exponential or gamma distribution, as is commonly assumed (see below), then a three-dimensional version of the ADE should describe the evolution of the particle cloud.

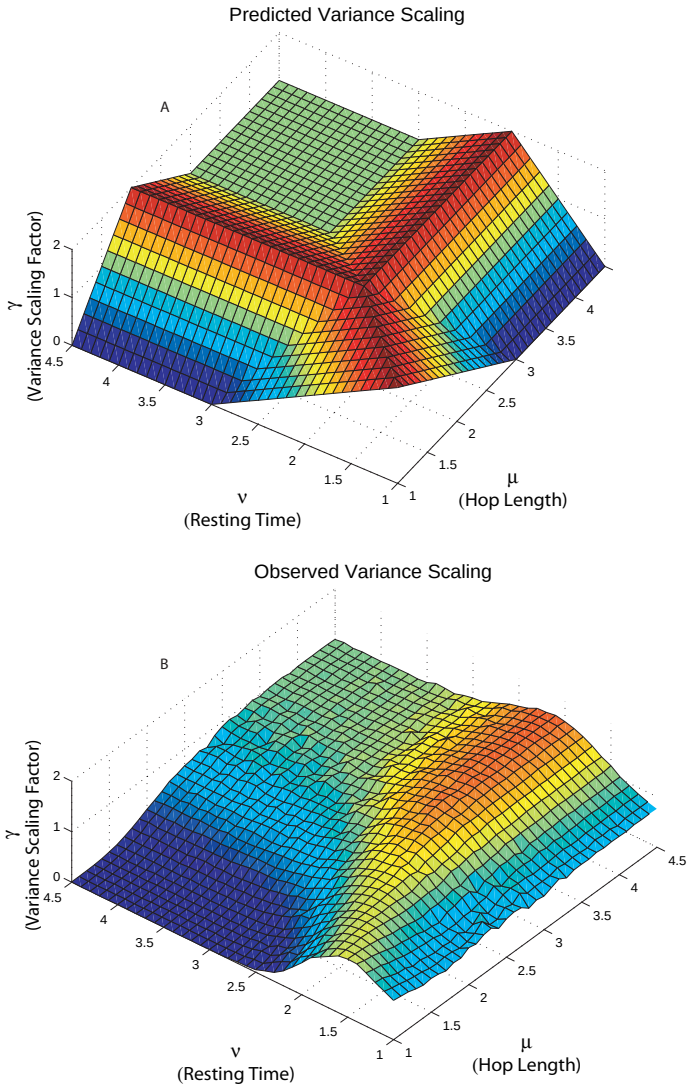

Figure 2.1: Analytical prediction for strongly asymmetric random walks from Weeks and Swinney (1998) (top) compared to numerical exploration of the CTRW parameter space (bottom). X- and Y-axes are the decay exponents on the power law distributions of resting time and step length. CTRW simulations (10,000 particles) were run for each parameter combination, and the slope of the variance vs. time plot in log-log space estimated with a least squares fit. Average of the five trials is plotted on the Z-axis. Our results show less extreme variation than the analytic results because of the finite number of random walkers and the upper bound on our step length and resting time PDFs.

On the other hand, if the resting time distribution is heavy-tailed, dispersion can be sub-diffusive or super-diffusive. This is shown by the variation along the resting time axis for fat-tailed distributions of resting time and narrow distributions of step length. This motivates focus on the role of storage in sediment dispersion.

It should be noted the analytical results differ in one respect from the numerical results. The analytic solution predicts that if one distribution is heavy-tailed and the other is not, one can still get the entire range of dispersive motion, from sub-diffusion (blue) to super-diffusion (red). The results do not show this for heavy-tailed distributions of step length. The "ridge" of variation for heavy-tailed distributions of step length and thin distributions of resting time shown on lower left of the analytical prediction is missing. This is likely because the analytical prediction is for distributions has an infinite upper limit, while the distributions in our simulations are bounded. Such bounded random walks are in many respects more realistic descriptors of sediment motion than traditional Lévy flights, and deserve further scrutiny in this context (see section *Nonlocality in Sediment Transport* below).

2.3 A model of the heavy-tailed, anomalous dispersion of radioactive tracer sand by a river

(Note: This section contains a manuscript in preparation for submission to the *Journal of Geophysical Research* special issue on Stochastic Transport and Emergent Scaling in Earth-Surface Processes, by D. Nathan Bradley, Gregory E. Tucker, and David Benson. The topic will also be presented at the American Geophysical Union 2008 Fall Meeting.)

2.3.1 Abstract

In 1960, the USGS and the U.S. Atomic Energy Commission measured the dispersion of radioactive tracer sand along the bed of the N. Loup River in Nebraska to test a stochastic model of sediment transport based on the work of H.A. Einstein. The model predicted the observed concentration profiles reasonably well, but with several weaknesses. First, it required an ad hoc parameter to match the location of the model curves to data. Second, the amount of tracer mass detected declined over the course of the experiment, which the model did not predict. To compensate for this, the data were normalized in a manner that was not theoretically supported by the model. Third, the observed tracer concentration well downstream from the peak concentration was much higher than predicted by the model. We revisit the data

from the N. Loup River experiment and apply a four-parameter mobile/immobile model with a heavy-tailed distribution of particle velocity that addresses all three weaknesses of the previous model. This result suggests that the variability in bed load particle velocity can be so great that the distribution of particle travel distance is heavy-tailed with a divergent variance. If this is the case, then the mode of sediment dispersion is anomalous rather than Fickian.

2.3.2 Introduction

Many, if not most, fluvial bed load transport models predict the bulk sediment flux in terms of a representative grain size subject to a spatially and temporally averaged driver such shear stress or stream power (Yang, 1996). While these models may be adequate for many applications, they provide little insight into the motion of individual particles. In some cases, it is useful to know details like the velocity of a grain, the fraction of the transport time that a grain spends at rest, and the variability and shape of the distributions of both velocity and resting time for a population of grains. Applications in which such knowledge would be useful include detrital dating techniques that depend on assumptions about the time a grain spends in the fluvial system, restoration of aquatic spawning habitat, and prediction of the spatial distribution and time in the fluvial system of a pollutant that travels in the solid phase or adsorbed onto sediment grains.

A model that attempts to describe the motion of individual sediment particles from first principles must take into account that a river bed is made up of a great many individual grains that vary in size, arrangement on the bed, and exposure to turbulent fluctuations in the velocity of the water. As a result, different grains may be exposed to very different forces and may respond to the same force differently (Kirchner et al., 1990). It is conceivable that if every single factor that affects the entrainment, transport, and deposition of sediment could be known precisely for every grain and for all time, one could construct a deterministic model of bed load transport. In practice, however, it is impossible to know all the forces acting on all grains precisely enough to predict the future. Even if were possible to know the physical conditions precisely, the sheer number of grains would make computation impossible.

An alternative to describing the motion of every single particle is to use probability distributions to describe the inherent variability in a fluvial transport system. H.A. Einstein (1937) recognized this and developed a model that breaks down the motion of a sediment grain into a series of alternating steps and rests. The Einstein model treats step length and rest duration as random variables and predicts

transport in terms of the probability that a grain occupies a particular position at a particular time. In this paper, we reanalyze data from an innovative and insightful tracer test of the Einstein model performed by W.W. Sayre and D.W. Hubbell of the US Geological Survey in the 1960s. We apply a model that is conceptually similar to the Einstein-Sayre-Hubbell model, but differs in a few key ways that combine to make our model a more accurate descriptor of the experimental data.

2.3.3 Sayre and Hubbell (1965) *Transport and Dispersion of Labeled Bed Material*

Tracer Dispersion Experiment

On November 3rd, 1960, W.W. Sayre and D.W. Hubbell used a small boat, an electric can opener, and a long funnel to spread forty pounds of radioactive sand across the bed of a river in Nebraska. Over the next 13 days, they measured the intensity of the gamma rays emitted by the tracer sand along 1800 feet of channel length. Using calibration curves developed in the laboratory, they estimated the concentration of the tracer sand in the river bed based on the intensity of the radiation. Finally, they compared the experimental results to the predictions of probabilistic transport model that is identical to Einstein's in its result but different in its development.

The experiment was one in a series of investigations that the U.S. Atomic Energy Commission and the U.S. Geological Survey performed in the early 1960s to study the transport and dispersion of radioactive waste through the environment. Sayre and Hubbell chose a man-made meander cutoff on the North Loup River near Purdum, NE as their study reach. The site map and a drawing of the reach are reproduced in Figure 2.2. The study reach was 1800 feet long, about 50 feet wide, and bent gently to the left. The median grain size of sand in the river bed was a little less than 0.3 mm.

The tracer used in the N. Loup River experiment was a sand with uniform size and shape and a median size (0.305 mm) slightly coarser than the bed material. The sand was plated with Iridium-192, which emits gamma rays and has a half-life of 74 days (in 1960, such plated sand was commercially available in two-pounds cans). Handling the cans with tongs (for radiation safety), they opened them with the can opener and poured them into a funnel resting on the riverbed. In all, Sayre and Hubbell placed twenty cans of tracer sand on the bed of the river at two-foot intervals across the channel.

To measure the intensity of the radiation emitted by the tracer sand, they towed a waterproof scintillometer mounted on a sled along the stream bed behind their boat.

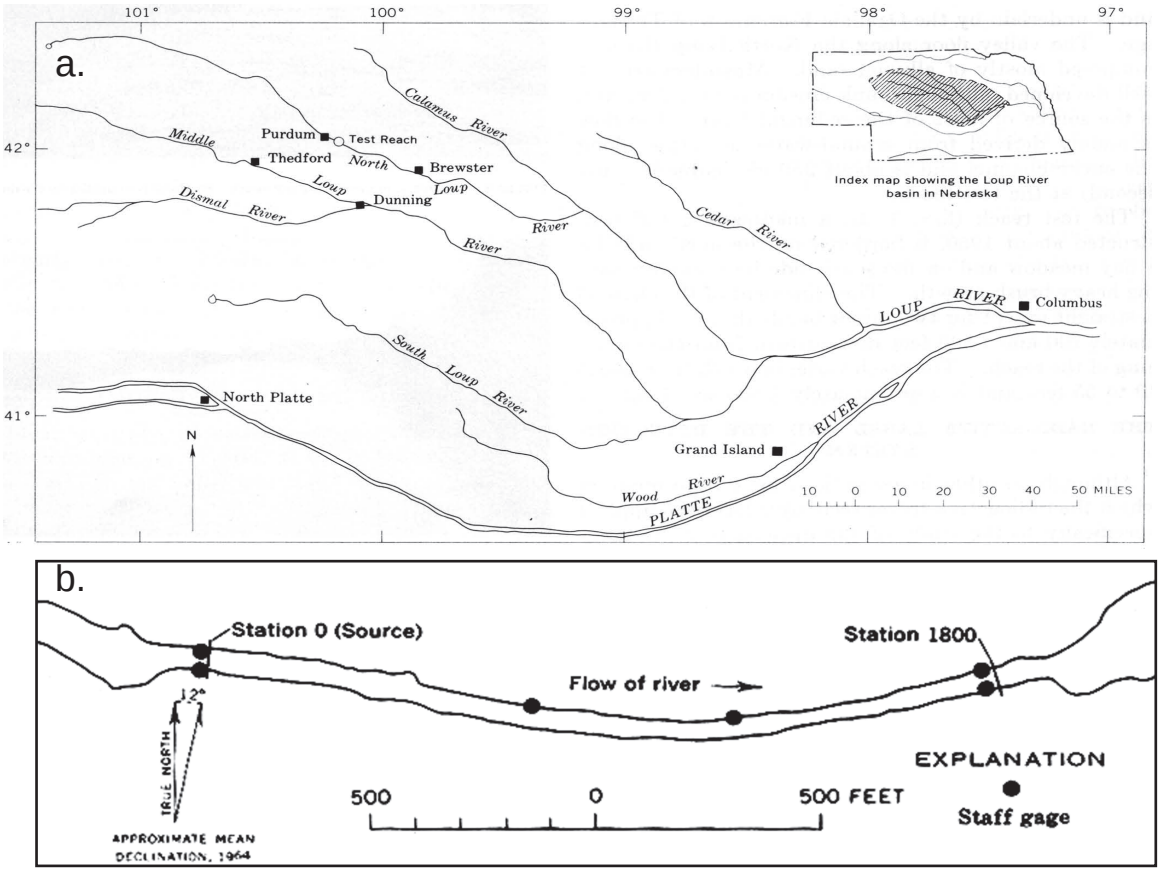

Figure 2.2: a) The location of the Sayre and Hubbell experiment on the North Loup River near Purdum, NE and b) a drawing of the study reach. Tracer particles were released at Station 0 and tracked along 1800 feet of river over 13 days.

The maximum detection range of the scintillometer was between 4 and 8 inches. The tracks of the two primary downstream traverses were along the right and left banks, approximately one third of a channel width from the nearest bank. They also performed downstream traverses along the center of the channel a lateral traverses on several days.

They converted the intensity of the radiation detected to a concentration of tracer material using empirical calibration curves that related the gamma ray count per minute to the grams of tracer per cubic foot of bed material. The curves were developed in the laboratory by mixing known quantities of tracer material through varying volumes of sand and measuring the radiation emitted. They estimated the tracer concentration in the bed by averaging the gamma ray count rate over some length of river (5-100 feet, based on the rate of change of the count rate) and assuming that the tracer was uniformly mixed into the bed to an average depth of 1.45 feet. This was the average depth to which tracer particles were mixed in core samples of the bed material taken over the course of the study.

Sayre and Hubbell traversed the right side of the channel on 10 of the 13 days of the study. Our digitization of their data is shown in Figure 2.3, along with the model they developed (see Appendix for procedures used to digitize data).

The concentration profiles are plotted as relative concentrations to facilitate comparison with the model, which predicts the probability that a particle occupies a particular position. The relative concentration, in units of inverse feet, is the estimated concentration, in grams per cubic foot, divided by the total area under the concentration curve in grams per square foot. The area under the concentration curve, A, is the total mass detected on a traverse divided by unit channel width and unit depth. This quantity is called the zeroth moment.

The profiles are roughly bell-shaped curves that show the tracer plume moving downstream and spreading out along the length of the reach. The plume is strongly skewed in the downstream direction. The peak concentration moves about half way down the length of the study reach over the course of the study, but the leading edge of the plume has nearly reached the end of the study reach by 96.2 hours. Figure 2.4 shows the mean position of the tracer plume at each measurement time. The mean velocity of the plume is about 2.8 feet per hour. Note that the regression does not intersect the y-axis at zero, which suggests that the tracers moved more quickly at the beginning of the study. We will revisit this issue below.

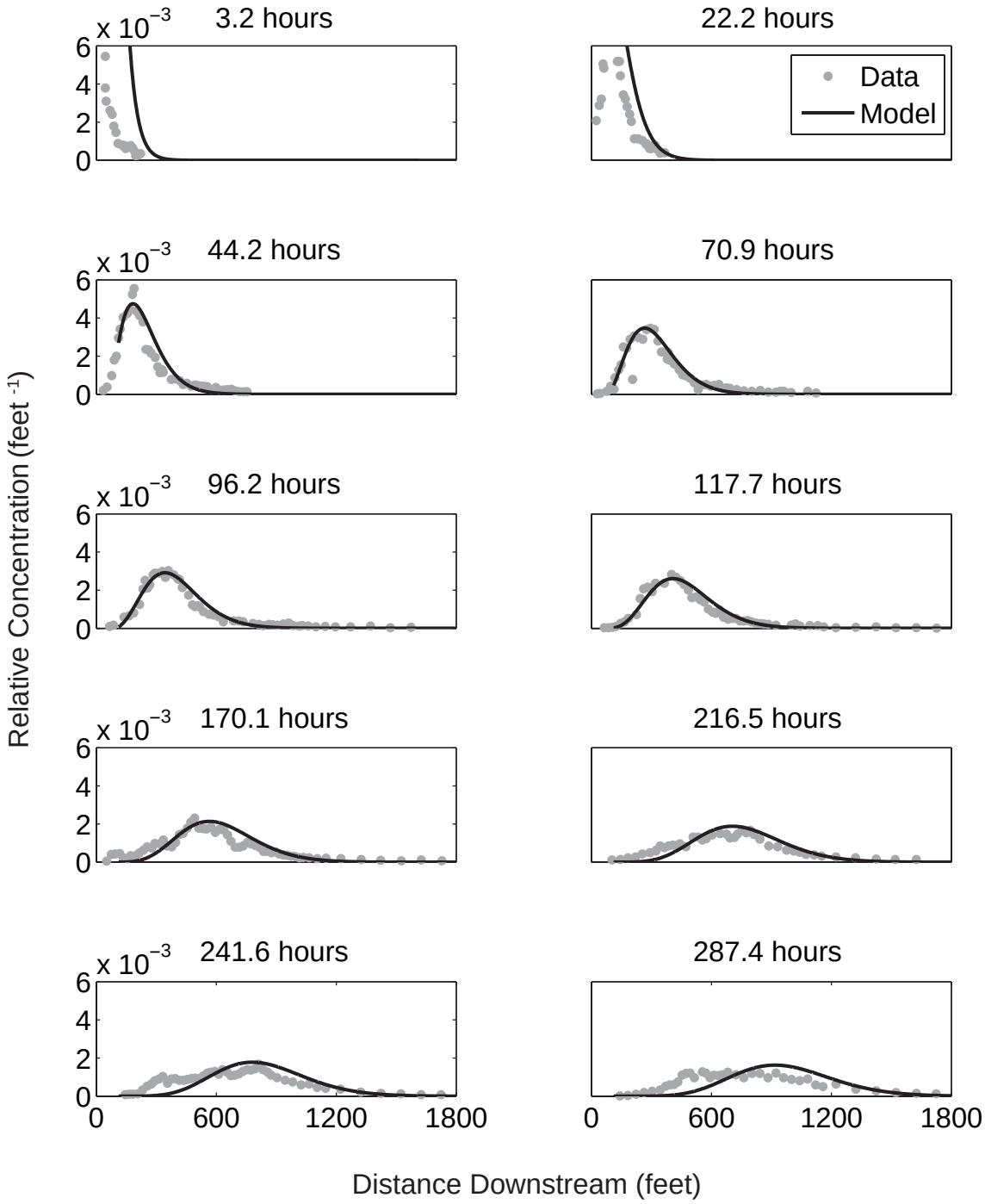

Figure 2.3: Estimated concentrations from the N. Loup River experiment are shown as gray dots and the Sayre and Hubbell theoretical model as a solid black line. Note the extra mass that appears left of the peak at 170.1 hours. Sayre and Hubbell interpreted this as material washed in from the left side of the channel.

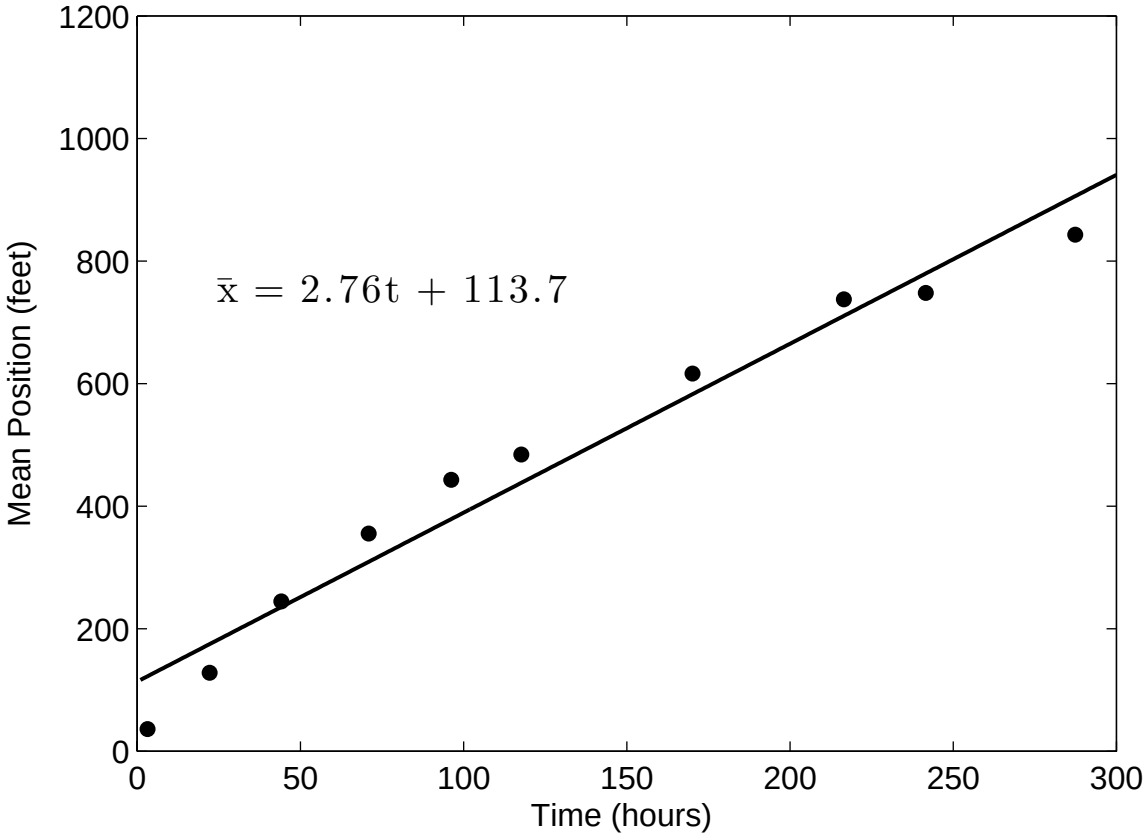

Figure 2.4: The mean position of the Sayre and Hubbell channel right tracer plume (black dots) over the course of the study plotted with a linear regression to the data (black line). The velocity of the tracer plume averaged over the study is 2.76 ft/hr but the non-zero intercept of the regression indicates that the plume moved faster at first. The slope and intercept of our regression are slightly different from those calculated by Sayre and Hubbell because they used data from the left, right, and center traverses in their regression, adjusted some data points, and excluded others. We use all the data from the right side of the channel and we do not correct for the extra mass that appears upstream of the peak at 170.1 hours in Figure 2.3.

Sayre-Hubble Transport-Dispersion Model

Sayre and Hubbell also developed a theoretical model of tracer transport that is ultimately equivalent to Einstein's (1937), but differs in the way that it is developed. The model treats particle motion an alternating series of steps and rests. If the step distance and the duration of the rest intervals are random variables that obey the conditions of a Poisson process, then the probability density functions (PDFs) of travel distance and resting time are exponential, as shown in equations (1) and (2). The parameter k_1 is the reciprocal of the mean travel distance and k_2 is the reciprocal of the mean resting time.

$$f(\Delta x) = k_1 e^{-k_1 \Delta x} \tag{2.3}$$

$$f(\Delta t) = k_2 e^{-k_2 \Delta t} \tag{2.4}$$

Combining equations (2.3) and (2.4) and assuming that the time spent is motion is negligible compared to the time at rest yields the joint probability density function of position and time:

$$f(x,t) = k_1 e^{(k_1 x + k_2 t)} \sqrt{\frac{k_2 t}{k_1 x}} I_1 \left(2\sqrt{k_1 x k_2 t} \right) \tag{2.5}$$

where x is distance from the tracers origin, t is elapsed time, and I_1 is a modified Bessel function of the first kind of order one. If the number of tracers is sufficiently large as to approximate infinity, then equation (2.5) is also a prediction of the relative concentration.

The two parameters of the Sayre and Hubbell model, k_1 and k_2, were calibrated by setting the theoretical predictions of the mean velocity and the rate of decay of the peak concentration equal the observed rates and solving for k_1 and k_2. Their parameter choices predict that a grain travels an average of 36 feet during an episode of motion followed by an average stationary interval of 12 hours.

$$k_1 = \frac{1}{36 \text{ ft}}, k_2 = \frac{1}{12 \text{ hrs}} \tag{2.6}$$

The model predicts that the mean position of the particle plume will move according to equation (2.13) at a mean velocity that is given by the ratio of average step distance and average resting time.

$$\bar{u} = \frac{k_2}{k_1} = 3 \text{ ft / hr} \tag{2.7}$$

The mean velocity Sayre and Hubbell used to calibrate their model is slightly higher than the regression shown in Figure 2.4 because they used data from the left, right, and center traverses in their regression, adjusted some data points, and excluded others. We use all the data from the right side of the channel in the regression shown in Figure 2.4.

The Sayre and Hubbell model given in equation (3) is shown as a solid black line in Figure 2.3. Qualitatively, the Sayre and Hubbell model predicts the observed concentration reasonably well. The amplitude and location of the theoretical curves are approximately the same as the data, though this is largely a result of the velocity calibration, the choice of how to scale the data, and an ad hoc parameter added to the model.

The model predicts observed concentration approximately, but it is not perfect. The most obvious weakness of the model is that it fails to capture the amount of mass in the leading edge of the tracer plume. Though this is difficult to see in linear space, it becomes evident when the data and the model are plotted in log space, as shown in Figure 2.6. The concentration of tracer particles several hundred feet downstream of the peak is as much as several orders of magnitude higher than the model predicts. This is especially clear during the middle of the study, from 70.9 hours to 107.1 hours. The reason that the model appears to catch up with the data towards the end of the study is that Sayre and Hubbell did not measure further downstream than 1800 ft. If they had, the leading edge of the tracer plume would presumably extend well downstream of 1800 ft.

A second weakness of the model is that it requires an ad hoc parameter, a 110-foot downstream shift, to match the location of the data. This is a consequence of the high initial high velocity of the tracer plume, probably because the tracer sand was poured onto the bed surface at the start of the experiment. The need for the offset is indicated by the intercept of the regression in Figure 2.4. As with the mean velocity, our regression differs slightly from theirs because we use a slightly different set of data in the regression.

A final drawback of the model is that it fails to predict that the total amount of mass detected on a traverse will decay with time. Figure 2.5 shows the zeroth moment of the concentration distribution at each measurement time. The observed decay in detectable tracer mass affected Sayre and Hubbells choice of how to convert the absolute concentrations to relative concentrations. The normalization factor that is supported by the theoretical model is the initial zeroth moment, $\mu_{0i} = W/Bd = 250.2$ grams/ft^2, but there are two problems with this choice. First, the observed μ_0 at the first two measurement times is greater than the assumed initial zeroth moment, indicating that more mass than that indicated by W/Bd is contributing to

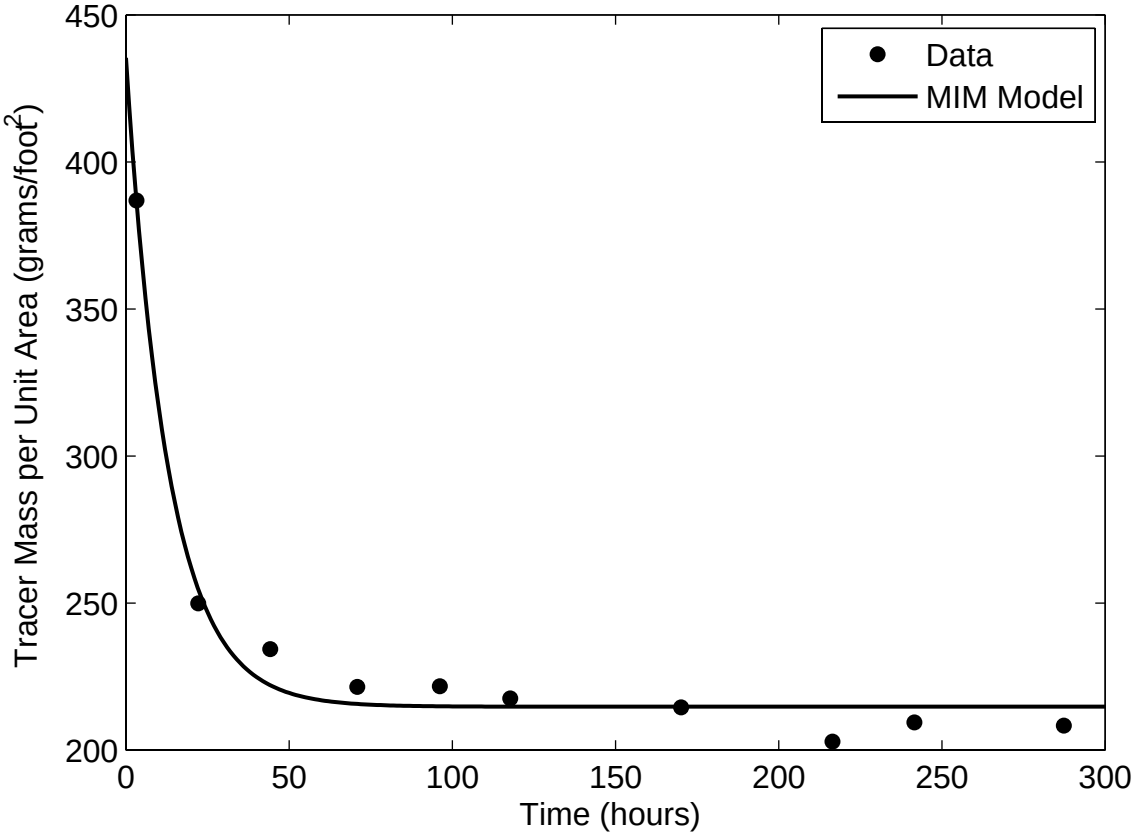

Figure 2.5: The total tracer mass detected per unit area (black dots), or zeroth moment, declines over the course of the study. The Sayre and Hubbell model does not predict this, but the mobile/immobile model does. The solid black line is the best fit of equation (2.9) to the data.

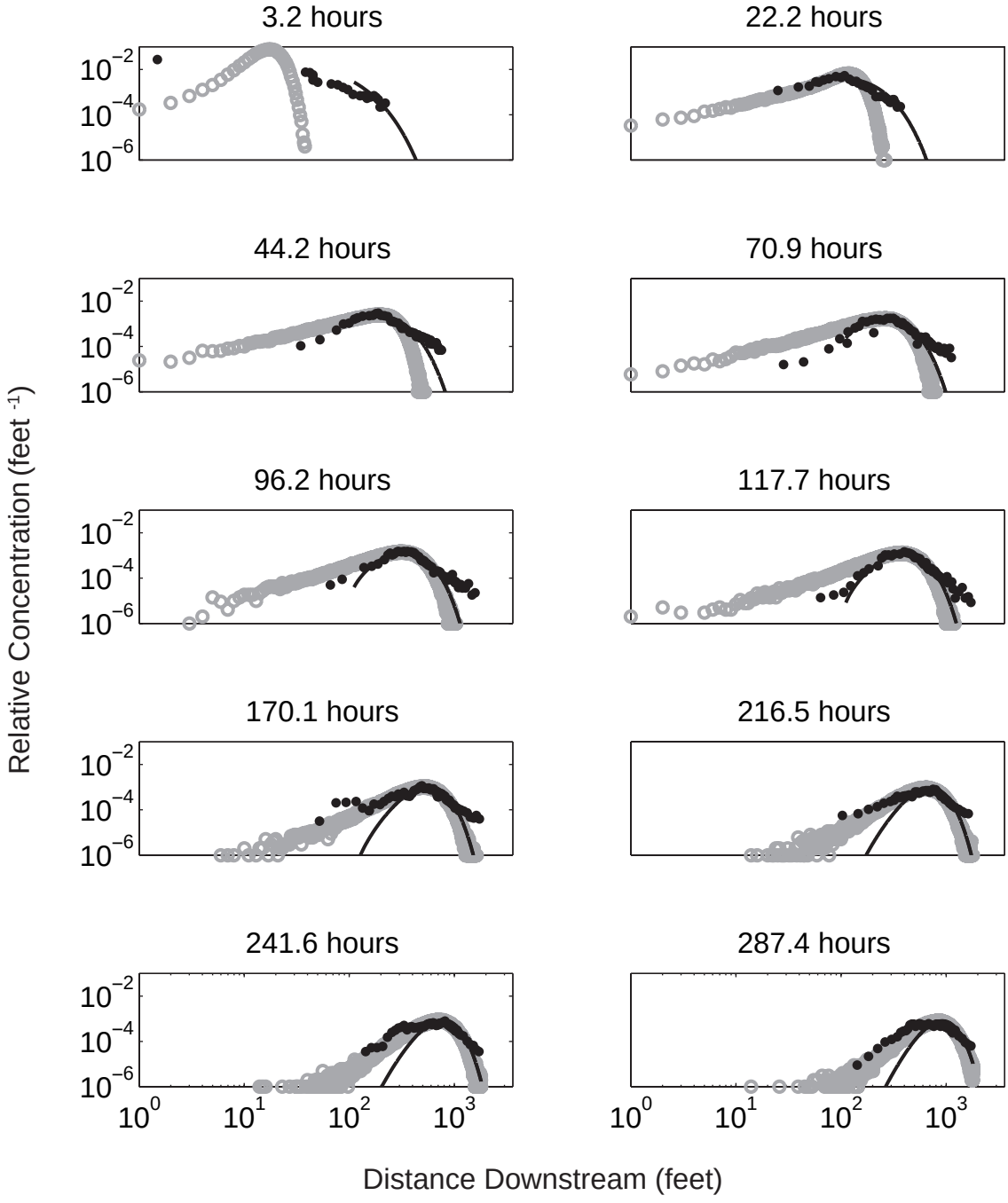

Figure 2.6: Our Gaussian mobile/immobile model (gray circles) compared to the N. Loup River data (black dots) and the Sayre and Hubble model (solid black line) in log-log space. The data and the Sayre and Hubbell model are scaled as shown in equation (2.11). The MIM predicts the observed concentrations about as well as the Sayre and Hubbell model, but fails to capture the relatively high concentration of tracer material downstream of the peak.

the tracer plume. Second, the observed concentration profiles scaled by μ_{0i} would have generally lower amplitudes than the model prediction because the total detected mass declines with time. To compensate for this, Sayre and Hubbell chose to scale the data by the current zeroth moment $\mu_0(t)$, which corresponds to the observed mass per unit longitudinal cross-section area at a particular time t, rather than μ_{0i}. The approximate equivalence of this normalization of the data and the model is expressed in equation (2.8).

$$\frac{C\,(x,t)}{\mu_0\,(t)} \sim f(x,t) \tag{2.8}$$

The fact that this normalization choice worked as well as it did is a hint there may be tracer mass exchanged between a mobile, detectable phase and an immobile, non-detectable phase. In the next section, we explore two versions of a model that accounts for exchanges between a detectable phase and an undetectable phase.

2.3.4 Re-analysis of Tracer Plume Data

In this section, we re-analyze the Sayre and Hubble tracer plume data using an alternative model that divides the plume into a mobile, detectable phase and an immobile, undetectable phase. The mobile-immobile model (MIM) predicts that at any given time during the Sayre and Hubble experiment, some fraction of the tracers was buried below the detection limit.

Mobile/Immobile Transport

The single rate mobile/immobile (MIM) model described by Harvey and Gorelick (2000, van Genuchten and Wierenga, 1976; Valocchi, 1989; Goltz and Roberts, 1987; Harvey and Gorelick, 1995; Haggerty and Gorelick, 1995) predicts that the tracer mass detected in a transport system will evolve over time to an equilibrium value that is less than the total tracer mass. This occurs because the model partitions transport into a detectable mobile phase and an undetectable immobile phase. Only mass in the mobile phase is visible to the detector. In groundwater contaminant transport, the immobile phase represents tracer mass that is somehow sequestered and therefore not flowing past the detector. In the case of the Sayre and Hubble experiment, the immobile fraction represents tracer grains that are buried so deeply that they are below the active transport layer and the gamma ray emissions are shielded by overlying sediment.

The MIM model is attractive because it predicts the decay in detected tracer mass shown in Figure 2.5. If all the tracer particles start in the mobile phase,

Table 2.1: Best-fit mobile/immobile parameters.

Parameter	Description	Range	Winning Value
μ_0	Initial mobile concentration	100–1000 g/ft^2	433.4 g/ft^2
τ_m	Mean time in mobile phase	1–50 hours	25.6 hours
τ_{im}	Mean time in immobile phase	1–50 hours	26.3 hours

the model predicts that the zeroth moment of the concentration profile will decay exponentially to an equilibrium value as particles are sequestered in the undetectable immobile phase. The decay curve for the mobile fraction, $\mu_0(t)$, as a function of time depends on the initial mobile zeroth moment, μ_{0i}, the average amount of time spent in the mobile phase, τ_m, and the average amount of time in the immobile phase, τ_{im} (Harvey and Gorelick, 2000):

$$\mu_0(t) = \frac{\mu_{0i}}{1+\beta}\left(1 + \beta e^{-\alpha(1+\beta)t}\right) \tag{2.9}$$

$$\beta = \frac{\tau_{im}}{\tau_m}, \alpha = \frac{1}{\tau_{im}} \tag{2.10}$$

The factor $1/1+\beta$ represents the fraction of mass in the mobile phase at equilibrium It is important to note that the transport phases of the MIM model are not strictly analogous to the steps and rests of the Sayre and Hubbell model. A particle in the mobile phase may be in motion or at rest at any given time. The only requirement of the mobile phase is that a particle is detectable. The immobile phase differs from a Sayre and Hubbell rest because immobile particles are undetectable. The Sayre and Hubbell model has no mechanism for representing undetectable particle.

We can estimate the three parameters in equation (2.9) by fitting it to the observed zeroth moment shown in Figure 2.5. The solid black line in Figure 2.5 shows equation (2.9) fit to the N. Loup River data. We varied the parameters over the ranges listed in Table 2.1 and selected the curve that minimized the sum of the squares of the residuals.

In equation (2.6), we stated that there is general agreement between the scaled data shown in Figure 2.3 and the Sayre and Hubbell model given in equation (2.5). Equation (2.8) is unsatisfying because the choice to normalize the data by the $\mu_0(t)$ has no theoretical support in the Sayre and Hubbell model. The MIM model, because it predicts a decay in detectable mass over time, suggests an alternate scaling. If we

move $\mu_0(t)$ to the right side of the equation (2.8) and divide both sides by the initial mobile zeroth moment μ_{0i}, we get equation (2.11).

$$\frac{C(x,t)}{\mu_{0i}} \sim \frac{\mu_0(t)}{\mu_{0i}} f(x,t) \tag{2.11}$$

The factor $\mu_0(t)/\mu_{0i}$ represents the fraction of the initial tracer mass that is detectable and is equivalent to $1/1+\beta$ (the equilibrium fraction of the total mass in the mobile phase) from equation (2.9). The reason why Sayre and Hubbells decision to scale the concentration profiles by $\mu_0(t)$ works as well as it does is that it implicitly transforms the model into a prediction of the mobile phase concentration.

In Figure 2.6, we show the alternate scaling of the Sayre and Hubbell data (black dots) and model (solid black line) described by equation (2.11) in log-log space. Since equations (2.8) and (2.11) are mathematically identical, the agreement between the Sayre and Hubbell model and data shown in Figure 2.6 is identical to that shown in Figure 2.3, but the scaling of the data is more satisfying. The Sayre and Hubbell model provides no theoretical justification for the scaling choices in equation (2.11), but the mobile/immobile model does. This suggests that the MIM model is a more appropriate representation of the transport system.

Particle Tracking Implementation of the MIM model

Our one-dimensional mobile/immobile particle-tracking model is similar to those described by Valocchi et al. (1989), Zhang et al. (2006) and by Benson and Meerschaert (in submission). Particle motion is governed by four adjustable parameters: the average amount of time spent in the mobile phase τ_m, the average amount of time in the immobile phase τ_{im}, the average velocity in the mobile phase $\bar{u}_m$, and the mean of a random velocity fluctuation, $\bar{u}'$. The values of the first two parameters, τ_m and τ_{im}, are determined by fitting equation (2.9) to the zeroth moment of the data, as described above. The choice of velocity parameters is discussed below.

All particles start in the mobile phase. The model assigns each particle a random "flight time" t_f chosen from an exponential distribution with mean τ_m and a velocity given by:

$$u = \bar{u} + u' \tag{2.12}$$

where u is a random fluctuation with mean $\bar{u}'$ (equal to zero in the first implementation of the model discussed below, but possibly non-zero in the second).

The total distance a particle travels during a visit to the mobile phase is$\Delta\, x = ut_f$. When a particle reaches the end of its time in the mobile phase, the model assigns it to the immobile phase for a random interval chosen from an exponential distribution

with mean τ_{im}. At each time step, the model computes the particle concentration by binning the "study reach" at 1-foot intervals and counting the number of particles in each bin. We run the model with a time step size of 2 minutes for 300 hours, the approximate duration of the Sayre and Hubbell study. In the following sections, we discuss two versions of the model outlined above which are identical in all respects except one. In the first, the velocity fluctuations are chosen from a standard normal distribution and in the second they are chosen from a distribution with a heavy power-law tail.

Gaussian Mobile/Immobile Model

The mean velocity of the model particle plume is a function of the four model parameters:

$$\bar{u} = \frac{(\bar{u}_m + \bar{u}')\tau_m}{\tau_{im} + \tau_m} \tag{2.13}$$

The average times spent in the mobile and immobile phases, τ_m and τ_{im}, respectively, are determined by fitting equation (2.9) to the observed decline in $\mu_0(t)$ as described above and shown in Figure 2.5. To determine the two components of particle velocity in equation (2.13), we set the right-hand side of equation (2.13) equal to the observed mean velocity, shown in Figure 2.4, and solve for $(\bar{u}_m + \bar{u}'_m)$.

In the first version of our model we follow the approach used by Valocchi (1989) to simulate solute transport in an aquifer. We dictate that the velocity fluctuation in equation (2.12) comes from a standard normal distribution, $N(0, 1)$. This eliminates the mean velocity fluctuation in equation (2.13), reducing the number of model parameters to three, all of which we can estimate from the Sayre and Hubbell data.

$$\bar{u} = \frac{\bar{u}_m \tau_m}{\tau_{im} + \tau_m} \tag{2.14}$$

$$\begin{aligned} \bar{u} &= 2.8 ft/hr \\ \bar{u}_m &= 5.6 ft/hr \\ \tau_m &= 25.6 hrs \\ \tau_{im} &= 26.3 hrs \end{aligned}$$

Figure 2.6 shows the concentration profiles from the Gaussian mobile/immobile model plotted as gray circles. Figure 2.7 shows the average position of the model particle plume. After 70 hours, the model describes the data about as well as the Sayre and Hubbell model, without the need for an ad hoc 110-foot offset. Our model

achieves a high initial velocity because all particles start in the mobile phase, moving at an average velocity of 5.6 ft/hr for an average time of 25.6 hours before exchange with the immobile phase slows the overall velocity to 2.8 ft/hr. The model lags behind the data early on because we only capture about half of the high initial velocity seen in the Figure 2.4. This is shown by the intercept of the regression in Figure 2.7 at about 55 feet, rather than at about 110 feet. The model does not capture the anomalously high concentrations in the leading edge of the data. For that, we turn to the second form of the model.

α-Stable Mobile/Immobile Model

In this version of the model, we replace the normally distributed velocity fluctuations with fluctuations drawn from a probability distribution with a power-law tail, the α-stable distribution. The α-stable distribution is useful for modeling highly variable data sets because it can be skewed positively or negatively and it assigns much higher probability to extreme values than a Gaussian or exponential distribution. A complete discussion of the properties of α-stable distributions is beyond the scope of this paper. We refer the reader to discussions by Samorodnitsky (1994), Benson et al. (2000), and Nolan (2009).

We use the parameterization described by Nolan (2009) as $S(\alpha, \beta, \gamma, \delta\,; 0)$, where α is the index of stability, β is the skewness, γ is the scale, and δ is the location. Following Zhang et al. (2006), we prescribe the value of three parameters of the distribution, $\beta = 1$, $\gamma = 1$, and $\delta = 0$, and vary α over the range $0 < \alpha \leq 2$. The parameter α controls how likely large deviations from the location parameter δ are. When $\alpha = 2$, the distribution reduces to a Gaussian and large deviations from the mean are very unlikely. When α is in the range $1 < \alpha < 2$, extreme values are so likely that the integral describing the second moment of the distribution, the variance, diverges. When α is in the range $0 < \alpha \leq 1$, the first moment, the mean, also diverges. In practice, a divergent first or second moment means that the statistic measured from a finite sample size is dominated by the largest value and will tend to increase with increasing sample size (Sornette, 2004).

A positively skewed ($\beta > 0$) α-stable distribution in the range $1 < \alpha \leq 2$ with a location parameter $\delta = 0$ has a non-zero mean given by $\mu_1 = -\beta\gamma \tan(\pi\alpha/2)$ (Nolan, 2009). We have found that calculating the mean mobile velocity according to equation (2.13) with $\bar{u}'$ equal to the mean of the α-stable velocity distribution results in poor agreement between the model mean velocity and the observed mean velocity. This is because the mean of a heavy-tailed distribution is dominated by the largest values and is not necessarily the best descriptor of the distribution. Instead,

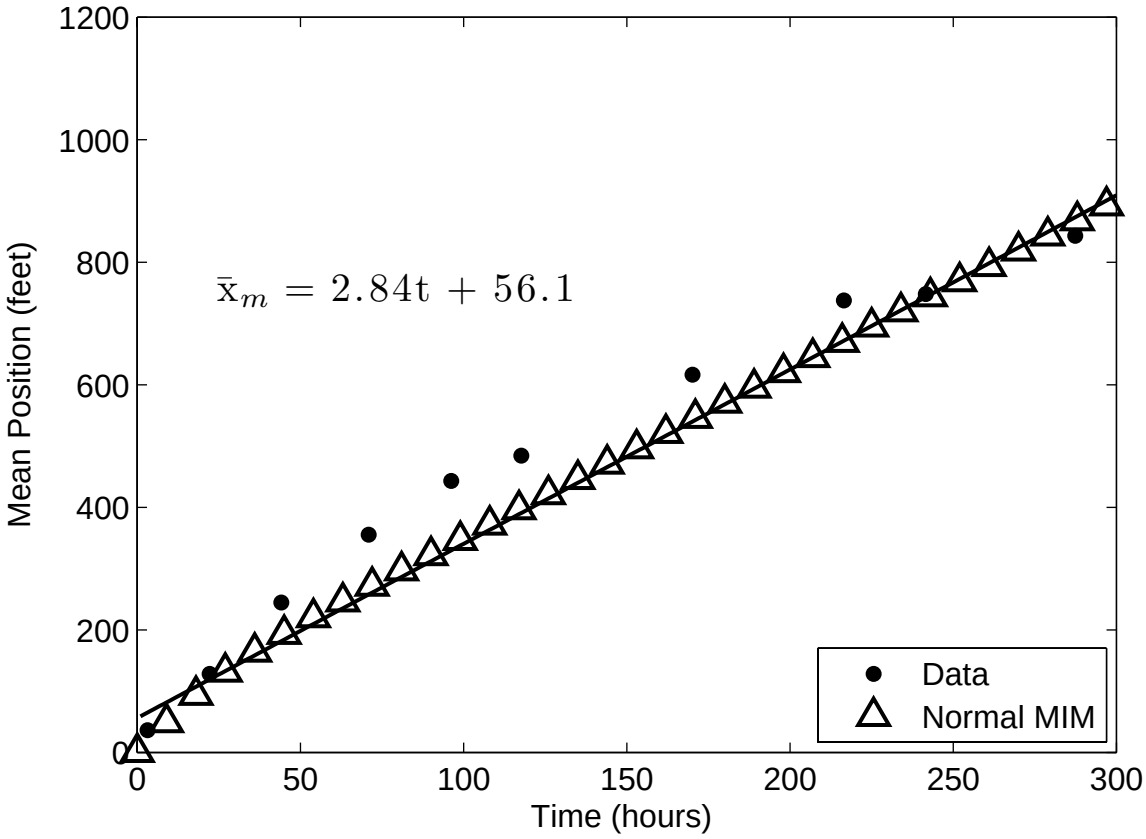

Figure 2.7: The mean position of the Gaussian mobile/immobile model concentration profiles (black triangles) shown in Figure 2.6, along with the data (black dots), and a regression on the model data (solid black line). Our model plume moves at an average velocity of 2.84 ft/hr, similar to the average observed velocity shown in Figure 2.4, but we do not capture all of the high initial velocity as indicated by the intercept of the regression.

we find that the median of the α-stable distribution is more useful for our purposes. We varied α until the tails of the model concentration curves had approximately the same slope as the data and then used the median of the velocity distribution in place of $\bar{u}'$ in equation (2.13) to solve for the mean mobile velocity.

Figure 2.8 shows the model concentration profiles for $\alpha = 1.1$, $\bar{u}_m = 5.0 ft/hr$, and $\bar{u}' = 0.6 ft/hr$. After 20 hours, the model accurately predicts the magnitude and location of concentration curve without any ad hoc adjustments. The model also predicts the concentration in the leading edge of the concentration profile. Figure 2.9 shows the mean position of the model tracer plume. The predicted mean velocity is about 4 inches per hour higher than the observed mean and the intercept of the regression is about 20 feet less than the Sayre and Hubbell regression. Other values of α in the range $0.8 \leq \alpha \leq 1.3$ also result in reasonable fits to the data. Higher values of α in this range slightly under predict the concentrations in the leading edge of the distribution. Values of α at the low end of the range match the tail, but the peak concentration drops below the data because the zeroth moment of the model distribution starts to drop well below the predicted curve shown in Figure 2.5. This is because low values of α make long travel distances so likely that many particles pass completely out of the measurement domain.

2.3.5 Discussion

The theoretical model Sayre and Hubbell developed to describe their data treats particle motion as a series of alternating steps and rests of random length and duration. With the addition of a third ad hoc parameter that shifts the predicted concentration curve downstream, the model approximates the observed concentration profiles, but has two remaining weaknesses. First, because the model does predict that the total amount of mass detected will decline over time, the data have to be normalized by the zeroth moment for the amplitude of the concentration curves to match the model. Second, the observed concentrations far downstream of the peak are much higher than the model predicts.

We applied a mobile/immobile model to the Sayre and Hubbell data that addresses these problems. The model predicts that the amount of detectable mass will decay to an equilibrium value based on the rate of exchange between the detectable mobile phase and the undetectable immobile phase. This model provides a theoretical justification for the way Sayre and Hubbell chose to normalize their data. We attribute the observed decay in detectable tracer mass to exchange with an undetectable, immobile zone in the bed, while Sayre and Hubbell suggested that mass loss during the experiment might be caused by abrasion of the radioactive coating on

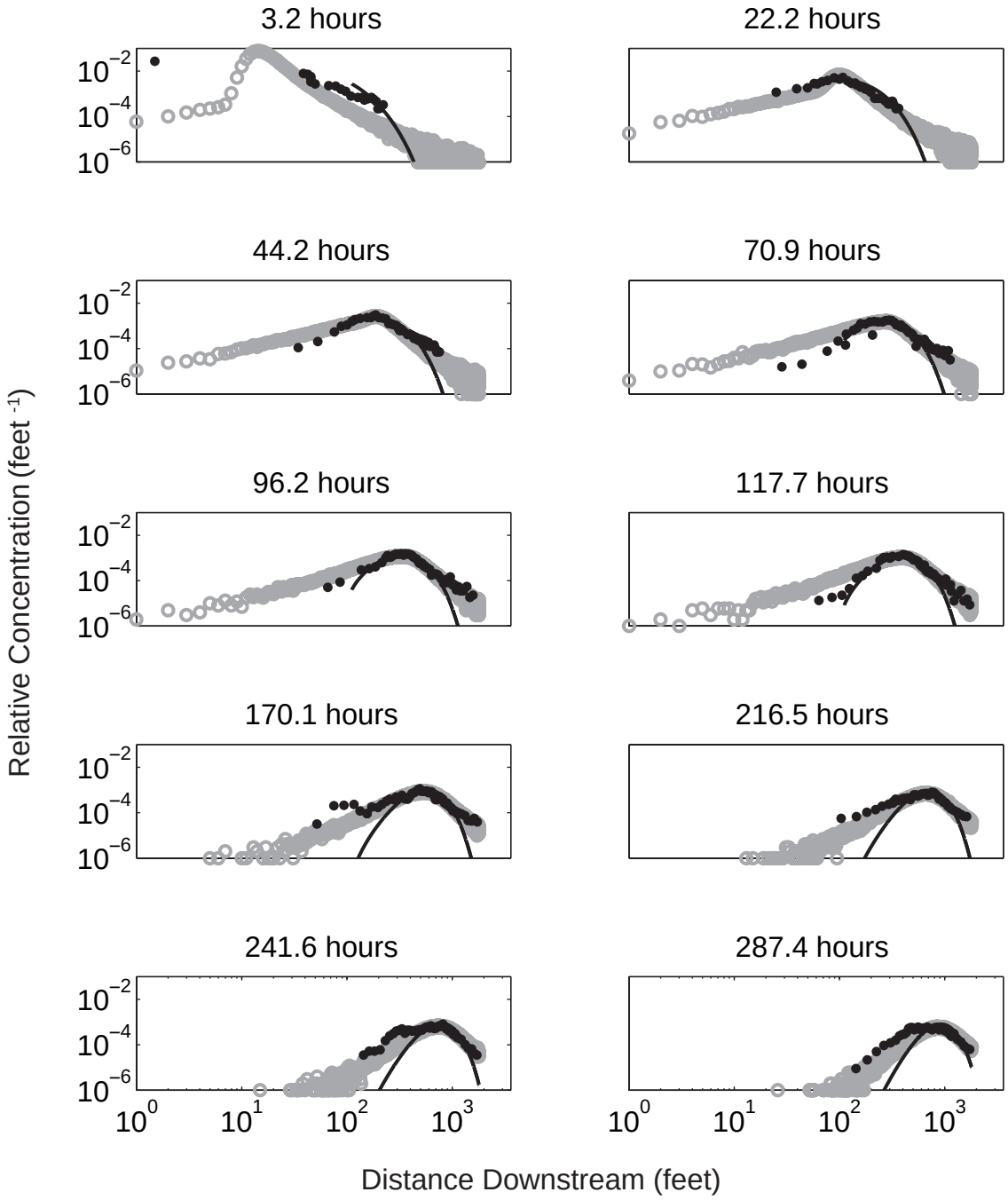

Figure 2.8: The α-stable mobile/immobile model (gray circles) compared to the Sayre and Hubbell data (black dots) and model (solid black line).

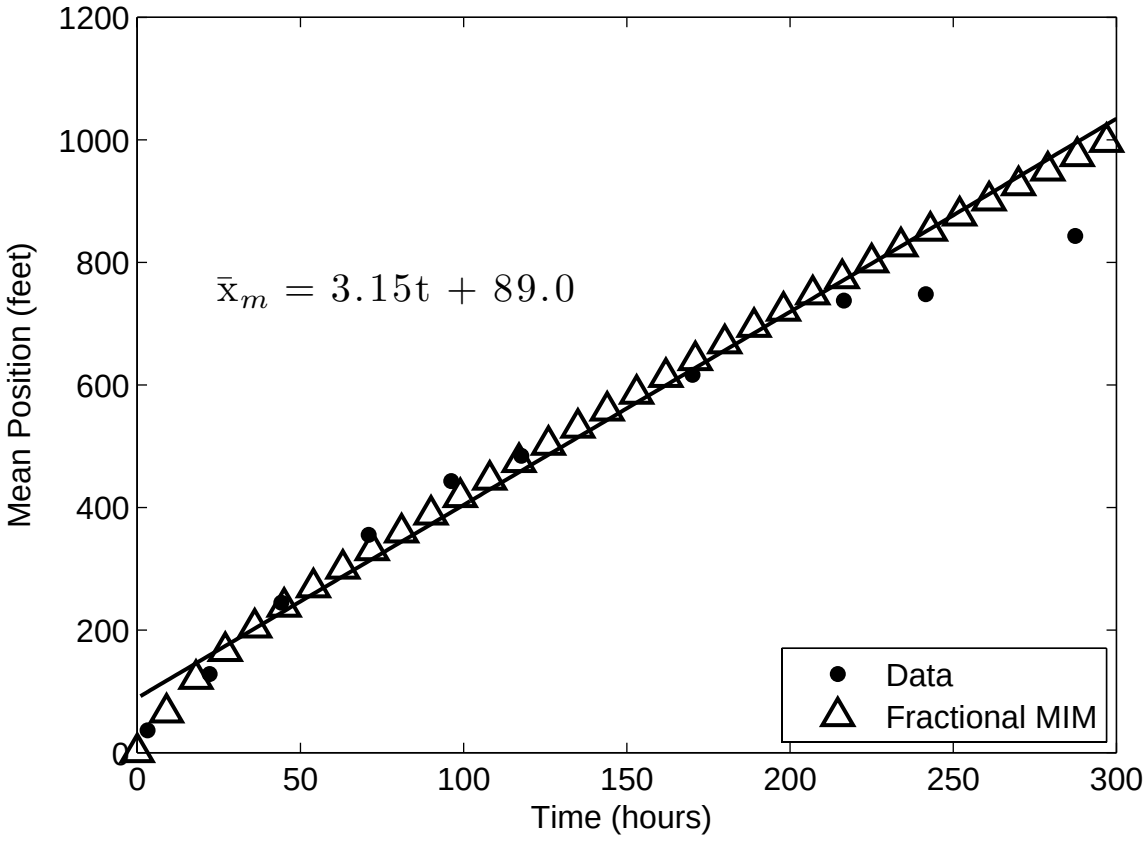

Figure 2.9: The mean position of the model concentration profiles shown in Figure 2.8.

the sand grains. Another possible explanation for the mass loss is that tracer mass exited the system all together. In reality, it seems likely that all three factors played a role, but the decay of the zeroth moment to an approximately equilibrium value and the success of the MIM model in predicting the concentration profiles suggest that the latter two factors may be safely ignored.

We implemented two versions of the model that differ only in the shapes of the mobile particle velocity distributions. The Gaussian version predicts the observed concentration curves about as well as the Sayre and Hubbell model, but fails to capture the high concentration in the leading edge of the tracer plume. The second version of the model uses a heavy-tailed distribution of velocity. This version predicts the data well, with just one more parameter than the Sayre and Hubbell model.

The α-stable MIM captures the relatively high concentrations observed far downstream of the peak because the broad distribution of particle velocity in the mobile phase results in a similarly broad distribution of particle travel distance. The agreement between our model concentration curves and the data suggests that a distribution with a heavy power-law tail is a better model for tracer travel distance than the exponential distribution used by Sayre and Hubbell.

Random walk models like ours and the Sayre and Hubbell model typically result in concentration profiles that can be described by an advection-diffusion equation (ADE). Since Einstein's (1905) paper on Brownian motion, it has been known that random walks in which the distributions of travel distance and resting time have finite first and second moments are described by the Ficks form of the ADE. The 1-dimensional form given in equation (2.15) describes the evolution of a tracer concentration profile in terms of the mean velocity, $\bar{u}$, and the diffusivity, D, which is a function of the variance of tracer position.

$$\frac{\partial C}{\partial t} = -\bar{u}\frac{\partial C}{\partial x} + D\frac{\partial^2 C}{\partial x^2} \tag{2.15}$$

$$D = \frac{\sigma_x^2}{2t}$$

The Sayre and Hubbell model treats step length and resting time as exponentially distributed random variables and therefore obeys equation (2.15) in the infinite time limit. The evolution of the first moment the Sayre and Hubbell model is given by equation (2.7). The second moment of the distribution, the variance, is a measure of how the plume spreads. The second moment of equation (2.5) is a function of the model parameters and time.

$$\sigma_x^2 = \frac{2k_2}{k_1^2}t \tag{2.16}$$

The linear growth of the variance with time shown in equation (2.16) is required for the diffusivity coefficient in equation (2.15) to be constant and to have the proper units (L^2/T). This scaling of the variance is the hallmark of Fickian transport described by equation (2.15).

Our Gaussian MIM model obeys a similar transport equation, with the addition of a term that describes exchange with the immobile phase. (Schumer et al., 2003).

$$\frac{\partial C_m}{\partial t} + \beta \frac{\partial C_m}{\partial t} = -\bar{u} \frac{\partial C_m}{\partial x} + D \frac{\partial^2 C_m}{\partial x^2} \tag{2.17}$$

The α-stable model uses a velocity distribution that has a divergent second moment, which requires a transport equation that is fractional in space (Meerschaert et al., 1999; Benson et al., 2000). This is accomplished by replacing the second-order spatial derivative in equation (2.15) with a fractional derivative of the same order as the index of stability of the velocity distribution, α. The space-fractional advection-dispersion equation (fADE) for the mobile phase is given by equation (2.17).

$$\frac{\partial C_m}{\partial t} + \beta \frac{\partial C_m}{\partial t} = -\bar{u} \frac{\partial C_m}{\partial x} + D \frac{\partial^\alpha C_m}{\partial x^\alpha} \tag{2.18}$$

Equation (14) predicts that the tracer plume will spread out, as measured by the growth of the variance, as a non-linear function of time. Specifically, the variance grows proportionally to $t^{2/\alpha}$ and the diffusivity has the dimensions of L^α/T instead of the usual length squared over time (Benson et al., 2000). This type of dispersion is known as anomalous dispersion, or non-Fickian transport. Anomalous dispersion has been observed in many transport systems (see Metzler and Klafter, 2000 and Metzler and Klafter, 2004 for discussions of anomalous transport in a variety of settings), but to our knowledge, only Nikora et al. (2002) has previously discussed anomalous transport in fluvial sediment transport. They videotaped gravel moving across the bed of a canal in New Zealand and estimated the growth of variance of particle position. Their result would correspond to an α of about 1.3 in our model.

Our model predicts that the velocity of particles in the North Loup River experiment is heavy-tailed. Heavy-tailed distributions can be produced by a number of mechanisms (see Newman, 2005 and Sornette, 2004 for an overview). One of the simplest is the combination of several thin-tailed distributions. For example, if the random variable X is exponentially distributed with a rate parameter λ, and λ is also a random variable that is exponentially distributed, then the overall distribution of X is a Cauchy distribution. A Cauchy distribution is equivalent to an α-stable distribution where $\alpha = 1$ (Sornette, 2004, Meerschaert, personal comm., 2007). To give another example, the step length distribution in the Sayre and Hubbell model is

exponentially distributed because they treat transport of an entrained grain a Poisson process: The probability of deposition during an episode of motion is constant, so the flight time and the travel distance (if the velocity is constant) are exponentially distributed. If the shear stress in the stream varies spatially or the transport characteristics of a population of grains are variable then the probability of deposition would also be a random variable. If probability of deposition is exponentially distributed, then the overall distribution of travel distances that is heavy-tailed. We are not suggesting that this is the specific mechanism responsible for the apparently broad distribution of particle velocity in the Sayre and Hubbell experiment. This example is chosen to illustrate that heavy-tailed distributions do not require exotic origins.

2.3.6 Appendix: Description of data digitization and moment computation

We were unable to obtain the data in table form from the USGS (Glenn Cook, USGS Field Records Librarian, personal communication 12/07), so we scanned the plots of the data from the 1965 publication at 300 dots per inch. Using ArcMap, we built a table of control points selected along the axes to map pixel space to data space. We rectified each image and picked the center of each data point in the transformed image, recording the longitudinal coordinate (in feet) and the concentration (in grams per cubic foot) for each measurement time presented by Sayre and Hubbell.

2.4 Laboratory Experiments on Fluvial Sediment Motion and Dispersion

In June 2008, we performed an experiment designed to determine the mode of dispersion of tracer particles across a homogenous bed driven by steady, uniform flow at a discharge that is near the threshold necessary to move sediment. We installed a patch of painted aquarium gravel on the bed of a flume and used digital cameras arrayed along the side of the flume to photograph the particles at one-minute intervals as they moved downstream. Using scripts that utilize functions from the Matlab Image Processing Toolbox, we can estimate the concentration of tracer particles (in number of tracers per unit length) along the full length of the flume. This experiment was designed to complement two other projects already in progress, the Halfmoon Creek tracer experiment and the reanalysis of the data from the N. Loup River experiment performed by Sayre and Hubbell in the early 1960s.

We used the 7-meter tilting flume at the USGS Geomorphology and Sediment Transport Laboratory in Golden, Colorado, for our experiment. The length of flume useable for gravel transport experiments is about 5 meters long. We covered bottom of the flume with 4-6 mm aquarium gravel to a depth of about 10 cm. Using a piece of plywood attached to a cart on rails running along the top of the plume, we scraped the surface of the gravel bed until it was parallel to the plexiglass bottom of the flume. We set slope of the flume to about 3.5×10^{-3} m/m and filled the flume with water to a depth of about 16 cm above the gravel bed. Then we increased the discharge until gravel began to move.

The flume did not have a mechanism for adding or re-circulating sediment so creating an equilibrium bed was something of a challenge. The inlet of water at the upper end of the flume tended to excavate sediment from the upper meter of the flume. The excavated sediment formed an aggradational wedge that migrated slowly downstream, raising the elevation of the bed by several centimeters as it passed. When the wedge reached the sediment trap at the bottom of the flume, about 3.5 meters of flume bed were at approximately equilibrium conditions as determined by steady sediment thickness at points along the flume and qualitatively uniform transport characteristics along the study reach. This process was extremely time consuming and limited the number of experimental runs we were able to perform.

Once the lower part of the bed reached approximate equilibrium, we turned off the pump and installed 1000 blue tracer grains in a 1 grain thick, 30 cm long, seed patch at the upper end. The tracer grains were aquarium gravel sieved to a size of 5.6 to 8 mm from the same source as the bed material and painted with several coats of bright blue spray paint. The tracer grains were slightly larger than the median grain size on the bed. Figure 2.10 shows initial arrangement of the grains from a run on June 17th.

To record the position of the grains along the flume, we used an array of digital cameras attached to the side of the flume and aimed diagonally through the plexiglass sidewall. We chose this camera orientation because turbulence on the surface of the water makes it difficult to get a clear picture from above. Using a laptop computer attached to the cameras via USB, we controlled the cameras remotely using a software package called PSRemote. The software was not as stable as we expected, but we were able to get reasonably good performance using six cameras taking one exposure per minute. PSRemote crashed sporadically and unpredictably, which caused us to miss exposures at some of the one-minute intervals. This was an inconvenience, but not a major problem since a typical flume run lasted three hours and the system did not evolve rapidly enough that a handful of missing measurements made a big difference.

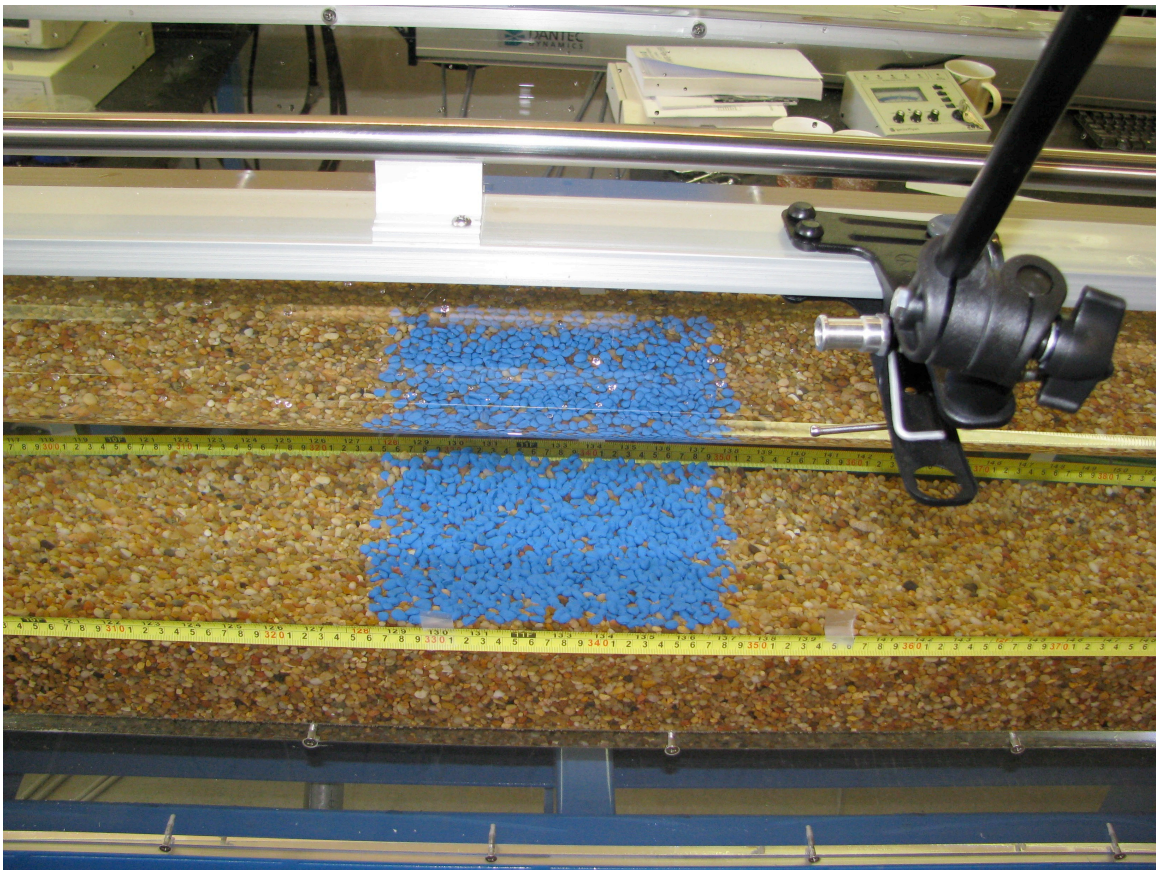

Figure 2.10: 1000 tracer grains arranged in a one-grain thick layer at the start of the experiement.

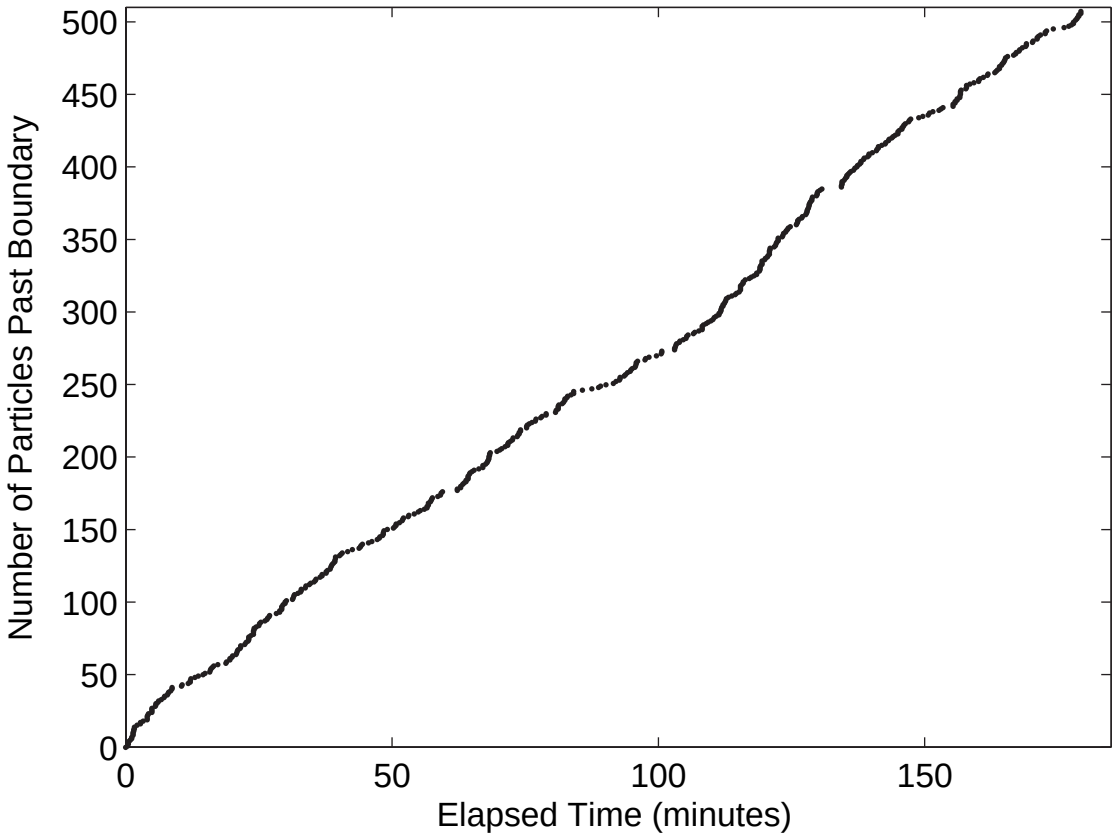

Figure 2.11: The number of particles past the downstream boundary of the flume vs. time. The flux is nearly constant, 2.8 particles per minute, across the boundary.

In one of the runs of the experiment, we also recorded the time at which tracer grains crossed a line at the bottom of the flume. We did this by clicking a key on a laptop keyboard each time tracer crossed the line and recording the time with a simple computer program. These data are shown in Figure 2.11 as the total number of particles past the boundary vs. time. The data show a nearly constant flux of about 2.8 particles per minute across the boundary.

Analysis of the photographs of a flume run is a multi-step process. First, we define the useful area of the image for each camera in terms of the upper left and lower right corner. These points are used to crop the image. Second, we build a table of control points for each camera that map the pixel space to the physical space. This done by manually picking and recording the pixel coordinates of corresponding locations

along the tape measure (see Figure 2.10) along the front and back of the flume. We use at least 7 pairs of points for each camera. With the table of control points, we use the Matlab Image Processing Toolbox to apply a piecewise linear transformation that removes the distortion in the image caused by shooting from the side of the flume. This transformation morphs the image into a rectangle with a direct linear mapping between pixel space and physical space. Finally, we examine the blue and red channels of the RGB image and select groups of pixels larger than a threshold that have a high amount of blue and a small amount of red. The location of the centroid of each selected pixel group is used as the location of the tracer grain.

Unfortunately, analysis of the data is not yet complete. The image-processing algorithm tends to undercount the number of tracer grains in a frame, particularly when the concentration is high and grains are touching. We anticipate that we will be able to resolve this problem in the near future. We are also limited because we have data from only two runs of the experiment. This is due to an injury that occurred during the experiment and limited the amount of time we could spend at the laboratory in June to two weeks. Once the data we have has been analyzed to our satisfaction, we plan to return to the lab to perform more runs of the experiment.

Despite the limitations described above, we may be able to draw some tentative conclusions if we assume that the undercounts are systematic and that the small data set we have is representative. First, the concentration profiles are approximately steady in time, at least early in the experiment. Figure 2.12 shows the estimated concentration profiles after 8 minutes and 63.6 minutes of elapsed time. Upstream is on the right side of the plot for consistency with the orientation of the cameras and tape measure during the experiment. The flume-wise coordinates of the tracers were binned at 10 cm intervals to compute a number density per unit length. The number density divided by the initial number density is the concentration. These profiles are consistent with our impression during the experiment that the overall spatial distribution of particles was approximately steady and that is consistent with the constant flux across the boundary shown in Figure 2.11. Second, the profiles appear to be consistent with a model in which the entrainment probability of a grain is low, but the probability distribution of travel distance is broad, but more work is required before we can assert this with confidence.

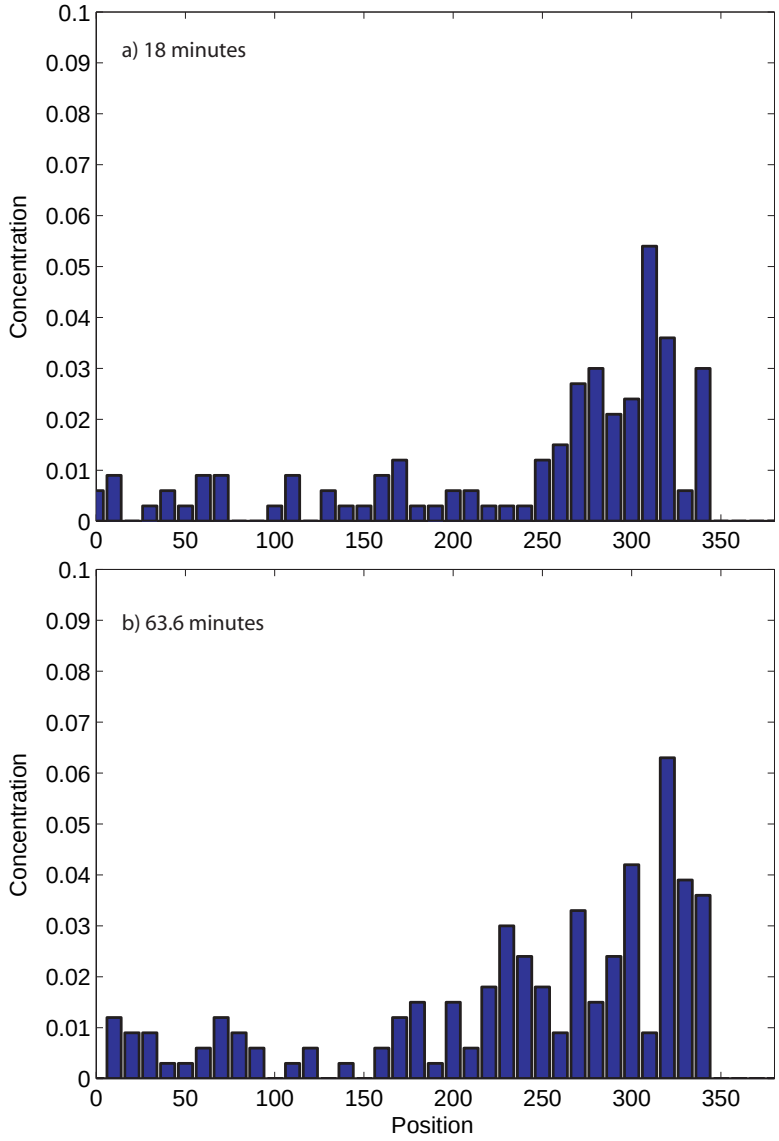

Figure 2.12: Preliminary concentration profiles for two times. Upstream is to the right. a) 18 minutes b) 63.6 minutes.

2.5 Field Experiment in Gravel Transport and Dispersion using Passive Radio Tracking

(Note: the experiment described in this section was jointly funded by this project and by a supporting Innovative Research Grant from the Cooperative Institute for Research in Environmental Sciences, which provided funds for the purchase of radio tags and detection equipment).

The most direct way to test the mode of sediment dispersion is with a time series of the positions of uniquely identifiable tracer particles. A sediment pulse that disperses normally will move downstream as a plume of particles in which the mean position and the peak concentration are not far apart and particles do not tend to stray far from the mean position plume. A plume that disperses anomalously will have a much larger fraction of the particles far from the mean, in the tails of the spatial distribution because the particle move at a wide range of velocities. Because anomalous dispersion is most evident in the tails the distribution, an experiment designed to measure the mode of dispersion requires a large number of tracers and a high recovery rate. Until recently, this has been difficult in a long-term study because painted tracers are hard to find and lose their paint over time and tracers such as magnetically tagged stones must be dug out of the streambed to be identified (e.g. Ferguson et al., 2002). The recovery process is time consuming and it disturbs the system being studied.

Passive Integrated Transponder (PIT) tags are a relatively new technology that have been used extensively to monitor migrating fish but only recently as tracers in fluvial systems. A PIT tag is a passive radio transponder encased in small, cylindrical glass case. When the antenna on the detection system passes nearby, the electric field generated by the antenna induces a current in the tag that gives it enough power to transmit its unique identification number to the receiver. Depending on the size of the antenna, the detector has a lateral range of about of 1m and can detect buried tracers down to a depth of about 1m. Manufacturers estimate that PIT tags will function for 50 years (Lamarre et al., 2005).

We prepared approximately 900 tracer stones by installing 32mm and 23mm PIT tags (Figure 2.13) into coarse gravel ($D_{50} = 57$mm). We used a hammer drill to drill a small hole, inserted the PIT tag and sealed the hole with marine epoxy putty. We weighed the stone, measured the A, B, and C axes, and recorded the unique identifier of the PIT tag. Approximately 10 of the tags were defective and had to be replaced. This failure rate is consistent with the manufacturers estimate of a 1% failure rate.

On May 13th and May 17th, 2007, we arranged 893 tracers on the bed of Halfmoon Creek, a small gravel bed river draining Mt. Elbert and Mt. Massive, south-

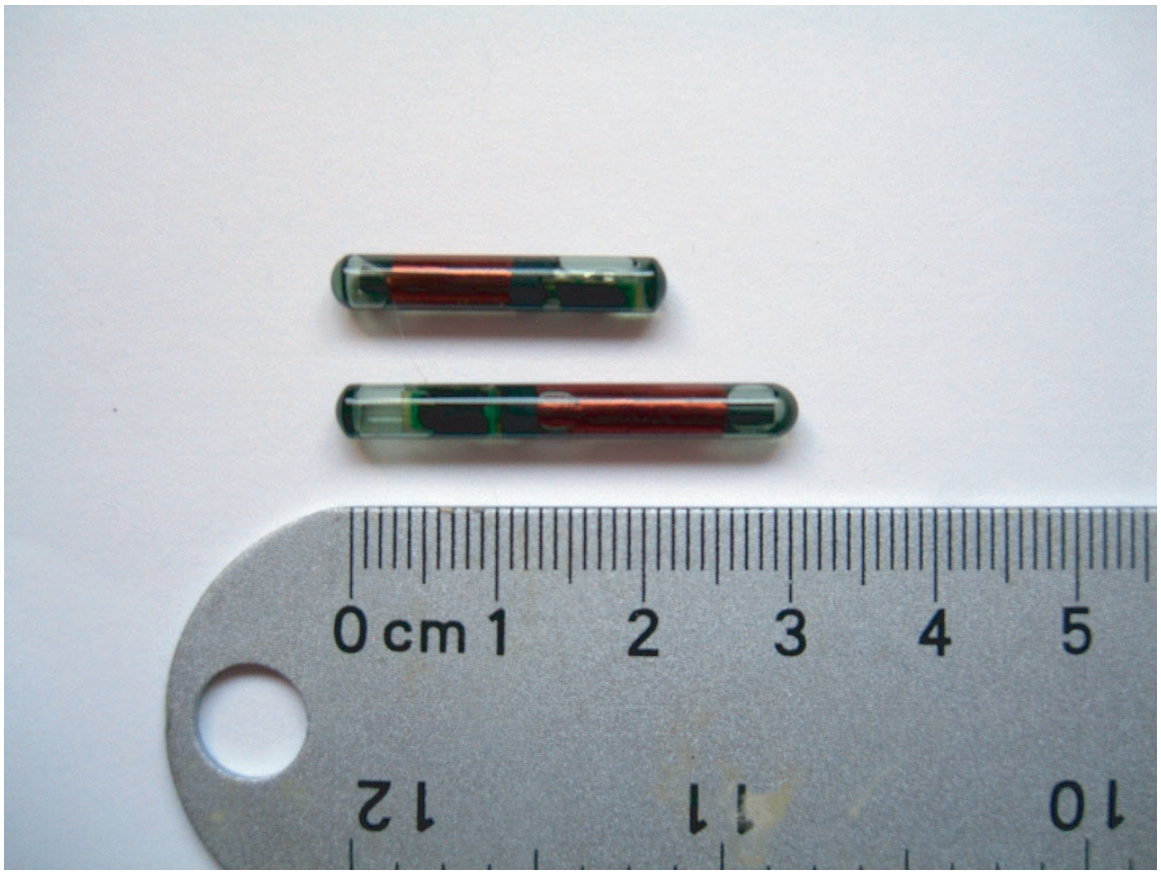

Figure 2.13: 23mm and 32mm Passive Integrated Transponder (PIT) Tags.

west of Leadville, CO. See Figure 2.14 and Figure 2.15. Installation took place shortly before the spring peak flow. We established fourteen cross sections at approximately 2m downstream spacing and surveyed the elevation of the streambed with a laser range finder at 0.5m intervals across the stream. The tracers were placed along each cross section to form a deformed grid with approximately 0.5m spacing between tracers in both the downstream and cross stream directions. The bed topography and tracers are shown in Figure 2.16. The original arrangement in comparison to later tracer positions is shown in Figure 2.17a.

We conducted the first survey of the displaced tracers in October 2007. We used a tripod mounted laser rangefinder and an electronic compass to measure the horizontal distance and azimuth from a benchmark and computed the position relative to the first right bank cross section end. We estimate that the accuracy of the location measurements is +/- 0.5 m. In 2007, 836 out of 893 were recovered, a 93.6% success rate. The distribution of the tracers in the channel is shown in Figure 2.17b. Most tracers moved only a short distance, but a few moved tens of meters downstream. The maximum displacement was about 50m.

The second survey took place in early August and late September of 2008 and is not yet complete. We have recovered 853 out of 893 tracers, a 95.5% recovery rate. The preliminary distribution of tracers is shown in Figure 2.17c. We plan to return to Halfmoon Creek in October to survey cross sections downstream of the seed patch and search for the remaining tracers. We estimate that we will be able to recover at least 20 more at that time. If so, our recovery rate for 2008 will be almost 98%. Both the 2007 and 2008 recovery rates compare very favorably to other large-scale tracer experiments (e.g. Ferguson et al., 2002).

The 2008 tracer locations indicate that transport during that season was much more vigorous than 2007. We attribute this to high runoff in 2008 due to a near record snow pack. There is a real-time USGS gauging station approximately 2 km downstream from our study reach and there are no tributaries between our reach and the gauge. The mean daily discharge for late spring and summer of 2007 and 2008 are shown in Figure 2.18. The peak discharge for 2008 was approximately 60% higher than that of 2007. The data from both the 2007 and 2008 transport season appear to indicate that there is a great deal of variability in the velocity of the particles. In 2007, approximately 90% of the particles move less than 12 m, with the remaining 10% moving between 12 and 50 m. Analysis of the 2008 travel distance distribution is still in progress, but the relatively even downstream distribution of particles shown in Figure 2.17c suggests a broad distribution of transport distances in 2008. There also appears to be no correlation between longer than average displacements in 2007 and the location at the end of 2008. The tracers marked in red in Figure 2.17c

Figure 2.14: The Halfmoon Creek study reach. The white rectangle indicates the approximate location of the tracer seed patch..

Figure 2.15: Tracer installation in a May thunderstorm. We placed a stick of four tracers at 0.5 m downstream intervals at 0.5 m spacing along the tape measure.

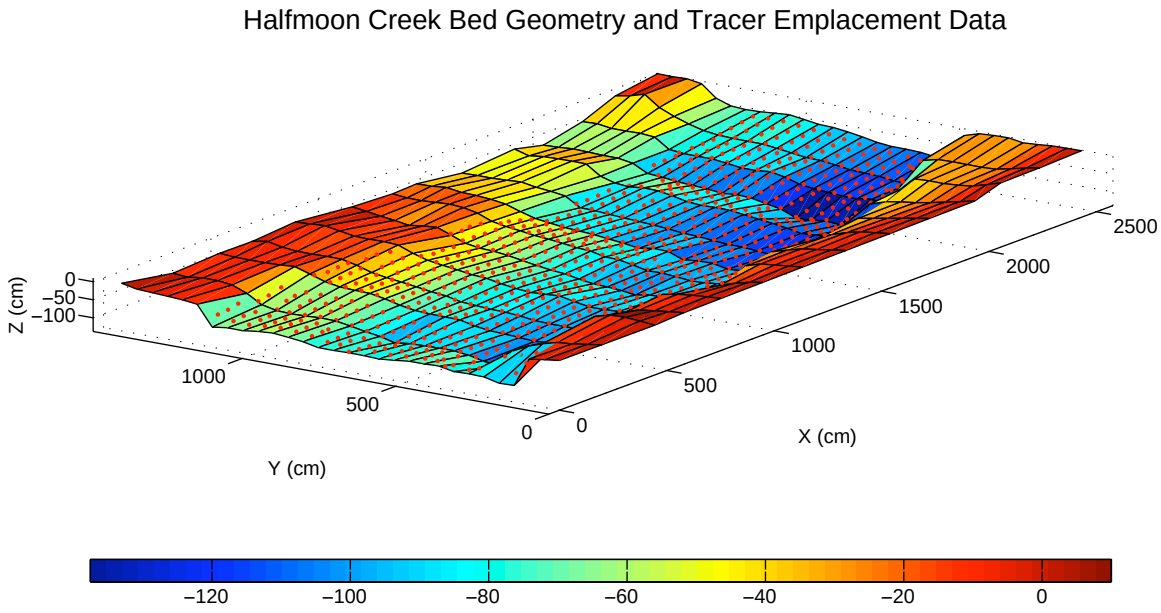

Figure 2.16: Bed geometry of seed patch with initial position of tracers in red. X is downstream and Y is across the stream.

moved at least 20 m during the 2007 transport season and they are evenly spread out along the stream. Preliminary analysis of the first two seasons suggest that an anomalous transport model may describe the transport and dispersion of the Halfmoon Creek tracers better than a Fickian model. The Halfmoon creek dataset needs to be augmented by additional transport seasons and requires further analysis.

2.6 Gambler's Ruin as a Model for Floodplain Sediment Storage

The residence-time distribution appears to be fundamental to predicting the mode of sediment dispersion. The following section presents a theoretical framework for predicting the residence time distribution for a simplified fluvial system that does not rely on the assumption that all particles are equally erodible.

Imagine a meandering channel that moves across its floodplain by cut bank erosion and point bar deposition. If in the long term, the channel location is approximately a random variable (Hancock and Anderson, 2002), then we can deconstruct its motion into a series of random displacements. The channel is taking a kind of

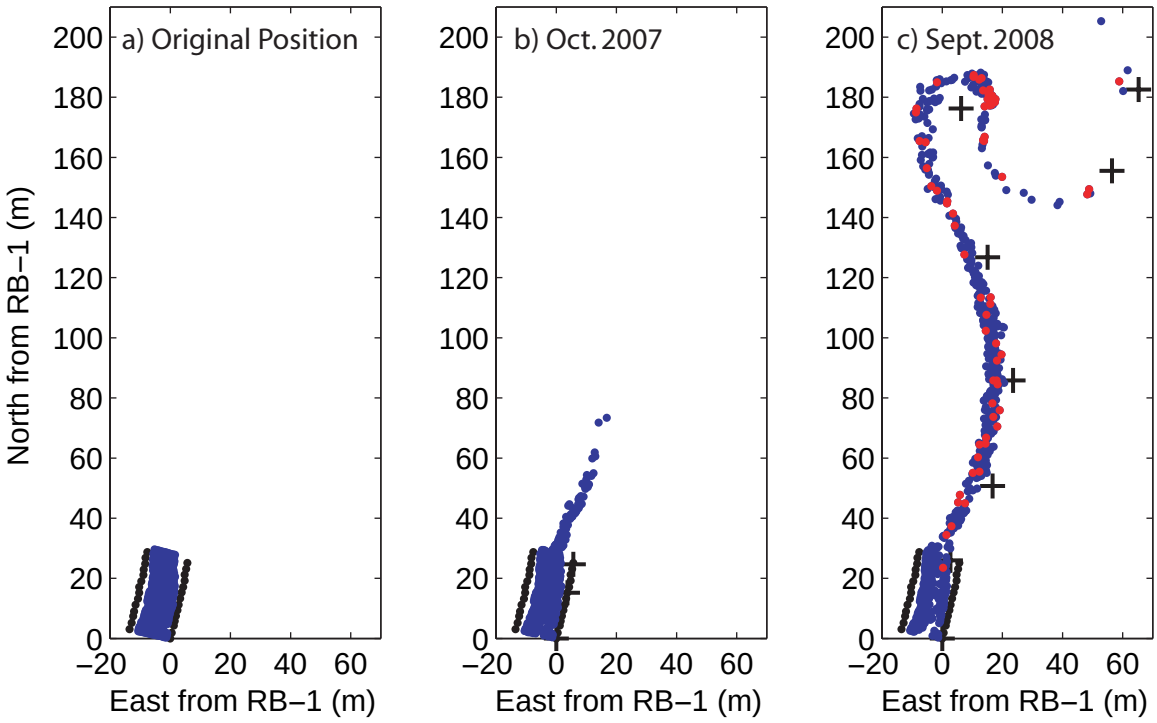

Figure 2.17: a) May 2007. Initial tracer positions. b) Oct. 2007. Tracer position at the end of the first transport season. c) Sept. 2008. Tracer position at the end of the second transport season. Tracer locations are shown in blue. Red dots in c) indicate tracers which moved more than 20 m in 2007. Black dots mark the ends of measured cross sections. Black crosses mark the different instrument locations used to survey the tracers.

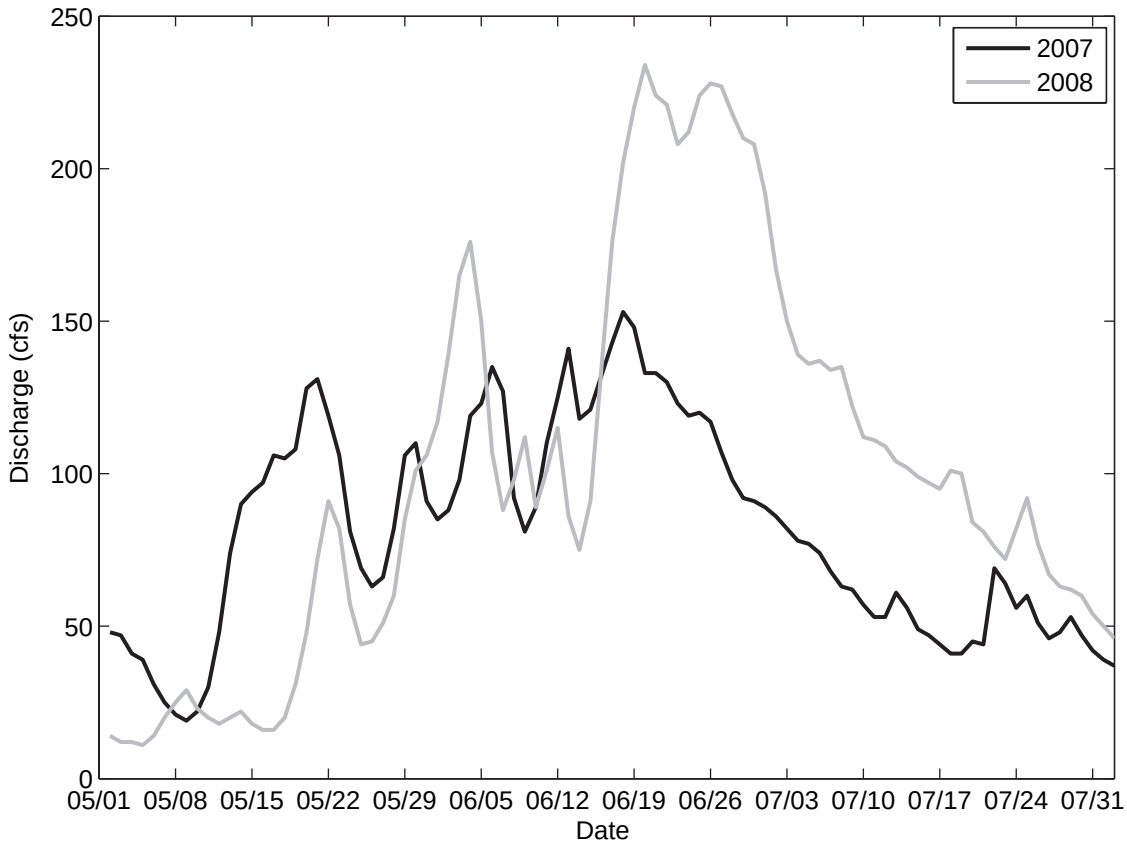

Figure 2.18: Mean daily discharge by Halfmoon Creek for May 1 Aug. 1, 2007 and 2008. Peak discharge for 2008 was approximately 60% higher than the 2007 peak.

random walk. Fix the frame of reference on the channel and assume that floodplain is so wide that the channel width can be neglected. Now, the channel location is always zero and it is the sediment particles in the floodplain that are moving randomly. Particles are deposited at the origin when the channel leaves and are eroded when they return to the origin. The time between deposition and the return to the origin is the particle residence time. A process that ends when its value reaches zero is known as gambler's ruin process. In the simplest case where a particle leaves the origin and moves left or right with equal probability and at a constant speed, the distribution of return times to the origin is a power law with a divergent mean (Newman, 2005). An illustration of this kind of Gambler's Ruin random walk is shown in Figure 2.19.

A similar distribution of return times results even if the steps in random walk are not completely random, which is probably a more realistic analog of channel motion. In this case, the Hurst exponent (H) quantifies the degree of long-term correlation in the time series of steps. As long as the random walk has an overall mean step size of zero, meaning that the average position of the channel doesnt change, the distribution of return times is

$$p(t) \sim t^{H-2}, 0 < H < 1 \tag{2.19}$$

A Hurst exponent of one-half indicates a perfectly uncorrelated motion. H greater than one-half indicates long-range positive correlation. H less than one-half indicates anti-correlation (Ding and Yang, 1995). Any value of the Hurst exponent results in a distribution with an exponent less than two, indicating a divergent mean value. Distributions with divergent first or second moments cause anomalous dispersion. Our conceptual model is illustrated in Figure 2.20 with channel position data from Eliot and Gyetvai (1999).

A tracer module was developed for the landscape evolution model CHILD (Tucker et al., 2001). When a flood deposits a layer of sediment, it adds a uniform concentration of time-stamped tracers. When this layer is touched by erosion, tracers are removed proportional to the amount of material eroded and the time is recorded. The time between deposition and erosion is the tracer residence time.

The floodplain section studied was 5 km long and 5 km wide. When the elevation of channel is held constant, the floodplain volume becomes approximately steady after 4,000 model years. The cumulative residence time distribution of tracers deposited and eroded between the end of the 4,000 year spin up and the end of the model run at 12,000 years are shown in Figure 2.21. Early results are encouraging. The distribution of tracers is approximately an infinite mean power law with an exponential tail caused by the finite length of the simulation. In the CTRW framework, this distribution of residence times would cause anomalous super-diffusion.

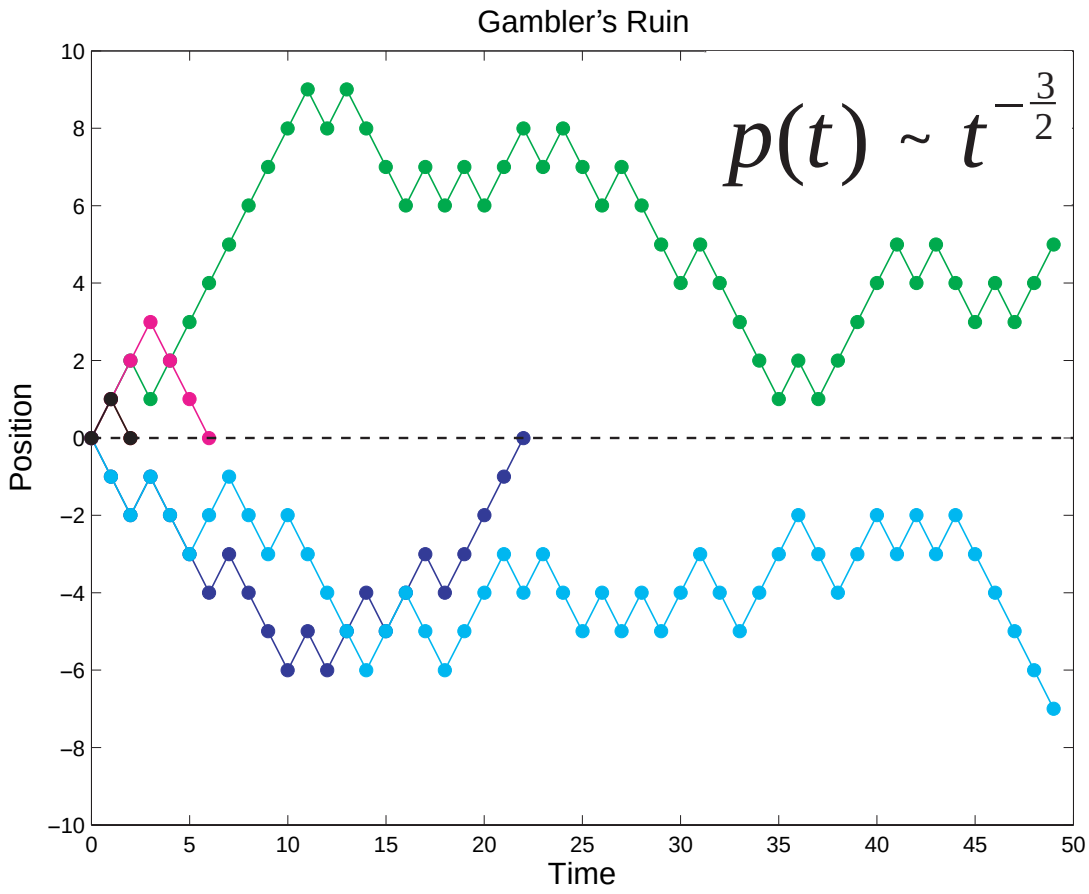

Figure 2.19: A one dimensional random walk illustration of the gambler's ruin concept. Time is on the X-axis and position is on the Y-axis. A particle starts at the origin and moves left or right with equal probability at a velocity of one unit per time step. As the number of particles becomes large, the distribution of return times is a power law with a divergent mean.

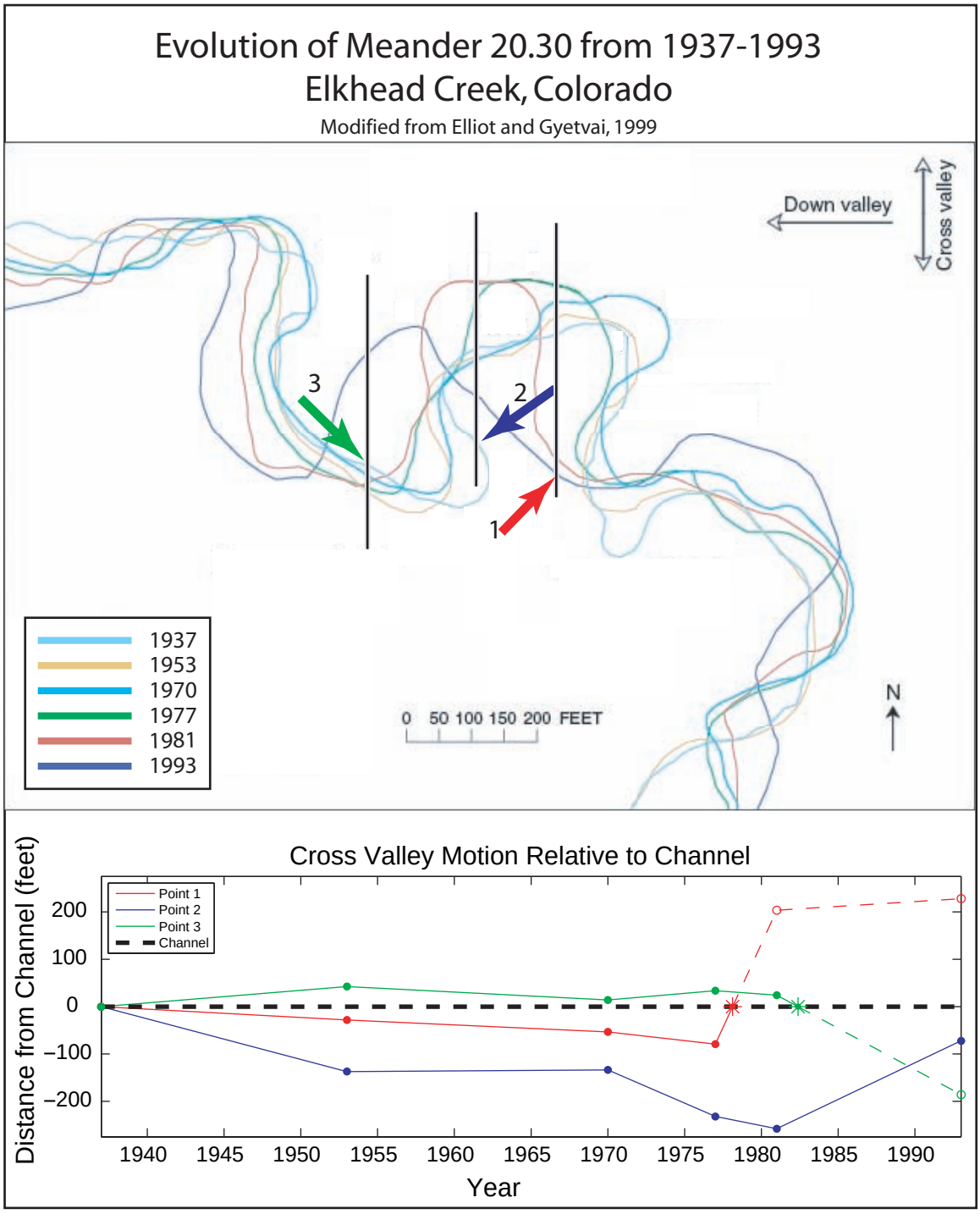

Figure 2.20: The gambler's ruin model illustrated with Eliot and Gyetvai's (1999) channel position map for a short reach of Elkhead Creek in northwest Colorado. At top, the channel position at six different times mapped. The colored arrows point to the 1937 channel position.

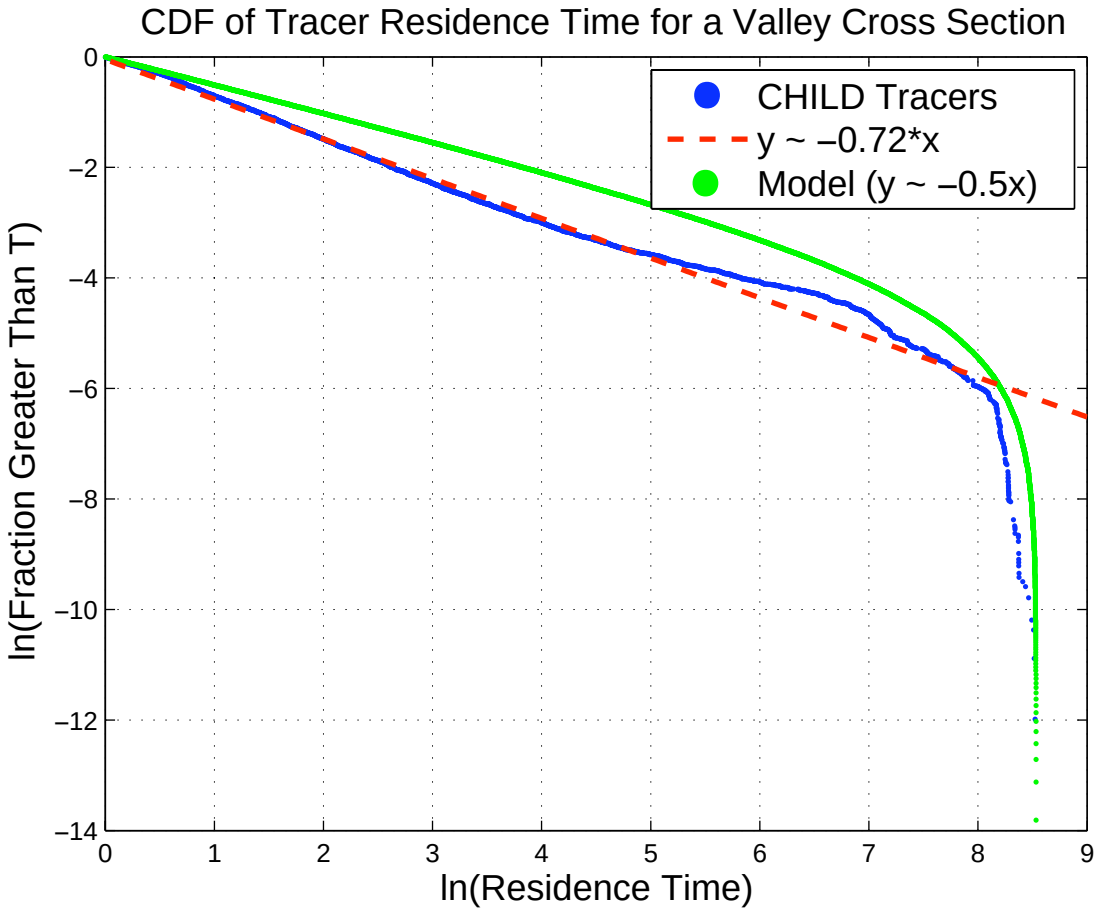

Figure 2.21: Cumulative distribution of residence time for a numerical implementation of a Gambler's Ruin process (green dots in upper curve) compared with the residence time distribution of numerical tracers in a floodplain erosion-sedimentation simulation run with the CHILD model (blue dots in lower curve). The dashed line shows a least-squares fit (above the truncated region).

This result is interesting because the gambler's ruin hypothesis does not account for over-bank deposition. The amount of material a flood deposits declines exponentially with distance from the channel in CHILD. It may be that the gambler's ruin model is not strongly sensitive to the starting position of particles.

2.7 Nonlocality in Sediment Transport: Implications of a Particle-Based Hillslope Evolution Model

2.7.1 Introduction

The physical and biological sciences have a long history of describing transport processes using standard differential-equation models. Some classic examples include mass transport by molecular diffusion (Fick's law), momentum transport in viscous fluids (Newton's law of viscosity), flow of fluid in porous media (Darcy's law), and contaminant transport by groundwater flow in porous media (standard advection-dispersion theory). Similar approaches have been used to model sediment transport on hillslopes (such as the linear soil-creep law; e.g., Nash, 1980; McKean et al., 1993; Small et al., 1999) and in stream channels (the many forms of gradient-dependent sediment-transport formulas, e.g. Yalin, 1977). A common ingredient among these disparate systems is that they all involve net fluxes arising from quasi-random motions in a many-particle system. In geomorphology, laws relating mass fluxes to topographic gradient (among other factors) are known as geomorphic transport laws (Dietrich et al., 2003). These laws are the cornerstone of theories and numerical models of landscape development (e.g., Tucker and Hancock, in review).

Continuum models like these are based on the assumption that there is a clear gap between the the micro-scales associated with particle motion (such as the mean free path of a molecule, or the characteristic scale of a representative elementary volume in a porous medium) and the macro-scales associated with the system of interest. However, as West et al. (2003) have pointed out, not all transport systems posses such a scale gap.

This leads one to ask: what sediment systems possess clear scale gaps that allow continuum models, and what systems lack such gaps? Do the scaling properties depend on aspects of the system that can vary in time and space? We address these questions from the point of view of a hillslope on which sediment transport is driven by processes responsible for soil creep. Soil creep, the gradual (and sometimes not so gradual) downslope motion of soil, arises from quasi-random displacements of

soil particles by processes such as animal burrowing, vegetation growth and decay, raindrop impact, dry ravel, expansion and contraction of soil due to wetting and drying, and growth and melting of interstitial ice lenses. On relatively gentle slopes, most of these processes have characteristic length scales that are small relative to the length of the hillslope. For example, animal burrow mounds have length scales on the order of tens of centimeters, while hillslopes typically have characteristic length scales of tens to hundreds of meters. The net rate of downslope transport by these processes depends strongly on the topographic gradient. In making such a statement, however, one has to be careful about scale. In continuum mechanics, we speak of gradient at an infinitesimal point. Strictly speaking, such a gradient is physically meaningless in a system of discrete particles, yet because of the strong scale gap between displacement length and system length, one can still speak of *local* gradient as one that is measured on a scale larger than the characteristic displacement length but much smaller than the system size.

As slope angle increases, there is evidence for increases in the both the frequency and average displacement distance of transport events in creep-related processes (e.g., Furbish et al., 2007; Roering et al., 2001). Moreover, as slope gradient approaches the angle of repose, various forms of landsliding can come into play, with displacement length scales comparable to that of the hillslope as a whole. Thus, we expect that as gradient increases, sediment transport becomes increasingly non-local. We study the nature and implications of this transition from local to non-local transport using a simple model of sediment-particle motions on a hillslope. We examine the frequency distribution of particle hop length as a function of gradient, and as a function of spatial scale. (Note that this topic is the subject of an abstract submitted to the American Geophysical Union 2008 Fall Meeting by Tucker and Bradley).

2.7.2 Particle-Based Model of Hillslope Evolution

The model is designed as a simple analogy for a host of different processes that displace sediment grains on hillslopes. It is similar in spirit to the famous sand pile model of Bak et al. (1987), but in this case the system is driven not by mass input from above but by random, gradient-dependent motions of the particles themselves. The hillslope is represented as a pile of two-dimensional particles with diameter ϵ. These particles undergo quasi-random motion according to the following rules: (1) during each iteration, a particle and a direction (left or right) are selected at random; (2) the particle hops one particle length in the direction of motion with a probability that depends on the its height relative to that of its immediate neighbor in the direction of travel; (3) the particle continues making hops in the same direction and

with the same probability dependence, until coming to rest or exiting the base of the slope.

The slope is N particles wide plus an additional boundary particle on each side. The model cycles through a series of global iterations. During each global iteration, N sites are selected at random as candidates for particle motion. For each site i selected, a direction (d, equal to 1 or -1) is also selected at random. The probability p that the particle will move one space in direction d depends on the height of the particle, Z_i, relative to that of the adjacent particle, Z_{i+d}, as follows:

$$p = \begin{cases} 0 & \text{if } Z_i < Z_{i+d} \\ \frac{1}{8} & \text{if } Z_i = Z_{i+d} \\ \frac{7}{8} & \text{if } Z_i - Z_{i+d} = 1 \\ 1 & \text{if } Z_i - Z_{i+d} > 1 \end{cases} \tag{2.20}$$

If motion occurs, the particle is moved one unit in the motion direction and the probability of motion is tested again, until either the particle comes to rest or it reaches one of the model edges.

One can explore a variety of different boundary conditions. Here, we focus on the case in which the system is driven by steady lowering at the lower boundaries of the hillslope. The baselevel is lowered by one unit (or equivalently, the interior is raised) every T global iterations, so that the lowering rate is ϵ/T. Starting from a flat surface, the system eventually reaches an equilibrium in which the total flux of particles from the hillslope, q (particles per global iteration), balances the input from below, or $q = N/T$.

The topography and motion statistics that emerge from these rules show a range of behavior that depends on the parameter $\alpha = N/T$, which governs the dimensionless relief $2Z_{max}/N$ (which is also the average slope angle). At low α, hillslope shape is parabolic, reflecting the diffusive character of the system (Figure 2.22). The mean hop length is on the order of two particle widths, and the probability distribution of displacement length is thin-tailed (approximately exponential) (Figure 2.23). The hop-length distribution is largely insensitive to N when α is small, indicating that there is a clean scale break between the motion scale and the system scale.

At high α, hillslopes become planar, and average displacement length increases by an order of magnitude (Figure 2.24). In this situation, the system exhibits "angle of repose" behavior in which many particles travel the full distance between their point of origin and the system boundary in one event. The hop-length distribution resembles a truncated, heavy-tailed distribution (Figure 2.25).

Across the spectrum of relief values, the relationship between mean flux and gradient resembles the family of nonlinear flux-gradient curves that has been used

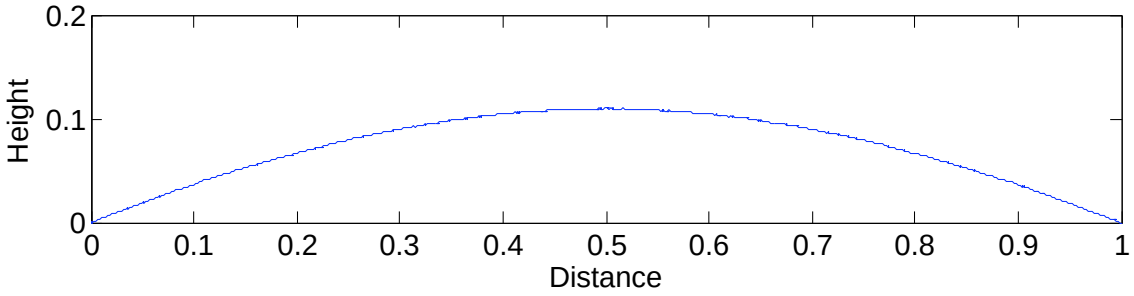

Figure 2.22: Simulated hillslope with $N = 2561$ and $T = 1000$.

to model hillslope evolution, with a linear relationship between local gradient and flux when gradients are relatively low and a nonlinear relationship when gradients approach a threshold (in this case on the order of unity). However, as gradient increases, the characteristic motion range undergoes a transition from being largely independent of system length to being largely controlled by system length. Particles passing through a given point have an increasingly high probability of originating from a distant ($>>\epsilon$) position. Thus, local gradient plays a decreasing role in controlling flux as α increases.

Further investigation is needed to determine what statistical model, and what corresponding flux law, best describes this transport process. Clearly, Fickian diffusion provides an excellent approximation at small α. At high α, the hop-length distribution resembles truncated or tempered Lévy motions (Mantegna and Stanley, 1994, 1995; Meerschaert et al., 2008; Rosiński, 2007), though a standard Lévy distribution (*sensu* Nolan, 2009), when exponentially tempered, does not appear to capture the either "fatness" of the mid-range or the sharpness of the cutoff.

The model we have presented raises an interesting mathematical question that to our knowledge has not yet been explored: what type of model best describes a system in which the motion statistics are themselves dependent on the system state, both in time and space? We suspect that there may be many analogous systems in which transport statistics vary according to system state variables. For example, the rheology of creeping flow in solids can change from Newtonian to non-Newtonian in response to increasing stress, as dislocation creep begins to play a role (e.g., Turcotte and Schubert, 2002). Similar behavior can be expected from water-borne sediment transport: as fluid stress increases, grain suspension becomes increasingly important, and grain motion lengths increase. The simple particle model

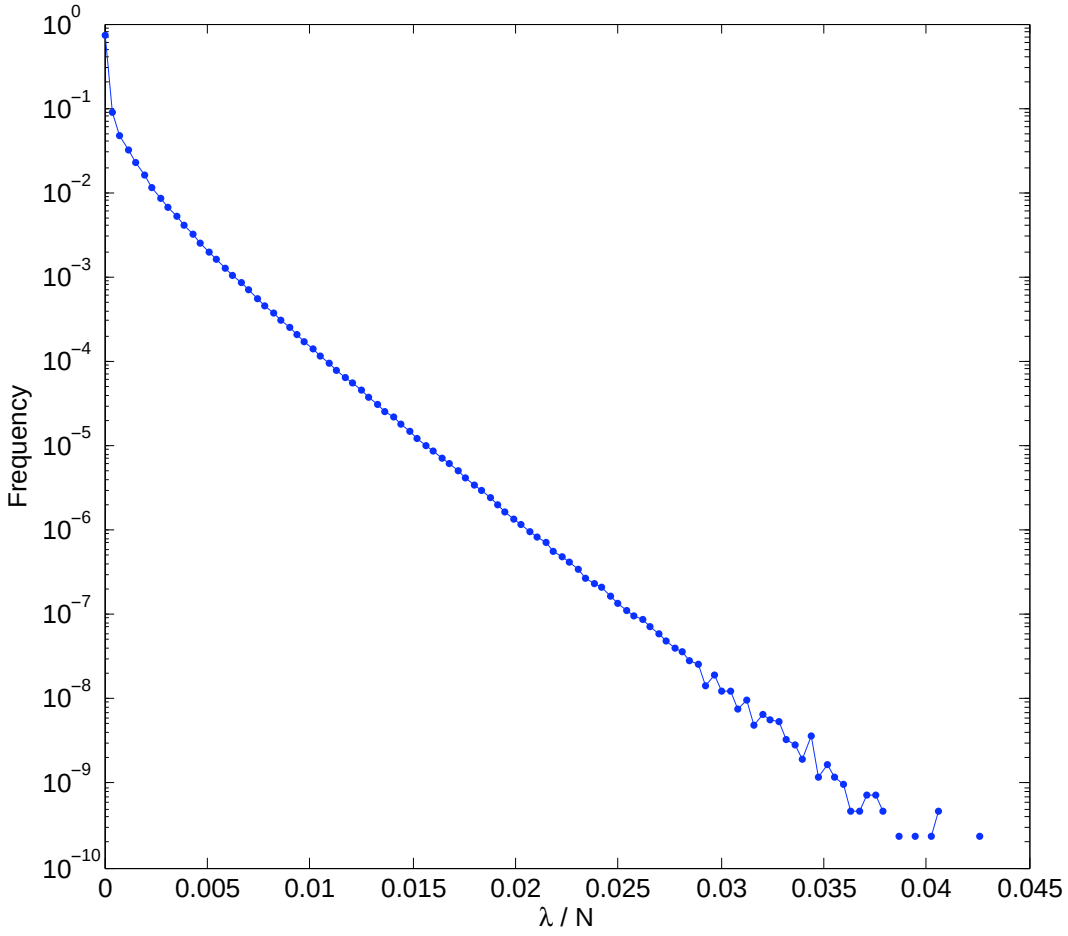

Figure 2.23: Normalized frequency distribution of hop length, λ, for $N = 2560$ and $T = 1000$. Each dot on the curve represents a displacement scale ϵ. Note the exponential tail.

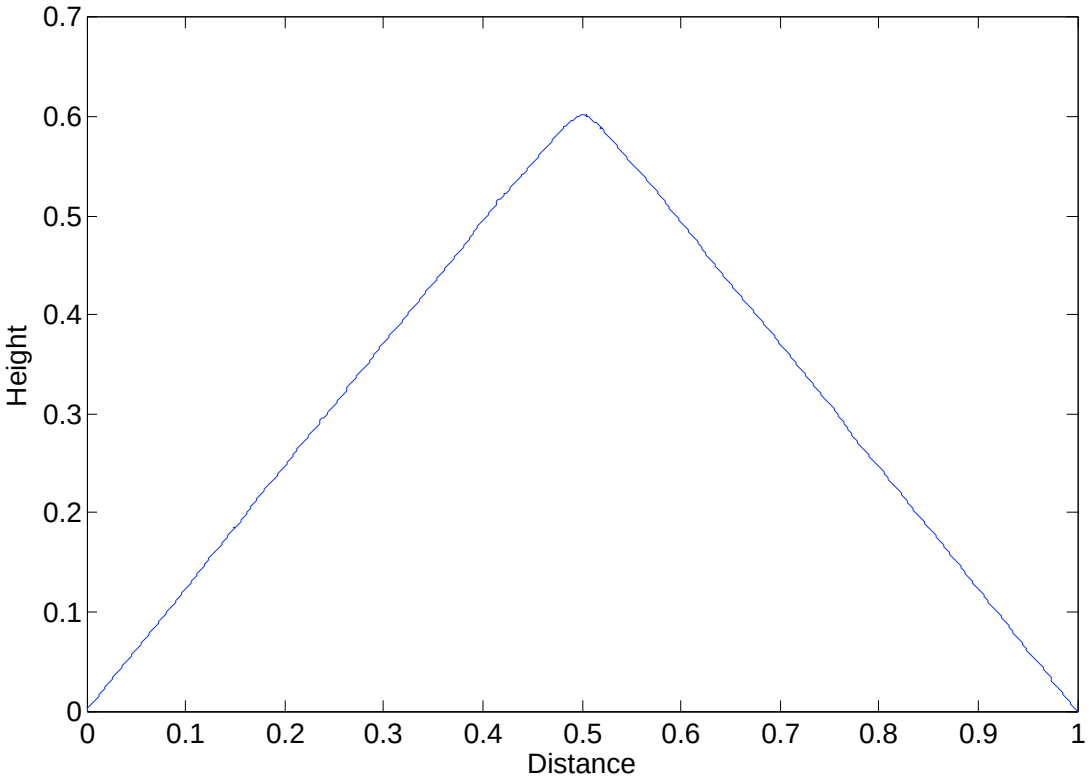

Figure 2.24: Simulated hillslope with $N = 2560$, and $T = 10$.

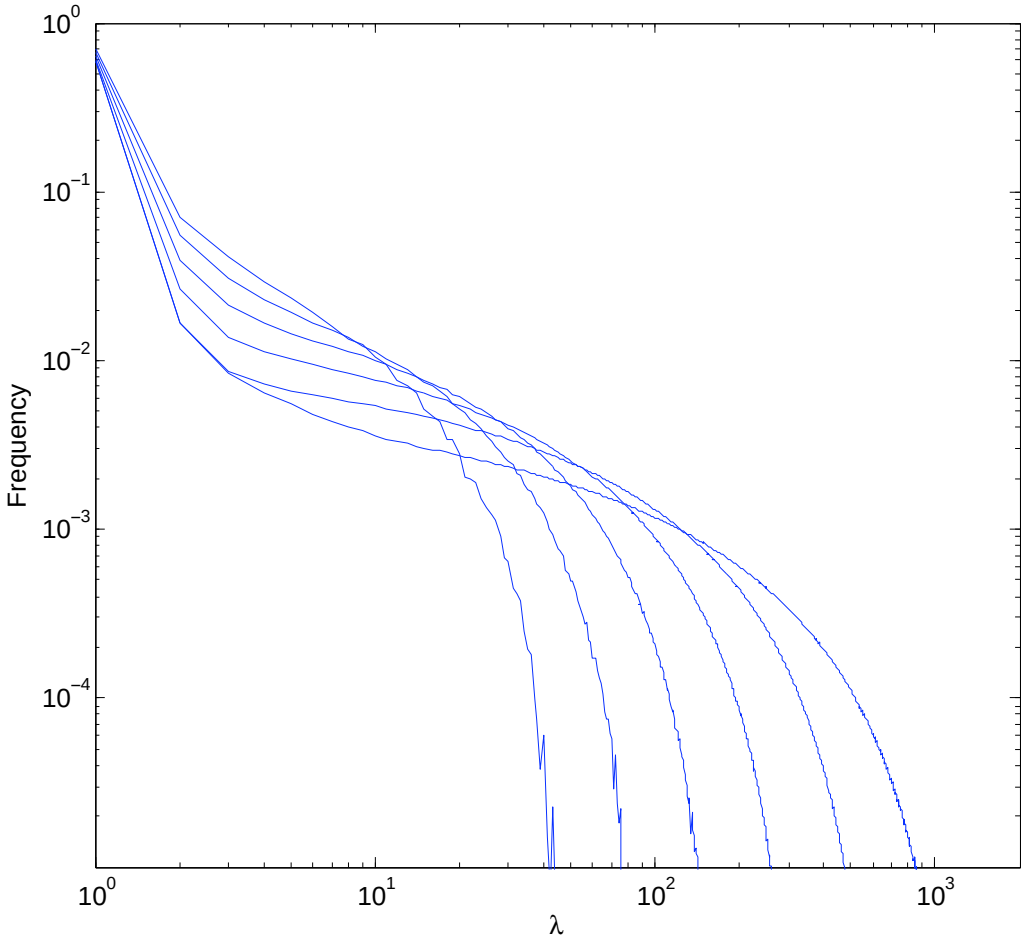

Figure 2.25: Normalized frequency distribution of hop length for $T = 10$ and $N = 80$, 160, 320, 640, 1280, and 2560. Note the scale dependence on the distribution.

we have developed provides a useful numerical framework for investigating dynamic transitions in motion statistics in a truncated system.

2.8 References

Bak, P., Tang C., and Wiesenfeld, K., 1987, Self-organized criticality: an explanation of the 1f noise. Phys. Rev. Lett. 59, 381 - 384.

Benson, D.A., and Meerschaert, M., 2008, A simple and efficient random walk solution of multi-rate mobile/immobile mass transport equations: submitted to Elsevier.

Benson, D.A., Wheatcraft, S.W., and Meerschaert, M.M., 2000, Application of a fractional advection-dispersion equation: Water Resources Research, v. 36, p. 1403-1412.

Berkowitz, B., and Scher, H., 1995, On characterization of anomalous dispersion in porous and fractured media: Water Resources Research, v. 31, p. 1461-1466.

Bolin, B. and Rodhe, H., 1973. A note on the concepts of age distribution and transit time in natural reservoirs. Tellus, 25: 58.

Church, M., 2006. Bed Material Transport and the Morphology of Alluvial River Channels. Annual Review of Earth Planetary Science, 34: 325-54.

Dentz, M. and Tartakovksy, D., M., 2006. Delay mechanisms of non-Fickan transport in heterogeneous media. Geophysical Research Letters, 33.

Dietrich, W. E., Bellugi, D., Heimsath, A. M., Roering, J. J., Sklar, L., and Stock, J. D., 2003, Geomorphic transport laws for predicting landscape form and dynamics, in Wilcock, P. R., and Iverson, R., eds., Prediction in geomorphology, Washington, D.C., American Geophysical Union.

Dietrich and Dunne, 1978. W.E. Dietrich and T. Dunne, Sediment budget for a small catchment in mountainous terrain. Z. Geomorphol. Suppl. 29 (1978), pp. 191206.

Dietrich, W.E., Dunne, T., Humphrey, N.F., Reid, L.M., 1982. Construction of Sediment Budgets for Drainage Basins. In: F.J. Swanson, Janda, R.J., Dunne, T., Swanston, D.N. (Editor), Sediment budgets and routing in Forested Drainage Basins. U.S. Dept. of Agriculture forest Services General Technical Report, pp. 5-23.

Ding, M. and Yang, W., 1995. Distribution of the first return time in fractional Brownian motion and its application to the study of on-off intermittency. Physical Review E, 52(1): 207 LP - 213.

Downing, S.L., Prentice, E.F., Frazier, R.W., Simonson, J.E. and Nunnallee, E.P., 2001. Technology developed for diverting passive integrated transponder (PIT)

tagged fish at hydroelectric dams in the Columbia River Basin. Aquacultural Engineering, 25(3): 149-164.

Drake, T.G., Shreve, R.L, Dietrich, W.E., Whiting, P.J., Leopold, L.B., 1988. Bedload transport of fine gravel observed by motion-picture photography. Journal of Fluid Mechanics, 192: 193-217.

Dunne, T., Mertes, L.A.K., Meade, R.H., Richey, J.E. and Forsberg, B.R., 1998. Exchanges of sediment between the flood plain and channel of the Amazon River in Brazil. Geological Society of America Bulletin, 110(4): 450-467.

Einstein, A., 1905. "On the MotionRequired by the Molecular Kinetic Theory of Heatof Small Particles Suspended in a Stationary Liquid", Annalen der Physik 17: 549560.

Einstein, A., 1905, The theory of the brownian movement: Ann. der Physik, v. 17, p. 549.

Einstein, H., 1937, Bedload transport as a probability problem: Mitteilung der.

Einstein, H.A., 1950. The Bed Load Function for Sediment Transport in Open Channel Flows. USDA Technical Bulletin(1026).

Eliot, J.G. and Gyetvai, S., 1999. Channel-Pattern Adjustments and Geomorphic Characteristics, U.S. Geological Survey Water-Resources Investigations Report 99-4098.

Eriksson, E., 1971. Compartment models and reservoir theory. Annual Review of Ecology and Systematics, 2.

Everitt, B.L., 1968. Use of the cottonwood in an investigation of recent history of a flood plain. American Journal of Science, 266: 417-439.

Ferguson, R.I., Bloomer, D.J., Hoey, T.B. and Werritty, A., 2002. Mobility of river tracer pebbles over different timescales. Water Resources Research, 38(5).

Feynman, R.P., Leighton, R.B. and Sands, M., 1963. The Feynman Lectures on Physics, 1. Addison-Wesley Publishing Company.

Furbish, D.J., Hamner, K.K., Schmeeckle, M., Borosund, M.N., and Mudd, S.M., 2007, Rain splash of dry sand revealed by high-speed imaging and sticky paper splash targets: Journal of Geophysical Research, v. 112, F01001, doi:10.1029/2006JF000498.

Goltz, M., and Roberts, P., 1987, Using the method of moments to analyze three-dimensional diffusion-limited solute transport from temporal and spatial perspectives: Water Resour. Res, v. 23, p. 15751585.

Graf, W.L., 1994, Plutonium in the Rio Grande. Oxford University Press.

Graf, W.L., 1996. Transport and Deposition of Plutonium-Contaminated Sediments by Fluvial Processes, Los Alamos Canyon, New Mexico. GSA Bulletin, 108(10): 1242-55.

Habersack, H.M., 2001. Radio-tracking gravel particles in a large braided river

in New Zealand: a field test of the stochastic theory of bed load transport proposed by Einstein. HYDROLOGICAL PROCESSES, 15: 337-391.

Haggerty, R., and Gorelick, S., 1995, Multiple-rate mass transfer for modeling diffusion and surface reactions in media with pore-scale heterogeneity: Water Resources Research, v. 31, p. 2383-2400.

Hancock, G.S. and Anderson, R.S., 2002. Numerical modeling of fluvial strath-terrace formation in response to oscillating climate. GSA Bulletin, 114(9): 1131-1142.

Harvey, C., and Gorelick, S., 1995, Temporal moment-generating equations: Modeling transport and mass transfer in heterogeneous aquifers: Water Resources Research, v. 31, p. 1895-1911.

Harvey, C., and Gorelick, S., 2000, Rate-limited mass transfer or macrodispersion: Which dominates plume evolution at the Macrodispersion Experiment(MADE) site?: Water Resources Research, v. 36, p. 637-650.

Kirchner, J., Dietrich, W., Iseya, F., and Ikeda, H., 1990, The variability of critical shear stress, friction angle, and grain protrusion in water-worked sediments: Sedimentology, v. 37, p. 647-672.

Lamarre, H., MacVicar, B. and Roy, A.G., 2005. Using Passive Integrated Transponder (PIT) Tags to Investigate Sediment Transport in Gravel-Bed Rivers. Journal Of Sedimentary Research, 75(4): 736-741.

Lancaster, S.T., 2006. Debris-Flow Deposition, Valley Storage, and Fluvial Evacuation in Headwater Valleys. AGU 2006 Fall Meeting.

Malmon, D.V., Dunne, T. and Reneau, S.L., 2003. Stochastic theory of particle trajectories through alluvial valley floors. Journal of Geology, 111(5): 525-542.

Malmon, D.V., Reneau, S.L., Dunne, T., Katzman, D. and Drakos, P.G., 2005. Influence of sediment storage on downstream delivery of contaminated sediment. Water Resources Research, 41(5).

Mantegna, R.N., and H.E. Stanley, Stochastic process with ultraslow convergence to a Gaussian: The truncated Lévy flight, Phys. Rev. Lett. 73 (1994) 29462949.

McKean, J. A., Dietrich, W. E., Finkel, R. C., Southon, J. R., and Caffee, M. W., 1993, Quantification of soil production and downslope creep rates from cosmogenic 10Be accumulations on a hillslope profile: Geology (Boulder), v. 21, p. 343-346.

Meerschaert, M., Benson, D., and Bumer, B., 1999, Multidimensional advection and fractional dispersion: Physical Review E, v. 59, p. 5026-5028.

Meerschaert, M.M., Zhang Y., and Baeumer, B., 2008, Tempered anomalous diffusion in heterogeneous systems. Geophysical Research Letters, vol. 35, L17403.

Metzler, R., and Klafter, J., 2000, The random walks guide to anomalous diffusion: a fractional dynamics approach: Phys. Rep, v. 339, p. 177.

, 2004, The restaurant at the end of the random walk: recent developments in the description of anomalous transport by fractional dynamics: J. Phys. A: Math. Gen, v. 37, p. R161-R208.

Montroll, E.W. and Weiss, G.H., 1965. Random walks on lattices. II. Journal of Mathematical Physics, 6(2): 167-181.

Nash, 1980b D.B. Nash, Forms of bluffs degraded for different lengths of time in Emmet County, Michigan, USA, Earth Surface Processes 5 (1980), pp. 331345.

Newman, 2005. Power laws, Pareto distributions and Zipf's law. Contemporary Physics, 46(5): 323-351.

Nikora, V., Heald, J., Goring, D., and I. McEwan, 2001. Diffusion of saltating particles in unidirectional water flow over a rough granular bed. Journal of Physics A: Mathematical and General, 24: 743-749.

Nikora, V., H. Habersack, T. Huber, and I. McEwan, 2002. On bed particle diffusion in gravel bed flows under weak bed load transport. Water Resources Research, 38(6).

Nolan, J.P., 2009, Stable Distributions - Models for Heavy Tailed Data: Boston, Birkhuser.

Phillips, J.D., Marden, M. and Gomez, B., 2006. Residence time of alluvium in an aggrading fluvial system. Earth Surface Processes and Landforms.

Pizzuto, J.E., 1994. Channel adjustments to changing discharges, Powder River, Montana. Geological Society of America Bulletin, 106(11): 1494-1501.

Plerou, V., Gopikrishnan, P., Nunes Amaral, L.A., Gabaix, X. and Eugene Stanley, H., 2000. Economic fluctuations and anomalous diffusion. Physical Review E, 62(3): R3023 LP - R3026.

Pyrce, R.S. and Ashmore, P.E., 2003. Particle path length distributions in meandering gravel-bed streams: results from physical models. Earth Surface Processes and Landforms, 28(9): 951-966.

Reneau, S.L., P.G. Drakos, D. Katzman, D.V. Malmon, E.V. McDonald, and R.T. Ryti. 2004: Geomorphic controls on contaminant distribution along an ephemeral stream. Earth Surface Processes and Landforms 29(10):1209-1223.

Roering, J. J., Kirchner, J. W., Sklar, L. S., and Dietrich, W. E., 2001, Hillslope evolution by nonlinear creep and landsliding; an experimental study: Geology (Boulder), v. 29, p. 143-146.

Rosinski, J., 2007, Tempering stable processes. Stochastic Processes and their Applications, 117, 677-707.

Samorodnitsky, G., and Taqqu, M., 1994, Stable Non-Gaussian Random Processes: Stochastic Models With Infinite Variance, Chapman and Hall/CRC.

Sayre, W.W. and Hubble, D.D., 1965. Transport and dispersion of labeled bed

material, North Loup River, Nebraska. U.S. Geological Survey Professional Paper, 433-C.

Scher, H., Shlesinger, M.F. and Bendler, J.T., 1991. Time-scale invariance in transport and relaxation. Physics Today (January): 26-34.

Schmidt, K.H., Ergenzinger, P., 1992. Bedload Entrainment, Travel Lengths, Step Lengths, Rest Periods - Studied with Passive (Iron, Magnetic) and Active (Radio) Tracer Techniques. Earth Surface Processes and Landforms, 17(2): 147-65.

Schumer, R., Benson, D., Meerschaert, M., and Baeumer, B., 2003, Fractal mobile/immobile solute transport.: Water Resources Research, v. 39, p. 1296.

Small, E. E., Anderson, R. S., and Hancock, G. S., 1999, Estimates of the rate of regolith production using ^{1}0Be and ^{2}6Al from an alpine hillslope: Geomorphology, v. 27, p. 131-150.

Sornette, D., 2004. Critical Phenomena in Natural Sciences. Chaos, Fractals, Selforganization and Disorder: Concepts and Tools. Springer.

Thompson, C.J., Rhodes, E. and Croke, J.C., 2007, The storage of bed material in mountain stream channels as assessed using Optically Stimulated Luminescence dating, Geomorphology, 83(3-4), 307-321.

Tucker, G.E., and Hancock, G.R., in review, Landscape evolution modeling.

Tucker, G.E., Lancaster, S.T., Gasparini, N.M. and Bras, R.L., 2001. The Channel-Hillslope Integrated Landscape Development (CHILD) Model. In: R.S. Harmon and W. Doe III (Editors), Landscape Erosion and Evolution Modeling. Kluwer Academic/Plenum Publishers.

Turcotte, D., and Schubert, G., 2002, Geodynamics, 2nd Edition. Cambridge University Press.

Valocchi, A., and Quinodoz, H., 1989, Application of the random walk method to simulate the transport of kinetically adsorbing solutes: IAHS-AISH publication, p. 35-42.

van Genuchten, M., and Wierenga, P., 1976, Mass Transfer Studies in Sorbing Porous Media I. Analytical Solutions: Soil Science Society of America Journal, v. 40, p. 473.

Wachsmuth, M., Waldeck, W. and Langowski, J., 2000. Anomalous Diffusion of Fluorescent Probes Inside Living Cell Nuclei Investigated by Spatially-resolved Fluorescence Correlation Spectroscopy. Journal of Molecular Biology, 298(4).

Weeks, E.R. and Swinney, H.L., 1998. Anomalous diffusion resulting from strongly asymmetric random walks. Physical Review E, 57(5): 4915 LP - 4920.

Weeks, E.R., Urbach, J.S., Swinney, H.L., 1996. Anomalous diffusion in asymmetric random walks with a quasi-geostrophic flow example. Physica D, 97(1): 291-310.

West, B., Bologna, M., and Grigolini, P., 2003, Physics of Fractal Operators: Institute for Nonlinear Science, Springer.

Yalin, M.S., 1977, Mechanics of Sediment Transport. Pergamon Press.

Yang, C., 1996, Sediment transport: Theory and practice: MCGRAW-HILL BOOK CO,(USA). 1996.

Zhang, Y., Benson, D., Meerschaert, M., and Scheffler, H., 2006, On Using Random Walks to Solve the Space-Fractional Advection-Dispersion Equations: Journal of Statistical Physics, v. 123, p. 89-110.

Chapter 3

Rangeland Landscapes as a Template for Complex Geomorphic Systems

3.1 Overview

Rangeland landscapes, which consist of low to moderate relief in semi-arid environments, are characteristic of large areas of the western United States and are common in mid-latitude environments worldwide. They are often considered to be somewhat fragile landscapes, vulnerable to rapid soil loss in response to land degradation and possibly climatic change (e.g., Leopold, 1951; Boardman et al., 2003). A number of U.S. Army installations are located in semi-arid to arid landscapes, and management of land resources requires on knowledge of how the landscape is likely to respond to different types of management activity (such as mechanized training). However, there are a number of important knowledge gaps regarding how such landscapes respond to changes in vegetation patterns, land use, and climate. While models exist to describe the rate of soil loss on individual hillslopes, there have been relatively few attempts to construct sediment budgets for entire watersheds or to quantify the factors that govern these budgets. In an effort to begin filling this gap, we have analyzed the processes and dynamics controlling erosion and sediment movement at three sites in the Colorado piedmont: the Fort Carson military reservation, the Pinon Canyon Maneuver Site (PCMS, a training area in southeastern Colorado administered by Fort Carson), and an area of intense gullying along the West Bijou Creek escarpment in eastern-central Colorado.

Our efforts have focused on three activities: (1) combining field evidence, aerial

photography, and hydro-meteorologiccal measurements at Fort Carson and PCMS in order to understand the key factors controlling the erosional development of ephemeral channels; (2) using optically stimulated luminescence (OSL) geochronology to discover the history of channel cutting and filling and determine whether it has been synchronous across the region; (3) using numerical models to analyze the dynamics of channel cross-section evolution in cohesive sediment and bedrock. Some of these activities were begun as part of an ARO-supported investigation of gully and arroyo formation (2001 to 2004), and were brought to completion during the course of the current project. Others are new to this project. The activities are described in the sections that follow.

3.2 Dynamics of Headwater Ephemeral Channels

Results from our study of ephemeral channel (gully and arroyo) dynamics are reported in a *Geological Society of America Bulletin* article by Tucker et al. (2006). A reprint of this article is included as Appendix A. In addition, we conducted a model-based analysis of the impact of different storm regimes — small-footprint convective storms versus large, frontal storms — on the shape of drainage networks, using the PCMS area as a test case. Results are reported by Sólyom and Tucker (2007), a reprint of which is attached as Appendix B.

3.3 Luminescence Chronology of Channel Cutting and Filling

One focus of our earlier project on gully erosion was using optically stimulated luminescence (OSL) dating of channel sediment to build a chronology of channel cutting and filling events at sites in Fort Carson and PCMS. Several aspects of this study have now been brought to completion. Arnold et al. (2007) report an analysis of the apparent ages, bleaching characteristics and age-determination procedures for Colorado samples. A reprint of this article is attached as Appendix C. Additional work is described in a doctoral dissertation by Lee Arnold (Arnold, 2006).

3.4 Data Collection on Rainfall and Flash Floods

One of the findings to emerge from the analysis of ephemeral headwater channel dynamics (Tucker et al., 2006) is the importance of the frequency and magnitude

of flash floods in these channels. While thousands of gauging stations exist in the U.S. for drainage basins of perhaps 50 km^2 and larger, there are very few data sets on hillslopes and small (one to a few km^2) drainage basins. This motivated us to set up a network of three flash-flood monitoring sites at PCMS and a fourth at the West Bijou Creek site (where proximity to the University of Colorado allows us to easily test data-storage programs and sensor configurations). Each station is equipped with a rain gauge, temperature sensor, and acoustic depth sensor. The data are stored on a programmable datalogger (Campbell Scientific CR800), and the equipment is powered by a solar panel. The Hydrological Sciences siphoning rain gauges are specially designed for accurately measuring heavy rain. The acoustic sensors obtain stage (water-surface height) estimates by measuring the two-way travel time of a high-frequency sound pulse between the instrument and the surface below. Using the temperature sensor data to calculate the speed of sound, the travel time is converted into distance between the sensor and either the ground or the water surface.

We have experimented with a variety of data-aquisition programs. There is a tradeoff between data resolution and storage capacity: high-resolution data are desirable to capture the details of the short-lived flash-flood hydrographs. However, storage space on the dataloggers is limited ($\sim$1 Mb), and in any event the channels are dry most of the time. We experimented with using changes in stage above a threshold for activating high-resolution data collection, but it turns out that this can lead to too many "false positivies" — the result of animals passing under the sensor, or wind-blown debris (e.g., tumbleweeds), and so on. The most successful algorithm involves using rainfall to trigger high-resolution recording of stage data. The algorithm takes advantage of the fact that the datalogger continually loops through a sequence at a specified time interval (typically set to 10 or 20 seconds), and it operates as follows:

1. If rain has been detected during this interval, set *event_flag* to *TRUE* and set *event_counter* to zero.

2. If *event_flag* == *TRUE*, record stage value and set *event_counter* = *event_counter* + *1*.

3. If *event_flag* == *TRUE* and *event_counter* $\geq$ *EventRecordingDuration*, set *event_flag* = *FALSE*.

An example hydrograph from one of the stations at PCMS is shown in Figure 3.1. This particular monitoring station is situated over a shallow, bedrock-floored in-channel depression. The stage curve indicates a peak flow depth between 4 and 11

cm. (The minimum number reflects the possibility that the curve's tail is simply recording the maximum depth of ponded water). The 2.8-hour rainstorm that triggered this event delivered a peak five-minute intensity of 7.3 cm per hour and a total rainfall depth of 3.1 cm. Interestingly, this particular event illustrates the importance of heterogeneity in surface infiltration capacity and run-on infiltration. The rainstorm was recorded at a second station situated a little over 800m downstream. The maximum intensity (7.6 cm/hr), total depth (2.5 cm), and duration (2.8 hours) were very similar to those measured upstream, yet no flow was detected in this reach of the channel (which is underlain by alluvium rather than bedrock) (Figure 3.2).

Although the formal project has now come to an end, it is our intention to continue collecting data from these instruments to the extent possible given the constraints of time and funding, in order to build up a record of flash-flood occurrence. We have recently teamed up with ARO Investigator Jeffrey Niemann of Colorado State University, who has installed a network of soil-moisture sensors at our PCMS monitoring site.

3.5 Scaling Analysis of Microtopography, Infiltration, and Runoff

A guiding theme of this project has been an effort to understand the connection between fine-scale and coarse-scale processes. In Chapter 2, we focused on this connection in the context of sediment motion and dispersion. Scaling also arises in the context of runoff generation in rangeland environments. Landscape evolution models (e.g., Tucker et al., 2001) and distributed hydrologic models (e.g., Ogden and Julien, 1993) typically operate at scales far coarser than the characteristic wavelength of microtopography on hillslopes. Consequently, hillslopes are treated as consisting of a series of hydrologically homogeneous, quasi-planar surfaces upon which runoff occurs as sheet flow. Yet there is evidence that fine-scale variability (on the order meters) in topography and infiltration capacity can play a fundamental role in altering the hydraulics of overland flow and the partitioning between infiltration and runoff (Figure 3.3).

In order to explore the role of heterogeneity on runoff production, we teamed up with Eric Small, a hydrologist with expertise in arid ecosystems, and his Ph.D. student David Bedford. We developed a 2-D numerical model of overland flow dynamics based on the diffusion-wave approximation of the shallow water equations. Bedford refined this model and used it, together with high-resolution measurements of microtopography and soil infiltration capacity at study sites in New Mexico and

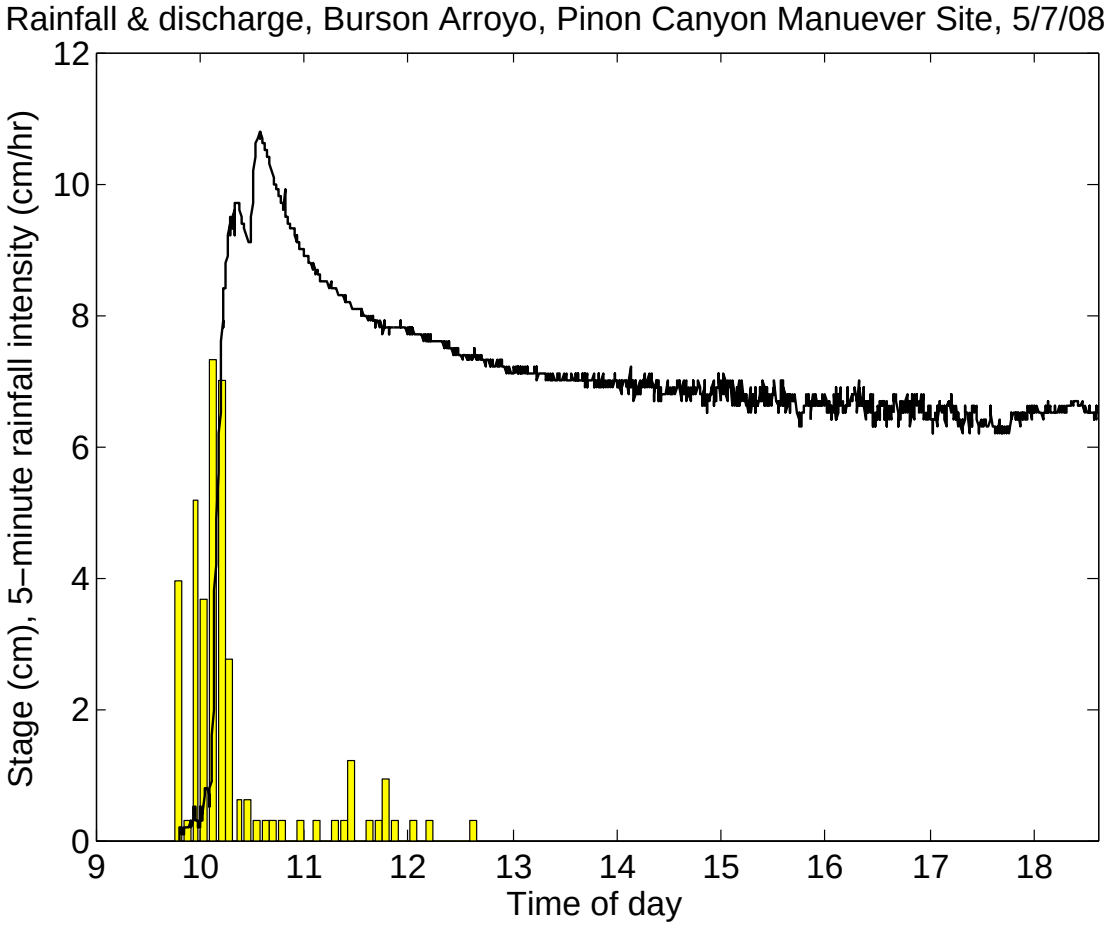

Figure 3.1: Water surface height in cm (black line) and five-minute average rainfall rate in cm/hr (bars) during a rainstorm on May 7, 2008 at Burson West monitoring site at Pinon Canyon Maneuver Site.

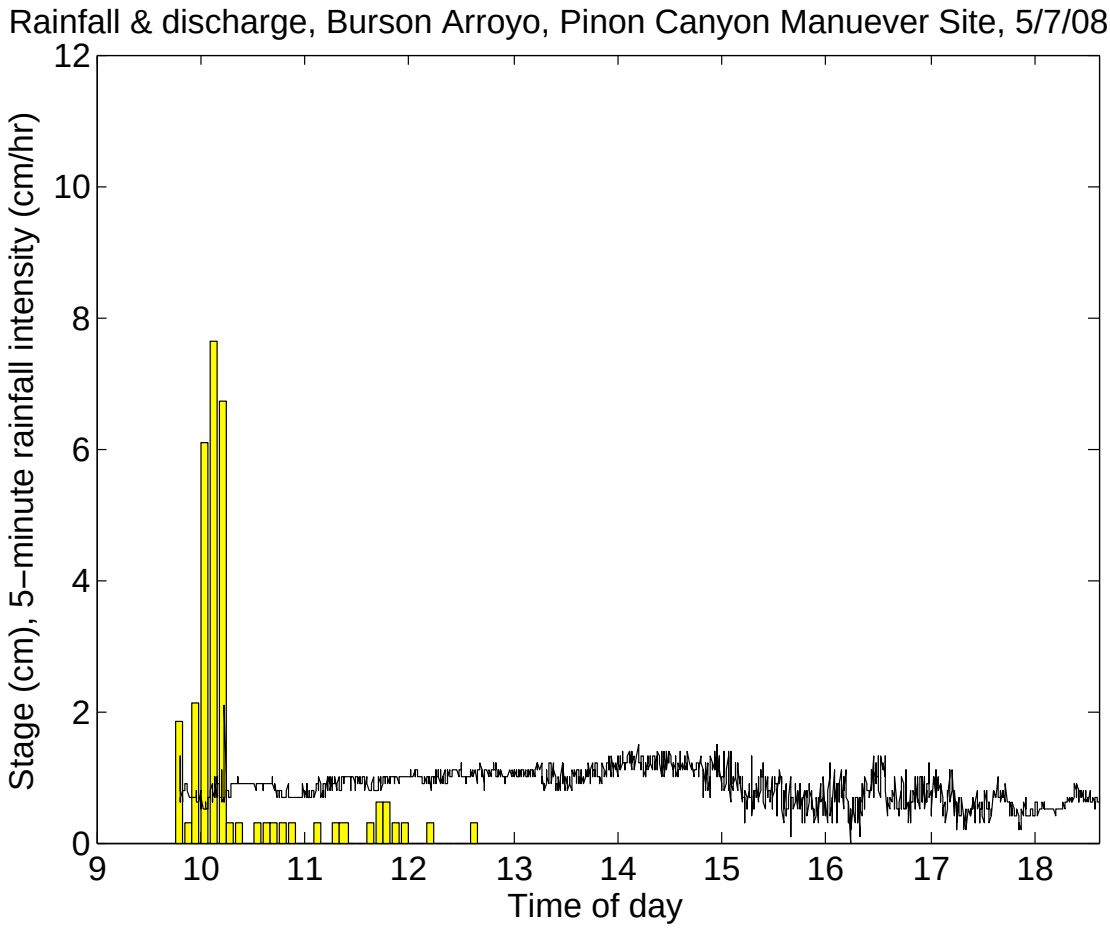

Figure 3.2: Surface height in cm (black line) and five-minute average rainfall rate in cm/hr (bars) during a rainstorm on May 7, 2008 at Burson Shed monitoring site at Pinon Canyon Maneuver Site, which lies a little over 800m downstream of the Burson West site (Figure 3.1). Although a flash flood was clearly detected at the upstream station, there is no evidence of flow at this station (the $\sim$1 cm variations in stage are indistinguishable from noise).

Figure 3.3: Photograph of overland flow on a shrubland area in Fort Carson, Colorado, following a 30-minute summer rain storm.

in the Mojave Desert, to investigate the impact of heterogeneity on runoff and infiltration. The results are the subject of a manuscript in preparation by Bedford, Small, and Tucker. In a nutshell, the results of the study indicate that presence of microtopography significantly reduces runoff (on the order of a factor of two to three) by impounding water in shallow depressions. The effect can, at least in principle, be parameterized using representative data on microtopography. The role of variability in soil infiltration capacity appears to be much less significant than that of microtopography at the study sites, for the simple reason that the amplitude of that variability is relatively small. Other workers have reported much larger variations in infiltration capacity at other sites, and the overall importance of these variations remains to be explored.

3.6 References

Arnold, L.J., 2006, Optical dating and computer modelling of Arroyo epicycles in the American Southwest [Ph.D. thesis]: Oxford, School of Geography and the Environment, University of Oxford, 426 p.

Arnold, L.J., Bailey, R.M., and Tucker, G.E. (2007) Statistical treatment of fluvial dose distributions from southern Colorado arroyo deposits: Quaternary Geochronology, v. 2, p. 162-167.

Boardman, J., Parsons, A.J., Holmes, P.J., Holland, R., and Washington, R., 2003, Development of badlands and gullies in the Sneeuberg, Great Karoo, South Africa: Catena, v. 50, no. 2-4, p. 165184, doi: 10.1016/ S0341-8162(02)00144-3.

Leopold, L.B., 1951, Rainfall frequency: An aspect of climatic variation: Eos (Transactions, American Geophysical Union), v. 32, p. 347357.

Ogden, F.L., and P.Y. Julien, 1993, Runoff Sensitivity to Temporal and Spatial Rainfall Variability at Runoff Plane and Small Basin Scales, Water Resour. Res., 29(8):2589-2597.

Sólyom, P.B., and Tucker, G.E. (2007) The importance of the catchment area-length relationship in governing non-steady state hydrology, optimal junction angles and drainage network pattern. Geomorphology, v. 88, p. 84-108.

Tucker, G.E., Arnold, L., Bras, R.L., Flores, H., Istanbulluoglu, E., Solyom, P. (2006) Headwater channel dynamics in semiarid rangelands, Colorado high plains, USA. Geological Society of America Bulletin, v. 118, no. 7/8, p. 959-974.

Chapter 4

Dynamics of Channel Cross-Section Development

4.1 Model for the Evolution of Channel Shape

Nature gives us many examples of self-organizing transport systems in which the flow of mass and/or energy becomes concentrated into narrow corridors. For instance, one finds examples of flow concentration in river networks, lightning bolts, blood vessels, leave veins, volcanic vents, and sub-glacial tunnels, to name a few. The origins of these self-organizing, often fractal structures have received considerable attention (e.g., Rodriguez-Iturbe and Rinaldo, 1997). They also raise interesting challenges with regard to modeling flows through networks. In the case of river networks, the dimensions and roughness of a channel exert fundamental control on hydraulics, erosion, sediment transport rates, and aquatic ecology. One can therefore ask: what is the nature of the self-organizing system that gives rise to the observed geometry and roughness properties of natural stream channels? It has been hypothesized that both individual channel segments and entire channel networks tend to adjust toward optimal states (e.g., Howard, 1990; Rodriguez-Iturbe and Rinaldo, 1997; Huang et al., 2004). Yet while optimality frameworks are valuable in understanding general properties, they do not necessarily shed light on the mechanisms by which optimality is achieved, nor do they say anything about the dynamics of channel change in response to external variables (climate, land use, tectonics, and so on) or simply in response to autocyclic variability. A theory of the dynamics behind channel geometry (a phrase which here means shape, size, and roughness characteristics) is an essential component behind models of landscape evolution (which usually rely on simple empirical rules for channel width and shape). Furthermore, from a practical point

of view, such a theory is important for channel engineering. These considerations motivated us to develop a two-dimensional numerical model for channel cross-section evolution under steady, unidirectional flow. The model is designed to operate on time spans long enough for channel shape to come into equilibrium, and to allow multiple cross-sections along a stream to be linked in a series. For reasons of computational efficiency, the flow field is approximated using linear, quasi-1D radial velocity profiles, rather than a complete 2D numerical solution of the flow equations. The model is described by Wobus et al. (2006), a reprint of which is attached as Appendix D.

An interesting prediction of the Wobus et al. (2006) model is that channel cross-sections tend toward an equilibrium state in which width-depth ratio is nearly constant, reflecting an equalization between the rate of bed lowering and the rate of (local) bank widening as the channel incises. This result supports a recent hypothesis (Finnegan et al., 2005). It also appears consistent with some, but not all, data collected along the Rio Torto, a bedrock river in central Italy (Whittaker et al., 2007a). The difference appears to lie in the degree of sediment cover: the morphology lower section of the channel, which is steep, narrow, and sediment-poor as a result of accelerated tectonic motion, shows a roughly constant width-depth ratio, while the upper reach, which is gentler and mantled with sediment, does not (for details of these studies, see Whittaker et al. 2007b, 2008). The results from the Wobus et al. (2006) model prompted us to explore the degree to which stream-power theory, combined with dynamic channel adjustment, could explain the observed longitudinal profile and cross-sectional geometry of the Rio Torto (Attal et al., 2008).

4.2 Numerical Testing by Comparison with a Ray-Isovel Model

In order to test the flow solution scheme used in the Wobus et al. (2006) model (WTA06), solutions were compared with those of a ray-isovel model written Jason Kean of the U.S. Geological Survey (Kean and Smith, 2004). A ray-isovel model is a boundary-value numerical solution to the equations of two-dimensional turbulent flow in a channel cross section. The name reflects the fact that the model iterates between a solution for flow velocities based on a gridded finite-difference scheme (which generates velocity contours, or isovels) and a solution for shear stresses based on curves orthogonal to the velocity contours (known as "rays") until the solution reaches an equilibrium in which there is no net acceleration on any element of water. The WTA06 algorithm was also modified to enable computation of the flow field in wider channels, in which the high-velocity core extends over a significant width

of channel. The revised algorithm (WKTA08) does a good job capturing the flow field with significantly less computational overhead than that required by a ray-isovel model. The results of the analysis are reported by Wobus et al. (2008), a copy of which is attached as Appendix E.

4.3 Using a 2D Flow Model to Analyze the Stability of Bank-Sloped Channels

We also conducted a pilot study to test the feasibility of using a cross-sectional flow model as a decision-support tool for channel modification. On Army training installations such as Fort Carson, steep-sided gullies present a hazard to tracked and wheeled vehicles. A common practice in mitigating this hazard has been to "bank slope" the gullies, which involves using earth-moving equipment to re-grade the channel banks, creating a smoothed cross-section that vehicles can navigate. The banks and channel floor are then re-seeded to encourage growth of a protective vegetation armor. In some instances, this method appears to have worked in the sense that channels have remained stable for years after being re-engineered. In other cases, flash floods have re-incised channels and returned them to their original U-shaped geometry (J. Linn and B. Miller, personal communication).

One risk of bank-sloping is that it can effectively increase the erosivity of flash floods by forcing flow into a narrow thalweg. Ideally, one would like to be able to mitigate this risk by estimating ahead of time the likelihood that a bank-sloped channel will be re-incised by a flash flood. In order to do so, one would have to be able to estimate three quantities for any particular channel: (1) the frequency and magnitude distribution of flash floods, (2) the peak shear stresses produced by floods of a given flood, and (3) the effective threshold shear stress below which erosion would be minimal. Data on flood frequency distribution requires either flow and rainfall monitoring in fairly small basins (as discussed in Chapter 3), distributed hydrologic modeling, or (ideally) both. Up-scaling of soil properties and microtopography also has a role to play here. The best method for estimating peak shear stress depends on the channel shape and roughness. If the width-depth ratio is sufficiently high and the roughness elements (chiefly vegetation) reasonably uniform across the channel, the standard depth-slope product method can be used. However, Wobus et al. (2008) showed that for width-depth ratios less than about ten, the depth-slope product method overestimates the peak shear stress because it fails to account for frictional losses to the side walls. Thus, for narrow, confined flows (or for those in which roughness is highly variable across a channel), a cross-sectional flow model like that of Kean and Smith

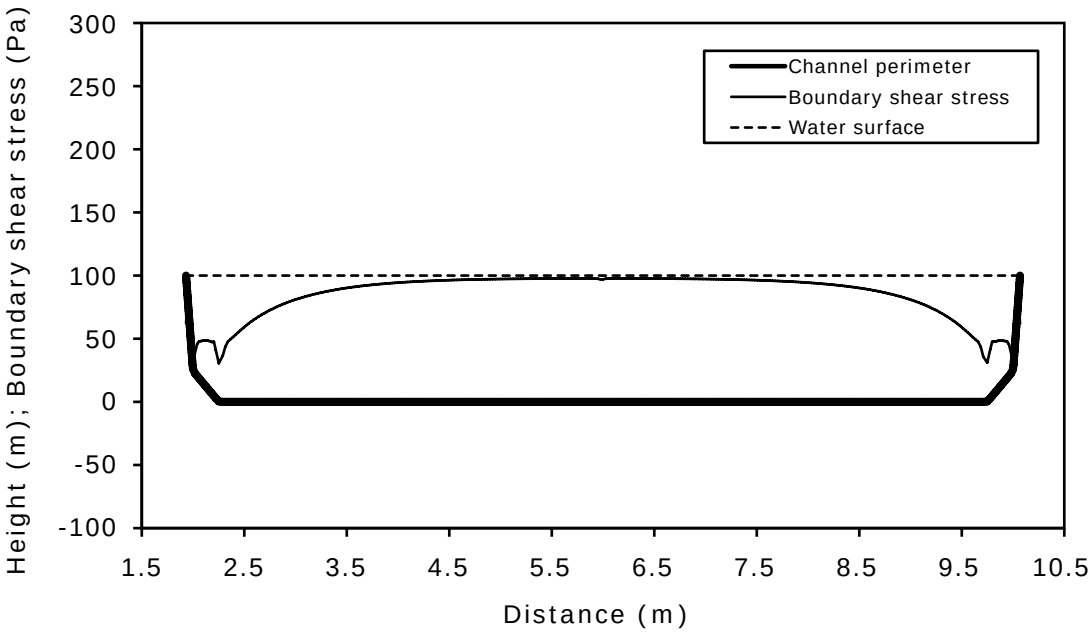

Figure 4.1: Flow and shear stress in a gully cross section calculated using the Kean-Smith ray-isovel model. Section is based on typical cross-section measurements of Burson Arroyo, Pinon Canyon Maneuver Site, Colorado.

(2004) or Wobus et al. (2008) would be more appropriate for estimating peak shear shear stresses. Figures 4.1-4.3 show the results of a boundary shear-stress calculation performed by Jason Kean using the Kean-Smith model. The calculations are based on a tributary channel to Taylor Arroyo at PCMS known informally as Burson Arroyo, under three different conditions: natural channel (Figure 4.1), bank-sloped inward (Figure 4.2), and bank-sloped partly outward (i.e., removing excavated wall material from the channel in order to leave a flat channel floor) (Figure 4.3). Parameters used in the calculation include gradient, discharge, and roughness height, which was estimated on the basis of in-channel vegetation. The calculations show that inward bank-sloping raises the peak shear stresses significantly more than the outward bank-sloping because the flow becomes concentrated at the narrow center of the trapezoidal cross section.

In order to estimate the relative stability of a natural or modified channel under

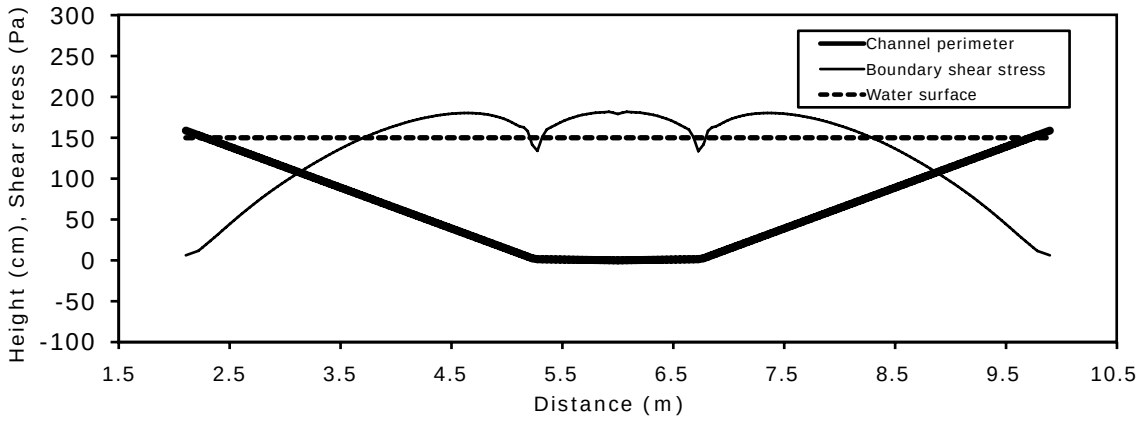

Figure 4.2: Flow and shear stress in a gully cross section that has been banksloped inward, calculated using the Kean-Smith ray-isovel model.

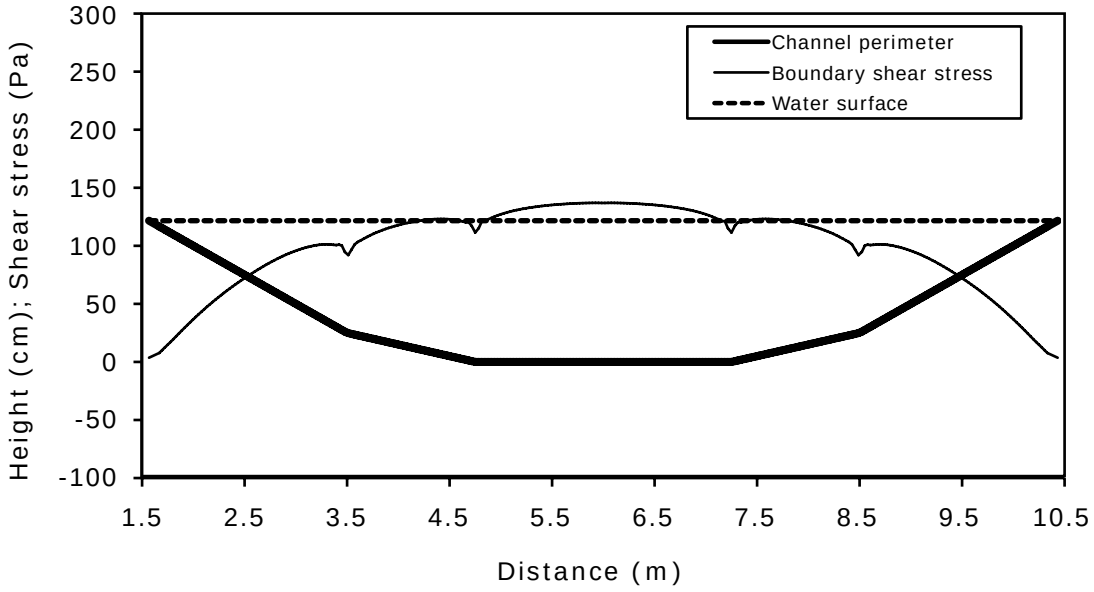

Figure 4.3: Flow and shear stress in a gully cross section that has been banksloped outward, retaining a portion of the original flat channel floor. Flow and stress calculated using the Kean-Smith ray-isovel model.

a given stress field, the effective peak shear stress can be compared with an estimate of the stress required for significant sediment detachment and transport. Two ways of doing this are (1) to calculate the portion of stress applied as skin friction to channel sediment (or rock), as opposed to vegetation or other roughness elements, and compare this with empirical estimates the detachment threshold (e.g., Istanbulluoglu and Bras, 2005), and (2) to compare the total (bulk) stress to estimates of the minimum bulk stress required for erosion as a function of vegetation cover fraction (e.g., Prosser and Slade, 1994). The first approach is potentially more accurate because it accounts for the partitioning of friction between form drag and skin drag, and between plants and sediment, while the latter has the advantage of simplicity. Tucker et al. (2006) provide an example of the latter method, as well as a compilation of published estimates of bulk critical shear stress values.

4.4 References

Attal, M., Tucker, G.E., Whittaker, A.C., Cowie, P.A., and Roberts, G.P. (2008) Modeling fluvial incision and transient landscape evolution: Influence of dynamic channel adjustment. Journal of Geophysical Research - Earth Surface, v. 113, F03013, doi:10.1029/2007JF000893.

Finnegan, N. J., Roe, G., Montgomery, D. R., and Hallet, B., 2005, Controls on the channel width of rivers: implications for modeling fluvial incision of bedrock: Geology (Boulder), v. 33, p. 229-232.

Howard, 1990. A.D. Howard , Theoretical model of optimal drainage networks. Water Resour. Res. 26 9 (1990), pp. 21072117.

Huang, H., Chang, H. and Nanson, G. C. (2004). Minimum Energy as the general form of Critical flow and maximum flow efficiency and for explaining variations in river channel pattern. Water Resources Research, 40 1-13.

Istanbulluoglu, E., and Bras, R.L. (2005) Vegetation-modulated landscape evolution: Effects of vegetation on landscape processes, drainage density, and topography. Journal of Geophysical Research, 110, F02012, doi:10.1029/2004JF000249.

Kean, J. W., and J. D. Smith (2004), Flow and boundary shear stress in channels with woody bank vegetation, in Riparian Vegetation and Fluvial Geomorphology, Water Sci. Appl. Ser., vol. 8, edited by S. J. Bennett and A. Simon, pp. 237252, AGU, Washington, D. C.

Prosser, I.P., and Slade, C.J., 1994, Gully formation and the role of valley-fl oor vegetation, southeastern Australia: Geology, v. 22, no. 12, p. 11271130, doi: 10.1130/0091- 7613(1994)022¡1127:GFATRO¿2.3.CO;2.

Rodriguez-Iturbe I, Rinaldo A. 1997. Fractal River Basins Chance and Self Organisation, Cambridge University Press, Cambridge, United Kingdom.

Whittaker, A. C., Cowie, P. A., Attal, M., Tucker, G. E., and Roberts, G. P., 2007a, Bedrock channel adjustment to tectonic forcing: Implications for predicting river incision rates: Geology (Boulder), v. 35, p. 103-106.

Whittaker, A. C., Cowie, P. A., Attal, M., Tucker, G. E., and Roberts, G. P., 2007b, Characterizing the transient response of rivers crossing active normal faults: New field observations from Italy: Basin Research, doi:10.1111/j.1365-2117.2007.00337.x.

Whittaker, A.C., Attal, M., Cowie, P.A., Tucker, G. E., and Roberts, G. P., 2008, Decoding temporal and spatial patterns of fault uplift using transient river long profiles: Geomorphology, in press.

Wobus, C.W., Kean, J.W., Tucker, G.E., and Anderson, R.S. (2008) Modeling the evolution of channel shape: balancing computational efficiency with hydraulic fidelity. Journal of Geophysical Research - Earth Surface, v. 113, F02004, doi:10.1029/2007JF000914.

Wobus, C.W., Tucker, G.E., and Anderson, R.S. (2006) Self-formed bedrock channels. Geophysical Research Letters, v. 33, L18408, doi: 10.1029/2006GL027182.

Appendix A

Reprint: Headwater channel dynamics in semiarid rangelands, Colorado high plains, USA

Reference: Tucker, G.E., Arnold, L., Bras, R.L., Flores, H., Istanbulluoglu, E., Sólyom, P. (2006) Headwater channel dynamics in semiarid rangelands, Colorado high plains, USA. *Geological Society of America Bulletin*, v. 118, no. 7/8, p. 959-974.

Headwater channel dynamics in semiarid rangelands, Colorado high plains, USA

Gregory E. Tucker[†]
Cooperative Institute for Research in Environmental Sciences (CIRES) and Department of Geological Sciences, University of Colorado, Boulder, Colorado 80309, USA

Lee Arnold[‡]
School of Geography and the Environment, University of Oxford, South Parks Road, Oxford OX1 3QY, UK

Rafael L. Bras[§]
Homero Flores[#]
Department of Civil and Environmental Engineering, Massachusetts Institute of Technology, Cambridge, Massachusetts 02139, USA

Erkan Istanbulluoglu[††]
Department of Geosciences, University of Nebraska, Lincoln, Nebraska 68588, USA

Peter Sólyom[‡‡]
School of Geography and the Environment, University of Oxford, South Parks Road, Oxford OX1 3QY, UK

ABSTRACT

Incised ephemeral channels provide a window into the fluvial processes that help sculpt rangeland landscapes. This paper presents observations of ephemeral channels and valley networks in the high plains of Colorado, USA, with an eye toward painting a picture of the ingredients that must be included in mathematical models of landscape evolution in such environments. Channel incision in the study area is driven by summer thunderstorms, which can with reasonable frequency (3–5 yr) generate boundary shear stresses high enough to penetrate the highly resistant vegetation armor, but only within erosional hot spots where hydraulic forces are amplified by channel constriction and locally steep gradients. Focusing of erosion at these hot spots (which correspond to knickpoints and channel heads) is amplified by the small areal footprint and short "erosional reach" of most convective storms. Upstream migration of knickpoints creates a pattern of short, active channel reaches separated by unchanneled or weakly channeled, fully vegetated stable reaches. Based on our observations, we interpret the necessary and sufficient conditions leading to the observed channel forms and dynamics as: (1) a resistant vegetation layer overlying an erodible substrate, which sets up a conditional instability through which erosional perturbations can grow by positive feedback; (2) high flow variability; (3) moderate to high substrate cohesion; and (4) a high volume fraction of fine-grained erodible material. Concave-upward valley long profiles are interpreted as a trade-off between downstream-increasing flood frequency and downstream-decreasing flood effectiveness. The observed process dynamics imply that long-term rates of valley incision should be especially sensitive to climatic oscillations between episodes of drought and warm-season convective rainfall.

Keywords: arroyos, climate, erosion, gullies, networks, streams.

INTRODUCTION

Understanding erosion and sediment transport in rangeland landscapes is important for a variety of reasons. From the perspective of land management, effective erosion control requires an understanding of the nature, frequency, and magnitude of the climatic, hydrologic, biotic, and geomorphic drivers. From the perspective of long-term landscape evolution, a quantitative understanding of the "rules of the landscape" is needed in order to answer questions such as: What are the frequency and magnitude properties of sediment movement, and how do these change with spatial scale? How sensitive are rates of sediment movement and topographic change to climatic, tectonic, or human forcing? What interpretations of the Quaternary landscape-change record are consistent with the mechanics and chemistry of the driving processes? In addition, in the particular case of the high plains bordering the Colorado Front Range, which we investigate here, quantitative models of rangeland dynamics are needed to test the plausibility of the hypothesis that climatic oscillation has driven late Cenozoic accelerated denudation along the margins of the Colorado Rockies (e.g., Gregory and Chase, 1994; Zhang et al., 2001).

In this contribution, we focus on the dynamics of low-order ephemeral channel networks. Ephemeral headwater channel systems are important to understand because they are primary conduits for water and sediment movement in arid and semiarid landscapes. They also tend to be highly dynamic, with gully systems capable of growing rapidly into formerly unchanneled valleys (e.g., Montgomery and Dietrich, 1992; Prosser et al., 1994; Bull, 1997; Fanning, 1999; Tucker and Slingerland, 1997; Boardman et al., 2003; Istanbulluoglu et al., 2004) and generating high sediment yields.

[†]E-mail: gtucker@cires.colorado.edu.
[‡]E-mail: lee.arnold@st-peters.ox.ac.uk.
[§]E-mail: rlbras@mit.edu.
[#]E-mail: homefc@mit.edu.
[††]E-mail: erkan@unl.edu.
[‡‡]E-mail: peter.solyom@geog.ox.ac.uk.

GSA Bulletin; July/August 2006; v. 118; no. 7/8; p. 959–974; doi: 10.1130/B25928.1; 13 figures; 5 tables.

Modern gully networks are often attributed to human impacts (typically livestock grazing; e.g., Graf, 1988; Fanning, 1999). For example, Dietrich et al. (1993) argued that the extent of channels in a California grassland catchment could only be explained by past vegetation disturbance; the extent of the mapped channel network corresponded to an overland flow erosion threshold of 16–32 Pa, while a flume study in the same catchment suggested an effective erosion threshold of over 100 Pa under complete grass cover (Prosser et al., 1995). Montgomery and Dietrich (1992) interpreted the extension of gullies in the same setting as a response to overgrazing. Yet the fact that this and other gully networks typically occupy preexisting valley networks (as opposed to hillslopes) suggests that periodic sediment evacuation by channel extension is a common natural process that does not require human disturbance (e.g., Reneau et al., 1990). In order to understand the dynamics of valley network extension and retreat over geologic time scales, and the sensitivity of the system to environmental change (e.g., Rinaldo et al., 1995; Tucker and Slingerland, 1997), we need to understand the natural trigger factors for channel growth and retreat. To what degree is channel network extension driven by rare, intense storms, as opposed to episodes of vegetation disturbance due to drought, grazing, and disease? What controls the frequency and magnitude of extension events? And what are the implications of these controls for catchment sensitivity to climate change?

Here, we report observations from ephemeral channel networks in Colorado, USA, to address these questions and provide data for testing quantitative models. Our aim is to paint a picture of the morphology, driving processes, and dynamics of low-order ephemeral streams in this region. Analyses of aerial photographs and recent erosion events provide insights into the tempo of channel extension. Paleohydrologic reconstructions provide evidence for the magnitude of shear stresses generated during convective summer storms, and the relative frequency of these events. From these observations, inferences are drawn regarding the geomorphic impact of localized, high-intensity storm cells. Collectively, these observations and inferences provide a necessary backdrop for developing process-based mathematical models to describe channel network dynamics in this type of setting.

BACKGROUND

The term rangeland is usually defined on the basis of vegetation (predominantly grasses, shrubs, and similar groups) or land use (suitable for grazing animals but not arable agriculture) or both. Here, we use a looser, geomorphically based definition: terrain with low to moderate relief in which either present-day or glacial maximum climate supported a climax vegetation of predominantly low-growing species such as shrubs and grasses. This definition includes the high plains and plateau landscapes of the North American west, much of southern Africa, the central Asian steppes, large areas of the Australian lowlands, Mediterranean regions, South American pampas, and similar regions.

The geomorphology of rangelands is commonly characterized by ephemeral or intermittent stream channels and unchanneled valleys. Dry channels, variously called "gullies," "arroyos," "wadis," or other regional terms, are common. Whatever the name, ephemeral channels in rangelands are often incised into valley-floor alluvium or occasionally bedrock (e.g., Cooke and Reeves, 1976; Graf, 1983; Bull, 1997; Prosser and Slade, 1994; Boardman et al., 2003). Some of these incised dry-land channels are continuous, while others (generally in smaller basins) are discontinuous, with entrenched reaches separated by nonincised valley segments (Bull, 1997). Here we use the term arroyo to refer generally to incised, ephemeral channels with steep sidewalls and a rectilinear to U-shaped cross section. (Note that by including incised ephemeral channels of all sizes, we depart from the definition of Graf [1988], who preferred the term "gully" for smaller channels. However, "gully" is commonly used to refer to any small, incised channel regardless of morphology, and is therefore too general for our purposes.)

Arroyo networks are zones of concentrated geomorphic activity, and an understanding of sediment budgets and landscape sensitivity therefore requires a quantitative understanding of their governing mechanisms. A great deal has been written on arroyo networks, particularly those in the western United States. The bulk of the literature, however, has concentrated on understanding the trigger factors (e.g., grazing, subtle climate change, or other causes) for widespread arroyo incision in the American west near the close of the nineteenth century (e.g., Antevs, 1952; Cooke and Reeves, 1976; Graf, 1983). Although "ultimate causes" have proven difficult to untangle, it is clear that there usually is a strong correlation between the advent of intensive grazing and widespread channel incision (e.g., Graf, 1988), but equally, in some parts of the world, ancient filled channels indicate that incision has occurred repeatedly during the late Quaternary, indicating that intensive livestock grazing is not the only possible trigger (e.g., Waters and Haynes, 2001).

A number of studies have focused on documenting patterns of channel change in dry lands, using repeat channel surveys, space-time substitution, and other methods. These studies resulted in a valuable database of observations and led to the development of conceptual models to describe a typical "arroyo cycle." Schumm (1977) argued that arroyos commonly undergo a phase of rapid incision, followed by widening and subsequent aggradation as stream power decreases and sediment supply from side walls increases. This view was modified by Elliott et al. (1999) to include the possibility of subsequent phases of incision. Leopold (1951) correlated arroyo trenching in the southwestern United States with a period of increased rainfall intensity and decreased mean rainfall, and argued that this subtle climate change was sufficient to drive widespread incision. This view was challenged by Schumm and Parker (1973) and Patton and Schumm (1975), who argued on the basis of field observations and laboratory experiments that repeated episodes of incision and infilling can occur due to internal dynamics within a drainage network and do not necessarily require direct external forcing. Likewise, Schumm et al. (1987) found experimental evidence for a "complex response" to external forcing, in which a single base-level fall stimulated a series of complex, localized erosion-deposition reverberations that were superimposed on an overall exponential-like decline in sediment yield. Slingerland and Snow (1988) later established a theoretical basis for these fluctuations. In a similar vein, Bull (1997) developed a conceptual model for discontinuous ephemeral streams in which deposition of a fan-like deposit below a discontinuous channel leads to a gradual increase in gradient, until stream power is sufficient to drive renewed incision.

Collectively, the evidence for complex internal dynamics in a drainage network implies that past episodes of incision or infilling will not necessarily provide much information about environmental change. It does not, however, imply that channel incision is unpredictable, but simply that the proximal causes are at least partly internal (e.g., variations in channel width, gradient, stream power, etc.) rather than external.

Despite these advances, we still lack a quantitative, process-based theory for arroyo formation and development, though recent models have begun to address this issue (Howard, 1999; Kirkby and Bull, 2000; Istanbulluoglu et al., 2004, 2005) and related problems, such as the role of vegetation dynamics in ephemeral channel networks (Collins et al., 2004). To develop and test a comprehensive, process-based theory, we require quantitative observations of arroyo hydrology, kinematics (rates of

morphologic change), vegetation patterns, and erosion and sedimentation rates. Here we report on observations collected from arroyo networks in central and southern Colorado, USA. These observations, together with inferences drawn from numerical modeling, point toward (1) an episodic pattern of arroyo initiation and growth in both time and space, (2) the importance of intense, convective storms in driving channel incision and advance, and (3) the central role of rangeland vegetation as an erosion mediator.

FIELD SETTING

We focus on two field areas in the Colorado high plains. The first lies in the Red Creek and Dry Creek drainage basins, just east of the central Colorado Front Range and south of the city of Colorado Springs (Figs. 1A and 1B). Topography comprises a mixture of rugged foothills, reflecting the progressive dissection of deformed Paleozoic through late Mesozoic sedimentary rocks, and open rangelands. The landscape is adorned with remnants of Quaternary gravel-capped terrace surfaces, which generally decrease in age, altitude, and extent from west to east. Valley networks in the more cohesive soils and/or lithologies are typically veined with steep-walled incised channels. The bulk of the underlying lithologies are sedimentary rocks related to the Cretaceous Western Interior Seaway. Mean annual rainfall in nearby Colorado Springs is 41 cm, with a late summer maximum. Most summer rain arrives in the form of convective thunderstorms, which can generate short-term (1–5 min) peak rainfall intensities ranging from a few tens of millimeters per hour to as high as 300 mm/h within the core of the cell (e.g., Goodrich et al., 1997; Bull et al., 1999; Ogden et al., 2000).

The second site lies along the northern margin of the Purgatoire River, a large tributary of the Arkansas, and includes Big Arroyo (40 km^2; tributary of Timpas Creek) and Taylor Arroyo (125 km^2; tributary of the Purgatoire River) drainage basins (Figs. 1A and 1C). The landscape is one of open, gently rolling rangelands interrupted by prominent bedrock scarps. Vegetation is primarily a mix of grassland and open piñon-juniper woodland. The Purgatoire River and the lower parts of its tributaries occupy steep-walled bedrock canyons. The bedrock geology consists of a subhorizontal sequence of Jurassic through late Cretaceous sedimentary rocks. To the northeast, an anticline belonging to the Apishapa Arch forms a dome slivered by steep-walled box canyons. Mean annual rainfall is ~30 cm, with a July maximum. Each year the area receives ~60 convective thunderstorms on average (von Guerard et al., 1987). Figure 2 shows the cumulative (one day) rainfall pattern of a typical summer thunderstorm system. All or most channels, except the Purgatoire itself, are ephemeral and often clearly incised into the underlying alluvium or bedrock. Based on U.S. Geological Survey flow records, Big and Taylor Arroyos convey an average of 5–6 flash floods each year. An overview of the hydrology and physiography of the area is given by von Guerard et al. (1987).

CHANNEL MORPHOLOGY

Occurrence and Lithology

A variety of different channel forms has been observed in these field areas and similar environments in the Colorado piedmont. As discussed above, we focus here on ephemeral valley networks containing incised channels with distinct, steep to vertical side walls (Fig. 3). Often, these incised channels are discontinuous, with segments terminating at their upstream end in an abrupt head scarp abutting

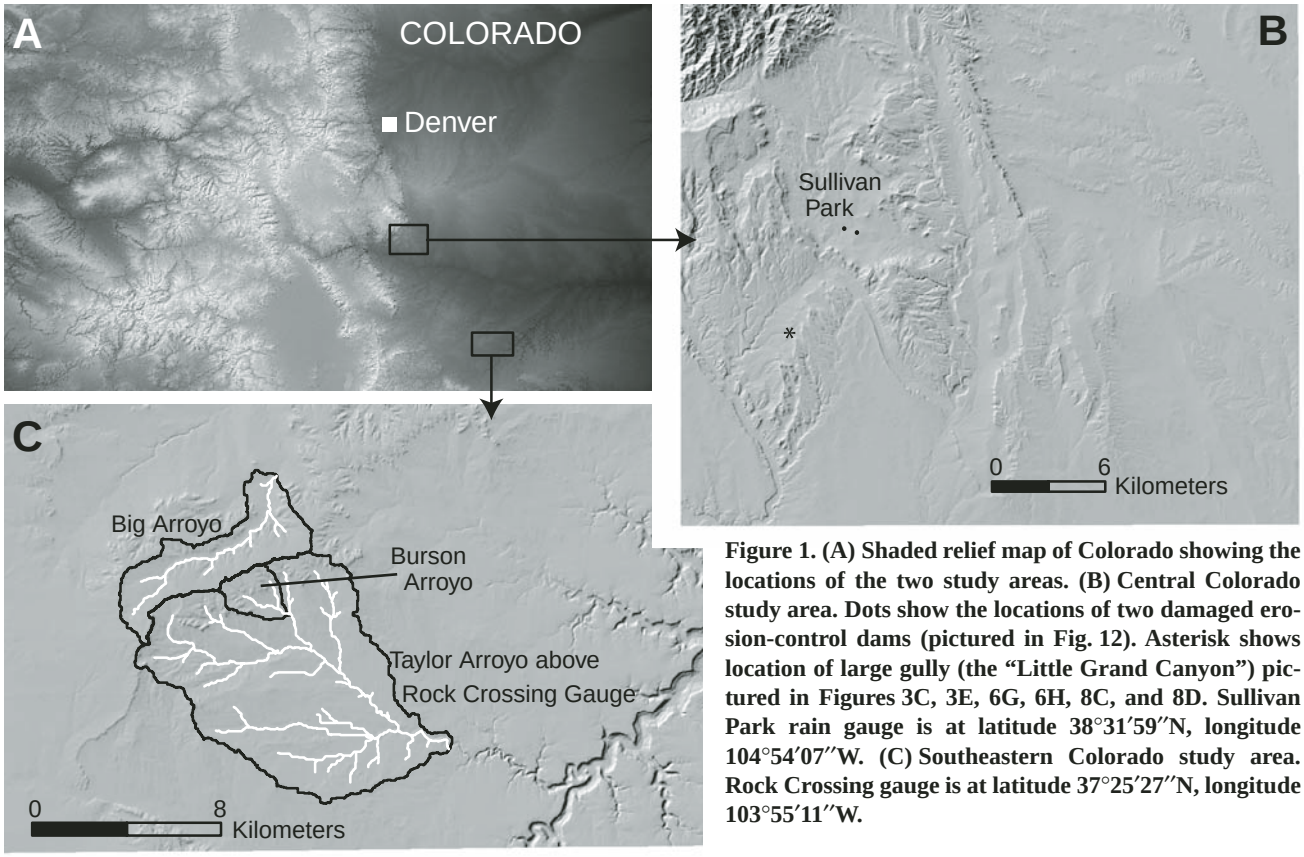

Figure 1. (A) Shaded relief map of Colorado showing the locations of the two study areas. (B) Central Colorado study area. Dots show the locations of two damaged erosion-control dams (pictured in Fig. 12). Asterisk shows location of large gully (the "Little Grand Canyon") pictured in Figures 3C, 3E, 6G, 6H, 8C, and 8D. Sullivan Park rain gauge is at latitude 38°31′59″N, longitude 104°54′07″W. (C) Southeastern Colorado study area. Rock Crossing gauge is at latitude 37°25′27″N, longitude 103°55′11″W.

a plunge pool (cf. Bull, 1997). Based on aerial photograph analysis and field reconnaissance, it is clear that these channels occur predominantly in cohesive valley alluvium and/or shale bedrock. Texture analysis shows that valley fills typically range from clay to sandy loam; the average median grain size from 41 field samples is 0.03 mm (medium silt; ϕ = 5.9 ± 1.8; Flores, 2004). Incised channels are rare or absent in more competent lithologies (e.g., the Fort Hayes limestone member of the Niobrara Formation), though they often occur in alluvial valley fills that overly these lithologies. Where channels have been observed to cut into bedrock, the bedrock is typically shale-rich. In several cases, we have observed vertical walls of alluvium overhanging fissile shale bedrock, suggesting that the fill is often more cohesive than the shale (Fig. 3C). Steep-walled ephemeral channels are also rare on the Quaternary gravel-capped pediments that drape the skirts of the Front Range, presumably due to lack of cohesion in the gravels (Istanbulluoglu et al., 2005).

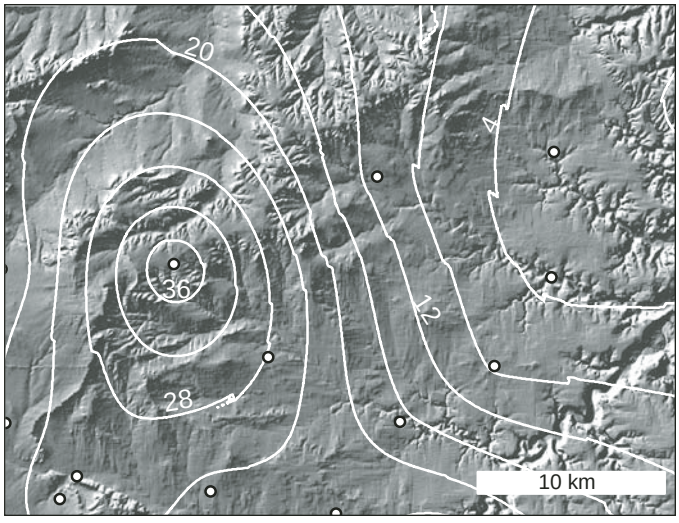

Figure 2. Map showing 24 h precipitation total over Big and Burson Arroyos on 8 August 2003. Contour interval is in mm. White circles show positions of tipping-bucket rain gauges. The *e*-folding distance for decay of rainfall total from the storm center is ~10–15 km. Peak precipitation was recorded at Burson Well, latitude 37°30′04″N, longitude 104°03′20″W.

Cross-Sectional Geometry and Side-Wall Stability

By definition, the channels investigated here are rectilinear to U-shaped in cross section. Side walls often show a near-vertical wall section above a sloping rampart (Fig. 3C). Vertical wall height is correlated to substrate cohesion (Fig. 4), and Istanbulluoglu et al. (2005) showed that this material control on wall stability can have a first-order impact on the morphological style of channel propagation. Unlike the valley and channel floors, and to a lesser extent ramparts, steep channel walls are nearly always devoid of vegetation (Fig. 3). Vegetation on channel floors ranges from essentially absent (Figs. 3C and 3E) to a full cover of woody and herbaceous riparian species (Fig. 3B).

Channel Heads

We have observed three types of channel head morphology, which often intergrade with one another:

1. Channels or channel segments that terminate abruptly with steep, vertical headcuts (ranging from "large step" to "large headcut" in the classification of Dietrich and Dunne, 1993, and corresponding to the "abrupt" channel-head morphology of Oostwoud Wijdenes et al., 1999) (Figs. 3A and 3D).

2. Channels in which a narrower, shallower reach extends tens of meters above a prominent, broader and deeper head scarp. In these cases, the head scarp is typically supported by tree roots or by a resistant rock stratum. This morphology corresponds to the "rilled-abrupt" classification of Oostwoud Wijdenes et al. (1999).

3. Flights of arcuate, discontinuous steps (Fig. 5). Steps often lack discernible banks; where present, these rarely extend more than a few meters below the step. Step flights often occur up-valley from a longer channel segment showing morphology type 1 or 2. In other cases, they grade gradually downstream into increasingly long discontinuous channel segments. Evidence from historical air photos (discussed in the following) shows that step flights are sometimes precursors to continuous incised channel segments.

Longitudinal Profiles

The longitudinal valley profiles are generally straight to moderately concave-upward (typical concavity index between 0.1 and 0.4, as defined by Whipple and Tucker, 1999), and often show lithologic control (Fig. 6). In some cases, the upward-concave profiles extend upstream of the modern channel network. For example, in the valley shown in Figures 6C and 6D, the upper portion of the valley is decorated with a flight of steps (Fig. 5), but is otherwise unchanneled.

Discontinuous incised channels with lengths on the order of a few hundred meters are often deepest at their head, and grade into the valley surface at their terminus (Figs. 3C and 6G). In some cases, the lower portion of the incised channel grades into a fan within the valley. Next, we explore the origins of this pattern.

RATES AND PATTERNS OF CHANNEL GROWTH

Cut-and-Fill Cycles

Several lines of evidence indicate that arroyos in the study area undergo alternating periods of channel incision and valley/channel aggradation, a behavior that is common to arroyo systems elsewhere in the western United States (e.g., Patton and Schumm, 1975; Cooke and Reeves, 1976; Graf, 1983; Bull, 1997; Elliott et al., 1999; Waters and Haynes, 2001). Unchanneled valley segments often alternate with incised channels (Fig. 7). Ancient, infilled channels are commonly observed in channel side walls (Fig. 3C). Optically stimulated luminescence (OSL) da ting of basal fills in paleochannels in the study area yields ages ranging from early to late Holocene (Arnold, 2006).

Historic Aerial Photograph Analysis

In order to estimate rates of gully-head advance, we compared historic and modern aerial photographs covering two quarter-quadrangles (3.75′ × 3.75′) that fall within the northern study area. The northeast quadrant of the U.S. Geological Survey (USGS) Pierce Gulch 7.5′ quadrangle and the northwest quadrant of the Steele Hollow 7.5′ quadrangle were chosen because they include arroyo networks that we have examined closely in the field. Two photograph series were used: 1937 USDA (U.S. Department of Agriculture) 1:20,000 photographs, and

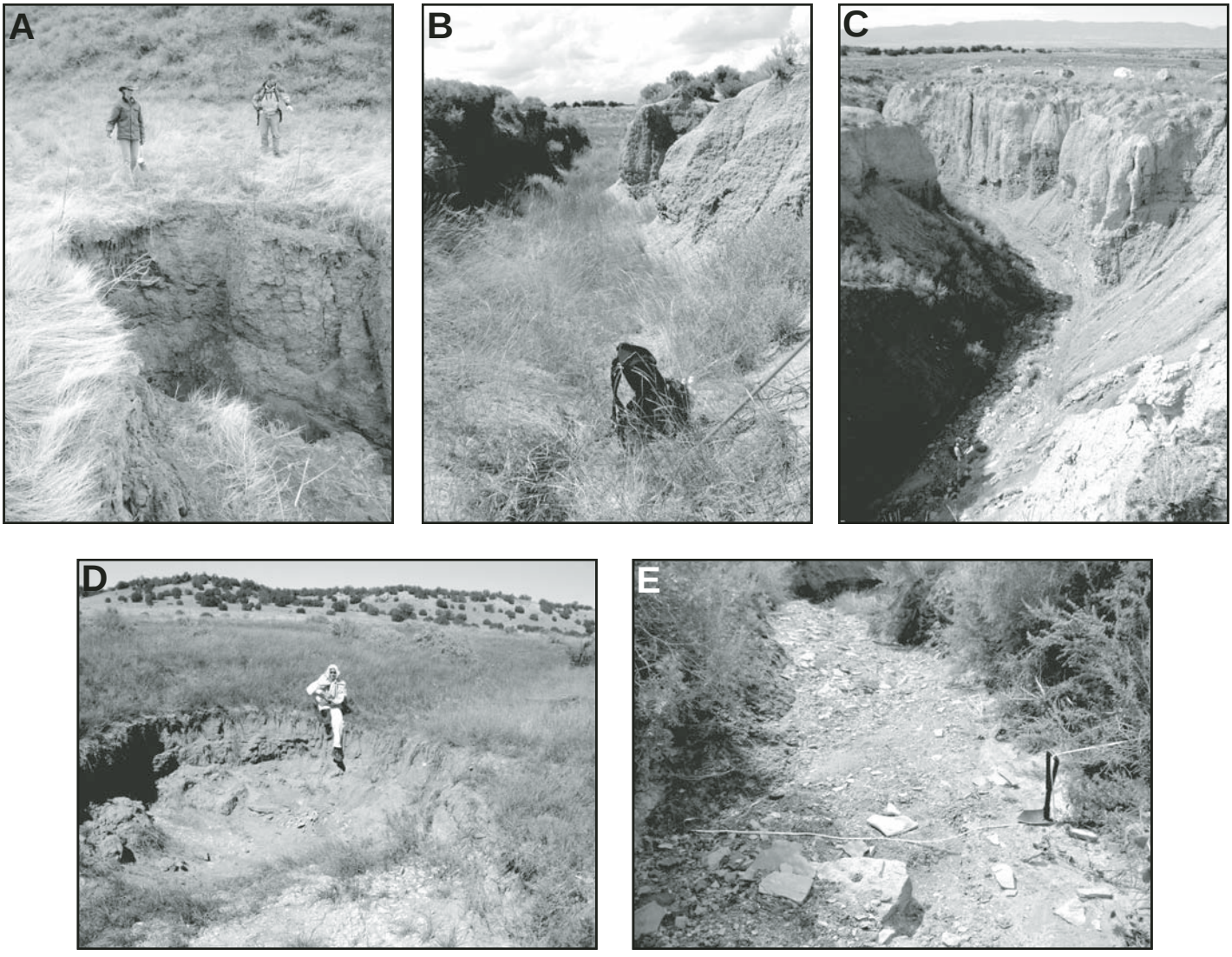

Figure 3. Examples of channels, channel heads, and discontinuous scarp flights. (A) Typical head scarp, West Bijou Creek drainage, central Colorado. The valley above is unchanneled. Note tension crack and incipient slab failure at center right. (B) Grass-lined channel in the Dry Creek drainage basin. Backpack is about half a meter high. (C) Deeply incised, scoured channel in the Red Creek basin. Along the right-hand wall, top center are two large paleochannels, marked by the light-colored fill inset into dark shale bedrock. (D) Head scarp with plunge pool along Big Arroyo (Fig. 1B). Above, the channel consists of a shallow, fully vegetated swale; below is an incised reach that grades downstream into a shallow, overgrown swale before reaching another head scarp. The drainage area here is ~15 km^2. (E) Close-up view of scoured channel in the Red Creek drainage (same channel as C).

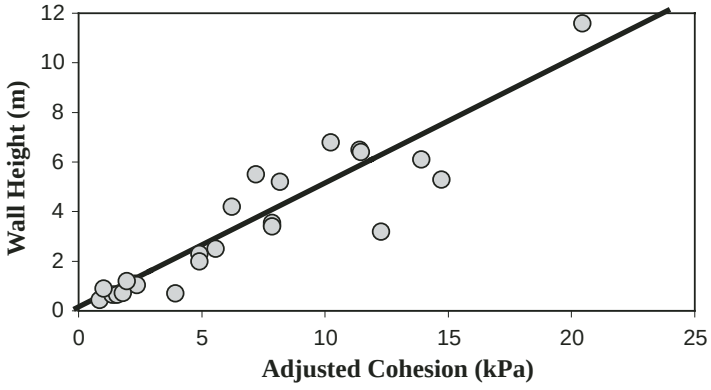

Figure 4. Vertical channel wall height as a function of cohesion (after Istanbulluoglu et al., 2005).

1999 USGS 1:12,000 digital orthophotos. The historic photographs were scanned at high resolution (~30 pixels per meter) and enlarged. All channel heads or prominent in-channel headcuts that were clearly identifiable in both photo series and not obscured by check dams, roads, or other features, were included in the analysis. Given limits in resolution and photograph distortion, the minimum identifiable extent of channel-head advance is on the order of 4–5 m, which represents an average rate of ~6–8 cm/yr. Figure 8 shows an example of two incised channel networks as they were in 1937 and 1999.

The majority of the channel segments analyzed experienced little or no discernible growth over the six-decade period between photo pairs (Fig. 9). The frequency distribution is strongly right-skewed. For example, although most of the networks appear essentially stable; five channel segments (13% of the data set) show average extension rates of more than 45 cm/yr over the 62 yr period between photo pairs. The most rapid average incision rate comes from an ~100-m-long tributary segment, which, by 1999, had incised a previously unchanneled alluvial flat. There is no apparent spatial clustering in the distribution of average extension rates. Given the observations of gully formation dynamics discussed herein, it is likely that the asymmetric spatial distribution of extension rates reflects a combination of varying storm history from site to site and variations in soil properties and land cover.

Figure 5. Example of discontinuous, arcuate steps in an otherwise unchanneled valley tributary to Big Arroyo.

Role of Vegetation

The study areas are mantled by grasslands and, to a lesser degree, shrub lands and piñon-juniper woodlands. Grassland cover is known to be highly resistant to overland flow erosion. A common and simple way to describe the erosion resistance of a soil or bedrock is in terms of a threshold shear stress, τ_c, below which the rate of material detachment is negligible:

$$D_c \propto \tau^{\alpha} - \tau_c^{\alpha}, \quad (1)$$

where D_c represents the detachment capacity (L/T), τ is bed shear stress, and α is a parameter that depends on the derivation of equation 1 (for example, $\alpha = 1$ for a linear shear-stress model [Howard and Kerby, 1983] and $\alpha = 3/2$ for a unit stream-power model [Whipple and Tucker, 1999; Moore and Burch, 1986]). In the presence of vegetation, some portion of the applied fluid shear stress will be expended on plants rather than on the soil directly; this effect is especially pronounced when grasses are flattened by overland flow, forming a barrier between the flow and the soil surface. Shear stress partitioning between plants and soil has been formalized in some models (e.g., Foster, 1982). Here, for consistency with field experiments, we adopt a simpler formalism in which τ_c is considered a bulk "effective" value that depends on vegetation cover and encapsulates the degree to which fluid shear is expended on stems, branches, etc., rather than directly on the soil surface. The erosion threshold will also reflect both intrinsic soil cohesion and effective cohesion imparted by roots.

Field studies conducted on grasslands in Australia (Prosser and Slade, 1994) and California (Prosser and Dietrich, 1995; Prosser et al., 1995) suggest that nondegraded grasses and similar herbaceous carpets are able to withstand overland flow shear stresses of a hundred or more pascals without significant erosion (Table 1). Clipping, grazing, and similar damage can apparently reduce this threshold by up to an order of magnitude. The very high resistance of intact herbaceous cover contrasts markedly with bare soils, on which soil detachment and rilling can occur at shear stresses on the order of a few pascals (Table 1).

This hundredfold contrast in erosion threshold between bare soil and full herbaceous cover implies a significant role for vegetation as a mediator of channel formation and development. We have observed a variety of vegetation states in channel floors, ranging from essentially bare to a full cover of herbaceous and woody riparian species (Fig. 3). We have also observed

Figure 6. Typical longitudinal arroyo profiles and slope-area trends. (A) Main stem of Big Arroyo, showing location of the channel head shown in Figure 3D, and a second large headcut that marks the upstream termination of another incised reach downstream. (B) Slope-area diagram for the Big Arroyo main stem. Drainage areas in all slope-area plots were mapped using standard digital elevation model (DEM) flow-routing procedures. Gradients were obtained from the DEM by taking the average gradient over a constant vertical drop (in this case, 5 m). (C) Southeastern tributary to Big Arroyo, indicating position of a flight of discontinuous, arcuate steps (pictured in Fig. 5). (D) Slope-area diagram for Big Arroyo tributary. (E) Burson Arroyo, showing the approximate positions of lithologic breaks and the location of the head of the main incised reach, which continues from this point at least as far as the confluence with the main stem of Taylor Arroyo. (The position of the Greenhorn Limestone is only approximately mapped, and may in fact be topographically higher.) (F) Slope-area diagram for Burson Arroyo. (G) Short, deep arroyo ("Little Grand Canyon") pictured in Figures 3C, 8C, and 8D. Location is indicated by asterisk on Figure 1B. Channel depth is at a maximum at the head (~15 m) and decreases downstream, where it grades into the regional valley slope. (H) Slope-area diagram for the Little Grand Canyon arroyo. Note lithologically related steep reaches on profile and in slope-area data. Profile vertical exaggeration is 50× in A, C, and E, and 20× in G. Lithologies in E and G: Knf—Fort Hayes Limestone member of Niobrara Formation, Kc—Carlile Shale, Kgh—Greenhorn Limestone, Kgr—Graneros Shale, Kd—Dakota Sandstone.

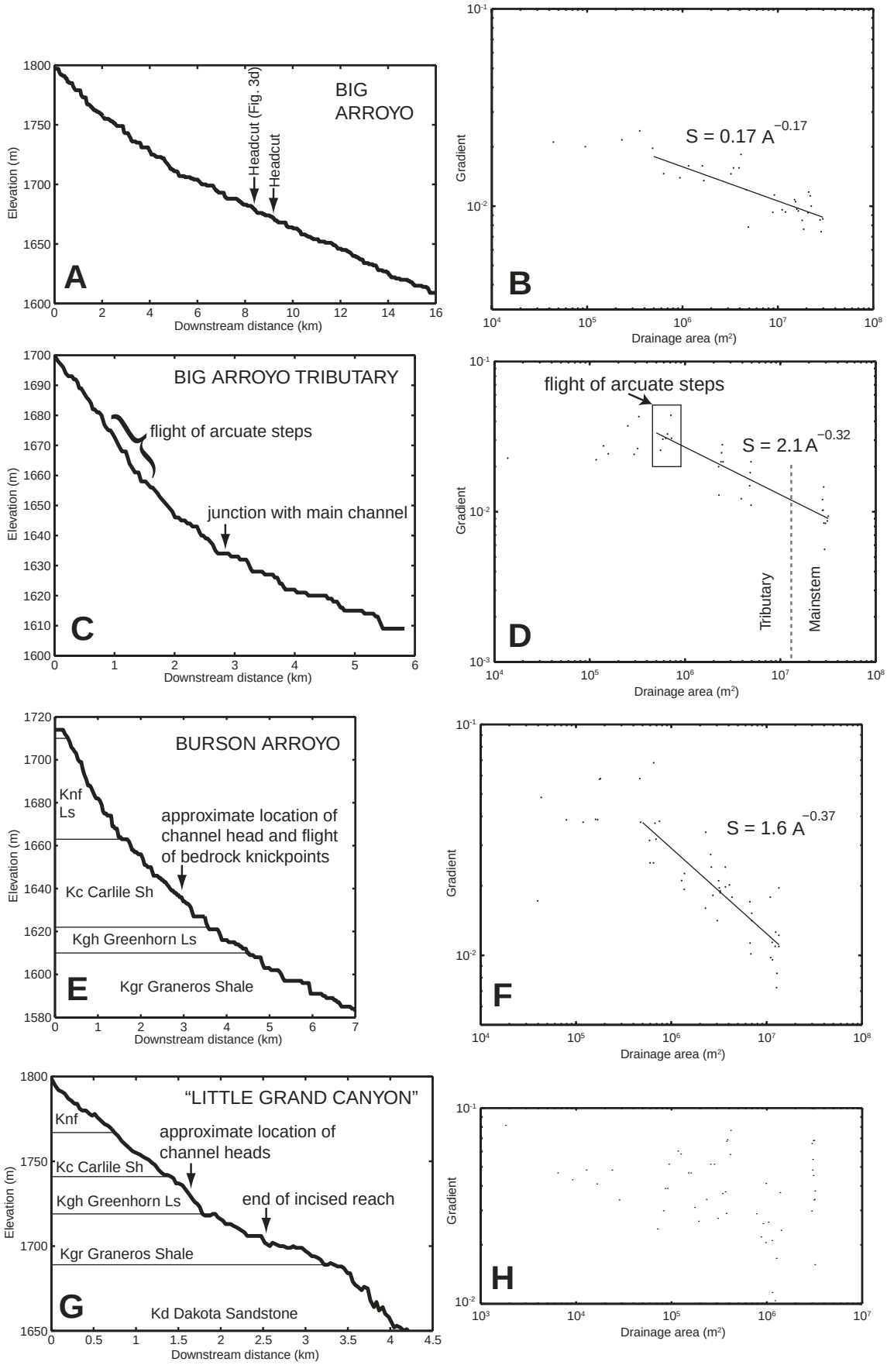
BIG ARROYO
Headcut (Fig. 3d)
Headcut
A
Elevation (m)
Downstream distance (km)
B
Gradient
Drainage area (m²)
S = 0.17 A^−0.17
BIG ARROYO TRIBUTARY
flight of arcuate steps
junction with main channel
C
D
Tributary
Mainstem
S = 2.1 A^−0.32
BURSON ARROYO
Knf
Ls
approximate location of channel head and flight of bedrock knickpoints
Kc Carlile Sh
Kgh Greenhorn Ls
Kgr Graneros Shale
E
F
S = 1.6 A^−0.37
"LITTLE GRAND CANYON"
approximate location of channel heads
end of incised reach
Kd Dakota Sandstone
G
H

plants recolonizing channel floors following scour or burial by flash floods. These observations imply a dynamic interaction between flash-flood erosion/deposition and channel-floor vegetation growth (Collins et al., 2004). A sufficiently powerful flash flood can damage or eliminate channel-floor vegetation. The resulting decrease in effective erosion threshold increases the frequency of channel erosion and/or deposition events, which in turn inhibits vegetation growth.

Collins et al. (2004) used a numerical model to examine some geomorphic consequences of this vegetation-erosion interaction. Here, we use a simple, zero-dimensional version of that model (i.e., a single point in a channel) to show how the vegetation state of the channel floor depends on the relative time scales of vegetation growth and flash-flood occurrence, which in turn is a function of climate and drainage-basin scale. The model rules are summarized in Table 2. The state variable, V, represents the degree of proportional vegetation cover in a single channel reach. The model calculates variations in V over time in response to a random, exponentially distributed (i.e., Poisson) sequence of flood events. Flood magnitude and duration also follow exponential distributions. When flood discharge exceeds a threshold value that depends on V (Table 2, rule 1), vegetation is damaged to a degree that depends on excess discharge (over and above the threshold; rule 2) and event duration. Between events, vegetation recovers at a rate that depends on the fraction of vegetation remaining and a specified regrowth time scale (Table 2, rule 3).

Results from three calculations are shown in Figure 10. When floods are rare relative to vegetation regrowth time scales ($T_g < T_b$, where T_b is average flood recurrence interval), the channel floor remains vegetated except in the immediate aftermath of exceptionally large floods, and there is no correlation between one event and the next (Fig. 10, top). When the flood recurrence interval is short relative to vegetation regrowth time ($T_g > T_b$), the vegetation remains sparse because it is frequently disturbed (Fig. 10, bottom) (such a cover might correspond to a thin carpet of young, fast-growing annuals and seedlings of slower-growing species, with seed stock provided from surrounding banks and hillslopes). Between these end cases, there is an interesting realm of behavior in which flood recurrence interval is comparable to vegetation regrowth time (Fig. 10, center). When $T_g \geq T_b$, the effectiveness of any given flood varies considerably, depending on the antecedent history of erosion and vegetation growth. Autocorrelation analysis reveals that when $T_g \geq T_b$, the modeled vegetation time series are autocorrelated on a time scale comparable to the regrowth time.

The ratio T_g/T_b will depend on several factors, including climate, soil moisture, vegetation type, soil physical properties, and catchment scale. In the southern study area, experience with vegetation restoration suggests that locally disturbed grassland can reach near-full recovery in about three years when reseeded, watered, and covered (B. Miller, 2002, personal commun.). This represents an e-folding time scale (T_g) on the order of one year, which is a minimum regrowth time: natural regrowth presumably can take longer, depending on the history of rainfall and soil moisture following disturbance. It is reasonable to suppose that vegetation properties and regrowth time T_g will vary somewhat between an open, unchanneled valley floor, and an incised channel floor. In the study region, incised channels tend to host more woody species (e.g., the invasive exotic *Tamarix*) relative to grasses, and contain higher soil moisture. Such effects are obviously not incorporated in the simple model summarized in Table 2. It would be interesting to discover the extent to which the interaction of soil moisture, topography, and species competition influences geomorphic behavior. This could be done with a combination of monitoring of vegetation type and density and greater attention to the role of soil moisture and plant species composition in an improved erosion-hydrology-vegetation model.

Vegetation regrowth time can be compared with flash-flood recurrence interval, which varies significantly with both climate and basin size. Table 3 shows a sample of recurrence-interval estimates for flash floods in ephemeral basins smaller than 150 km^2 in south-central Colorado. These are generally shorter than the time scale for vegetation regrowth, though it is likely that the recurrence interval for erosionally effective events is larger, perhaps on the order of regrowth time. These data indicate that ephemeral channels in the study area tend to lie in the realm of behavior corresponding to $T_g/T_b \geq 1$ (Fig. 10, middle and bottom).

The foregoing observations and analysis indicate that the role of vegetation in arroyo dynamics varies systematically with basin scale, among other factors. Because of the surprisingly high erosional resistance of grassland vegetation, channel initiation in semiarid grasslands is likely to require either very intense storms or significant degradation of the vegetation armor. In the next section, we examine, via two case studies, the necessary conditions for generating sufficiently high shear stresses to penetrate an intact turf cover.

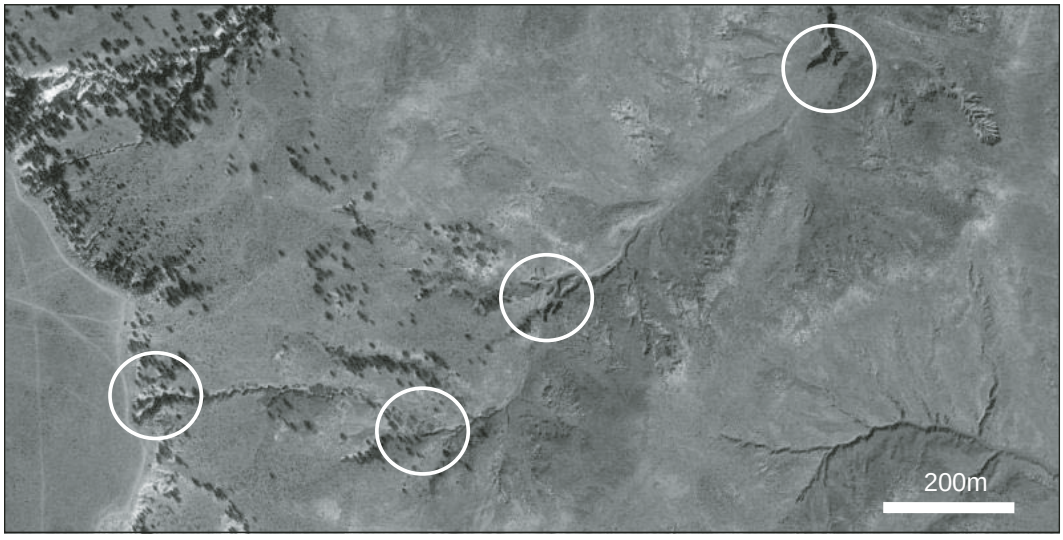

Figure 7. Example of multiple, discontinuous channel segments along a drainage, West Bijou Creek basin, Colorado. Circles show the positions of active channel heads (source: U.S. Geological Survey digital orthophoto, 1999; latitude 39.458°N, longitude 104.327°W).

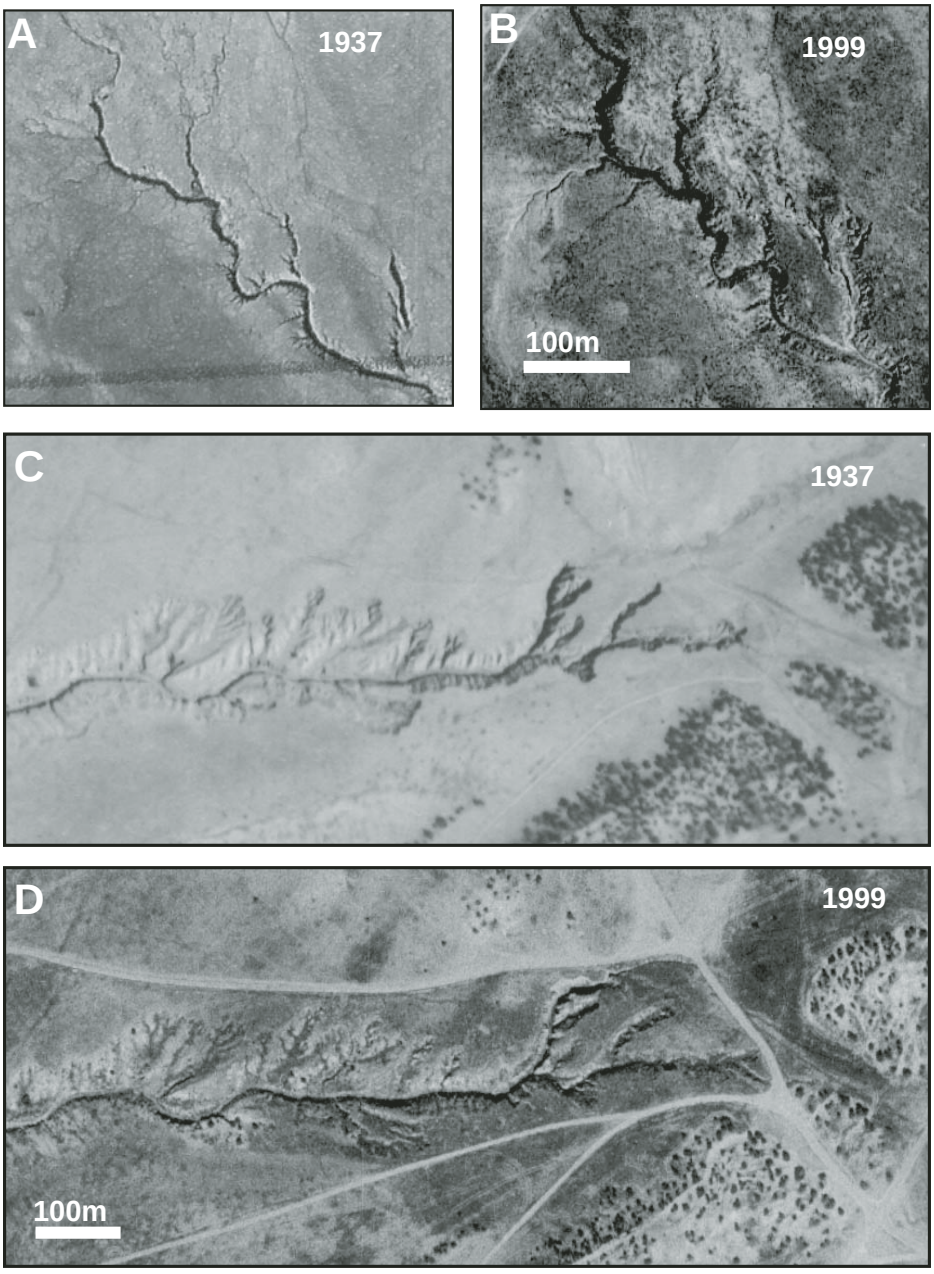

Figure 8. Aerial photographs of two arroyo networks in 1937 and 1999. (A, B) Network in the Dry Creek drainage basin (latitude 38.447°N, longitude 104.697°W). (C, D) Network in the Red Creek drainage basin (location shown by asterisk on Fig. 1B; latitude 38.467°N, longitude 104.935°W; see also Figs. 3C, 6G, and 6H).

HYDROLOGY AND FLASH-FLOOD DISCHARGE RECONSTRUCTION

Runoff Generation

Observations at the study sites indicate that rainfall generated by summer convective storms can generate large volumes of infiltration-excess overland flow within the storm core (Fig. 11). Because the water table in the study sites is normally tens of meters below the ground surface (von Guerard et al., 1987), saturation-excess overland flow is likely to be rare.

Measurements of soil infiltration capacity were obtained using a Guelph permeameter at several locations within the study area (Table 4). These point-estimates of final infiltration capacity range widely, from <1 to ~300 mm/h, with mean values by site on the order of a few tens to ~100 mm/h. By comparison, inspection of USGS 2004 peak rainfall and runoff data for three ephemeral tributaries of the Purgatoire (Bent Canyon Creek, Lockwood Arroyo, and Taylor Arroyo) shows that storms with a peak 5 min intensity as high as several tens of mm/h and total rainfall depths of 1–2 cm measured at a stream gauging station can nonetheless fail to generate measurable flow. Thus, although we do not have very good estimates of effective infiltration and interception capacities at scales comparable to the width of a convective cell's core (say, hundreds of meters to a few kilometers), flash-flood generation in the study area is likely to require peak rainfall intensities of a few tens of mm/h at a minimum.

Case Studies of Flash-Flood Occurrence

Given that grassland vegetation imposes a significant threshold for runoff erosion—up to two orders of magnitude higher than that for bare soil—it is important to consider under what conditions runoff of sufficient magnitude can be generated. If, given the topography of the region, flow events capable of generating hundreds of pascals of bed shear stress are common, then it is likely that arroyo initiation in the region would also be common under modern climate conditions, even in the absence of land disturbance. On the other hand, if the recurrence interval of events large enough to cut channels is comparable to or greater than the time scale of significant climate shifts, major droughts, and/or vegetation changes (10^3–10^4 yr), this would suggest that some form of disturbance is needed for the formation of widespread channel networks under modern climate conditions. To some extent, this is a question of basin scale. In this section, we examine documented examples of flash-flood occurrence.

An intense convective storm struck a group of small watersheds in the Sullivan Park area of the Red Creek basin (Fig. 1B) in August 1999. A second one hit the same area on 13 July 2001. Both events caused check dams to overspill, and the spillways of at least two of these dams were heavily damaged (Fig. 12). The first event was sufficient to cut through the turf mat lining the spillway and carve a channel ~4 m deep and ~7 m wide (Fig. 12A).

Between the two events, the spillways had been lined with geotextile and armored with ~21-cm-diameter granite boulders. During the 2001 event, at one location, the boulder armor and geotextile were completely undermined and eroded. At a second location, the armor was stripped off only from the steepest portion of the spillway; it remained intact on the lower-gradient upper portion (Fig. 12B). Observation

of flood marks along the throat of one spillway immediately after the 2001 event (J. Kulbeth, 2001, personal commun.) allows estimates to be made of peak discharge and runoff intensity. The gradient along the spillway was measured using a hand level, which is accurate to about ± 0.5 degrees. Spillway throat dimensions were provided by J. Kulbeth. The mean flow velocity, $\bar{U}$, and peak discharge, Q_p, at the spillway throat were estimated using the Law of the Wall for fully turbulent flow:

$$Q_p = \bar{U}A = \frac{AU_*}{\kappa H}\int_{z_0}^{H}\left(\frac{z}{z_0}\right)dz\,, \qquad (2)$$

where A is channel cross-sectional area, κ is von Kármán's constant, H is flow depth, $U_* = \sqrt{gRS}$ is shear velocity, g is gravitational acceleration, R is hydraulic radius, S is gradient, z is height above the bed, and z_0 is roughness length. Measured bed slope was used as an estimate of hydraulic gradient, and z_0 was taken to be 1/30th of the boulder diameter. Allowing up to 50% error in hydraulic gradient (i.e., 1 ± 0.5°), the estimated peak discharge ranges from 9 to 16 cm (Table 5). This corresponds to a peak effective runoff rate, averaged over the ~0.5 km² catchment, of 65–113 mm/h. By comparison, a tipping-bucket rain gauge ~1 mile to the north recorded a peak 5 min rainfall intensity of 78 mm/h. The low end of the runoff estimates is comparable to measured peak rainfall and allows a plausible ~10 mm/h infiltration rate. The upper end requires rainfall to have been several tens of mm/h higher over the catchment than at the rain gauge; given the small radius and high spatial variability typical of thunderstorm cells, this is also plausible.

The estimated peak shear stress at the spillway throat falls in the range 40–130 Pa. The equivalent shear stress at the steepest (5°) portion of the spillway channel was estimated using the Manning equation with roughness coefficient n = 0.033, which most closely matches the previous Law of the Wall calculation. For a 5° gradient, the estimated peak shear stress is just short of 300 Pa. By comparison, the critical shear stress for entrainment of 21 cm boulders on a uniform bed (as this was) ranges from ~100–200 Pa for critical Shields stress values of 0.03–0.06 (cf. Buffington and Montgomery, 1997). Thus, our discharge and shear stress estimates are consistent with the fact that boulders were entrained and removed only on the steeper section of the channel.

These two case studies provide an example of the dramatic form and magnitude of incision that can occur when the vegetation armor (or, in the case of the 2001 event, artificial cover)

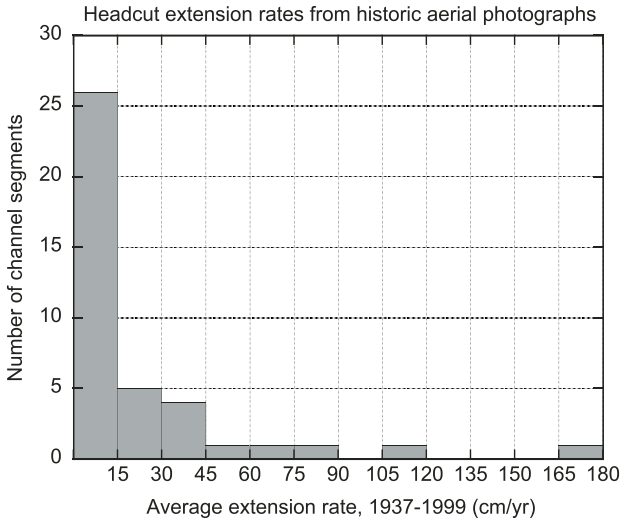

Figure 9. Rates of channel headcut extension estimated from 1937 U.S. Department of Agriculture (USDA) (1:20,000) and 1999 U.S. Geological Survey (1:12,000) aerial photographs. First column includes channel segments for which the extension rate was indistinguishable from zero. Estimated precision of the method is about ±6–8 cm/yr.

TABLE 1. ESTIMATED EROSION THRESHOLDS FOR BARE AND GRASS-COVERED SOIL

Condition	Estimated threshold shear stress (Pa)	Source
Bare agricultural soil	3.1 ± 1.8†	Elliott et al. (1989)
Bare agricultural soil	1.7–10.6	Gilley et al. (1993)
Bare, poorly cohesive soils	0.6–4.4	(see note ‡)
Bare clay	21	Reid (1989)
Clipped bunch and sod grass	20–40 (>70–80)#	Prosser and Dietrich (1995)
Lightly disturbed tussock grass and sedge	>180	Prosser and Slade (1994)§
Bunch and sod grass	100–180 (>150–230)#	Prosser and Dietrich (1995)
Grass and sedge	> 240	Prosser and Slade (1994)§
Grass	>80–200	Reid (1989)††

†Mean and standard deviation from 32 soil-plot experiments on different soils; each data point represents an average of six runs at the same site.

‡Data compiled by Prosser and Dietrich (1995) from Crouch and Novruzi (1989), Slattery and Bryan (1992), and Merz and Bryan (1993).

§Prosser and Slade (1994) found that flows generating basal shear stresses between 160 and 330 Pa were unable to cause incision in a cover of dense grass and sedge; when the cover was lightly disturbed, flows greater than 180 Pa caused patchy scour without incision.

#The first values represent thresholds for sediment transport, while those in parentheses indicate minimum thresholds for incision into the vegetation mat, which Prosser and Dietrich (1995) estimated as at least 50–60 Pa higher than the sediment-transport threshold.

††Reid's (1989) estimate combines Ree's (1949) estimates of nonerosive flow velocities with velocity-stress relation. They are thus minimum estimates for τ_c.

TABLE 2. VEGETATION GROWTH-EROSION MODEL FOR EPHEMERAL CHANNEL FLOORS

Governing equations	Symbols
1. VEGETATION INCREASES EROSIONAL RESISTANCE $\hat{H}_c = \hat{H}_{cs} + \hat{H}_{cv}V$	V = Proportional surface vegetation cover $\hat{H}$ = Flood depth (stress per unit water weight per unit hydraulic gradient) normalized by threshold depth for V = 1 $\hat{H}_c$ = Threshold flood depth relative to maximum threshold at V = 1 $\hat{H}_{cs}$, $\hat{H}_{cv}$ = Proportion of erosion threshold due to soil cohesion and vegetation resistance, respectively, at V = 1 t = Time E = Vertical erosion/sedimentation rate [L/T] L_r = Characteristic root depth [L] T_e = Time scale for vegetation erosion/damage T_g = Time scale for vegetation regrowth
2. VEGETATION IS DAMAGED BY EROSIVE FLOODS $\left.\frac{dV}{dt}\right\|_{\text{erosion}} = -\frac{EV}{L_r} = -\frac{\left(\hat{H}-V\right)V}{T_e}$	
3. VEGETATION GROWS BACK BETWEEN FLOODS $\left.\frac{dV}{dt}\right\|_{\text{growth}} = \frac{1-V}{T_g}$	

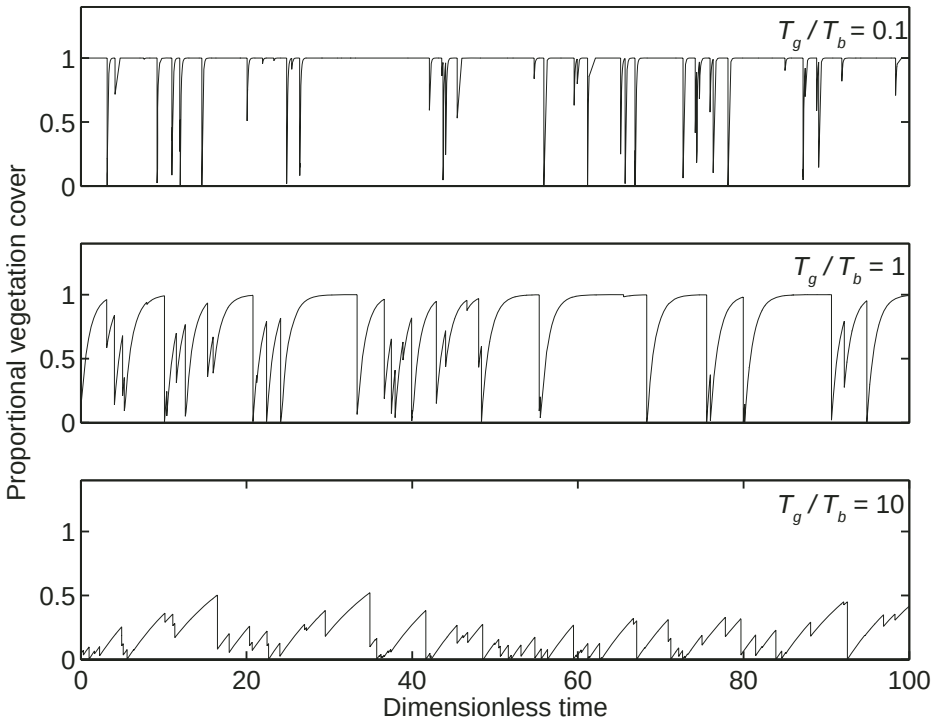

Figure 10. Time evolution of channel-floor vegetation cover computed using the model in Table 2. The three graphs compare solutions with different ratios of vegetation regrowth time scale (T_g) to average storm return period (T_b). Other parameters are: H_{cv} = 1, T_e/T_b = 0.05, T_r/T_b = 0.01, and $\langle H \rangle / H_{c0}$, where T_r is mean flood duration, $\langle H \rangle$ is mean flood depth, H_{c0} is minimum flood depth (shear stress per unit downslope water weight) for erosion, and the other parameters are as defined in Table 2.

TABLE 3. RECURRENCE INTERVALS FOR FLASH FLOODS IN EPHEMERAL BASINS <150 km² IN SOUTH-CENTRAL COLORADO

Basin	Drainage area (km²)	Recurrence interval (yr)
Big Arroyo	40	0.20
Burke Arroyo tributary	12	0.56
Taylor Arroyo	125	0.15
Red Rock Canyon Creek	126	0.41
Bent Canyon Creek	146	0.47
Lockwood Canyon Creek	127	0.11

Note: Data are from U.S. Geological Survey. For purposes of calculating recurrence interval, an event is defined as a daily flow that exceeds the flow on both previous and subsequent days.

is penetrated. It is worth asking: what is the typical recurrence interval for a gully-forming event in an unchanneled valley (or, as is common in basins of several km² or larger, a valley containing a shallow and fully carpeted swale-like channel form that lacks sharp banks)? The estimated recurrence intervals for the 1999 and 2001 Sullivan Park storms, recorded at a station ~1 mile from the erosion site, are listed in Table 5. The recorded peak rainfall intensity for both events has an estimated return period of 1–3 yr based on the NOAA Atlas 2 database (Miller et al., 1973; Arkell and Richards, 1986). Thus, these two channel-forming events were reasonably common, and they suggest that localized convective storms can, with reasonable frequency, generate Hortonian runoff with short-term peak runoff rates of several tens to possibly over 100 mm/h in small (order 1 km²) basins. However, because gully formation occurred in the spillways of check dams, where the gradient is significantly steeper than the valley gradient, the recurrence interval for the Sullivan Park events is not necessarily indicative of the frequency of gully-forming events in natural valleys.

Peak Discharge Reconstruction in Existing Arroyo Networks

Because rangeland vegetation is such an effective barrier to runoff erosion, it is also worth asking: what are typical recurrence intervals for flash floods in small basins (~0.5–15 km²)? This is not easy to determine without gauging data, which do not exist in our study areas for basins smaller that 40 km². However, estimates can be obtained by combining rain gauge data with estimates of peak discharge obtained from flood debris. To that end, we measured high-water marks, channel cross sections, and channel gradients along reaches of two arroyos that conveyed flash floods in August 2003 (Fig. 2). Using the Law of the Wall method (equation 2) to estimate flow velocity and discharge, the estimated peak discharge, based on three cross sections, was on the order of 3–4 m³/s along the lower reach of Burson Arroyo (drainage area ~7 km²; see Fig. 1C). A central reach of Big Arroyo, which is both larger (drainage area ~15 km²) and appears to have been closer to the storm core (Fig. 2), had a peak discharge on the order of 50–60 m³/s.

The floods were triggered by a thunderstorm with a peak 15 min rainfall intensity of 86 mm/h recorded at a rain gauge located ~1.5 km and 3.5 km from the Big Arroyo and Burson Arroyo sites, respectively (Fig. 2). This rainfall intensity has a 3 yr recurrence interval (Table 5). In Burson Arroyo, the flood produced an estimated cross-section–averaged shear stress of 40–50 Pa, and a peak (thalweg) shear stress of 50–90 Pa. These shear stresses fall below the estimated minimum vegetation-undermining stress in Table 1, and indeed evidence of scour was limited to occasional patches along the channel thalweg. Based on three cross sections, the larger flood in Big Arroyo produced cross-section–averaged shear stresses on the order of 85 Pa in two sections with gradients typical of this stretch of the valley (~0.013), and ~170 Pa in a locally steeper (slope = 0.03) section. Corresponding estimated peak thalweg shear stresses are ~130 and ~350 Pa, respectively. Thus, this roughly 3 yr event produced peak shear stresses that begin to approach, and locally exceed, the minimum threshold for undermining an intact turf mat. These estimates are consistent with an observed pattern of localized intense scour around knickpoints but limited channel incision elsewhere, as discussed below.

Next, we briefly consider the extent to which a 100 yr flood might be capable of driving large-scale channel incision in the study areas. Let us assume, for the sake of argument, that flood magnitude scales with recurrence interval in the same way that rainfall magnitude does—that is, for example, $Q_{100}/Q_2 = P_{100}/P_2$. This probably underestimates flood magnitude, given likely nonlinearities in rainfall-runoff transformation, but is about the best we can hope for, given the uncertainties. Based on this, a rough estimate of the equivalent 100 yr flood in the studied reach of Big Arroyo is ~120 m³/s. Calculating the likely impact of such an event using the same three cross sections in Big Arroyo reveals

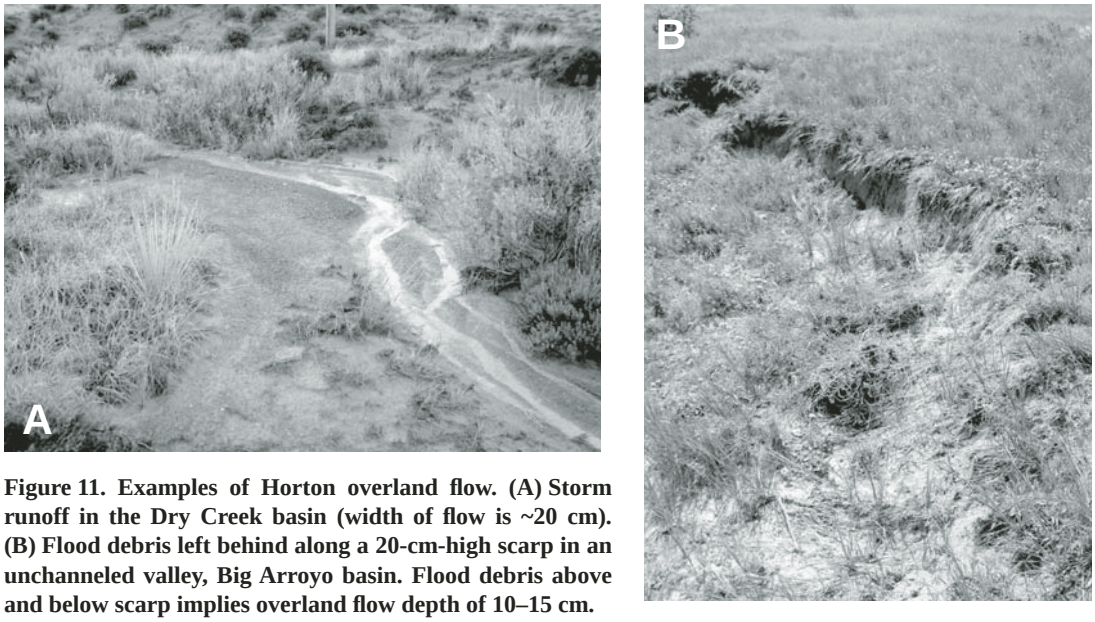

Figure 11. Examples of Horton overland flow. (A) Storm runoff in the Dry Creek basin (width of flow is ~20 cm). (B) Flood debris left behind along a 20-cm-high scarp in an unchanneled valley, Big Arroyo basin. Flood debris above and below scarp implies overland flow depth of 10–15 cm.

the critical role played by locally constricted and oversteepened reaches. The role of channel constriction can be appreciated by comparing the impact on representative incised versus unincised sections (Fig. 13). Assuming for the moment that the gradient is the same in both reaches (equal to the reach average channel gradient of 0.013), we find that our estimated 100 yr event produces a 73% higher section-averaged shear stress in the incised channel as compared to the unincised valley floor upstream (Figs. 13A and 13B). The incised reach also happens to be steeper by a factor of >2 relative to the average valley gradient. Accounting for this oversteepening (Fig. 13C), peak shear stress in the incised reach is nearly twice as large as it would otherwise be; in this case, the estimated 100 yr mean and peak stresses both exceed the estimated threshold for ripping out the turf cover (Table 1).

This example illustrates the importance of local channel slope and constriction in generating shear stresses sufficient to drive significant erosion during flash floods. What does it mean for channel form and dynamics? A common channel pattern in the study area is the presence of stretches of incised channel with an active headcut and plunge pool, or sequence of these, at the upstream end (Figs. 3A, 3D, and 7). Above this, there is usually a nonincised valley segment that is either completely unchanneled (common in basins on the order of 1 km^2 or less) or contains a shallow and subtle channel form that is completely mantled by vegetation (e.g., basins on the order of several tens of km^2) (Fig. 7). Next, we interpret this pattern in terms of hydraulic force and erosional susceptibility.

DISCUSSION AND CONCLUSIONS

Form and Dynamics

The foregoing observations provide a picture of the dynamics of these ephemeral channel networks and lead to the following interpretation. Consider an unchanneled, grass-carpeted rangeland valley floor underlain by cohesive alluvium and/or friable bedrock. Based on the field studies listed in Table 1, the vegetation carpet will have an effective erosion threshold comparable to that of decimeter-scale boulders, while the threshold for eroding the underlying material is up to two orders of magnitude lower (Table 1). Thus, the valley floor is conditionally unstable, in the sense that any local perturbation sufficient to break through the vegetation armor will tend to grow by positive feedback. As the depth of erosion increases and root density decreases, the substrate will tend to weaken, and the gradient above the growing scour will grow, possibly forming a "shock" with a vertical scarp and plunge pool (Figs. 3, 5, and 11B). However, there are several negative feedback mechanisms that prevent runaway growth. Scour depth will be limited by the need to maintain a downslope hydraulic gradient sufficient to transport eroded material. If a plunge pool forms, its depth will be limited by subaqueous diffusion of the incoming turbulent jet (e.g., Stein et al., 1993). Headward retreat of the growing scarp will also inhibit concentrated deepening in one spot. The importance of headward retreat as a negative feedback to local deepening is supported by the observation that the deepest head scarps tend to form where headward retreat is inhibited, for example, by an outcrop of locally resistant bedrock (Fig. 3C) or by tree roots. In addition, the short duration of flash floods limits the depth of scour during a single event. Finally, any lateral widening immediately below a head scarp can lead to reduction in mean and maximum bed shear stress.

The latter negative feedback also illustrates the important role of substrate cohesion. In noncohesive sediment, rapid and efficient channel widening would act as a powerful negative feedback against focused scour. Istanbulluoglu et al. (2005) provided numerical examples of how low cohesion is associated with significant gully-head widening, and vice versa. Thus, a cohesive substrate is a necessary, though not sufficient, condition for the observed morphology and dynamics of incised arroyos.

Sediment concentration is another factor that promotes focusing of erosion around a retreating head scarp. A flash flood moving along an

TABLE 4. HYDRAULIC CONDUCTIVITY AND GRAIN SIZE OF SURFACE SOILS

Site	D_{50} (mm)	Field-saturated hydraulic conductivity (cm/hr)
HRT	0.028 ± 0.025 (n = 9)	10.3 ± 5.2 (n = 5)
BV	0.046 ± 0.069 (n = 6)	4.1 ± 2.4 (n = 2)
LGC	0.012 ± 0.012 (n = 6)	2.2 ± 2.0 (n = 5)
BA1	0.016 ± 0.022 (n = 7)	6.4 ± 10.8 (n = 7)
BA2	0.044 ± 0.029 (n = 5)	4.5 ± 2.5 (n = 4)
LW	0.054 ± 0.069 (n = 8)	11.7 ± 10.2 (n = 6)

Note: Table shows mean and standard deviation. Data are from Flores (2004).

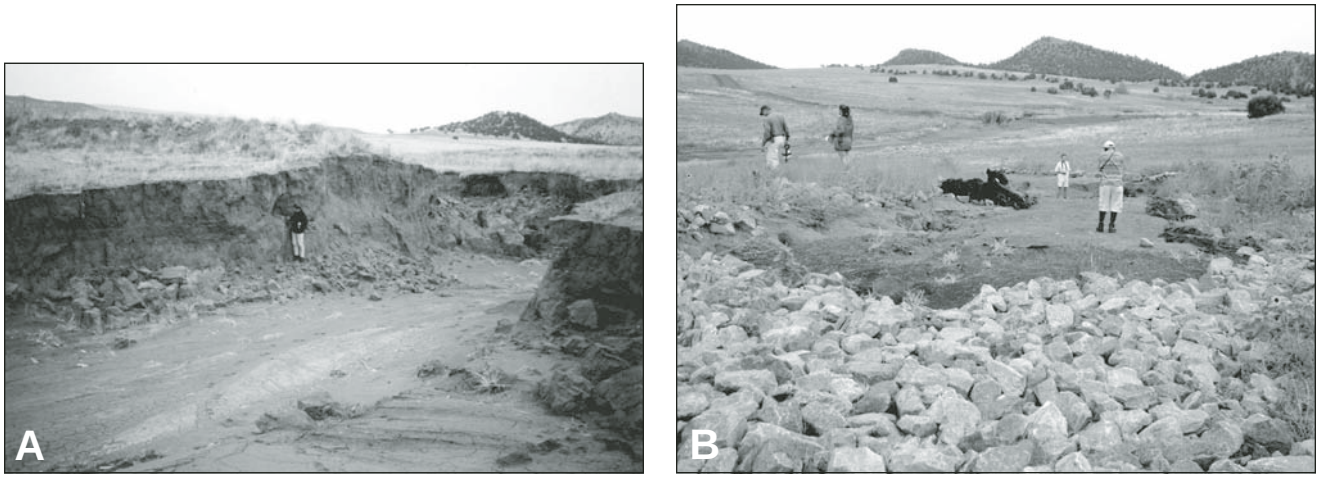

Figure 12. (A) Gully carved in check-dam spillway by convective storm in August 1999. The spillways had recently been worked on, so that the turf mat was weaker than a mature cover (B. Goss, 2005, personal commun.). (B) Damage to a boulder- and geotextile-lined spillway by convective storm on 13 July 2001.

unchanneled valley segment will tend to have negligible bedload concentration, because any coarse sediment entrained from an upstream incised segment will tend to come to rest near or above the termination of the channelized reach, where channel widening leads to a reduction in boundary shear stress. Thus, flow entering the head of an incised reach will tend to have a high transport capacity for coarse sediment. Sediment concentration will rapidly increase where the flow crosses an actively eroding/retreating head scarp, and the resultant reduction in excess transport capacity—together with downstream channel widening and the consequent reduction in boundary shear stress—will further inhibit scour downstream. This interpretation is supported by the observation in our study areas that gravel bars containing locally derived sediment commonly drape the channel bed within meters to tens of meters below an active scarp or channel head.

This conceptual model suggests the following necessary and sufficient conditions for the formation of incised ephemeral channels containing one or more headward-propagating segments. A resistant surface layer overlying a weaker substrate sets up an instability in which erosional perturbations can grow by positive feedback. High flow variability (e.g., an ephemeral channel subject to occasional flash floods) allows for vegetation growth between flood events, while providing erosive floods with great enough frequency to maintain a valley form. Moderate to high substrate cohesion (on the order of several kPa or higher; Istanbulluoglu et al., 2005) is necessary to prevent a growing erosional perturbation from being rapidly dissipated by bank collapse and channel widening. A high volume fraction of fine-grained material allows for significant, long-distance removal of sediment away from the zone of focused erosion (Kirkby and Bull, 2000), while the presence of a minor but not negligible coarse (bedload) fraction tends to inhibit further sediment entrainment and channel incision downstream of an active headcut.

Role of Convective Storms and Implications for Long-Profile Evolution

Our observations of recent flash-flood events show that despite the low relief and gentle valley gradients in the study areas, convective summer storms are able to generate tens to hundreds of pascals of shear stress, depending on channel or valley morphology and local gradient. In locally steep and/or constricted channel reaches, fairly common (3–5 yr) events appear to be able to locally exceed the significant erosion thresholds associated with grassland vegetation (~200–300 Pa; Table 1). On the other hand, the analysis in Figure 13 suggests that even very large and rare (100 yr) events are generally incapable of generating widespread incision of open, essentially unchanneled valley segments. Thus, valley incision appears to be driven primarily by episodic retreat of channel heads and within-channel knickpoints.

The limited footprint of most convective storms has important implications for the style of valley evolution. The core of a convective cell may cover only several square kilometers (Fig. 2; Goodrich et al., 1997; Bull et al., 1999). Below their source area in the storm core, flash floods will also attenuate due to in-stream infiltration; for example, the Big Arroyo flash flood of 2003, which produced an estimated peak flow of 50 m^3/s of rainfall in its middle reaches (see rainfall pattern in Fig. 2), generated a peak flow of less than 1 m^3/s at the catchment outlet (D. Sharps, 2003, personal commun.). Thus, the common assumption in landscape evolution models that channel-forming discharge is proportional to basin area is inapplicable in this type of setting. However, although flood magnitude will tend to diminish rather than increase downstream (outside of the storm core), flood frequency will still increase with basin area. This downstream increase in flood frequency is a likely explanation for the upward concavity of channel profiles (Fig. 6), for the following reason: Over time, and in the absence of strong local forcing (e.g., an active fault), there is a natural tendency for the long-term rate of incision to equilibrate along a channel network (e.g., Hack, 1960; Snow and Slingerland, 1986; Willgoose, 1994). In a convective-dominated

TABLE 5. ESTIMATED RECURRENCE INTERVALS OF FLASH FLOODS, 1999–2003

Location	Date	Peak rainfall rate (mm/hr): 15 min / 30 min / 60 min	Recurrence interval (yr)
Sullivan Park	4 August 1999	61 / 42 / 22	1.3 / 1.3 / 1.1
Sullivan Park	13 July 2001	78 / 60 / 34	2.3 / 3.4 / 2.8
Burson Well	8 August 2003	86 / 70 / 36	3.1 / 5.0 / 3.3

climate like that of the high plains, higher-order valley segments experience more frequent flash floods than lower-order ones. If denudation rates are similar throughout a given network, then greater flood frequency in the higher-order branches must be balanced by reduced average flood effectiveness. Downstream reduction in gradient ensures this. Thus, we interpret the concave-upward valley profiles in our study area as a delicate adjustment between flood frequency and valley gradient, which controls average flood effectiveness. Erosional "punches," according to this interpretation, become stronger but less frequent with decreasing basin size. A corollary is that time-variability in sediment yield will tend to decrease systematically with basin size, a behavior that appears generally applicable to fluvial systems (e.g., Farnsworth and Milliman, 2003).

Our findings also support the view that relatively small variations in valley gradient can have a large impact on susceptibility to channel incision (e.g., Patton and Schumm, 1975; Dietrich et al., 1993; Bull, 1997). This sensitivity is a direct reflection of the nonlinear relation between boundary shear stress and erosion rate (represented here by an erosion threshold).

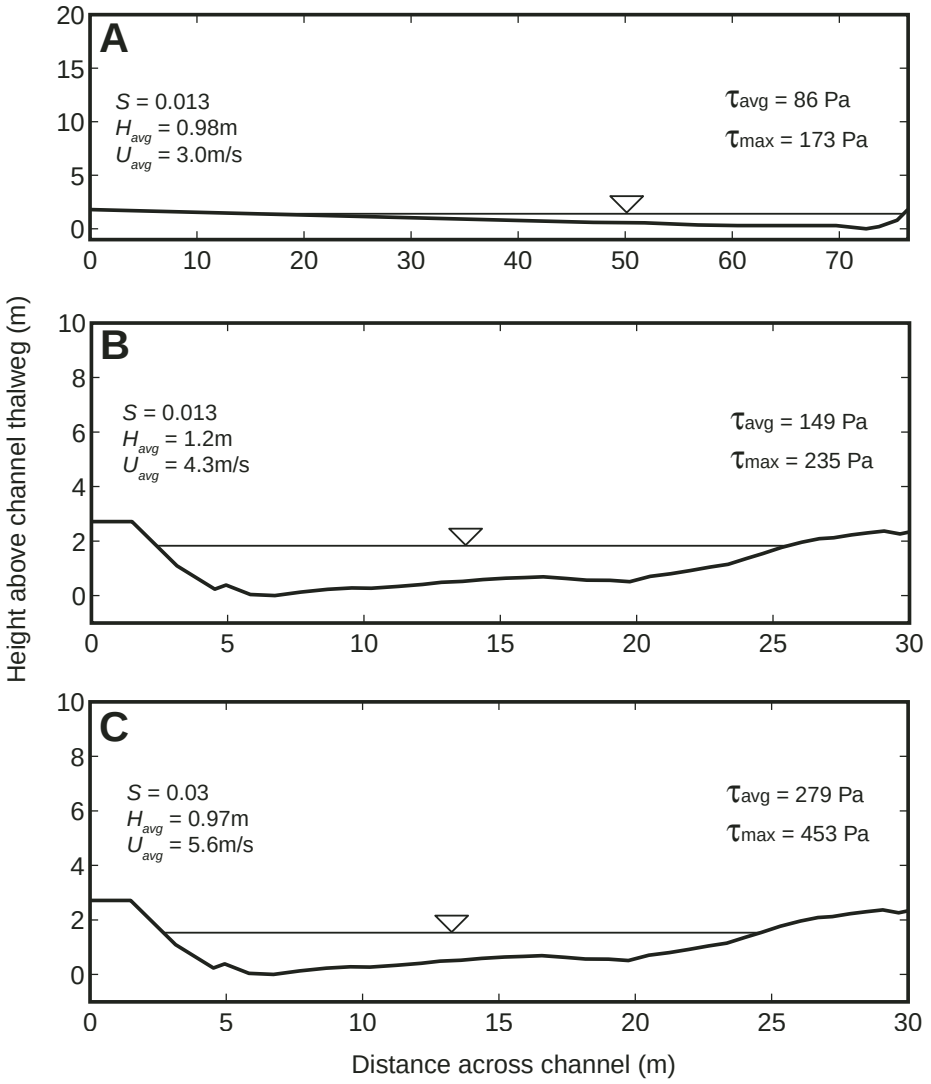

Figure 13. Cross sections in the central reach of Big Arroyo, showing calculated 100 yr flood inundation; there is no vertical exaggeration (but note scale difference in top figure). (A) Shallow, fully vegetation-draped upstream section. (B) Downstream section, with flow parameters calculated using the same reach average valley gradient as in A. Increased shear stress relative to upstream section is solely due to channel constriction. (C) Same as B but using local channel gradient of 0.03.

Scaling Analysis of Long-Profile Concavity

Is a balance between flash-flood frequency and geomorphic effectiveness a plausible explanation for long-profile concavity in this field setting? The following is a brief justification based on scaling arguments. We wish to examine the relative importance of valley slope versus basin size in controlling the average rate of geomorphic work. A simple way to describe the average rate of geomorphic work done by flash floods is $P = F\,M$, where P represents the average rate of work per unit channel length, F is the frequency of flash floods (T^{-1}), and M is the average work per unit channel length performed by a single flood (which might be taken to scale with the product of event duration and stream power per unit channel length). (Note that work, in the mechanical sense, is only one possible measure of geomorphic effectiveness; but it is adequate for this demonstration.) The goal is to estimate how F and M will vary with basin area and gradient, and whether it is reasonable to expect a balance between these two quantities given the characteristic topography in our study areas.

Consider a dryland catchment in which the predominant rainfall events have a small footprint relative to basin size. Assume that the events are short enough such that, beyond a relatively small length scale (10^1–10^2 m), peak discharge and flood duration are roughly independent of drainage area. Implicit here is the assumption that in-stream losses are small; although this is not necessarily true of typical dryland streams, one might imagine that, on average, in-stream losses (leading to downstream reduction in discharge) might be roughly compensated by a tendency toward increasing runoff downstream even for small-footprint convective storms. If the at-a-point storm arrival rate is homogeneous (that is, the average arrival rate at a point is the same across the basin), then the total storm arrival rate, and thus flood frequency, for the catchment as a whole will be proportional to drainage area. Thus, we can express flood frequency as $F = bA$, where A is basin area and b is the arrival rate of flood-producing storms per unit area.

The average effectiveness of a given flood discharge Q, in terms of potential geomorphic work, will depend on a variety of factors, including slope, valley/channel geometry, substrate (rock or sediment) properties, and surface roughness. Let us suppose, however, that all of these effects except slope are similar throughout the network. To what extent does the average erosional work performed by a flash flood depend on slope? This issue is a matter of some debate—different erosion models have different implications—but for our purposes, the important

thing is that, due to the presence of an erosion threshold, the relationship is both positive and nonlinear: doubling the channel or valley slope will tend to produce more than twice the erosive potential (e.g., Tucker, 2004). A simple way to approximate such nonlinearity is with a power law: $M = cS^d$, where S is valley or channel gradient, d is an exponent >1, and c is the average work done at unit gradient. This power law is a purely heuristic device designed to capture the fact that an increase in gradient both increases the erosive potential of a given flood (all else equal) and increases the fraction of floods that generate boundary shear stresses sufficiently high to cross the resistance threshold. Based on the arguments advanced in several recent papers (Snyder et al., 2003; Tucker, 2004; Lague et al., 2005; Molnar et al., 2006), the value of d that best approximates the threshold effect will vary according to the strength of the threshold relative to a characteristic shear stress; as an example, data on gradient versus incision rate from a set of catchments along the northern California coast can be fit with $d \approx 4$ (Snyder et al., 2003), though this number is surely not universal. Using this device, our average rate of work is:

$$W = bcAS^d. \quad (3)$$

In order for the average rate of work to be the same throughout a valley network, it must be true that

$$S \propto A^{-1/d} = A^{-\theta}. \quad (4)$$

The argument above, that d should be greater than unity in the presence of an erosion threshold, implies that θ should be less than unity, as is usually observed (for a compilation of θ values, see Tucker and Whipple, 2002). Values of concavity, θ, from the study areas imply d in the vicinity of 3–6, which could be interpreted as indicating a strong degree of nonlinearity in the relationship between gradient and erosive potential. This is as expected given the substantial erosion threshold associated with grassland vegetation. Thus, the slope-area relationship in catchments in the study area (and likely other typical rangeland catchments) is consistent with our hypothesis that the observed network concavity reflects a balance between the frequency and magnitude of flash floods at different points within the network.

Sensitivity to Climate Change

It is important to consider the sensitivity of arroyo networks to climate change. Given the importance of convective precipitation as a driving force and herbaceous vegetation as a resisting factor, rates of valley incision should be particularly sensitive to convective activity and to drought-induced vegetation disturbance (Table 1). In the context of the American west, it is logical to expect that the greatest susceptibility to channel incision will occur when the return of convective summer rain marks the end of a significant drought cycle.

Holocene climate records from the southwestern United States are sometimes contradictory; for example, while the middle Holocene (ca. 5–7 ka) has historically been considered a warm and dry period in the southwestern United States (e.g., Waters, 1989; Davis and Schaefer, 1992; Waters and Haynes, 2001; Menking and Anderson, 2003), a variety of reconstructions point toward a maximum in summer monsoon rainfall during that period (Thompson et al., 1993; Metcalfe et al., 2000; Harrison et al., 2003; Poore et al., 2005). In any event, the predicted sensitivity of arroyo incision rates to both drought (via vegetation weakening) and summer thunderstorms is consistent with the observation of Waters and Haynes (2001) that arroyo activity in Arizona correlates with the strength of El Niño–Southern Oscillation (ENSO) cycles. It is also broadly consistent with dating of Holocene channel fills in the study areas (Arnold, 2006; Arnold et al., 2006), the results of which suggest more vigorous cut-fill behavior during the early-middle Holocene (as well as near the Pleistocene-Holocene boundary and the late Holocene neoglacial).

Given the apparent importance of short-term climate variability, it is interesting to speculate on how longer-term variations in the degree of climate variability might impact denudation rates in rangeland settings. Significant denudation—on the order of several hundred meters (Leonard, 2002)—has occurred along the high plains east of the southern Rockies since the end of deposition of the Ogallala Group, ca. 5 Ma (e.g., Trimble, 1980). The mechanism for this denudation is the subject of much debate; some have attributed it to increased climate variability and/or storminess beginning in the Pliocene (Molnar and England, 1990; Gregory and Chase, 1994; Zhang et al., 2001). The apparent sensitivity of ephemeral channel incision rates to climate variability—specifically, alternating episodes of drought, which damages vegetation and can potentially reduce erosional resistance by an order of magnitude (Table 1), and intense summer convective storm activity, which generates high boundary shear stresses—provides a plausible mechanism for a climate-driven acceleration in denudation rates in the high plains. In order to properly evaluate this hypothesis, it will be necessary to quantify the relation between climatology and long-term rates of hillslope and valley sediment transport and erosion in rangelands.

ACKNOWLEDGMENTS

This research was supported by the U.S. Army Research Office (grants DAAD190110513, DAAD190110615, W911BF0410340), and by a cooperative agreement between Massachusetts Institute of Technology (MIT) and the Consiglio Nazionale delle Ricerche, Italy. This research would not have been possible without the generous logistical support of the Fort Carson Directorate of Environmental Compliance and Management; in particular, we thank Brian Goss, James Kulbeth, Jeff Linn, Bruce Miller, Linda Moeder, Caron Rifici, and Dan Sharps for assistance, enthusiasm, and insights. John Kuzmiak of the U.S. Geological Survey, Pueblo, kindly provided storm rainfall data. We are also grateful for field assistance from Mikaël Attal, Nate Bradley, Domenico Capolongo, Quintijn Clevis, Daniel Collins, Nicole Gasparini, Salvatore Grimaldi, Vanessa Teles, and Vanessa Winchester. Finally, we thank Brian Goss, Alan Howard, and Ian Prosser for constructive and helpful review comments.

REFERENCES CITED

Antevs, E., 1952, Arroyo-cutting and filling: The Journal of Geology, v. 60, p. 375–385.

Arkell, R.E., and Richards, F., 1986, Short duration rainfall relations for the western United States, *in* Conference on Climate and Water Management: Asheville, North Carolina, American Meteorological Society, p. 136–141.

Arnold, L.J., 2006, Optical dating and computer modelling of Arroyo epicycles in the American Southwest [Ph.D. thesis]: Oxford, School of Geography and the Environment, University of Oxford, 426 p.

Arnold, L.J., Bailey, R.M., and Tucker, G.E., 2006, Statistical treatment of fluvial dose distributions from southern Colorado arroyo deposits: Quaternary Geochronology, (in press).

Boardman, J., Parsons, A.J., Holmes, P.J., Holland, R., and Washington, R., 2003, Development of badlands and gullies in the Sneeuberg, Great Karoo, South Africa: Catena, v. 50, no. 2-4, p. 165–184, doi: 10.1016/S0341-8162(02)00144-3.

Buffington, J.M., and Montgomery, D.R., 1997, A systematic analysis of eight decades of incipient motion studies, with special reference to gravel-bedded rivers: Water Resources Research, v. 33, no. 8, p. 1993–2029, doi: 10.1029/97WR03190.

Bull, L.J., Kirkby, M.J., Shannon, J., and Hooke, J.M., 2000, The impact of rainstorms on floods in ephemeral channels in southeast Spain: Catena, v. 38, p. 191–209, doi: 10.1016/S0341-8162(99)00071-5.

Bull, W.B., 1997, Discontinuous ephemeral streams: Geomorphology, v. 19, p. 227–276, doi: 10.1016/S0169-555X(97)00016-0.

Collins, D.B.G., Bras, R.L., and Tucker, G.E., 2004, Modeling the effects of vegetation-erosion coupling on landscape evolution: Journal of Geophysical Research, v. 109, F03004, doi: 10.1029/2003JF000028.

Cooke, R.U., and Reeves, R.W., 1976, Arroyos and environmental change in the American South-West: London, Oxford University Press, 213 p.

Crouch, R.J., and Novruzi, T., 1989, Threshold conditions for rill initiation on a vertisol, Gunnedah, N.S.W. Australia: Catena, v. 16, p. 101–110, doi: 10.1016/0341-8162(89)90007-6.

Davis, O.K., and Schafer, D.S., 1992, A Holocene climatic record for the Sonoran Desert from pollen analysis of Montezuma Well, Arizona, USA: Palaeogeography, Palaeoclimatology, Palaeoecology, v. 92, p. 107–119.

Dietrich, W.E., and Dunne, T., 1993, The channel head, *in* Beven, K., Kirkby, M.J., Channel network hydrology: Chichester, UK, John Wiley and Sons, p. 175–219.

Dietrich, W.E., Wilson, C.J., Montgomery, D.R., and McKean, J., 1993, Analysis of erosion thresholds, channel networks, and landscape morphology using a digital

terrain model: Centennial special issue: Chicago, Illinois, University of Chicago Press, p. 259–278.
Elliott, J.G., Gellis, A.C., and Aby, S.B., 1999, Evolution of arroyos; incised channels of the Southwestern United States, *in* Darby, S.E., and Simon, A., eds., Incised river channels: Chichester, New York, John Wiley, p. 152–185.
Elliott, W.J., Liebenow, A.M., Laflen, J.M., and Kohl, K.D., 1989, A compendium of soil erodibility data from WEPP cropland soil field erodibility experiments 1987 and 1988: W. Lafayette, Indiana, Ohio State University and USDA Agricultural Research Service National Soil Erosion Research Laboratory Report no. 3.
Fanning, P.C., 1999, Recent landscape history in arid western New South Wales, Australia; a model for regional change: Geomorphology, v. 29, p. 191–209, doi: 10.1016/S0169-555X(99)00014-8.
Farnsworth, K.L., and Milliman, J.D., 2003, Effects of climatic and anthropogenic change on small mountainous rivers: The Salinas River example: Global and Planetary Change, v. 39, p. 53–64, doi: 10.1016/S0921-8181(03)00017-1.
Flores Cervantes, J.H., 2004, Headcut retreat resulting from plunge pool erosion in a 3D landscape evolution model [M.S. thesis]: Cambridge, Massachusetts Institute of Technology, 143 p.
Foster, G.R., 1982, Modeling the erosion process, *in* Haan, C.T., ed., Hydrologic modeling of small watersheds: St. Joseph, Michigan, American Society of Agricultural Engineers Monograph 5, p. 295–380.
Gilley, J.E., Elliot, W.F., Laflen, J.M., and Simanton, J.R., 1993, Critical shear stress and critical flow rates for initiation of rilling: Journal of Hydrology, v. 142, p. 251–271, doi: 10.1016/0022-1694(93)90013-Y.
Goodrich, D.C., Lane, L.J., Shillito, R.M., and Miller, S.N., 1997, Linearity of basin response as a function of scale in a semiarid watershed: Water Resources Research, v. 33, no. 12, p. 2951–2965, doi: 10.1029/97WR01422.
Graf, W.L., 1983, The arroyo problem; palaeohydrology and palaeohydraulics in the short term, *in* Gregory, K.L., ed., Background to palaeohydrology; a perspective: New York, John Wiley, p. 279–302.
Graf, W.L., 1988, Fluvial processes in dryland rivers: Caldwell, New Jersey, Blackburn Press, 346 p.
Gregory, K.M., and Chase, C.G., 1994, Tectonic and climatic significance of a late Eocene low-relief, high-level geomorphic surface: Journal of Geophysical Research, v. 99, v. B10, p. 20,141–20,160, doi: 10.1029/94JB00132.
Hack, J.T., 1960, Interpretation of erosion topography in humid temperate climate: American Journal of Science, v. 258, p. 80–97.
Harrison, S.P., Kutzbach, J.E., Liu, P., Bartlein, J.Z., Otto-Bliesner, B., Muhs, D., Prentice, I.C., and Thompson, R.S., 2003, Mid-Holocene climates of the Americas; a dynamical response to changed seasonality: Climate Dynamics, v. 20, p. 663–688.
Howard, A.D., 1999, Simulation of gully erosion and bistable landforms, *in* Darby, S.E., and Simon, A., eds., Incised river channels: New York, John Wiley & Sons, p. 277–300.
Howard, A.D., and Kerby, G., 1983, Channel changes in badlands: Geological Society of America Bulletin, v. 94, p. 739–752, doi: 10.1130/0016-7606(1983)94<739:CCIB>2.0.CO;2.
Istanbulluoglu, E., Tarboton, D.G., Pack, R.T., and Luce, C.H., 2004, Modeling of the interactions between forest vegetation, disturbances and sediment yields: Journal of Geophysical Research, v. 109, F01009, doi: 10.1029/2003JF000041.
Istanbulluoglu, E., Bras, R.L., Flores, H., and Tucker, G.E., 2005, Implications of bank failures and fluvial erosion for gully development: Field observations and modeling: Journal of Geophysical Research, v. 119, F01014, doi: 10.1029/2004JF000145.
Kirkby, M.J., and Bull, L.J., 2000, Some factors controlling gully growth in fine-grained sediments: A model applied in southeast Spain: Catena, v. 40, p. 127–146, doi: 10.1016/S0341-8162(99)00077-6.
Lague, D., Hovius, N., and Davy, P., 2005, Discharge, discharge variability, and the bedrock channel profile: Journal of Geophysical Research, v. 110, F04006, doi: 10.1029/2004JF000259.
Leonard, E.M., 2002, Geomorphic and tectonic forcing of late Cenozoic warping of the Colorado piedmont: Geology, v. 30, no. 7, p. 595–598, doi: 10.1130/0091-7613(2002)030<0595:GATFOL>2.0.CO;2.
Leopold, L.B., 1951, Rainfall frequency: An aspect of climatic variation: Eos (Transactions, American Geophysical Union), v. 32, p. 347–357.
Menking, K.M., and Anderson, R.Y., 2003, Contributions of La Niña and El Niño to middle Holocene drought and late Holocene moisture in the American Southwest: Geology, v. 31, p. 937–940.
Merz, W., and Bryan, R.B., 1993, Critical conditions for rill initiation on sandy loam Brunisols; laboratory and field experiments in southern Ontario, Canada: Geoderma, v. 57(4), p. 357–385.
Metcalfe, S.E., O'Hara, S.L., Caballero, M., and Davis, S.J., 2000, Records of late Pleistocene–Holocene climate change in Mexico—A review: Quaternary Science Reviews, v. 19, p. 699–721, doi: 10.1016/S0277-3791(99)00022-0.
Miller, J.F., Frederick, R.H., and Tracey, R.J., 1973, Precipitation-frequency atlas of the western United States: Silver Spring, Maryland, National Oceanic and Atmospheric Administration, v. III, 67 p.
Molnar, P., and England, P., 1990, Late Cenozoic uplift of mountain ranges and global climate change—Chicken or egg?: Nature, v. 346, no. 6279, p. 29–34, doi: 10.1038/346029a0.
Molnar, P., Anderson, R.S., Kier, G., and Rose, J., 2006, Relationships among probability distributions of stream discharges in floods, climate, bedload transport and river incision: Journal of Geophysical Research (in press).
Montgomery, D.R., and Dietrich, W.E., 1992, Channel initiation and the problem of landscape scale: Science, v. 255, no. 5046, p. 826–830.
Moore, I.D., and Burch, G.J., 1986, Sediment transport capacity of sheet and rill flow: Application of unit stream power theory: Water Resources Research, v. 22, p. 1350–1360.
Ogden, F.L., Sharif, H.O., Senarath, S.U.S., Smith, J.A., Baeck, M.L., and Richardson, J.R., 2000, Hydrologic analysis of the Fort Collins, Colorado, flash flood of 1997: Journal of Hydrology, v. 228, p. 82–100, doi: 10.1016/S0022-1694(00)00146-3.
Oostwoud-Wijdenes, D., Poesen, J., Vandekerckhove, L., and De Baerdemaeker, J., 1999, Gully-head morphology and implications for gully development on abandoned fields in a semi-arid environment, Sierra de Gata, southeast Spain: Earth Surface Processes and Landforms, v. 24, p. 585–603, doi: 10.1002/(SICI)1096-9837(199907)24:7<585::AID-ESP976>3.0.CO;2-#.
Patton, P.C., and Schumm, S.A., 1975, Gully erosion, northwestern Colorado: A threshold phenomenon: Geology, v. 3, p. 88–90, doi: 10.1130/0091-7613(1975)3<88:GENCAT>2.0.CO;2.
Poore, R.Z., Pavich, M.J., and Grissino-Mayer, H.D., 2005, Record of the North American southwest monsoon from Gulf of Mexico sediment cores: Geology, v. 33, no. 3, p. 209–212, doi: 10.1130/G21040.1.
Prosser, I.P., and Dietrich, W.E., 1995, Field experiments on erosion by overland flow and their implication for a digital terrain model of channel initiation: Water Resources Research, v. 31, no. 11, p. 2867–2876, doi: 10.1029/95WR02218.
Prosser, I.P., and Slade, C.J., 1994, Gully formation and the role of valley-floor vegetation, southeastern Australia: Geology, v. 22, no. 12, p. 1127–1130, doi: 10.1130/0091-7613(1994)022<1127:GFATRO>2.3.CO;2.
Prosser, I.P., Chappell, J., and Gillespie, R., 1994, Holocene valley aggradation and gully erosion in headwater catchments, south-eastern highlands of Australia: Earth Surface Processes and Landforms, v. 19, no. 5, p. 465–480.
Prosser, I.P., Dietrich, W.E., and Stephenson, J., 1995, Flow resistance and sediment transport by concentrated overland flow in a grassland valley: Geomorphology, v. 13, p. 71–86, doi: 10.1016/0169-555X(95)00020-6.
Ree, W.O., 1949, Hydraulic characteristics of vegetation for vegetated waterways: Agricultural Engineering, v. 30, p. 184–198.
Reid, L.M., 1989, Channel initiation by surface runoff in grassland catchments: Seattle, University of Washington, 135 p.
Reneau, S.L., Dietrich, W.E., Donahue, D.J., and Jull, A.J.T., 1990, Late Quaternary history of colluvial deposition and erosion in hollows, central California Coast Ranges: Geological Society of America Bulletin, v. 102, p. 969–982, doi: 10.1130/0016-7606(1990)102<0969:LQHOCD>2.3.CO;2.
Rinaldo, A., Dietrich, W.E., Rigon, R., Vogel, G.K., and Rodriguez–Iturbe, I., 1995, Geomorphological signatures of varying climate: Nature, v. 374, no. 6523, p. 632–635, doi: 10.1038/374632a0.
Schumm, S.A., 1977, The fluvial system: New York, John Wiley, 338 p.
Schumm, S.A., Mosely, M.P., and Weaver, W.E., 1987, Experimental fluvial geomorphology: New York, John Wiley, 413 p.
Schumm, S.A., and Parker, R.S., 1973, Implications of complex response of drainage systems for Quaternary alluvial stratigraphy: Nature, v. 243, no. 128, p. 99–100.
Slattery, M.C., and Bryan, R.B., 1992, Hydraulic conditions for rill incision under simulated rainfall: Earth Surface Processes and Landforms, v. 17, p. 127–146.
Slingerland, R.L., and Snow, R.S., 1988, Stability analysis of a rejuvenated fluvial system: Zeitschrift für Geomorphologie, v. 67, p. 93–102.
Snow, R.S., and Slingerland, R.L., 1986, Mathematical modeling of graded river profiles: Journal of Geology, v. 95, p. 15–33.
Snyder, N.P., Whipple, K.X., Tucker, G.E., and Merritts, D.J., 2003, The importance of a stochastic distribution of floods and erosion thresholds in the bedrock river incision problem: Journal of Geophysical Research, v. 108, no. B2, doi: 10.1029/2001JB001655.
Stein, O.R., Julien, P.Y., and Alonso, C.V., 1993, Mechanics of jet scour downstream of a headcut: Journal of Hydraulic Research, v. 31, no. 6, p. 723–738.
Thompson, R.S., Whitlock, C., Bartlein, P.J., Harrison, S.P., and Spaulding, W.G., 1993, Climate changes in the western United States since 18,000 yr B.P., *in* Wright, H. E., Jr., Kutzbach, J.E., Webb, T., III, Ruddiman, W.F., Street-Perrott, F.A., and Bartlein, P.J., eds., Global climates since the Last Glacial Maximum: Minneapolis, University of Minnesota Press, p. 468–513.
Trimble, D.E., 1980, Cenozoic tectonic history of the Great Plains contrasted with that of the southern Rocky Mountains: A synthesis: The Mountain Geologist, v. 17, p. 59–69.
Tucker, G.E., 2004, Drainage basin sensitivity to tectonic and climatic forcing: Implications of a stochastic model for the role of entrainment and erosion thresholds: Earth Surface Processes and Landforms, v. 29, p. 185–205, doi: 10.1002/esp.1020.
Tucker, G.E., and Slingerland, R., 1997, Drainage basin responses to climate change: Water Resources Research, v. 33, no. 8, p. 2031–2047, doi: 10.1029/97WR00409.
Tucker, G.E., and Whipple, K.X., 2002, Topographic outcomes predicted by stream erosion models: Sensitivity analysis and intermodel comparison: Journal of Geophysical Research, v. 107, no. B9, p. 2179, doi: 10.1029/2001JB000162.
von Guerard, P., Abbot, P.O., and Nickless, R.C., 1987, Hydrology of the US Army Pinon Canyon maneuver site, Las Animas County, Colorado: Denver, Colorado, Water-Resources Investigations Report 87-4227, U.S. Department of the Interior.
Waters, M.R., 1989, Late Pleistocene and Holocene lacustrine history and paleoclimatic significance of pluvial Lake Cochise, southern Arizona: Quaternary Research, v. 32, p. 1–11.
Waters, M.R., and Haynes, C.V., 2001, Late Quaternary arroyo formation and climate change in the American Southwest: Geology, v. 29, no. 5, p. 399–402, doi: 10.1130/0091-7613(2001)029<0399:LQAFAC>2.0.CO;2.
Whipple, K.X., and Tucker, G.E., 1999, Dynamics of the stream-power river incision model; implications for height limits of mountain ranges, landscape response timescales, and research needs: Journal of Geophysical Research, ser. B, Solid Earth and Planets, v. 104, no. b8, p. 17,661–17,674, doi: 10.1029/1999JB900120.
Willgoose, G., 1994, A Physical Explanation for an Observed Area-Slope-Elevation Relationship for Catchments with Declining Relief: Water Resources Research, v. 30(2), p. 15–159.
Zhang, P., Molnar, P., and Downs, W.R., 2001, Increased sedimentation rates and grain sizes 2–4 Myr ago due to the influence of climate change on erosion rates: Nature, v. 410, no. 6831, p. 891–897, doi: 10.1038/35073504.

Manuscript Received 3 November 2005
Revised Manuscript Received 3 February 2006
Manuscript Accepted 20 February 2006

Printed in the USA

Appendix B

Reprint: The importance of the catchment area-length relationship in governing non-steady state hydrology, optimal junction angles and drainage network pattern

Reference: Sólyom, P.B., and Tucker, G.E. (2007) The importance of the catchment area-length relationship in governing non-steady state hydrology, optimal junction angles and drainage network pattern. *Geomorphology*, v. 88, p. 84-108.

Available online at www.sciencedirect.com
ScienceDirect
ELSEVIER
Geomorphology xx (2006) xxx–xxx
GEOMORPHOLOGY
www.elsevier.com/locate/geomorph

The importance of the catchment area–length relationship in governing non-steady state hydrology, optimal junction angles and drainage network pattern

Peter B. Sólyom [a,*], Gregory E. Tucker [b]

[a] School of Geography and the Environment, Oxford University, Mansfield Rd, Oxford, OX1 3TB, UK
[b] Cooperative Institute for Research in Environmental Sciences and Department of Geological Sciences, University of Colorado, Boulder, CO 80309-0399, USA

Received 3 March 2005; received in revised form 24 October 2006; accepted 29 October 2006

Abstract

Analytical and numerical models of landscape evolution in general either assume steady state hydrology or use empirically based functions in the form of a drainage area power law to model runoff. A method to compute non-steady state runoff on the basis of the area–length relationship of river basins is proposed, for application in landscape evolution models. This shape-sensitive runoff function is derived analytically for environments with short storm duration (storm duration < concentration time) and it is supported numerically for environments with small storms (storm cell size < basin size). The effect of these area–length dependent relationships on drainage network development is analysed. The methodology is optimization through stream power minimization both on the level of individual junctions and on the level of the entire network. It is demonstrated that the way the area–length dependent runoff function influences the stream power of the network yields a systematic downstream increase of the network's optimal junction angles. An example for this prediction is given by a DEM-derived network from the Colorado High Plains. The inverse dependence of the runoff rate on the basin's flow path length implies that minimum total stream power is achieved through maximizing the flow path length of the system. This effect is responsible for the lateral instability of junction positions when runoff conditions shift from steady towards non-steady state. We offer this phenomenon as an explanation for the lateral instability and pronounced planation activity of semi-arid channels, especially on gently sloping piedmont surfaces. Finally throughout the paper much attention is paid to the runoff character in terms of advectivity vs. diffusivity, defined as the ratio between instream flow and lateral inflow. It is shown how optimal network pattern also relates to the advectivity/diffusivity of the runoff conditions.

Keywords: Landscape evolution; Non-steady state runoff; Network optimization; Junction angles and lateral planation

1. Introduction

Many drainage basins worldwide are shaped in part by runoff generated during high intensity, short duration convective storm cells. The characteristic diameter of convective cells can be as small as a few kilometers, and the duration of the high intensity storm period is on the order of minutes to hours (e.g., Ogden and Julien, 1994; Goodrich et al., 1997; Ogden et al., 2000). Runoff generated in larger catchments of these landscapes cannot be treated as steady and uniform, because in many

* Corresponding author.
E-mail address: psolyom@ouce.ox.ac.uk (P.B. Sólyom).

0169-555X/$ - see front matter © 2006 Elsevier B.V. All rights reserved.
doi:10.1016/j.geomorph.2006.10.014

cases the storm cell does not cover the entire catchment, and the duration of the storm is usually shorter than the time needed for the water particles from the most distant locations of the catchment to reach the outlet. Therefore hydrologic steady state rarely occurs in either (a) catchments larger than the typical areal extent of storms, or (b) catchments with concentration times longer than the duration of typical rainfall or snowmelt events (e.g., Dick et al., 1997; Sólyom and Tucker, 2004).

Convective storms are well known to be significant in terms of extreme runoff production, and therefore they represent significant potential erosive power despite their short duration. Given that in arid and semiarid regions characterized by convective storms, surface vegetation cover is typically low and soils are crusted, the geomorphic impacts of high intensity storms are even further accentuated through low infiltration capacity and consequently high runoff rates (e.g., Langbein and Schumm, 1958). Convective cells often represent a serious hazard to human life and goods in the form of severe flash floods accompanied by intense erosion or sedimentation (e.g., Ogden et al., 2000; Coppus and Imeson, 2002; Eaton et al., 2003). A more precise understanding of runoff production in these environments is important to produce flood sensitivity maps and to help design land management policies.

Describing the space-time variability of runoff production is one of the challenges in long-term landscape evolution modelling. Ultimately erosion models depend heavily on the treatment of runoff production (Ijjasz-Vasquez et al., 1992; Dietrich et al., 1993; Kirkby, 1993; Tucker and Bras, 1998; Sólyom and Tucker, 2004; Tucker, 2004). Landscape evolution models over the past 20 years have successfully reproduced different types of landforms (e.g. Ahnert, 1976, 1987; Willgoose, 1991a,b; Howard, 1994b; Tucker and Bras, 1998) and have provided mechanistic interpretations for landforms in terms of the dominant erosive processes (e.g. Kirkby, 1971, 1986; Howard, 1994a, 1997; Tucker and Slingerland, 1997; Whipple and Tucker, 1999; Tucker and Bras, 2000). Runoff production, particularly in channel network models, is usually modelled on the assumption of steady flow, in the sense that effective discharge is assumed equal to the product of runoff rate and catchment area (e.g., Ahnert, 1987; Tucker and Bras, 1998). Some studies have used a power-law relation between basin area and peak discharge (e.g., Willgoose et al., 1991a,b; Howard, 1994b), which is supported by theoretical studies (e.g., Huang and Willgoose, 1992, 1993; Gupta et al., 1996). This approach, however, omits possible basin-shape, network-geometry, and storm-pattern effects. Given that non-steady state runoff is likely to dominate and to shape extensive areas on the Earth surface, especially in arid and semi-arid environments, it is essential that the landscape evolution theory takes into account the significant hydrologic properties of these environments.

The central aim of this paper is to explore the effects of steady state versus non-steady state runoff in drainage network evolution. We present numerical junction-angle and network-optimization analyses to study the long-term effect of runoff production triggered by convective storm bursts on drainage network evolution. The effect of small convective storms on runoff production and erosion will be broken up into two distinct phenomena: the case of the limited storm cell size and the case of the limited storm duration. In both cases it is shown that runoff production both influences and is influenced by the shape (specifically, area–length properties) of a catchment. We use network-optimization theory to demonstrate how predicted junction-angle characteristics and network patterns change as a function of runoff state (size or duration of typical storm).

The Theory section develops a relationship between storm properties (size and duration) and the distribution of peak discharges within a drainage basin. In the two Methods and Results sections, we first review the general dynamics of these optimised systems, and then clarify characteristics of source-dominated vs. lateral inflow-dominated runoff. Finally, the effect of non-steady state runoff is analysed. Wherever possible we try to link the numerical results to prevailing landforms and processes in order to further the understanding of dryland morphogenesis.

2. Theory

The analysis consists of three parts: first, construction of a means to approximate peak discharge as a function of catchment shape and rainfall pattern; second, an assessment of the impact of storm size and duration on junction angle at a single channel junction, using optimal junction angle theory (Roy, 1984; Howard, 1990); and third, an evaluation of impacts of storm size and duration on drainage network patterns, using the Optimal Channel Network (OCN) concept (Rodriguez-Iturbe et al., 1992). This section describes the theoretical framework, and the following sections present the results of the analyses.

2.1. Hydrologic theory: geometric controls on peak discharge distribution

2.1.1. The limited storm size case

We consider first the manner in which storm size and basin shape together influence the spatial distribution of

Please cite this article as: Sólyom P.B., Tucker G.E. The importance of the catchment area–length relationship in governing non-steady state hydrology, optimal junction angles and drainage network pattern. Geomorphology (2006), doi:10.1016/j.geomorph.2006.10.014

peak discharges. Our objective is to identify an approximate scaling function for peak discharges of the form

$$\frac{Q_p}{I_0 A} = f\left(\frac{L}{W}, \frac{L_0}{\sqrt{A}}\right) \quad (1)$$

where Q_p is peak discharge, A is basin area, L is basin length, W is basin width, and I_0 and L_0 describe the characteristic intensity and size of a rainfall cell, respectively, as described below (Eq. (2)). The term on the left is a dimensionless peak discharge, while the two terms on the right represent, respectively, the catchment's shape and its size relative to storm-cell size.

For spatially homogeneous rainfall and infiltration fields, the storm runoff volume produced in a catchment is linearly proportional to the catchment's size and independent of its shape. Furthermore, if the rainfall duration is long relative to the maximum travel time in the catchment, the resulting discharge will be steady and peak flows will be linearly proportional to catchment area. However, both of these conditions are unusual in large catchments. If, on the other hand, the rainfall distribution is inhomogeneous in space, runoff produced in the catchment not only depends on the size of the catchment but also on its ability to capture the areas of intense rainfall. This means that a basin's "capture efficiency" will depend on its shape relative to the footprint of a storm system. For example, storms with round footprints would be most effectively captured by round catchments.

In order to be able to deal with an idealized inhomogeneous rainfall field, we represent storm footprints as circular patterns in which rainfall intensity decreases exponentially outward from a peak at the storm's centre. We also exclude orographic effects, aspect controls, and directionality in storm tracks, by either assuming stationary storms or assuming random and therefore on the average balanced storm cell movements during the precipitation events. The idealized "wizard's cap" storm intensity field is represented mathematically as

$$I = I_0 \exp(-L_s/L_0) \quad (2)$$

where I is at-a-point rainfall intensity, I_0 is storm intensity in the centre of the storm, L_s is Euclidian distance from the centre of the storm, and L_0 is a characteristic length scale associated with the spatial decline rate of the storm intensity.

Total storm runoff in a given catchment is the integral of the intensity function over its duration and over the catchment area. The runoff produced according to the model in a given catchment during a particular storm depends on the position of the storm relative to the catchment and the shape of the catchment. With all else equal, volumetric runoff is the highest if the centre of the storm is at the centre of the catchment. In this analysis we trace the maximum possible discharge value that a catchment can produce under a given storm size and intensity. We term this the maximum peak discharge. The maximum peak discharge is of crucial importance from both the hydrological and geomorphological point of view: obviously it is responsible for the most devastating flood events, and high discharge values are often considered to be the major geomorphological agents (e.g., Wolman and Miller, 1960; Baker, 1977; Wolman and Gerson, 1978). Unlike the mean discharge, the peak discharge is sensitive to the basin shape. Basins with near-circular form in a small-storm dominated environment tend to produce higher peak discharges than elongated basins with the same size (Strahler, 1964). The relation between storm footprint and catchment shape counts. At the same time mean discharge production is shape independent; if we assume that there is no water stored in the basins and the time-integrated intensity of the precipitation is spatially homogeneous, mean discharge relates merely to the basin size (and altitude distribution, if orographic precipitation is a factor). An implication of these effects is that the frequency distribution of runoff rates for round catchments will show higher variance than the frequency distribution for elongated catchments: round catchments tend to produce more extreme discharges than elongated ones, although total runoff over a longer period can be equal. In the following we evaluate and quantify these statements via numerical integration of rainfall fields over differently shaped idealized catchments.

To simplify the analysis, we examine the hydrologic response of idealized, rhomboid (diamond-shaped) catchments with equal size but different length-to-width ratios (elongation). Each catchment is subjected to a steady, non-uniform rain field (Eq. (2)) with the middle of the storm sitting at the point of intersection of the rhomboid axes. The resulting steady (maximum peak) discharge is computed by numerically integrating the rain field over the rhomboids.

Fig. 1a presents the results and illustrates the tendency of skinnier basins to produce smaller peak discharges for a given basin size. Obviously real basins are not exactly rhomboid shaped, and neither are storms stationary or perfectly circular. Nonetheless, this idealized analysis shows that, in general, non-uniform rainfall patterns introduce catchment shape sensitivity into the rainfall–runoff relationship, and therefore influence the geomorphic system. Other effects, such as

Please cite this article as: Sólyom P.B., Tucker G.E. The importance of the catchment area–length relationship in governing non-steady state hydrology, optimal junction angles and drainage network pattern. Geomorphology (2006), doi:10.1016/j.geomorph.2006.10.014

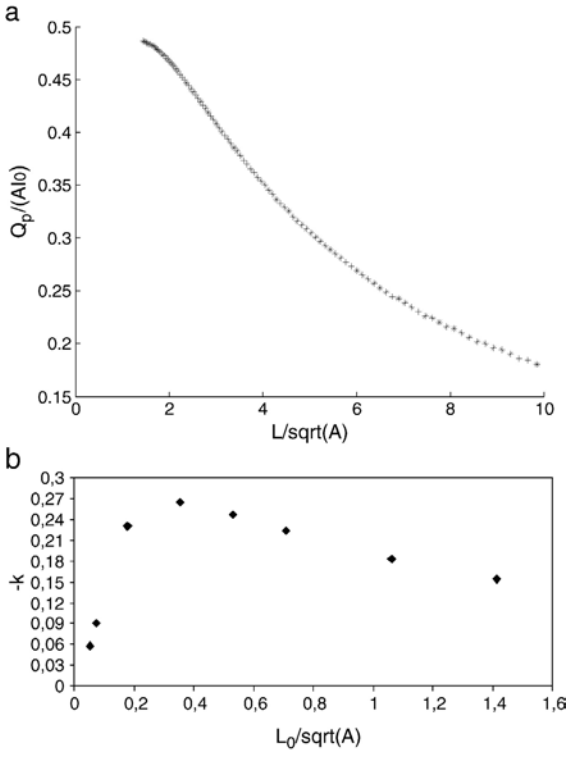

Fig. 1. a) Numerically integrated dimensionless peak discharge $Q_p/(A^*I_0)$ values for rhomboid shaped catchments. Catchment area is kept constant, the nondimensional length over area ratio ($L/\sqrt{A}$) is changed over the x axes. Nondimensional storm intensity decline scale ($L_0\sqrt{A}$) is unity. b) Peak discharge decline rates (k) for different relative storm decline rates ($L_0\sqrt{A}$). Note that shape sensitivity shows a distinct maximum and decreases both towards very small and very large relative storm scales.

prevailing wind direction which shifts the characteristic effective storm shape from circular to oval, and an inhomogeneous infiltration field, would be superimposed onto this basic catchment shape sensitivity of runoff production.

The experiment in Fig. 1a was performed with a fixed storm intensity decline rate (L_o in Eq. (2)). The numerically obtained peak discharge values for a given catchment size and storm intensity decline rate can be approximated e.g. with a power law function of catchment elongation ($L/\sqrt{A}$). We propose the power law form in order to fit the conventional form of empirical relationships in hydrology, but other decreasing functions could also express the effect of basin geometry on peak discharge.

The power is termed here the shape exponent (k) and gives the degree of runoff production dependence on catchment shape. The shape exponent depends on the ratio of storm scale to basin scale ($L_0/\sqrt{A}$). For a given basin scale there is a specific storm intensity decline rate (or for a given decline rate a specific basin scale) that induces the highest elongation sensitivity (Fig. 1b). Both below and above this spatial scale, shape sensitivity decreases and the power law exponent k goes to zero.

For comparison to Fig. 1b, observed elongation ratios ($L_0/\sqrt{A}$) appear to range typically between about 1 and 3. The empirical relation $L = \sqrt{3A}$ derived by Montgomery and Dietrich (1992) implies an average elongation ratio of about 1.7. Some basins show marked elongation due to structural or other controls. For example, Table 1 lists shape data for eight unusually elongated drainages (>100 km^2) in east-central Utah, USA (note that length shown is the maximum distance to the basin outlet rather than the length of the main stream). The highest elongation ratios are on the order of 2.5. It seems unlikely that elongation ratios ever exceed 3.0.

According to Fig. 1b the greatest shape-sensitivity occurs when the storm decline rate L_0 is about half of the catchment radius. In this case storm intensity at the edges of the catchment is about 14% of the intensity in the middle of the storm (I_0). Based on this we can give the rough estimate that the highest shape sensitivity is present when characteristic catchment and storm diameters are equal.

The physical interpretation of this numerical result is that if storm intensity declines very fast in space (i.e., storm area is small), the overwhelming proportion of runoff is produced in the vicinity of the storm centre, and total runoff is relatively insensitive to the shape of the catchment as long as the storm centre falls near the middle of the catchment. In contrast, if the spatial storm decline is small relative to catchment scale, total runoff is primarily influenced by the area of the catchment and

Table 1
Geometry data for elongated catchments in east-central Utah, USA

Drainage basin	Drainage area (km^2)	Euclidean basin length (km)	$L/A^{0.5}$
Willow Creek	113.4	19.7	1.85
Timber Canyon	116.8	21.0	1.94
Avintaquin Canyon	346.3	31.5	1.69
Lake Canyon	109.4	26.0	2.49
Indian Canyon	250.5	42.0	2.65
Sowers Canyon	316.1	37.3	2.10
Antelope Canyon	142.3	26.2	2.20
Argyle Creek	202.9	34.9	2.45

Please cite this article as: Sólyom P.B., Tucker G.E. The importance of the catchment area–length relationship in governing non-steady state hydrology, optimal junction angles and drainage network pattern. Geomorphology (2006), doi:10.1016/j.geomorph.2006.10.014

it is only slightly dependent on its shape. This storm-size effect on runoff-area sensitivity has been demonstrated empirically. For example, Goodrich et al. (1997) presented data from Walnut Gulch, Arizona, USA, showing a strong departure from near-linear Q_p–A scaling that coincides with the point at which storm-core area drops below about half of the basin area. Shape dependency goes to zero when rainfall rate is spatially homogeneous.

Between these two end cases there is an optimum, a spatial scale that exhibits the greatest shape sensitivity. Fig. 2a,b show families of curves for different elongation and storm size values. This *discontinuous* shape sensitivity represents a significant difference between the two runoff environments dealt with in this paper: one dominated by spatially inhomogeneous rainfall fields, and the other in which characteristic storm duration is below the concentration time, called here the relative storm duration environment. As will be shown in the next section, shape sensitivity of runoff production within the relative storm duration environment is *continuous*ly increasing with catchment scale.

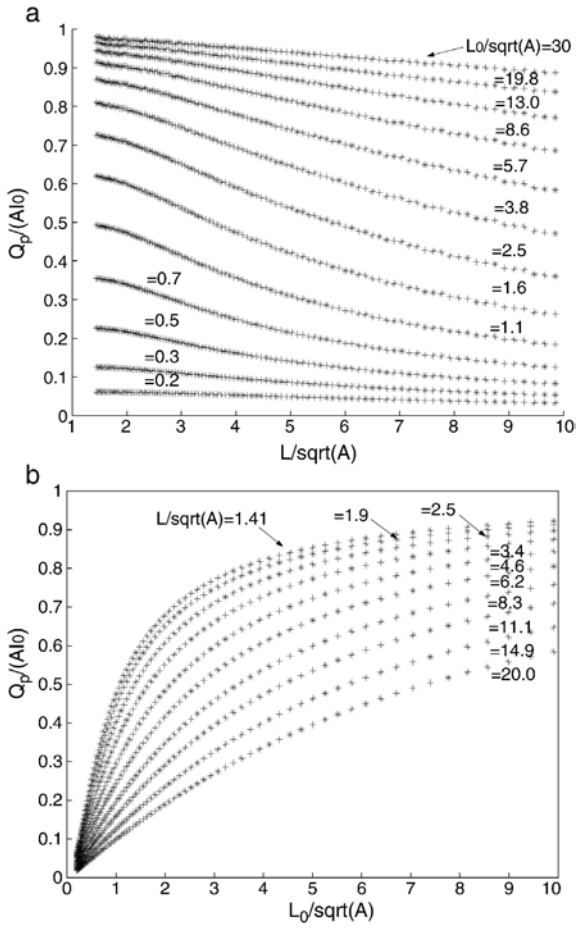

Fig. 2. a) Numerically integrated peak discharge values for different relative storm sizes as a function of catchment shape. Note that elongation sensitivity goes to zero for very small and very extensive storms, while in between there is a privileged scale showing the strongest shape sensitivity. b) Numerically integrated peak discharge values for differently shaped catchments as a function of relative storm scale. Among the rectangular rhomboids, squares show the highest sensitivity to the storm size, due to the fact that squares are the closest footprints of the circular storms among the rhomboids.

To illustrate the effect of catchment shape in determining peak discharge, non-steady runoff simulations were conducted on a synthetic topographic surface. The topography used for this simulation was produced with a landscape evolution model, but the experiment can be readily reproduced on real world DEMs or on any other topography, as long as the topography is organized into drainage basins with typical drainage-network properties. The simulation window was subjected to storms with a spatially declining rain field such that the storm centre was varied iteratively and runoff was recorded for each pixel and for each iteration. The highest runoff on each pixel that occurred during the course of the simulation was chosen as the maximal peak discharge.

Fig. 3 shows the resulting distribution of peak discharge values as a function of the contributing area. The overall tendency of Fig. 3 illustrates well the nonlinear discharge-area relation that results from nonuniform rainfall distribution. For small contributing areas (large $L_0/\sqrt{A}$) peak discharge goes linearly with contributing area, whereas for higher contributing area this positive relationship breaks down. The more important message of Fig. 3 is that for higher contributing areas there are separate dot clusters showing the different position of individual subcatchments in the dot cloud. These differences are caused solely by the varying geometry of the individual subcatchments.

The numerical calculations discussed above can be used as the theoretical basis for an analytical approximation for peak discharge distribution. A good approximation is given by:

$$Q_p = K_j I_0 A (L/L_0)^{-j} \tag{3}$$

where K_j is a dimensionless proportionality constant, and j is an exponent. This yields a better correlation than the simple power law expression $Q_p \sim A^{-j}$, because runoff production in the limited storm size environment depends on both the shape and size of the drainage area. Using the dataset underlying Fig. 3 best correlation with peak discharge is achieved for the product: $AL^{-0.3}$. This example also illustrates that non-steady state runoff

Please cite this article as: Sólyom P.B., Tucker G.E. The importance of the catchment area–length relationship in governing non-steady state hydrology, optimal junction angles and drainage network pattern. Geomorphology (2006), doi:10.1016/j.geomorph.2006.10.014

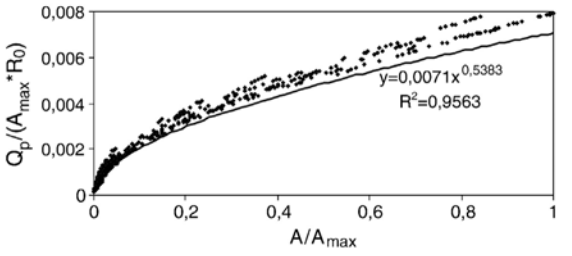

Fig. 3. Peak discharge values obtained by simulating small storm runoff production on a 2D topography. The storm decline rate (L_0 in Eq. (2)) was tuned to produce a pronounced catchment shape sensitivity. The individual dot clusters in the figure correspond to individual subcatchments on the simulation field, illustrating the effect of morphometry on runoff production within the limited storm size environment. The exponent 0.53 of the best fit curve illustrates the lack of linear discharge-area relationship. Note: the bulk of the dots lies in the small drainage area region, that is why the best fit curve can deviate from the dots within the high drainage area region.

approximation for small sized convective storms is recommended to use a function with the basic form: $Q_p \sim AL^{-j}$.

2.1.2. The limited storm duration model

An earlier paper by the authors (Sólyom and Tucker, 2004) deals with the morphological outcomes of the limited storm duration environment, such as the effect of storm duration on equilibrium profile concavity and valley density, and the interactions between storm duration, hydrograph shape and landform development. Here we briefly review the runoff model presented in that paper and investigate an aspect that was not dealt with earlier, the relationship between storm duration and the drainage network pattern. Runoff production of short storms is also compared to runoff generated by spatially inhomogeneous precipitation.

The runoff model for "short storm" conditions (i.e., duration ≪ travel time to the outlet) makes use out of the fact that runoff can be calculated both via the hydrograph volume and via the contributing area. Hydrograph volume can be given by:

$$V = Q_p T_h F_{hs} \tag{4}$$

where T_h is hydrograph duration and F_{hs} (which ranges from 0–1) is a hydrograph shape factor giving the proportion of the hydrograph in the $Q_p T_h$ window.

Flood hydrograph duration can be given as:

$$T_h = T_r + T_t \tag{5}$$

where T_r is storm duration, and T_t is travel time of a water particle from the most distant location of the catchment to the outlet. If runoff is steady and spatially uniform, storm runoff volume in a catchment can also be calculated from the runoff rate, basin area, and storm duration:

$$V = RAT_r \tag{6}$$

where R is runoff rate per unit area.

Here we assume that travel time is expressed as L_f/U_f, where L_f is the longest flow path length within the basin and U_f is a spatially constant routing velocity (ignoring the very slight discharge dependence of $U_f \sim Q^{0.1}$ (Leopold and Maddock, 1953). From this assumption and Eqs. (4) and (6), peak discharge can be calculated as

$$Q_p = \frac{RA}{F_{hs}}\left(\frac{T_r}{T_r + L_f/U_f}\right). \tag{7}$$

No separate routing velocities for hillslopes and for channels are applied to the case above. It can be shown that applying an extra constant for overland flow runoff velocity decreases the bracket part of Eq. (7), but does not alter the dynamics of the system. Hydrograph shape F_{hs} is also considered to be constant. It again can be shown that in channels F_{hs} stays relatively stable around 0.4 as long as $T_r < T_t$ (Sólyom and Tucker, 2004, Fig. 3), so that we approximate F_{hs} with this characteristic value. The ratio $T_r/(T_r+L/U_f)$ is termed the storm duration number (N_{SD}). It is a spatially inhomogeneous nondimensional variable expressing the united effect of storm duration, flow path length, and routing velocity on peak discharge. We also define here a characteristic storm duration number, N_{SD0}, as $T_r/(T_r+L_c/U_f)$ where L_c is a characteristic horizontal scale, here set equal to the width of the simulation domain. Finally, it is convenient to simplify the storm duration number by defining a dimensionless mainstream length as, so that $N_{SD} = 1/(1+L'_f)$.

Eq. (7) is sensitive both to the storm duration-concentration time relationship and to the length–area relationship. Both of these relationships depend on catchment geometry. Note that mainstream length, L_f, typically grows with catchment size as $L_f \sim A^h$, where h=0.5–0.6 (Hack, 1957; Montgomery and Dietrich, 1992; Rigon et al., 1996). Thus, in the case of short storms or big catchments, the (flow path length related) concentration time will tend to be greater than the storm duration, and peak discharge will increase only less than linearly with the contributing area (see, e.g., Goodrich et al., 1997; Finlayson and Montgomery, 2003). At the same time peak discharge is also a function of the overall geometry of the flow path structure defining the area–length relationship of catchments. The physical

Please cite this article as: Sólyom P.B., Tucker G.E. The importance of the catchment area–length relationship in governing non-steady state hydrology, optimal junction angles and drainage network pattern. Geomorphology (2006), doi:10.1016/j.geomorph.2006.10.014

explanation behind the geometry sensitivity of peak discharge within the relative storm duration environment lies in the difference of the concentration times among differently shaped basins, with round catchments showing shorter concentration times than elongated catchments (Strahler, 1964). Therefore basins with higher area–length ratios produce higher peak discharges for the same area and precipitation input than elongated basins. This basin-shape dependence is also often incorporated in empirical unit hydrograph models (e.g., Bras, 1990).

Fig. 4a illustrates peak discharge as a function of the nondimensional flow path length. Fig. 4b shows a family of curves of peak discharge values against catchment shape and demonstrates the elongation sensitivity of runoff production within the limited storm duration environment. This finding is in accordance with the message of the previous section where it has been shown that basin shape under an inhomogeneous rainfall field influences peak discharge production. Hence runoff computation for both of these cases of non-steady state discharge production is physically better founded if based on the length–area relationship and not only on an area power law relationship as used in conventional approximations.

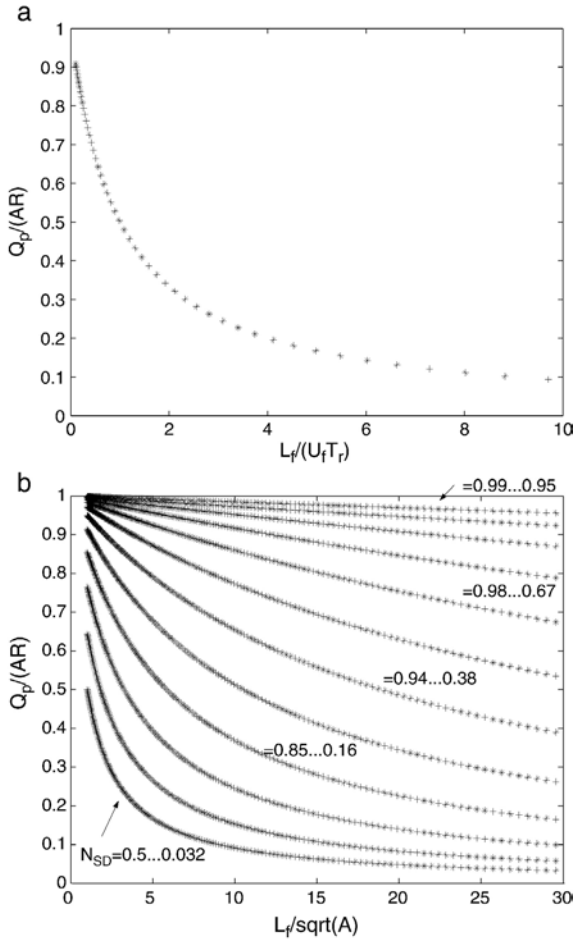

Fig. 4. a) Peak discharge values in the limited storm duration environment as a function of the relative flow path length. b) Peak discharge values in the limited storm duration environment as a function of catchment shape. The curves correspond to different storm durations invoking different ranges in the storm duration number over the plotted profile. The high shape sensitivity for low storm duration dissepares as storm duration increases.

There is a significant difference, however, between runoff production of the two environments ("short storm" versus "small storm"). In the short-storm case, sensitivity to catchment shape grows monotonically, continuously with basin size (Fig. 4b), in the sense that N_{SD} shrinks with increasing basin size, and sensitivity is highest for the lowest N_{SD}. By contrast, the discontinuous shape sensitivity in the small-storm case shows a distinct maximum and goes to zero for both relatively very small and very large storms due to the spatial interrelationship between the characteristic storm size and catchment size (Fig. 2a).

Below we consider the effects of the shape sensitive non-steady state runoff production on drainage network development, using the stream power minimization concept for junction angle and network optimization.

2.2. Optimization theory

Drainage network pattern is one of the most characteristic features of fluvially shaped landscapes. Already the very first papers of quantitative geomorphology (Horton, 1932, 1945; Lubowe, 1964; Strahler, 1964) dealt with channel network characteristics. The indices identified during this early period of research were later extensively used by subsequent authors, e.g. to test random, stochastic models of drainage networks (Shreve, 1966; Smart, 1968; Shreve, 1969; Smart and Werner, 1976; Smart, 1978). Nonetheless non-random patterns recognised in drainage networks (Abrahams, 1984) can better be explained by models that account for the physics of erosion and energy expenditure, such as network optimization models (e.g., Rodriguez Iturbe and Rinaldo, 1997). We use the optimization framework here as an efficient substitute for full numerical simulations of basin evolution and channel junction adjustment mainly because the lower energy states enable a greater ease of drainage rearrangement (Ibbitt et al., 1999). It has also been demonstrated that the outcomes of optimization models are consistent with those of numerical landscape evolution models (Banavar et al., 1997). At the same

Please cite this article as: Sólyom P.B., Tucker G.E. The importance of the catchment area–length relationship in governing non-steady state hydrology, optimal junction angles and drainage network pattern. Geomorphology (2006), doi:10.1016/j.geomorph.2006.10.014

time one has to be aware that network optimality arguments derive from two different sources. One is the empirical correspondence between OCNs and real networks. The other is a theory that demonstrates analytically that the solution of a simple, detachment-limited erosion equation is indeed an optimum solution (Banavar et al., 2001).

Network optimization happens through cost-function minimization, where the cost function is stream power (rate of energy transfer) per unit channel length. It is argued that the pursuit of nature towards a minimum energy level can also be traced in erosional systems by looking at the way these systems develop energy-related quantities (Rodriguez Iturbe and Rinaldo, 1997). Stream power per unit channel length is considered here as the energy-related quantity and this paper explains characteristics of individual junction angles and of whole drainage networks following the theory that the work of erosion tends to minimize its driving quantity.

In this paper we consider both individual-junction and network-wide optimization. Optimization within individual components of the network, such as junction angles, is a necessary but not sufficient condition for optimization at the level of the entire network. Thus, we begin by examining how variations in hydrologic input influence this local optimization. Local optimality does not ensure global optimality, however. In terms of system-wide optimization, Rodriguez Iturbe and Rinaldo (1997) have argued that drainage networks tend toward a state of "feasible optimality": a configuration which does not represent a global optimum because of basic constraints placed on the mobility of the drainage network. Rather, a state of feasible optimality is equivalent to the most efficient state that is dynamically accessible to the system. They have shown that 'standard' OCN lattice models reproduce both the characteristics of a feasibly optimal network and closely match the statistics of observed networks. We therefore use the OCN lattice model to examine hydrological impacts on the feasibly optimal network form.

Here we use stream power per unit length as the cost function (Howard, 1990). The usage of the stream power concept in the literature is well-founded. It is highly correlated with rates of sediment transport (e.g., Bagnold, 1957, 1966; Bull, 1979), and recently has been proposed as a primary control on the rate of bedrock incision (Seidl and Dietrich, 1992; Whipple and Tucker, 1999). In the following we use non-steady state runoff production to compute stream power and analyse its effect both on the level of individual junction angles and of the entire network structure.

3. Methods and results I: The effect of shape-sensitive runoff production on the optimal junction angles

3.1. Methods

Howard (1971a, 1990) used the following model to minimize total cost Ω for an individual junction consisting of three links:

$$\Omega = \sum_{i=1}^{3} C_i L_i \tag{8}$$

where C_i is cost per unit channel length and L_i is link length at the point i.

The model used in the present paper has the same framework. Three points in the space are fixed: the two sources of the two tributaries, and the outlet of the main stream. The optimization model seeks the position of the junction that minimizes Eq. (8) (Fig. 5). The cost function, stream power per unit channel length, is defined as

$$C_i = \rho g Q_i S_i \tag{9}$$

where ρ is bulk density, g is gravitational acceleration, Q_i is runoff through a channel segment and S_i is slope at the point i. The physical interpretation for this minimization is as follows. The three channel segments at a junction will undergo essentially random variations in position due to bank erosion and bar migration. If the magnitude or frequency of position shifts depends on the stream power available for bedload transport and bank erosion, then there will be a natural statistical tendency for the channel confluence to oscillate around a position of minimum stream power.

In this section we discuss how the optimal junction angle depends on the way the cost function is computed. This includes

1. how discharge relates to link length,
2. what proportion of discharge is source discharge versus lateral inflow,
3. how slope relates to discharge and
4. what is the effect of non-steady state discharge production.

Runoff (Q_i) is computed in one of three different ways:

1. Standard linear runoff model (Howard, 1990):

$$Q_i = RA_{0i} + RA_i = RA_{0i} + RK_W L_i, \tag{10}$$

where A_{0i} is contributing area draining to the top of the link, A_i is local contributing area, that is, the amount of

Please cite this article as: Sólyom P.B., Tucker G.E. The importance of the catchment area–length relationship in governing non-steady state hydrology, optimal junction angles and drainage network pattern. Geomorphology (2006), doi:10.1016/j.geomorph.2006.10.014

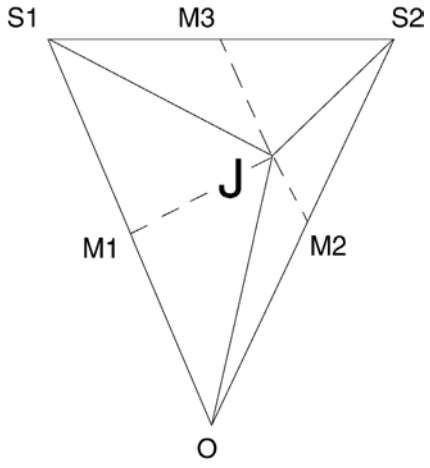

Fig. 5. The spatial framework for the participation of the available drainage area among the three links. S1, S2, O and J stand for sources one and two, the outlet and the junction, respectively. Thin solid line gives the boundaries of the triangle defining the available drainage space, thick line represents the three links, and dashed line the imaginary drainage divides leading from the junction position to the midpoints of the links (M1–M3). The junction angle is the S1JS2 angle.

extra hillslope area added between the top and bottom of the link, the constant K_W relates to the width of the contributing area (W), and L_i is link length (L) at the point i. This model assumes that discharge is linearly proportional to link length if the source term (RA_{0i}) is zero. This way of computing runoff is hereafter termed the *linear runoff calculation*. In Eq. (10), geometric constraints on the drainage area around a link are not considered (i.e., two links of equal length will have the same hillslope area regardless of the position and geometry of adjacent links).

2. Geometrically based runoff model:

$$Q_i = RA_{0i} + RA_i = RA_{0i} + Rf(\text{geometry}), \tag{11}$$

where function f relates discharge to the available drainage space. This represents a somewhat new approach incorporating the effect of the available drainage area into the optimization process. In Eq. (10) total runoff changes as a function of total link length, but this approximation is de-coupled from the available drainage space. In contrast, Eq. (11) satisfies the law of mass conservation, because contributing area is computed explicitly from the geometry of adjacent links, rather than being approximated using link length. The method used to compute local drainage areas around a junction is illustrated in Fig. 5. In the model the three fixed points in space, the two sources (S1, S2) and the outlet (O) define a triangle, which represents the available drainage area. Midpoints of the sides of the triangle (M1–M3) are defined as the ends of imaginary drainage divides connecting the midpoints to the junction (J) and separating the individual contributing areas of the links. Function f in Eq. (11) returns the area draining immediately to the individual links, e.g. for the S1J link it is the area of the S1M1JM3 quadrangle. Other approaches, such as defining a hexagonal drainage space, where the three fixed points represent three opposite corners of the hexagon, are also possible. It will be shown in Sections 3.2 and 3.4 that the geometrically based approach of runoff calculation alters the length–area relationship and consequently the resulting optimal junction angle, although the main tendencies of junction angle sensitivity remain similar. The main significance of this approach is that it opens the way towards the incorporation of the role of potentially available drainage space in the interpretation of landscape evolution. Further improvement is possible through dynamic definitions of the divide positions after establishing theoretically or empirically founded rules for divide migration (Howard, 1971b). This way of computing runoff is hereafter termed the *geometry based runoff computation*.

3. Nonlinear runoff model:

$$Q_i = F_{\text{hs}}^{-1}(RA_{0i} + RK_W L_i)N_{\text{SD}i} \tag{12}$$

$$Q_i = K_\varphi(RA_{0i} + RK_w L_i)L_{\text{f}}^{-\varphi} \tag{13}$$

$$Q_i = F_{\text{hs}}^{-1}(RA_{0i} + Rf(\text{geometry}))N_{\text{SD}i} \tag{14}$$

$$Q_i = K_\varphi(RA_{0i} + Rf(\text{geometry}))L_{\text{f}}^{-\varphi} \tag{15}$$

These functions represent non-steady state discharge production and were obtained by combining Eqs. (3), (7), (10) and (11). Eqs. (12) and (14) represent the limited storm duration case, while Eqs. (13) and (15) are the generalized form for both the limited storm duration and the limited storm size case with φ being the exponent of the flow path length dependence, and K_φ the proportionality constant. Here we are assuming that the stream power to be minimized is not the mean-flow stream power (which presumably would vary linearly with area if the long-term average precipitation and infiltration fields are uniform) but the stream power produced by a flood of unspecified magnitude. In order to be able to account for the special feature of non-steady runoff production, its dependence on the shape of the contributing area, flow path length L_{f} has been introduced into the optimization. For zero-source terms,

Please cite this article as: Sólyom P.B., Tucker G.E. The importance of the catchment area–length relationship in governing non-steady state hydrology, optimal junction angles and drainage network pattern. Geomorphology (2006), doi:10.1016/j.geomorph.2006.10.014

flow path length corresponds to the link length in the case of the two tributaries, and it is mainstream length plus the length of the longer of the two tributaries in the case of the main stream. For nonzero source terms, the Hackian relationship between source discharge and source flow path length (L_{f0}) is assumed ($L_{f0}=K_h A_{0i}^{0.6}$, where K_h is a constant) and added to the flow path length calculated for zero source terms, as $L_f=L_{f0}+L_i$.

Slope is computed as a power law function of runoff:

$$S = K_s Q^{-z} \tag{16}$$

where K_s and z are constants. Therefore Eq. (9) is reduced to

$$C_i = KQ_i^{\gamma} \tag{17}$$

where $K=K_s\rho g$ and $\gamma=1-z$.

The optimization algorithm (Howard, 1990) scans all the points within the triangle, and computes the cost function that results when the junction occupies each point. The three links are defined, and link length, flow path length, runoff and total stream power values with corresponding junction angle are computed for each junction position. At the end of the loop the junction position with the lowest total cost is selected, and the resulting junction angle is returned. This angle is termed the optimal junction angle for the given conditions. Sensitivity analysis is performed to quantify the reaction of the system to changes of its parameters: γ, source term-lateral inflow ratio and the degree of the non-steady state character of runoff.

3.2. Optimal junction angle sensitivity: the role of γ

Figs. 6–8 show optimal junction angle dependence on the exponent γ and on the source discharge-within link runoff contribution relationship. Recall from Eqs. (16) and (17) that $\gamma=0$ represents a strong inverse relation between slope and discharge, $\gamma=1$ represents no correlation between the two, and $\gamma>1$ represents a positive relationship (which tends to occur only sporadically in most river networks). The two different symbols in the figures stand for the runoff computed as a linear function of the link length (Eq. (10)) and for the runoff computed based on the geometry of the available drainage space (Eq. (11)). The optimal junction angle is furthermore dependent on the shape of the boundary triangle. In the simulations presented in this paper the triangle is set up such that the angle at the outlet is 45° (Fig. 5). The spread of points at fixed angles in all the junction angle figures is an outcome of the finite resolution of the optimization model. Within a continuous framework the optimal junction angle gives a continuous function. The source discharge terms for the two tributaries always have the same value; in other words no asymmetrical link discharges are considered here.

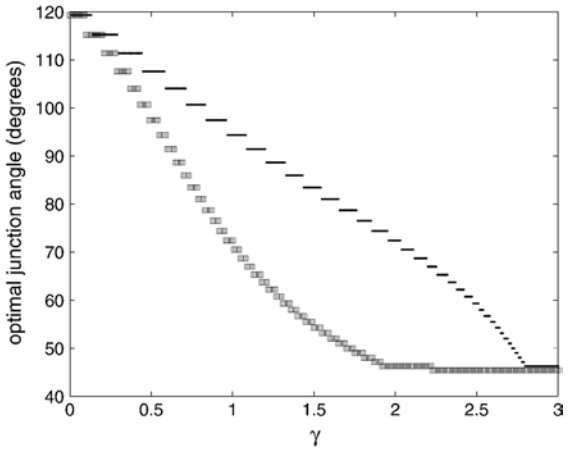

Fig. 6. Optimal junction angles for the case in which source discharges are zero. Dots stand for cost computation based on a linear discharge function, squares stand for the geometry-based cost calculation. With increasing γ junction angles decrease until they reach the angle of the drainage area triangle at the outlet (45°). For $\gamma=0$ junction value goes to 120° representing the shortest connection among three points.

Figs. 6 and 7 demonstrate that the optimal junction angle decreases as γ increases, as has been shown by Howard (1990). The tendency is valid both for the linear runoff calculation and for the geometrical runoff function. For high γ values the optimal junction angle reaches a minimum. This minimum represents the situation in which the junction is pushed to the outlet of the system, so that practically there is no main stream, only the two tributaries joining at this position. In this case the junction angle coincides with the preset angle of the initial triangle.

Although the cost function is the product of a runoff-related term and of a link-length term, link length also affects runoff immediately as defined in Eqs. (10)–(15). The interpretation of the optimal junction position has to take into account separately the dynamics of all of the involved parameters. For $\gamma>1$ the main stream routing the sum of the tributary discharges has higher stream power than the sum of the stream power rates of the two individual tributaries. Therefore no junctions would occur for $\gamma>1$, if it were not for the total link length shortening effect of the junction. This effect and consequently the diminishing of the total stream power counterbalance the effect of the exponent being higher than 1.

Please cite this article as: Sólyom P.B., Tucker G.E. The importance of the catchment area–length relationship in governing non-steady state hydrology, optimal junction angles and drainage network pattern. Geomorphology (2006), doi:10.1016/j.geomorph.2006.10.014

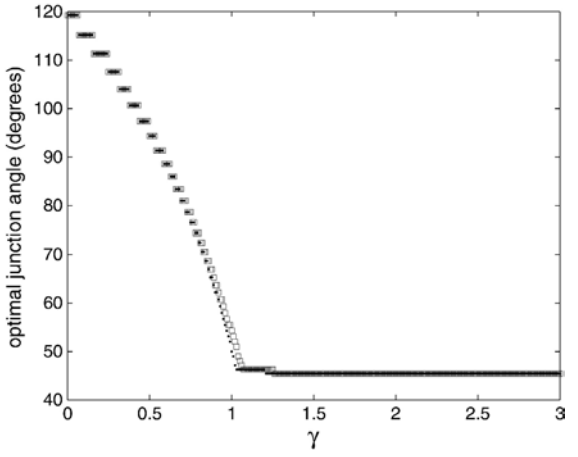

Fig. 7. γ sensitivity of optimal junction angles for source discharge dominated runoff production. Source discharges are considerably higher than within link runoff contribution. Dots stand for linear runoff calculation, squares for geometry-based runoff calculation. The two almost coincide in this figure, because within link runoff contribution is negligible.

Minimum angle is reached only at $\gamma=2.2$ for the geometry-based runoff calculation and for $\gamma=2.7$ for the linear runoff calculation (Fig. 6)). The slight difference between the linear and geometry based calculation is due to the way the geometry function subdivides the available drainage space among the three links. Given that the imaginary drainage divides connect the junction to the midpoints of the sides of the triangle, an asymmetric junction position induces bigger asymmetry in the link length distribution than in the link area distribution. Therefore a short main stream link has a proportionally higher drainage area than length, and minimum angle is reached already for a somewhat lower γ value than for the linear runoff calculation.

For $\gamma<1$ the main stream's stream power is lower than the sum of the stream powers of the two individual tributaries, so that junction becomes favourable also without the link length shortening effect. In the vicinity of $\gamma=0$ the difference between the main stream's cost and the tributaries' cost vanishes. At $\gamma=0$ (for $z=1$) the stream power per unit length for all the three links is the same, and the system finds its cost minimum by minimizing the length terms in Eq. (7). This is achieved with a junction angle of 120° (Fig. 6).

3.3. Optimal junction angle sensitivity: the role of source vs. lateral inflow

Fig. 7 demonstrates the case in which source discharges are significantly higher than the runoff contribution from hillslopes within the individual links. A somewhat different pattern emerges, with optimal junction angle reaching a minimum at $\gamma=1$. Neither the link length, nor the geometry of the available drainage space affects the runoff term significantly. Because link length does not influence runoff, junctions do not occur for $\gamma>1$. Furthermore, because within-link runoff contribution is insignificant, the optimal junction angles obtained for linear versus geometry-based runoff show no difference. The junction angles of Fig. 7 coincide for low γ values with the analytically derived junction angles of Roy (1983) (published also in Howard, 1990, Table 1) and of Woldenberg and Horsfield (1983, 1986). The deviance for high γ values is due to the boundary condition of the numerical optimization: the preset minimum angle at the junction (45°) does not allow the junction angle to go to zero at $\gamma=1$.

Figs. 6 and 7 show that optimal junction angle is strongly dependent on the source discharge-lateral inflow ratio. An important consequence of this is that high-order junctions are significantly narrower, all else being equal, than low-order junctions (Fig. 8).

3.4. Optimal junction angle under non steady-state runoff conditions: unstable junctions

Figs. 9–12 treat the situation in which runoff characteristics shift from steady state to non-steady state. Eqs. (12)–(15) were used in the model runs to compute discharge. The common pattern among the

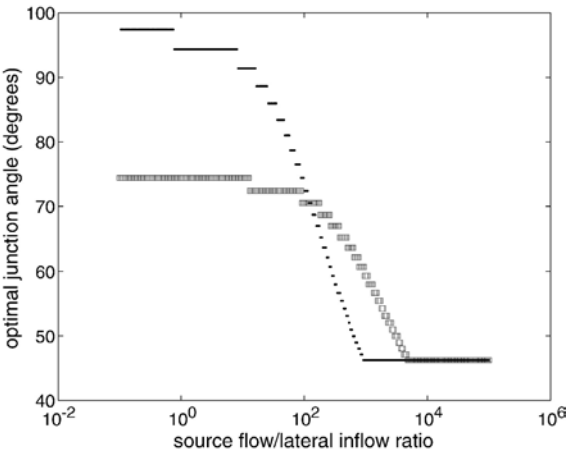

Fig. 8. Optimal junction angle sensitivity to the source discharge-lateral inflow ratio. As in Figs. 6 and 7, dots stand for the linear, squares for the geometry-based runoff calculation. $\gamma=0.95$ in order to cover a wide junction angle range, because for lower γ values the difference between the advective and diffusive angles is less pronounced. Increasing ratio imitates increasing distance from the crest (assuming uniform hillslope length). Junction angles decrease with the increasing ratio.

Please cite this article as: Sólyom P.B., Tucker G.E. The importance of the catchment area–length relationship in governing non-steady state hydrology, optimal junction angles and drainage network pattern. Geomorphology (2006), doi:10.1016/j.geomorph.2006.10.014

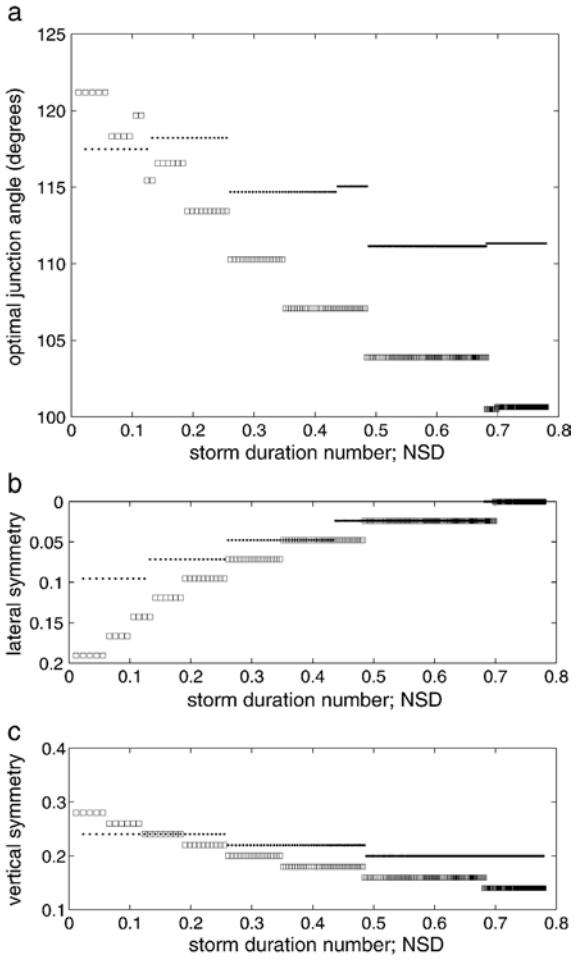

Fig. 9. a) Storm duration sensitivity of optimal junction angles. Dots stand for linear runoff calculation, squares for geometry-based runoff calculation. Runoff is lateral inflow-dominated, $\gamma=0.5$. The storm duration number (Eq. (7)) on the x axes refers to the main link. b) and c) Spatial position of the junction. Lateral symmetry (b) shows the normalized deviance of the junction from the longitudinal axes of the simulation field with 0.5 standing for the edge of the simulation field. Vertical symmetry (c) refers to the relative position compared to the horizontal axes of the simulation field, with positive going towards the tributary sources.

figures is that optimal junction angle increases as runoff conditions shift towards the non-steady state. Given that the total cost relates to length both in terms of runoff calculation and in terms of link length term, the incorporation of flow path length into the discharge calculation is expected to have a direct effect on the total cost and on the optimal junction angle.

Increasing flow path length has a runoff and therefore total cost decreasing effect (Eqs. (12)–(15)). Therefore the system prefers junction positions that increase flow path length (Note: flow path length, L_f in Eqs. (12)–(15), is not the same as link length). As a consequence, the interesting situation of asymmetric junction position emerges. Figs. 9–12) illustrate the change of the optimal junction angle and the lateral and vertical shifts of the optimal junction positions as a function of the storm duration number and flow path length exponent φ. In Figs. 6–8 the junction is always laterally symmetric. In Figs. 9 and 10 the junction becomes asymmetric, shifting laterally towards one of the tributary sources. Lateral shift reduces one of the links in length, and increases the other. Hence flow path length L_f of the main stream (main stream length+ the longer of the two

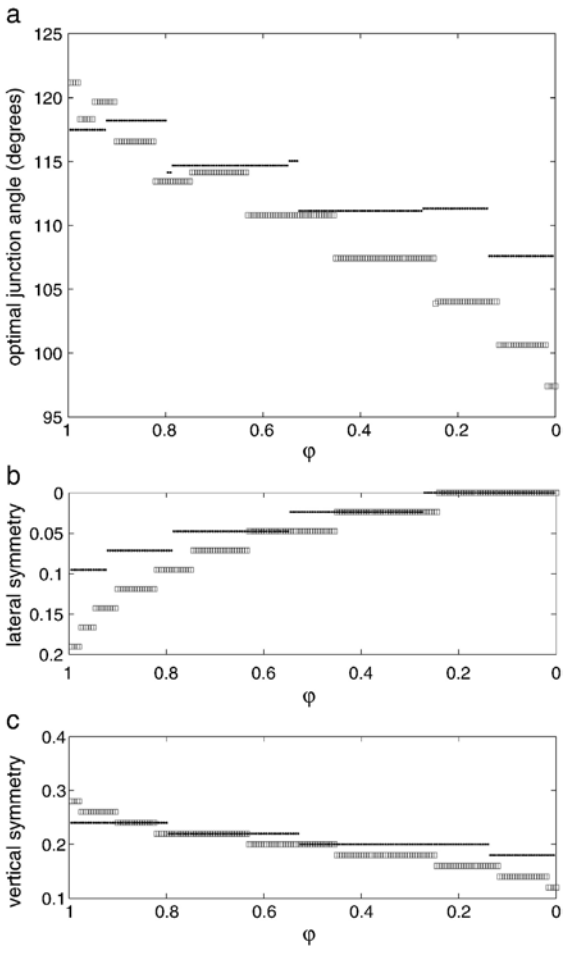

Fig. 10. a) Flowpath length sensitivity of optimal junction angles. Dots stand for linear runoff calculation, squares for geometry-based runoff calculation. Runoff is lateral inflow-dominated, $\gamma=0.5$. φ is the flowpath length exponent in Eq. (13). b) and c) Spatial position of the junction. Lateral symmetry (b) shows the normalized deviance of the junction from the longitudinal axes of the simulation field with 0.5 standing for the edge of the simulation field. Vertical symmetry (c) refers to the relative position compared to the horizontal axes of the simulation field, with positive going towards the tributary sources.

Please cite this article as: Sólyom P.B., Tucker G.E. The importance of the catchment area–length relationship in governing non-steady state hydrology, optimal junction angles and drainage network pattern. Geomorphology (2006), doi:10.1016/j.geomorph.2006.10.014

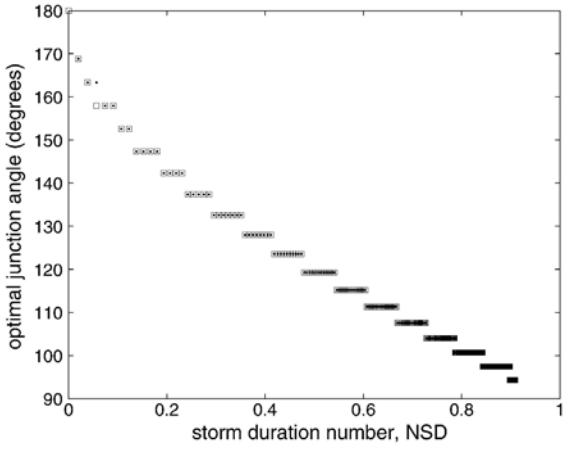

Fig. 11. Storm duration sensitivity of optimal junction angles. Dots stand for linear runoff calculation, squares for geometry-based runoff calculation. Runoff is source term-dominated, $\gamma=0.5$. The storm duration number (Eq. (7)) on the x axes refers to the main link. Junction position stays laterally symmetrical.

tributaries) increases, and runoff and total cost decrease. The stronger the *flow path length-dependence of the runoff* production, the more pronounced the junction asymmetry.

Lateral shift occurs only in low-order junctions, for which lateral inflow dominates. For high-order junctions (source-dominated runoff), flow path length is significantly higher than individual link lengths, and as a result runoff becomes insensitive to link length and consequently junction shift. Basically the junction position influences neither the total link length nor the flow path length of the system. In this case, no asymmetry occurs and total cost can only be reduced (when $\gamma<1$) through merging of the two streams, and shortening of the two tributaries. It is noteworthy that under source-dominated non-steady runoff the optimal junction angles grow up to 180° (Figs. 11 and 12) when the flow path length dependence of runoff is at maximum. The reason behind this extreme value compared to the 120° for the steady-runoff case is that the constant total link length cannot limit the system in reducing the tributaries. Shortest tributaries are reached when the junction is pushed to the upper border of the simulation triangle (Figs. 11 and 12) producing the 180° junction angle. This effect only prevails for $\gamma<1$ because this gamma range reduces the weight of the main stream compared to the tributaries. The physical interpretation is that when storms are small or short, peak discharge does not grow very strongly with drainage basin size, and so the increased cost (i.e., stream power) below a junction is more than offset by the reduced total channel length.

Here we wish to identify two more effects connected to the phenomenon of lateral junction shift. A negative feedback for the lateral shift is that a sideways shifted junction increases the total link length of the system, increasing the total cost in parallel with the cost-decreasing effect of flow path length dependence. This is why lateral shift occurs only for $N_{SD}<0.4$ and $\varphi<-0.5$ for the local-runoff case in Fig. 9b, and not immediately when flow path length-dependence appears.

The second effect is a positive feedback that also contributes to the lateral shift of the junction position. Through lateral shift the link length and therefore runoff contribution of the two tributaries becomes asymmetric. For $\gamma<1$ this on its own decreases total cost, because the weight of the higher runoff is reduced compared to the weight of the smaller runoff. This additional effect of runoff partitioning favouring lateral junction instability remains invisible for steady state runoff, because increased link length and hence total cost would override this advantage of asymmetric distribution of tributary runoff rates.

3.5. Lateral planation

A morphological application of this phenomenon is to use it as one possible explanation for lateral planation. Under non-steady state runoff conditions junctions become laterally unstable when the flow path length dependence of the runoff function is strong enough to reduce the total cost of the system. Junctions shift sideways to minimize total cost through the augmentation of flow path length. This shifting can take the form

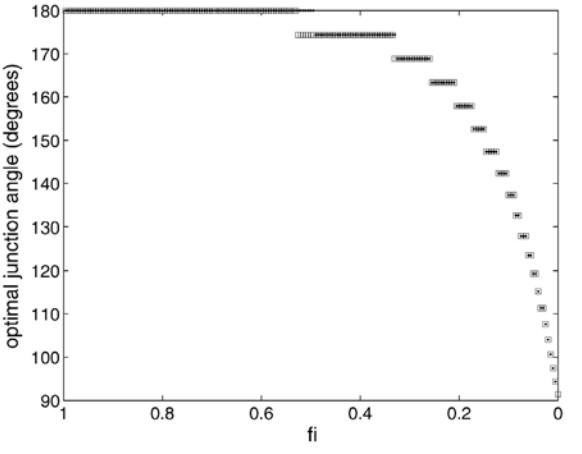

Fig. 12. Flowpath length sensitivity of optimal junction angles. Dots stand for linear runoff calculation, squares for geometry-based runoff calculation. Runoff is source term-dominated, $\gamma=0.5$. φ is the flowpath length exponent in Eq. (13). Junction position stays laterally symmetrical.

Please cite this article as: Sólyom P.B., Tucker G.E. The importance of the catchment area–length relationship in governing non-steady state hydrology, optimal junction angles and drainage network pattern. Geomorphology (2006), doi:10.1016/j.geomorph.2006.10.014

of valley migration (Howard, 1971b) on a bigger scale, or it can take the form of lateral planation through wandering, unincised streams on a smaller scale.

Figs. 9–12 have demonstrated that headwater, local-inflow dominated channels are more prone to asymmetric position and lateral migration than high-order channels with source-dominated runoff. According to the model, the condition for this phenomenon to occur is that dominant storms are either small or short enough to generate flow path-dependent runoff production. Here we suggest that storm duration is more likely to be the primary cause, because dominant storm sizes usually exceed the scale of hillslopes and low order channels. Assuming a typical duration (10–20 min) of an infiltration excess overland flow triggered by a convective storm, and a typical overland flow velocity (0.1 m s^{-1}; Kirkby, 1993), overland flow routing length is 60–120 m during a storm. Calculating on a typical hillslope length (300 m), the corresponding storm duration numbers are in the range of 0.15 to 0.3. According to Fig. 9b this degree of non-steady state runoff is already enough to initiate lateral shift of the junction positions.

Our interpretation of the asymmetric junction position also includes a dynamic component, which will be more understandable when looking at network scale optimization. The asymmetry in Figs. 9b and 10b involves a shift of the junction toward one of the two tributary sources. In parallel with this, the asymmetric junction geometry is more sensitive to random flow path fluctuations than the symmetric geometry. In the asymmetric case the flow path runs in the vicinity of the boundary of the drainage area, which makes it more vulnerable to capture activities of the neighbouring channels. Once an asymmetrically located stream has been captured, a new lateral migration shifts the junction to reach the optimal, asymmetric position again. Without any random noise the system indeed freezes to the asymmetric position, but once local fluctuations in erosion efficiency are present, and this is certainly a permanent characteristic of nature, channel capture and the following lateral migration are an inherent characteristic of the non-steady state runoff system. Systems dominated by steady state, hence flow path insensitive runoff, are less characterized by captures due to the symmetric optimal position of the junctions, therefore lateral channel migration is also less characteristic.

The space and time integration of the lateral migration of individual streams leads to the idea of lateral planation on hillslopes. Incised channels confined to valleys produce valley migration (Howard, 1971b). Unincised channels on hillslopes only have to overcome channel bank resistance to shift laterally, therefore lateral shift is potentially faster than in the case of the incised valleys. It is worth considering whether the more frequent and dominant occurrence of planated surfaces and pediments in arid to semiarid environments can be attributed to the fact that runoff under these climates is more often in non-steady state than under the humid climate.

3.6. Summary

Very briefly we would like to remind the reader of a few conclusions of this section. We arrived at the somewhat contradictory results that with increasing stream order, junction angles become narrower due to the increasing source and lateral inflow ratio, while under non-steady state runoff production junction angles should at the same time get wider in the downstream direction due to the increasing flow path dependence of runoff rates. Howard (1990) has similarly demonstrated downstream decreasing junction angles, although his analysis was based on the ratio of the two tributary discharges, and concluded that increasing asymmetry in the tributary discharges, which grows inherently in the downstream direction, leads to decreasing junction angles. Our similar conclusion is based on the analysis of the ratio between the source and lateral inflow. We come back to this contradictory result at the end of the paper and show that the non-steady runoff effect overrides the effect of the source and lateral inflow ratio.

Another important result is that non-steady state stream junctions are prone to lateral migration as a consequence of the role of flow path length in the runoff function. We used this phenomenon to explain lateral planation of wandering streams in arid environments.

4. Methods and results II: the effect of shape-sensitive runoff production on drainage network optimization

4.1. Methods

Understanding the behavior of individual junctions is not sufficient to understand drainage network patterns, because the spatial constraints (boundary conditions and outflow conditions) also impose limits on junction angles and can limit optimality. In fact local optimality (in this case the junction angles) is a necessary but not sufficient condition for global optimality. The initial configuration of the network and various factors affecting its evolution (e.g., tectonic forcing, lithology/structure, climate/hydrology) also influence the final network pattern. Rodriguez Iturbe and Rinaldo (1997) summarized these modifying effects under the notion of "feasible optimality", the closest state to the theoretical

Please cite this article as: Sólyom P.B., Tucker G.E. The importance of the catchment area–length relationship in governing non-steady state hydrology, optimal junction angles and drainage network pattern. Geomorphology (2006), doi:10.1016/j.geomorph.2006.10.014

optimality that the network is able to reach within the given constraints on its evolution.

In our analysis we focus on the question of how drainage network patterns are modified when runoff conditions become unsteady and/or non-uniform. The methodology is network optimization through cost minimization. We examine how the properties of Optimal Channel Networks (Rodriguez-Iturbe et al., 1992) are altered when the runoff is either non-steady ("short storms") or non-uniform ("small storms"). In each case, the cost function is stream power per unit length as in Howard (1971a, 1990).

The optimization algorithm consists of the following steps:

1. In order to get an initial random network, a raster-based drainage network with one corner outflow is generated on a randomly perturbed topography. Flow is directed towards the steepest slope. Depressions on the random surface are filled with a pit-filling algorithm. The drainage direction network is then used to compute contributing area for each individual pixel.

2. Total stream power of the entire network Ω is computed using

$$\Omega = \sum_i \rho g Q_i S_i L_i \tag{18}$$

L_i is equal to unity and for cardinal and diagonal links, respectively. The discharge at any given link is computed in one of two ways:

$$Q_i = R A_i N_{\mathrm{SD}}, \text{ or} \tag{19}$$

$$Q_i = R A_i L_{\mathrm{f}i}^{-\varphi} \tag{20}$$

Eq. (19) represents discharge for the limited storm duration environment. Eq. (20) is the generalized form for non-steady state runoff production for both the limited storm duration and the limited storm size environments. Under steady-state runoff, N_{SD} is unity and φ is zero, respectively.

Combining Eqs. (16), (18) (19) and (20) reduces to

$$\Omega = \sum_i K A_i^{\gamma} {N_{\mathrm{SD}i}}^{\gamma} L_i, \text{ or} \tag{21}$$

$$\Omega = \sum_i K A_i^{\gamma} L_{\mathrm{f}i}^{-\varphi\gamma} L_i, \tag{22}$$

where $K = K_{\mathrm{s}} \rho g$.

3. At a random location the flow direction is altered. Eventual infinite loops are filtered out, and then for the new network drainage area and total stream power are computed.

4. The new total stream power is compared to the old total stream power. If the new total cost of the network is below the old total cost, the change in the flow direction is accepted. If the new cost is higher than the old cost, the change is still accepted with a certain probability that declines over time. This allows the algorithm the opportunity to break out of local minima. The algorithm then repeats this procedure until a stable minimum is identified. These so-called "hot" networks reach finally a lower total cost than "cold" networks in which only those changes are accepted which diminish the total cost (Rodriguez Iturbe and Rinaldo, 1997). In these latter networks the initial network configuration is often conserved and this prevents the network reaching theoretical optimality. The probability governing the acceptance of higher total cost networks is a function of the time dependent "temperature" of the system. Temperature declines as the simulation time goes by. High temperatures at the beginning of the evolution provide higher chance to reorganise the initial network structure. Lower temperatures at the end of the simulation runs allow only rarely or do not allow at all flow direction to change towards a higher cost level.

The aim of the following section is to further understand the controlling factors on drainage networks, and to compare the findings obtained on the level of individual junctions (Section 3) with those obtained for the network structure. Simulations have been performed to analyze the sensitivity of optimized networks to the exponent γ, to the source vs. lateral inflow ratio and to the character of runoff. The resulting networks were quantified through their average junction angle and through the drainage area-junction angle graph. To derive junction angles a trunk network is defined within the optimized network by setting an area threshold. In this way triple junctions were filtered out.

4.2. Drainage network sensitivity to γ

Figs. 13–15 present simulated networks for three different γ values under steady-state runoff. Previous studies have examined the effect of γ on the network pattern (Rodriguez-Iturbe et al., 1992; Rodriguez Iturbe and Rinaldo, 1997), and here we review these results in order to facilitate the interpretation of non-steady runoff generated networks. There are a number of different metrics for evaluating channel-networks. Rinaldo et al. (1998) note that networks can be uniquely characterized by a set of scaling exponents of frequency distributions of drainage area and length; however, in this contribution

Please cite this article as: Sólyom P.B., Tucker G.E. The importance of the catchment area–length relationship in governing non-steady state hydrology, optimal junction angles and drainage network pattern. Geomorphology (2006), doi:10.1016/j.geomorph.2006.10.014

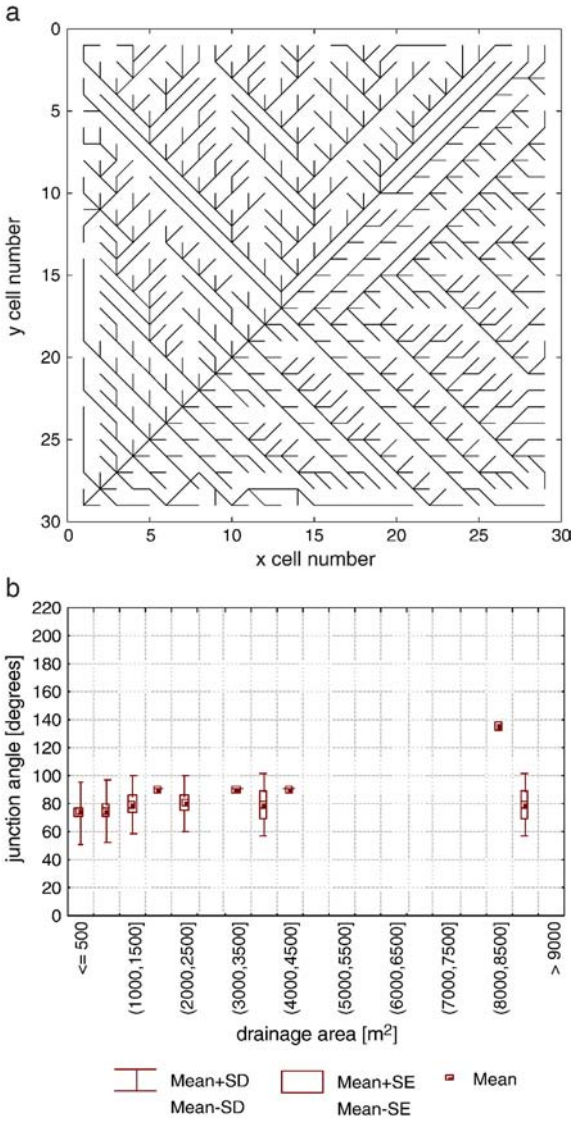

Fig. 13. a) Optimal drainage network, $\gamma = 0.95$, lateral inflow-dominated runoff conditions. Note the often parallel network segments and the low junction angles. b) Junction angle averages as a function of drainage area. The overall mean is 77.3°.

we focus simply on quantitative comparison of junction angles and bifurcation ratios and on qualitative evaluation because the visual appearance of networks is described by these indices most directly. The optimization process with γ close to unity yields explosion-like networks with nearly parallel flow path structure and low junction angles (Fig. 13a). For lower γ values the network becomes branching with high junction angles (Figs. 14a and 15a). The inverse relation between γ and junction angle is consistent with the single-link analysis. However both the network framework and the eight flow directions significantly affect the average of the optimal junction angles. Therefore apart from the general tendencies there is no linear correspondence between the optimal values obtained for individual junctions (Figs. 6–12) and for the junction angle average of the optimized networks (Figs. 13–15). Intuitively one can imagine that low γ encourages flow path junctions, because the low exponent reduces the significance of high runoff values in the total cost. When γ is high the system avoids channels with high runoff rates, hence junctions are rare, and a parallel flow path structure is characteristic. The bifurcation ratio for the networks can

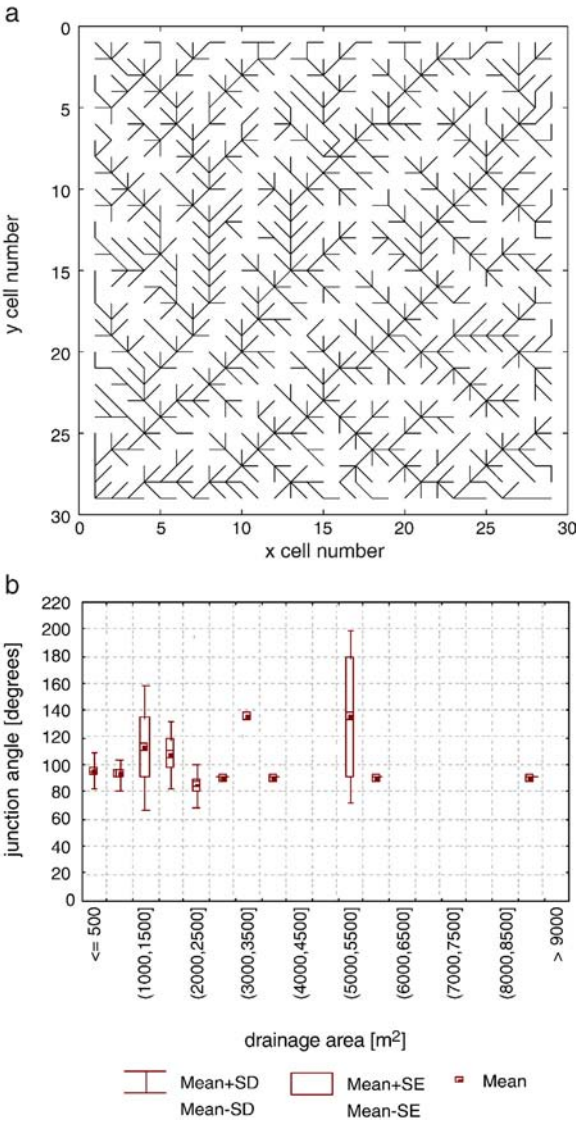

Fig. 14. a) Optimal drainage network, $\gamma = 0.5$, lateral inflow-dominated runoff conditions. Note the branching network and the often rectangular drainage junctions. b) Junction angle averages as a function of drainage area. The overall mean is 96.0°.

Please cite this article as: Sólyom P.B., Tucker G.E. The importance of the catchment area–length relationship in governing non-steady state hydrology, optimal junction angles and drainage network pattern. Geomorphology (2006), doi:10.1016/j.geomorph.2006.10.014

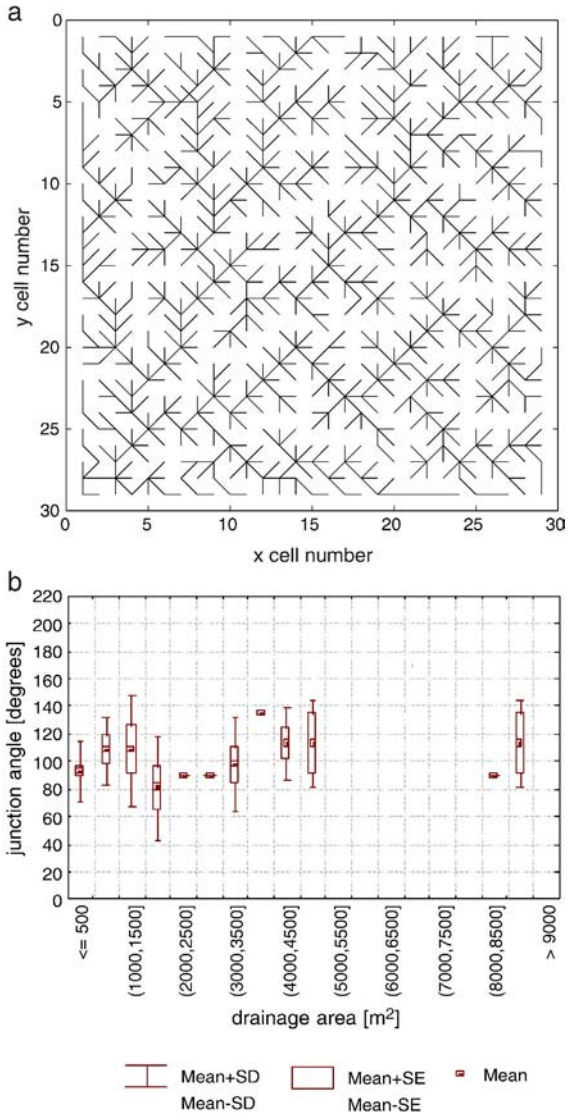

Fig. 15. a) Optimal drainage network, $\gamma = 0.1$, lateral inflow-dominated runoff conditions. Note the highly branching network and the high junction angles. b) Junction angle averages as a function of drainage area. The overall mean: is 97.3°.

be computed by applying an area threshold to filter out triple and higher order junctions. For second and higher order streams the bifurcations ratio is in the vicinity of unity for Fig. 13a, whereas it is close to two for Figs. 14a and 15a.

Figs. 13b–15b illustrate the junction angle characteristics of the above networks. Trunk networks were derived by setting an area threshold, and junction angles were measured on the basis of the three joining pixels. In the lattice framework, angles are limited to values such as 45°, 90°, 135° etc, but their average within a given drainage area range still proved to be characteristic for the given network. Total averages for the trunk networks were also computed. In accordance with the results obtained for individual junctions, junction angle is inversely correlated with γ. Low γ initiates a highly branching network with high typical junction angles, while high γ leads to networks that are less branching, with quasi-parallel streams and low typical junction angles.

4.3. Drainage network sensitivity to the source vs. lateral inflow ratio

Another question to answer is how network structure changes as a function of the source runoff or lateral inflow dominance. A way to test the observations discussed in Section 3.2 is to introduce a source discharge term even into the network optimization. Physically source terms can either represent at-a-point sources welling up as subsurface-return flow or saturation overland flow; or they can represent through flow entering the edge of the simulation field. In all of these scenarios drainage pattern initiation goes on under the constraint that runoff enrichment within the simulation field is small compared to the incoming runoff. In nature this latter case can be found e.g. at the bottom of steep undissected hillslopes with parallel flow path structure routing water onto a gentler surface where the actual drainage pattern initiation goes on, or at the bottom of escarpments where often spring sapping provides the base flow for drainage network initiation. The aim of this analysis is to test the effect of this extra starting discharge on network formation. Fig. 16 presents a simulated optimal network in which edge-pixels opposite to the outlet produce a significantly higher runoff than is produced within the simulation field itself. In order to get a clear impression about the effect, source flow over the edge length has been set to be 100 times higher than runoff enrichment within the simulation domain. γ is set to 0.5, so it corresponds to the lateral inflow dominated network in Fig. 14a. As in the single-junction analysis (Fig. 8), increased source-dominance leads to narrower junction angles (Fig. 16). The explanation used for the junction angle model can be recycled within the network framework. In the source dominated network the optimal junction angle is merely determined by the two source discharges and their sums. Within a given link discharge does not change noticeably, therefore an eventual backward shift of the junction position (the increase of the length of the main stream on the cost of the length of the tributaries) does not reduce tributary runoff rates. At the same time a backward shift of the junction position in a lateral inflow

Please cite this article as: Sólyom P.B., Tucker G.E. The importance of the catchment area–length relationship in governing non-steady state hydrology, optimal junction angles and drainage network pattern. Geomorphology (2006), doi:10.1016/j.geomorph.2006.10.014

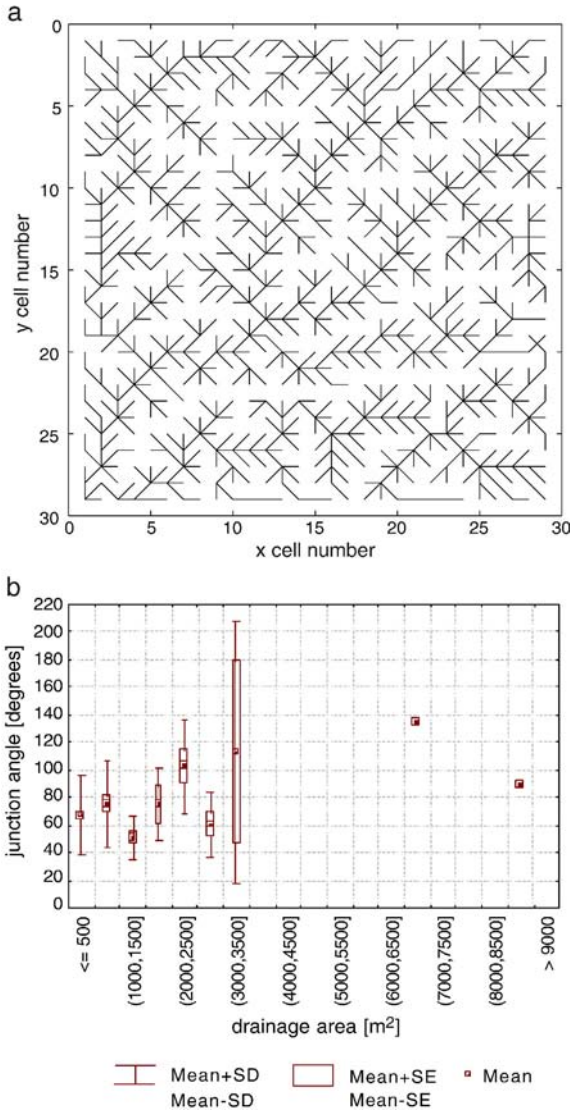

Fig. 16. a) Optimal drainage network, $\gamma = 0.5$, source flow-dominated runoff conditions. Note the parallel network segments, and the overall smaller junction angles than in corresponding Fig. 14a. b) Junction angle averages as a function of drainage area. The overall mean is 71.3°.

dominated network does change the discharge ratio between the tributaries and the main stream. For $\gamma < 1$ total cost is lowered through the backward shift of the junction, because the length of the high-cost tributaries is reduced. These networks therefore are highly branching and junction angles are high. For the same reason source flow dominated networks are less inclined to branch. The network in Fig. 16a is characterized by straight, unbranched channel segments, and low junction angles. However, the bifurcation ratio for the second and higher order streams (~2) does not differ significantly from that of Fig. 14a.

4.4. Source flow-dominated networks in nature

We would like to draw attention to two possible applications of the above numerical observations and thought experiments. First, source-term dominated stream networks should have a different pattern from lateral inflow-dominated networks, just as Figs. 14 and 16 have different appearances. At the same time, we realize that possible source-terms in nature (sources, returning shallow subsurface flow and overland flow from steeper slopes) are relatively low discharge flows even under wet climates, and that these networks might also be more significantly fed by lateral inflow than by source flow. Hence in nature the difference between the two networks might not be traceable because of the numerous further effects influencing drainage network pattern. Karst terrains might represent testable exceptions, given the often significant and permanent discharge of karst sources.

As for the second remark, the typical location of the source flow-dominated and of the lateral inflow-dominated runoff should be associated with certain types of landforms. Mountain fronts and valley slope bottoms are locations where source flow-dominated runoff is characteristic. Subsurface return flow and occasionally significant overland flow from the steep slopes at the hillslope–piedmont boundary and on a smaller scale at the hillslope–thalweg boundary shift runoff conditions towards source flow dominance on piedmonts and thalwegs. In contrast, within-range network formation can be considered to be rather lateral flow dominated, because the contributing area of the channel heads in the majority of the cases is limited to the hollow.

The more parallel optimal structure of source-dominated networks (Fig. 16) can be used in the interpretation of mountain front and footslope drainage network structure. Piedmonts and footslopes rarely develop a typical branching drainage pattern like dissected mountain ranges and plateaus do. Piedmonts are characterized by parallel and in many cases continuously laterally shifting streams. We hypothesize that the source term dominance of runoff conditions at these geomorphological locations plays an important part in developing and maintaining the parallel drainage structure.

4.5. Drainage network characteristics under non-steady state runoff conditions

Fig. 17a presents characteristics of a network optimized under non-steady state runoff conditions. We consider two aspects of this type of network: the systematically downstream increasing junction angles, and

Please cite this article as: Sólyom P.B., Tucker G.E. The importance of the catchment area–length relationship in governing non-steady state hydrology, optimal junction angles and drainage network pattern. Geomorphology (2006), doi:10.1016/j.geomorph.2006.10.014

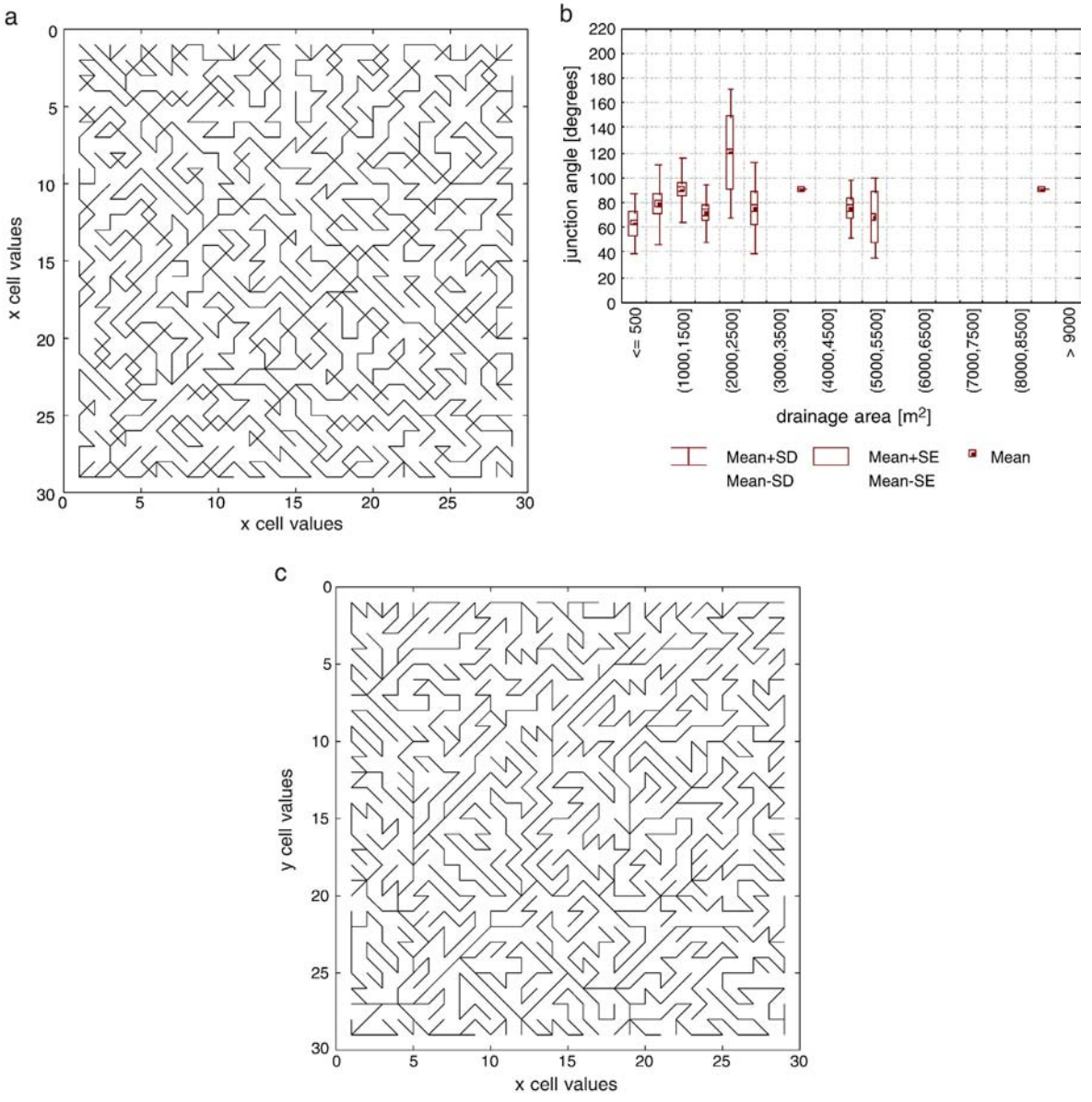

Fig. 17. a) Optimal drainage network simulated via non-steady state runoff, $\gamma = 0.95$, N_{SD0} is 1/3, lateral inflow-dominated runoff conditions. Note the downstream increasing junction angles and the winding first order streams. b) Junction angle averages as a function of drainage area. Junction angle tends to increase with increasing area below 2500 m^2, but it tends to decrease above 2500 m^2. The increasing tendency can be attributed to the effect of the flow path length sensitivity of non-steady runoff, whereas the decreasing tendency to the effect of the boundary conditions (one corner outflow). The overall mean is 80.5°. c) Optimal drainage network with the same model parameters as for a) (non-steady state runoff, $\gamma = 0.95$, N_{SD0} is 1/3, lateral inflow dominance), but without the possibility of crossing flow lines. Note the extremely long first order streams, as efficient means to minimize total cost due to h being 1 within these links.

the winding drainage pattern of the first order streams. The simulation demonstrates how optimal junction angles increase with increasing contributing area in the limited storm duration environment. $\gamma = 0.95$ was chosen because the difference in network pattern in the range of $0.5 < \gamma < 1$ is more pronounced than in the range of $0 < \gamma < 0.5$, but the same tendencies occur when the experiment is run with $\gamma = 0.5$, which corresponds to a common value occurring in nature (Tucker and Whipple, 2002, Table 1). Fig. 17 is the non-steady state version of Fig. 13. Runoff was computed using Eq. (19), and the characteristic storm duration number N_{SD0} is 1/3.

Please cite this article as: Sólyom P.B., Tucker G.E. The importance of the catchment area–length relationship in governing non-steady state hydrology, optimal junction angles and drainage network pattern. Geomorphology (2006), doi:10.1016/j.geomorph.2006.10.014

The effect of the flow path length dependent runoff calculation on the optimal network shape can be understood if we consider the relationship between drainage area and flow path length. Using the empirically based Hack's law, $L_f \sim A^h$ ($h=0.6$; Hack, 1957), the cost function (Eqs. (21) and (22)) can be rewritten for the limited storm duration case as

$$\Omega = \sum_i K A_i^{\gamma} \left(\frac{1}{1 + \frac{A_i^h}{U_f T_r}} \right)^{\gamma} L_i \tag{23}$$

and for the generalized non-steady state runoff conditions:

$$\Omega = \sum_i K A_i^{\gamma} A_i^{-h\gamma\varphi} L_i = \sum_i K A_i^{\gamma(1-h\varphi)} L_i \tag{24}$$

In Fig. 17, Eq. (21) has been used to compute total cost. As flow path length increases downstream in a channel, the cost C asymptotically goes from $C \sim A^{\gamma}$ to $C \sim A^{\gamma(1-h)}$. This is due to the fact that the storm duration number converges $1/L_f' \propto A^{-h}$ to with increasing flow path length. The effective γ, defined as $\gamma(1-h)$, decreases downstream. Because $h \sim 0.6$, the cost function exponent shrinks downstream, converging toward about 0.4 times its upstream value. As γ decreases, the optimal network structure shifts towards a more branching structure with high average junction angles. This effect can be traced in Fig. 17b: junction angles increase downstream for the lower drainage areas. Opposite to the outlet, where flow path length is low, the network is less branching (the contorted pattern is due to another effect, which we discuss below). Close to the outlet, where flow path length is high, junction angles are also higher, and the network is strongly branching. Obviously the one corner outflow structure forces to some extent convergence on the network and decreases junction angles for higher contribution areas, but compared to Fig. 13 where γ has a constant value, the difference is evident.

The other notable feature of Fig. 17a is the winding drainage pattern in the exterior links, in which channels form contorted loops. It is of particular importance that winding occurs in the exterior links, links connecting drainage sources with the first junctions. Within these links flow path length and contributing area are linearly proportional to one another. Note that we are on a raster basis, and that the network extends to all pixels of the simulation field. In the case of a network, where channel source is defined through a threshold, first order streams (exterior links) do not show necessarily linear area–length relationship, because catchments of first order streams in this case can have individual shapes, and therefore individual area–length relationships. In this paper no threshold to define first order streams was applied, therefore the importance of the shape of the contributing areas appears only for the second or higher order streams. In the first order streams the shape is linear, hence the area–length exponent is unity.

Because h is unity for the first order streams the effective γ drops below the value taken for the higher order streams. Effective γ can drop to zero or close to zero if the flow path length is long enough or φ is one, or it can even become negative if the area–length exponent h grows above unity (Sólyom and Tucker, 2004, Fig. 6). A system like this minimizes its total cost by linking all the points with one path (Stevens, 1974; Rodriguez-Iturbe et al., 1992). This structure increases the length over which h is unity and γ is around zero. The winding network pattern reflects this tendency. As soon as the first junction appears the area–length exponent drops below unity, the area dependence of the cost function becomes positive again, and a "normal" branching pattern develops. Fig. 17c presents an OCN where channel crossing was disabled. It is visible that first order streams in this figure also tend to be as long as possible producing similarly a contorted network pattern, but without crossings.

Although such winding patterns in natural first-order streams are physically impossible, certain consequences are to be kept in mind. In Section 3.4 it has been shown in connection with the effects of non-steady state runoff production on the individual junction angles that the negative flow path length dependence of runoff resulted in the instability and lateral shift of the junction position. We argue that a similar effect may operate on the network scale. Winding network segments are the manifestation of junction shifts within the OCN framework. In nature we expect them to appear as laterally shifting first order streams that do not settle down to a constant shape, because branching network structure represents a higher total cost level than the reorganizing pattern. The described OCN winding tells about the governing principles of the system.

Arid landscapes where this phenomenon is likely to be dominant show indeed geomorphic locations where lateral channel shift is the main erosional process. Footslopes on valley sides and gently sloping piedmont planes are subject to laterally shifting stream erosion (Bryan, 1922). Here we wish to offer the dependence of the flow path length sensitive runoff generation on the geometry of the first order streams (more just flow lines) as one of the causes hindering the development of a classical, branching drainage network at footslopes and piedmont planes. At the same time we realize that other

Please cite this article as: Sólyom P.B., Tucker G.E. The importance of the catchment area–length relationship in governing non-steady state hydrology, optimal junction angles and drainage network pattern. Geomorphology (2006), doi:10.1016/j.geomorph.2006.10.014

factors beside non-steady state runoff hydrology may also be partly if not dominantly responsible for the drainage particularities at these locations.

4.6. Summary

The sensitivity analysis of the network optimization has confirmed the already well-documented fact (Rodriguez-Iturbe et al., 1992; Rodriguez Iturbe and Rinaldo, 1997) that the exponent γ plays a major role in determining the network's character. With increasing γ the network shifts from strongly branching towards a parallel flow path structure.

A somewhat more novel observation is that the source vs. lateral inflow dominance of runoff also affects the optimal network. With increasingly source-derived runoff, the network becomes less branching and parallel segments begin to dominate. This observation is hypothesized as the origin of the parallel network structure of piedmont slopes and footslopes, where runoff production is more source-dominated than in the more lateral inflow-dominated within-range networks.

Furthermore, the particular winding of first order streams in the non-steady state network points in our interpretation to the lateral instability of streams in these environments. The area–length geometry of subcatchments has a special significance, because it alters the area exponent (effective γ) of the cost function. As long as the exponent h can be kept in the vicinity of one, the cost's sensitivity to the area is close to zero. This is obviously the most favorable constellation for a system tending to minimize the area dependent total cost.

5. Discussion

5.1. A real world example

A first test is whether predicted patterns qualitatively resemble observed patterns. We used a 30 m resolution USGS NED DEM from the Colorado High Plains to identify drainage patterns and to measure junction angles. This area was chosen because the High Plains has a semi-arid climate with roughly 500 mm precipitation a year, the bulk of which falls during the summer months in the form of convective thunderstorms. This climatology makes the Colorado High Plains a good location to test hypotheses about drainage network formation under non-steady state runoff. The aim is to investigate the relative importance of two effects: (1) increased source-dominance downstream, which should tend to decrease junction angles, and (2) downstream-decreasing peak discharge per unit area, which should tend to increase junction angles. The results (Fig. 18) show a tendency for the second of the two effects to dominate. In smaller basins (lower A), junction angles on average increase with drainage area. For the junctions with the highest drainage areas, angles drop back to 90°, which probably reflects the tendency for junction angles to decrease with increasing tributary discharge asymmetry (Howard, 1990).

It is worth examining the rate of change of junction angles as a result of a shift in the source vs. lateral inflow ratio and in peak discharge per unit area, respectively. The shift of the runoff conditions from the lateral inflow dominance to source dominance for $\gamma=0.95$ induces a junction angle shift in the range of 97°–45° (Fig. 8), for $\gamma=0.5$ in the range of 106°–90°, and for $\gamma=0.1$ in the range of 120°–112°. The shift of runoff conditions towards the non-steady state for $\gamma=0.5$ shifts the junction angle from 100° to 120° when runoff is lateral inflow dominated, and from 90° to 180° when runoff source flow-dominated.

A γ value of around 0.5 is a reasonable assumption for many morphoclimatic environments, because z in Eq. (16) for natural rivers is found to be commonly in the range of 0.4–0.6, though values ranging from 0.3 to greater than 1 have been found for individual basins (Tucker and Whipple, 2002). Furthermore, the derivation of Rodriguez-Iturbe et al. (1992) predicts that the

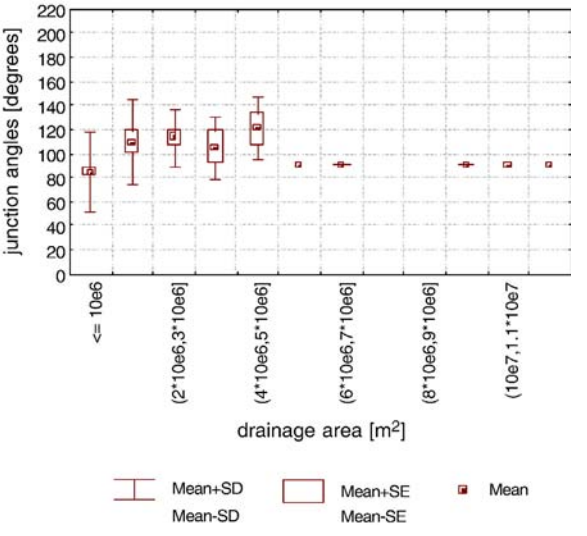

Fig. 18. Junction angles measured from a DEM of the Colorado High Plains. Junction angles increase with increasing drainage area, possibly as an outcome of prevailing non-steady state runoff conditions. Compare with the tendency of Fig. 17b. The overall mean is 91.5°.

Please cite this article as: Sólyom P.B., Tucker G.E. The importance of the catchment area–length relationship in governing non-steady state hydrology, optimal junction angles and drainage network pattern. Geomorphology (2006), doi:10.1016/j.geomorph.2006.10.014

rate of energy expenditure in river networks scales with drainage area with the exponent 0.5.

Comparing the rate of change of the optimal junction angles for $\gamma = 0.5$, we can conclude that the shift towards the non-steady runoff conditions triggers a stronger modification of the optimal junction angles than the shift towards source flow-dominance. This is especially true considering that runoff becomes more source flow-dominated going downstream, and that junction angle sensitivity to non-steady peak discharge increases with source dominance. We propose this as an explanation for the fact that DEM junction data support the second of the two hypotheses.

Another explanation relates to a possible scale difference between the two effects, with the source-versus-lateral effect manifesting on smaller scales, and with the non-steadiness manifesting on a bigger scale. Given the high uncertainty level in judging the exact scales associated with these processes we simply suggest that lateral-inflow dominance characterizes low-order streams, whereas for non-steady state runoff to develop fully, especially with the consideration of storm size effects, higher order streams are necessary. This contention is supported by data from Walnut Gulch (Goodrich et al., 1997), which shows that a strongly nonlinear Q_p–A relation takes hold only above a minimum basin size. Nonlinear Q_p–A scaling is also known to extend over very large basin scales. For example, plotting yearly peak discharge values of Kentucky basins against drainage area, a non-linear relationship appears with a scaling exponent of 0.62 (Sólyom and Tucker, 2004, Fig. 2). O'Connor and Costa (2004) illustrate, based on a database from nearly 15,000 stream-gaging stations, a similar relationship between peak flow and basin area, with scaling exponents between 0.5 and 0.6. In their analysis, these relationships apply over four orders of magnitude (1 to 10,000 mi^2) showing that non-steady state runoff dominates at large scales.

5.2. Advectivity vs. diffusivity

Continuity of mass for an alluvial stream is commonly written as an advection-diffusion equation.

$$-\frac{\partial z}{\partial t} = \frac{\partial q_s}{\partial x} = \frac{K_f \partial (A^m S^n)}{\partial x} = K_f m A^{m-1} S^{n-1} \frac{\partial A}{\partial x}\frac{\partial z}{\partial x} + K_f n S^{n-1} A^m \frac{\partial^2 z}{\partial x^2} \qquad (25)$$

where z is elevation above a given base level, t is time, q_s is volumetric sediment flux through unit contour length, x is distance in the steepest descent direction, K_f is erodibility constant for wash processes, A is drainage area as a proxy for discharge, S is slope, and m and n are positive constants (Kirkby, 1986; Willgoose et al., 1991a,b). The two terms on the right-hand side of Eq. (25) represent mass advection and diffusion, respectively. The ratio of the coefficients of these two terms (the celerity coefficient and the diffusivity coefficient), called the advectivity ratio, R_A (Willgoose, 1989), is

$$R_A = \frac{m A^{m-1} S^{n-1} \frac{\partial A}{\partial x}}{n S^{n-1} A^m} = \frac{m}{n} A^{-1} \frac{\partial A}{\partial x}, \qquad (26)$$

Willgoose (1989) and Willgoose et al. (1991a) showed that this ratio characterises the behaviour of transport limited erosional systems. The ratio explains the degree of slope decline versus slope retreat (Willgoose, 1989), and also the way in which the system propagates information: whether perturbations spread with a wave-like character, or whether they dissipate with a diffusive character (Whipple and Tucker, 1999; Tucker and Whipple, 2002). Substituting the area-length relation $A = K_h x^h$ into Eq. (26), $R_A = m/nhx^{-1}$. Thus, in a typical drainage network, the advectivity decreases systematically downstream.

There is an important link with basin hydrology here. Consider that $\partial A/\partial x$ corresponds to lateral inflow, and A corresponds to source flow. Thus, the ratio between the source flow and lateral inflow is identical to the advectivity ratio of Eq. (26). An important point emerges from this identity. The advectivity ratio not only determines information propagation through the channel network, but it also seems to exert an effect on the channel network pattern as a whole, as demonstrated in Section 3.3. Going downstream in the channel the advectivity ratio decreases, and runoff character becomes more diffusive (i.e., more source-dominated). This happens because instream flow (Q) overcomes lateral inflow ($\partial Q/\partial L$) as discharge increases from the headwaters towards the outlet. Hence downstream-increasing diffusivity of runoff exerts an effect on the junction angles and on the network structure as a whole.

6. Conclusions

Non-steady state hydrology is likely to dominate most basins in semi-arid to arid environments of the planet, but only the larger basins in more humid areas. Dry morphoclimatic environments show a characteristic landform patterns that may result in part from this difference. In this paper we identified characteristics of non-steady state runoff production, its effects on

Please cite this article as: Sólyom P.B., Tucker G.E. The importance of the catchment area–length relationship in governing non-steady state hydrology, optimal junction angles and drainage network pattern. Geomorphology (2006), doi:10.1016/j.geomorph.2006.10.014

drainage network structure, and tried to link these to the typical landforms and patterns of these climatic environments.

The two focus points of the paper are an explanation for the downstream-increasing characteristic junction angles of the Colorado High Plains, and the identification of links between non-steady hydrology and the planation of laterally unstable piedmont streams. The non-linear relationship between drainage area and peak discharge consequently affects the stream power distribution within the network. Stream power per unit channel length was used to conduct optimization runs both on the level of individual junctions and on the level of the whole network. The non-linear dependence of peak discharge on the drainage area modifies the area exponent that is key to the optimization. In the light of the systematic downstream decrease of the area exponent we interpreted the downstream increasing junction angles of the High Plains drainage networks as a manifestation of network optimization.

Under non-steady state hydrology, the area–length relationship of individual subcatchments influences the optimal network pattern. The optimization model implies that a downstream lateral shift of junction positions will tend to occur, both on the level of the individual junctions and of the entire network. The system tends towards maximum possible flow path length because peak discharge per unit area is inversely related to flow path length. In this case, the area–length exponent h approaches unity and the generalized non-steady state flow path length exponent φ is unity as well; then the area exponent goes to zero and the area dependence of the cost function disappears. This unique opportunity to minimize total cost is exploited by the system by maximizing the length of those links in which h is unity. In our interpretation this phenomenon can play a role in semi-arid climates in the initiation of the characteristic piedmont planation surfaces that are characterized by laterally shifting channels and the absence of a well-developed drainage network. Although the characteristics of these surfaces perfectly fit the findings of our numerical runs, we acknowledge that other factors are likely to contribute to creating these characteristics of dryland piedmont surfaces.

In this paper we have not emphasized the difference between the limited storm duration induced and the limited storm size induced runoff production, but it too may have a morphologic impact. Further research can decode specifically the effect of the discontinuous flow path length dependence-characteristics of the limited storm size environment—on drainage network development and landscape evolution. Similarly more work has to be done in general on the validation of the theoretical results of the paper.

References

Abrahams, A.D., 1984. Channel network: a geomorphological perspective. Water Resources Research 20, 161–188.

Ahnert, F., 1976. Brief description of a comprehensive three-dimensional process-response model of landform development. Zeitschrift für Geomorphologie 25, 29–49.

Ahnert, F., 1987. Process-response models of denudation at different spatial scales. Catena. Supplement 10, 31–50.

Bagnold, R.A., 1957. The flow of cohesionless grains in fluids. Philosophical Transactions of the Royal Society of London, Series A: Mathematical and Physical Sciences 249, 49–63.

Bagnold, R.A., 1966. An approach to the sediment transport problem from general physics. U.S. Geological Survey Professional Paper 422-I, 1–137.

Baker, V.R., 1977. Stream-channel response to floods, with examples from central Texas. Geological Society of America Bulletin 88, 1057–1071.

Banavar, J.R., Colaiori, F., Flammini, A., Giacometti, A., Maritan, A., Rinaldo, A., 1997. Sculpting of a fractal river basin. Physical Review Letters 78, 4522–4525.

Banavar, J.R., Colaiori, F., Flammini, A., Maritan, A., Rinaldo, A., 2001. Scaling, optimality, and landscape evolution. Journal of Statistical Physics 104, 1–48.

Bras, R.L., 1990. Hydrology: An Introduction to Hydrologic Science. Addison-Wesley, Reading, Mass.

Bryan, K., 1922. Erosion and sedimentation in the Pagogo Country, Arizona. US Geological Survey Bulletin 730B, 19–90.

Bull, W.B., 1979. The threshold of critical power in streams. Geological Society of America Bulletin 90, 453–464.

Coppus, R., Imeson, A.C., 2002. Linking sediment delivery from hillslope to catchment scale. Earth Surface Processes and Landforms 27, 1365–1375.

Dick, G.S., Anderson, R.S., Sampson, D.E., 1997. Controls on flash flood magnitude and hydrograph shape, upper Blue Hills badlands, Utah. Geology 25, 45–48.

Dietrich, W.E., Wilson, C.J., Montgomery, D.R., McKean, J., 1993. Analysis of erosion thresholds, channel networks, and landscape morphology using a digital terrain model. Journal of Geology 101, 259–278.

Eaton, S.L., Morgan, B.A., Kochel, R.C., Howard, A.D., 2003. Role of debris flows in long-term landscape denudation in the Central Appalachians of Virginia. Geology 31, 339–342.

Finlayson, D.P., Montgomery, D.R., 2003. Modeling large-scale fluvial erosion in geographic information systems. Geomorphology 53, 147–164.

Goodrich, D.C., Lane, L.J., Shillito, R.M., Miller, M.N., Syed, K.H., Woolhiser, D.A., 1997. Linearity of basin response as a function of scale in a semiarid watershed. Water Resources Research 33, 2951–2965.

Gupta, V.K., Castro, S.L., Over, T.M., 1996. On scaling exponents of spatial peak flows from rainfall and river network geometry. Journal of Hydrology 187, 81–104.

Hack, J.T., 1957. Studies of longitudinal stream profiles in Virginia and Maryland. U.S. Geological Survey Professional Paper 294-B, 1–97.

Horton, R.E., 1932. Drainage basin characteristics. Transactions American Geophysical Union 13, 348–352.

Please cite this article as: Sólyom P.B., Tucker G.E. The importance of the catchment area–length relationship in governing non-steady state hydrology, optimal junction angles and drainage network pattern. Geomorphology (2006), doi:10.1016/j.geomorph.2006.10.014

Horton, R.E., 1945. Erosional development of streams and their drainage basins; hydrophysical approach to quantitative morphology. Geological Society of America Bulletin 56, 275–370.

Howard, A.D., 1971a. Optimal angles of stream junction: geometric stability to capture, and minimum power criteria. Water Resources Research 7, 863–873.

Howard, A.D., 1971b. Simulation model of stream capture. Geological Society of America Bulletin 82, 1355–1376.

Howard, A.D., 1990. Theoretical model of optimal drainage networks. Water Resources Research 24, 713–722.

Howard, A.D., 1994a. Badlands. In: Abrahams, A.D., Parsons, A.J. (Eds.), Geomorphology of Desert Environments. Chapman and Hall, London, pp. 213–242.

Howard, A.D., 1994b. A detachment-limited model of drainage basin evolution. Water Resources Research 30, 2261–2285.

Howard, A.D., 1997. Badland morphology and evolution: interpretation using a simulation model. Earth Surface Processes and Landforms 22, 211–227.

Huang, H.Q., Willgoose, G.R., 1992. Numerical Analysis of Relations between Basin Hydrology, Geomorphology and Scale. Research Report No. 075.04.1992. Department of Civil Engineering and Surveying, The University of Newcastle, New South Wales, Australia.

Huang, H.Q., Willgoose, G.R., 1993. Flood frequency relationships dependent on catchment area: an investigation of casual relationships. Engineering for Water Resources Conference, Newcastle, Australia.

Ibbitt, R.P., Willgoose, G.R., Duncan, M.J., 1999. Channel network simulation models compared with data from the Ashley River, New Zealand. Water Resources Research 35, 3875–3890.

Ijjasz-Vasquez, E.J., Rodriguez-Iturbe, I., Bras, R.L., 1992. On the multifractal characterization of river basins. Proceedings of the 23rd Binghampton Geomorphology Conference, pp. 24–27.

Kirkby, M.J., 1971. Hillslope process-response models based on the continuity equation. In: Brunsden, D. (Ed.), Slopes: Form and Process. . Institute of British Geographers Special Publication, vol. 3. Institute of British Geographers, London, pp. 15–30.

Kirkby, M.J., 1986. A two-dimensional simulation model for slope and stream evolution. In: Abrahams, A.D. (Ed.), Hillslope Processes. Allen & Unwin, Winchester, Mass, pp. 203–222.

Kirkby, M.J., 1993. Long term interactions between networks and hillslopes. In: Beven, K., Kirkby, M.J. (Eds.), Channel Network Hydrology. John Wiley and Sons, New York, pp. 255–293.

Langbein, W.B., Schumm, S.A., 1958. Yield of sediment in relation to mean annual precipitation. Transactions American Geophysical Union 39, 1076–1084.

Leopold, L., Maddock, T., 1953. The hydraulic geometry of stream channels and some physiographic implications. U.S. Geological Survey Professional Paper 252, 1–57.

Lubowe, J.K., 1964. Stream junction angles in the dendritic drainage pattern. American Journal of Science 262, 325–339.

Montgomery, D.R., Dietrich, W.E., 1992. Channel initiation and the problem of landscape scale. Science 255, 826–830.

O'Connor, J., Costa, J.E., 2004. Spatial distribution of the largest rainfall-runoff floods from basins between 2.6 and 26,000 km2 in the US and Puerto Rico. Water Resources Research 40, 1–11.

Ogden, F.L., Julien, P.Y., 1994. Runoff model sensitivity to radar rainfall resolution. Journal of Hydrology 158, 1–18.

Ogden, F.L., Sharif, H.O., Senarath, S.U.S., Smith, J.A., Baeck, M.L., Richardson, J.R., 2000. Hydrologic analysis of the Fort Collins, Colorado, flash flood of 1997. Journal of Hydrology 228, 82–100.

Rigon, R., Rodriguez-Iturbe, I., Giacometti, A., Maritan, A., Tarboton, D., Rinaldo, A., 1996. On Hack's law. Water Resources Research 32, 3367–3374.

Rinaldo, A., Rodriguez-Iturbe, I., Rigon, R., 1998. Channel networks. Annual Review of Earth and Planetary Sciences 26, 289–327.

Rodriguez Iturbe, I., Rinaldo, A., 1997. Fractal River Basins; Chance and Self-Organization. Cambridge University Press, Cambridge.

Rodriguez-Iturbe, I., Rinaldo, A., Rigon, R., Bras, R.L., Marani, A., Ijjasz-Vasquez, E., 1992. Energy dissipation, runoff production and the three-dimensional structure of river basins. Water Resources Research 28, 1095–1103.

Roy, A.G., 1983. Optimal angular geometry models for river branching. Geographical Annales 15, 87–96.

Roy, A.G., 1984. Optimal models of river branching angles. In: Woldenberg, M.A. (Ed.), Models in Geomorphology. George Allen and Unwin, Boston, Mass, pp. 269–285.

Seidl, M.A., Dietrich, W.E., 1992. The problem of channel erosion into bedrock. Catena. Supplement 23, 101–124.

Shreve, R.L., 1966. Statistical law of stream numbers. Journal of Geology 74, 17–37.

Shreve, R.L., 1969. Stream length and basin areas in topologically random channel networks. Journal of Geology 77, 397–414.

Smart, J.S., 1968. Statistical properties of stream length. Water Resources Research 4, 1001–1014.

Smart, J.S., 1978. The analysis of drainage basin composition. Earth Surface Processes and Landforms 3, 129–179.

Smart, J.S., Werner, C., 1976. Applications of the random model of drainage basin composition. Earth Surface Processes and Landforms 1, 219–233.

Sólyom, P.B., Tucker, G.E., 2004. The effect of limited storm duration on landscape evolution, drainage basin geometry and hydrograph shapes. Journal of Geophysical Research 109, F03012.

Stevens, P.S., 1974. Patterns in Nature. Little, Brown and Co., Boston.

Strahler, A.N., 1964. Quantitative geomorphology of drainage basins and channel networks. In: Chow, V.T. (Ed.), Handbook of Applied Hydrology. McGraw-Hill, New York, pp. 439–476.

Tucker, G.E., 2004. Drainage basin sensitivity to tectonic and climatic forcing: implications of a stochastic model for the role of entrainment and erosion thresholds. Eart Surface Processes and Landforms 29, 185–205.

Tucker, G.E., Bras, R.L., 1998. Hillslope processes, drainage density, and landscape morphology. Water Resources Research 34, 2751–2764.

Tucker, G.E., Bras, R.L., 2000. A stochastic approach to modeling the role of rainfall variability in drainage basin evolution. Water Resources Research 36, 1953–1964.

Tucker, G.E., Slingerland, R.L., 1997. Drainage basin response to climate change. Water Resources Research 33, 2031–2047.

Tucker, G.E., Whipple, K.X., 2002. Topographic outcomes predicted by stream erosion models: sensitivity analysis and intermodel comparison. Journal of Geophysical Research B-107, 1–16.

Whipple, K.X., Tucker, G.E., 1999. Dynamics of the stream power river incision model: implications for height limits of mountain ranges, landscape response timescales and research needs. Journal of Geophysical Research 104, 17,661–17,674.

Willgoose G.R., 1989, A Physically Based Channel Network and Catchment Evolution Model. PhD Thesis, Ralph M. Parsons Lab. Dep. of Civil Engineering. Mass. Inst. of Technol., Cambridge.

Willgoose, G.R., Bras, R.L., Rodriguez-Iturbe, I., 1991a. Results from a new model of river basin evolution. Earth Surface Processes and Landforms 16, 237–254.

Please cite this article as: Sólyom P.B., Tucker G.E. The importance of the catchment area–length relationship in governing non-steady state hydrology, optimal junction angles and drainage network pattern. Geomorphology (2006), doi:10.1016/j.geomorph.2006.10.014

Willgoose, G.R., Bras, R.L., Rodriguez-Iturbe, I., 1991b. The relationship between catchment and hillslope properties: implications of a catchment evolution model. Geomorphology 5, 21–38.

Woldenberg, M.J., Horsfield, K., 1983. Finding the optimal lengths for three branches at a junction. Journal of Theoretical Biology 104, 301–318.

Woldenberg, M.J., Horsfield, K., 1986. Relation of branching angles to optimality for four cost principles. Journal of Theoretical Biology 122, 187–204.

Wolman, M.G., Gerson, R., 1978. Relative scales of time and effectiveness in watershed geomorphology. Earth Surface Processes 3, 189–208.

Wolman, M.G., Miller, J.P., 1960. Magnitude and frequency of forces in geomorphic processes. Journal of Geology 68, 54–74.

Please cite this article as: Sólyom P.B., Tucker G.E. The importance of the catchment area–length relationship in governing non-steady state hydrology, optimal junction angles and drainage network pattern. Geomorphology (2006), doi:10.1016/j.geomorph.2006.10.014

Appendix C

Reprint: Statistical treatment of fluvial dose distributions from southern Colorado arroyo deposits

Reference: Arnold, L.J., Bailey, R.M., and Tucker, G.E. (2007) Statistical treatment of fluvial dose distributions from southern Colorado arroyo deposits: *Quaternary Geochronology*, v. 2, p. 162-167.

Available online at www.sciencedirect.com
ScienceDirect
Quaternary Geochronology 2 (2007) 162–167
QUATERNARY GEOCHRONOLOGY
www.elsevier.com/locate/quageo

Research paper

Statistical treatment of fluvial dose distributions from southern Colorado arroyo deposits

L.J. Arnold[a,b,*], R.M. Bailey[c], G.E. Tucker[d]

[a]*Oxford University Centre for the Environment, Oxford, UK*
[b]*School of Earth and Environmental Sciences, University of Wollongong, Wollongong, NSW 2522, Australia*
[c]*Department of Geography, Royal Holloway College, University of London, Surrey, UK*
[d]*CIRES, Department of Geological Sciences, University of Colorado, Boulder, CO, USA*

Received 12 October 2005; accepted 1 May 2006
Available online 16 June 2006

Abstract

Many of the small-scale arroyo systems found across southern Colorado contain well-preserved sedimentary records of prehistoric fluvial erosion and aggradation epicycles. In the following paper, we date a set of 50 ephemeral fluvial samples from four southern Colorado arroyo systems using a combination of single-grain and single-aliquot OSL techniques. Analysis of the sample D_e distribution characteristics reveals that these arroyo sediments were subjected to a diverse array of bleaching conditions prior to deposition. The use of appropriate burial dose estimation procedures is therefore deemed vital to ensuring that accurate age estimates are produced for each of these samples. In this study we apply the formal 'age model' decision procedures of Bailey and Arnold [Statistical modelling of single-grain quartz D_e distributions and an assessment of procedures for estimating burial dose. Quaternary Science Reviews, in press.] and Arnold [2006. Optical dating and computer modelling of arroyo epicycles in the American Southwest. D.phil. Thesis, University of Oxford, unpublished] to our fluvial sample dataset in order to enable a more objective selection of appropriate burial dose estimates. The resultant OSL chronostratigraphies are examined and discussed. These formal decision procedures yield sample ages that are stratigraphically consistent for 94% of the 50 fluvial samples examined. The resulting OSL ages also display a greater degree of stratigraphic consistency in comparison to those ages that would have been generated by simply applying a single type of age model to all samples.

Keywords: OSL dating; Single grain; Age model; Arroyo

1. Introduction

The potential for heterogeneous bleaching is of foremost concern in any optical dating study of fluvial sediments. For optical dating to be suitable in a fluvial context we not only need suitable statistical procedures that can identify heterogeneously bleached samples, but also methods that can provide accurate estimates of true burial doses from these identified partially bleached samples. Several schemes have been published to address the problem of deriving the most accurate burial dose estimates from heterogeneously bleached D_e distributions. Notable among these are the approaches of Olley et al. (1998), who advocated taking the mean of the lowest x% of measured D_e values (where x was calibrated and found to equal 5 for their sediments); the 'leading edge' approach of Lepper et al. (2000); and the minimum-age model of Galbraith et al. (1999), in which the distribution of D_e values is approximated by a truncated log-normal distribution, with the truncation point giving the best estimate of the true burial dose.

Each of these statistical methods can potentially yield significantly different burial dose estimates for a given D_e distribution. Thus the question remains as to which of these approaches is/are the most suitable for routine use with heterogeneously bleached samples? Furthermore, on what basis do we decide to use these more complex types of burial dose estimation procedures instead of simpler

*Corresponding author.
E-mail address: lee.arnold@ouce.ox.ac.uk (L.J. Arnold).

1871-1014/$ - see front matter © 2006 Elsevier Ltd. All rights reserved.
doi:10.1016/j.quageo.2006.05.003

measures of central tendency? In the following study we use formal decision procedures to inform the selection of appropriate burial dose estimates on a sample-by-sample basis. This approach provides a transparent and systematic basis for choosing between the results of the different 'age model' techniques, and in doing so provides more defensible final OSL age estimates. The decision procedures employed in this study have been derived independently using empirical and modelled ephemeral fluvial D_e datasets (following Bailey and Arnold, in press; Arnold, 2006). The main aim of this research is thus to apply these previously generated age model selection procedures to a set of unrelated fluvial samples that lack independent age control and to examine the resultant OSL chronostratigraphies obtained.

The samples being dated in this study are taken from four separate arroyo systems located across Fort Carson Military Reservation and Pinon Canyon Maneuver Site, southeastern Colorado. A total of 50 samples were collected from various palaeochannel infill deposits and intervening alluvial units exposed along sidewalls of the present-day channels (Table S1). These former channel and overbank flood deposits accumulated during previous arroyo cut-fill epicycles and represent an important record of Late Quaternary fluvial dynamics in this region.

2. The age model decision procedures

2.1. The single-grain decision procedure

Bailey and Arnold (in press) have recently formulated an age model decision procedure using experiments undertaken on simulated single-grain D_e populations with known pre-burial, burial and post-burial doses. This decision procedure employs a range of measurable descriptive statistics to characterise single-grain D_e distributions. These statistical criteria are then used to inform the selection of an appropriate age model for burial dose estimation (i.e. choose between the 3-parameter minimum-age model (MAM-3); the 4-parameter minimum-age model (MAM-4); the central-age model (CAM); and the lowest 5% age model (L-5%)). The proposed decision procedure is summarised in Fig. S1. For further details the reader is referred to Bailey and Arnold (in press). In the following research, this theoretically derived decision procedure is used to obtain single-grain burial dose estimates for the Colorado arroyo samples.

2.2. The single-aliquot decision procedure

The single-aliquot burial dose estimates are determined using the age model decision procedure proposed by Arnold (2006). This decision procedure was formulated empirically using 41 independently dated OSL samples (34 samples with ^{14}C age control and 7 modern-age analogue samples) from two similar Southwestern arroyo systems (Cuyama River and Murray Springs-Curry Draw) (Fig. S2). This single-aliquot decision process is similar in principle to the single-grain procedure of Bailey and Arnold (in press) in that it uses broadly similar descriptive statistics (though different criteria) to inform age model selection. Only two age models (i.e. the CAM and MAM-3) are considered in this single-aliquot decision process because, between them, these statistical procedures provided the most accurate optical age estimates for all of the known-age samples tested.

3. Optical dating protocols

Refinement of pure coarse-grained quartz separates (typically 90–125, 125–180, or 180–250 μm fractions; Table S1) was achieved using the standard laboratory preparation procedures outlined by Aitken (1998). Individual D_e estimates were measured using small aliquots (100–300 grains/disc) for all 50 of the Colorado arroyo samples. Due to machine and time constraints replicate single-grain D_e measurements were only made on a small (randomly selected) subset of 14 of these 50 samples. All D_e measurements were made using Risø TL-DA-15 readers. The OSL signals were detected using a blue-sensitive EMI9235QA photomultiplier tube fitted with two 3 mm thick U-340 filters.

Single-grain and single-aliquot D_e estimates were both calculated using the SAR protocol (Murray and Wintle, 2000) shown schematically in Fig. S3. Single-aliquot D_e estimates were accepted for further analysis if they displayed (i) recycling ratios within 10% of unity, (ii) OSL-IR depletion ratios (Duller, 2003) >0.9, (iii) thermal transfer $<5\%$ of the natural signal. Single-grain D_e's were only accepted where (i) the recycling ratio L_x/T_x points were consistent with each other within their 1σ errors, (ii) OSL-IR depletion ratios (Duller, 2003) were >0.9, (iii) thermal transfer was $<10\%$ of the natural signal, (iv) the error on the natural test dose signal was $<20\%$, (v) calculated D_e uncertainty was $<30\%$, (vi) the natural signal intensity was $>3\sigma$ of the late-light background signal. Any accepted grains or aliquots whose D_e values represented statistical outliers (taken as >3 standard deviations from the mean D_e value) were also eliminated from further analysis. Together these prior selection criteria typically lead to the rejection of $<10\%$ of the total measured single-aliquots and $>95\%$ of the measured single grains (compare n and n_1 in Tables S2–S3). Individual D_e errors are comprised of three uncertainty terms: (i) Random uncertainty arising from photon counting statistics. (ii) A growth curve fitting error. (iii) A systematic uncertainty of 1.5% per paired single-aliquot L_x/T_x measurement (cf. Armitage, 2003) and 3.5% per paired single-grain L_x/T_x measurement (cf. Thomsen et al., 2005).

Environmental dose rates (Table S1) were calculated using a combination of field gamma spectrometry (FGS), inductively coupled plasma mass spectrometry (ICP-MS) and neutron activation analysis (NAA). Where possible,

external γ-dose rates were calculated using FGS for those samples taken from inhomogeneous sedimentary units or from locations within 30 cm of a stratigraphic boundary. In all other cases, external γ-dose rates were calculated using the laboratory-based evaluation techniques of NAA or ICP-MS. External β-dose rate contributions were calculated using either ICP-MS or NAA measurements for all samples. Cosmic ray dose rate contributions were determined using the methods of Prescott and Hutton (1994).

4. Analysis of dose distributions

4.1. D_e distribution characteristics

The single-aliquot and single-grain D_e distributions obtained for these fluvial samples vary markedly in type and form (Fig. 1). The observed dose distributions may be broadly categorised into three characteristic groups:

Type 1: 36% of the single-aliquot D_e distributions and 43% of the single-grain D_e distributions exhibit 'characteristic' heterogeneously bleached forms (e.g. Fig. 1i). These samples typically have large overdispersion values (generally $>30\%$ for single-grain distributions and $>20\%$ for single-aliquot distributions) and display clear asymmetry with a statistically significant positive skewness.

Type 2: 10% of the single-aliquot D_e distributions and 7% of the single-grain D_e distributions display relatively little scatter and a limited range of individual D_e values (e.g. 17–25 Gy in Fig. 1ii). This small group of adequately bleached samples is characterised by lower overall overdispersion values (typically $<15\%$) and dose distributions that are either symmetric or only slightly (though not statistically significantly) positively skewed.

Type 3: The remainder of the fluvial samples represent an intermediary group of D_e distributions that encompass a broad range of dose values (e.g. 14–40 Gy in Fig. 1iii), but which display only slight, if any, asymmetry (i.e. not statistically significant). It is likely that other sources of D_e scatter besides/as well as heterogeneous bleaching (e.g. post-depositional mixing or variations in beta microdosimetry) are important in these types of samples.

There does not appear to be any obvious site-specific bias in these dose distribution patterns (cf. Tables S2 and S3). Furthermore, individual samples do not necessarily display the same types of dose distribution at both the single-grain and single-aliquot scales of analysis; only 6 of the 14 single-grain samples exhibit the same D_e distribution types as their single-aliquot counterparts. The variety and complexity of these D_e distributions indicates that the Colorado arroyo samples have been subjected to a diverse array of bleaching conditions and post-depositional processes. Appropriate characterisation of D_e dispersion by selection of the most suitable age model procedure is therefore deemed vital to ensuring that accurate age estimates are produced.

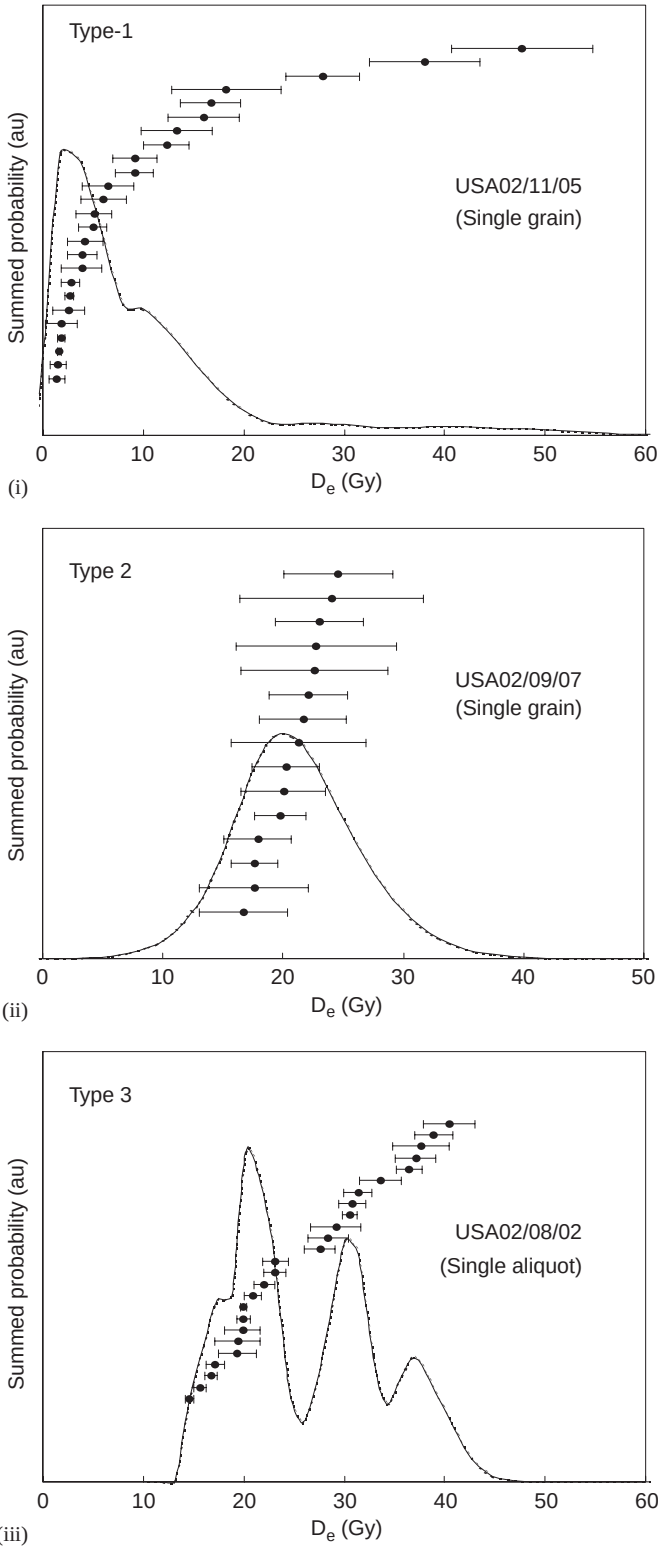

Fig. 1. A selection of single-aliquot and single-grain D_e distributions showing the different types of fluvial dose distributions observed in the Colorado arroyo samples.

4.2. Application of age model decision procedures

Tables S2 and S3 show the range of OSL ages that can be derived by applying the different age models considered in

the single-aliquot and single-grain decision procedures. These two tables also summarise the descriptive statistics used to inform the age model decision procedures of Bailey and Arnold (in press) and Arnold (2006). For each sample, the suggested age model selections of the single-aliquot and single-grain decision procedures are highlighted in bold.

These suggested age models yield OSL ages that are stratigraphically consistent (i.e. 'bracketed' by surrounding sample ages within their 1σ errors) for 45 of the 50 single-aliquot samples tested. Moreover, all 14 of the single-grain samples exhibit stratigraphically consistent ages (although fewer of these samples have surrounding ages for direct comparison against). It is interesting to note that the decision procedures favour the CAM in 50% of the single-grain samples measured, compared to only 26% of the single-aliquot samples. This trend is believed to reflect (i) the increased significance of other sources of D_e scatter besides heterogeneous bleaching at the single-grain level (e.g. beta-dose heterogeneity, D_e intrinsic grain-to-grain variations in luminescence characteristics and their consequent responses to fixed SAR conditions, and the introduction of scatter due to poorer counting statistics and measurement error). The 'averaging out' effects of multi-grain analysis ensure that these additional sources of variability contribute far less to single-aliquot D_e scatter. (ii) Different 'acceptance criteria' are used at the single-grain and single-aliquot scales of analysis. Particularly poorly bleached grains that contribute to the cumulative light sums of multi-grain aliquots may otherwise be rejected at the single-grain level if they yield imprecise D_e's or represent lone statistical outliers.

Table S4 and Fig. 2 show comparisons of the decision procedure age selections for the 14 samples that have replicate single-grain and single-aliquot D_e measurements. Half of these samples have single-grain and single-aliquot ages that are statistically indistinguishable; the remaining 50% deviate from unity by $> \pm 10\%$. Assuming there are no significant systematic inconsistencies between the results of single-grain and single-aliquot measurement protocols, these paired age disparities likely reflect either (i) inappropriate age model selection at the single-grain/single-aliquot scale of analysis, (ii) appropriate age model selection but inherent problems of dating particularly poorly bleached samples using multi-grain approaches. It is difficult to distinguish between the relative importance of these two factors and it is likely that both have contributed to the single-grain and single-aliquot age inconsistencies. It is worth noting that the single-aliquot age estimates of 5 of these 7 discordant samples overestimate their paired single-grain counterparts. Furthermore, this systematic overestimation remains even if the MAM-3 age model is selected for all these single-aliquot samples. These observations suggest that (ii) above may be the more important factor. In addition, there appears to be a site-specific bias to these trends; there is excellent correspondence between the single-grain and single-aliquot ages of all samples from Big Valley and Big Arroyo Site 1. In contrast, systematic single-aliquot age overestimations occur with all the samples from Big Arroyo Site 3 (Table S4). It is possible that the bleaching conditions of these latter deposits were so poor that none of the measured single-aliquots actually yielded fully reset D_e estimates.

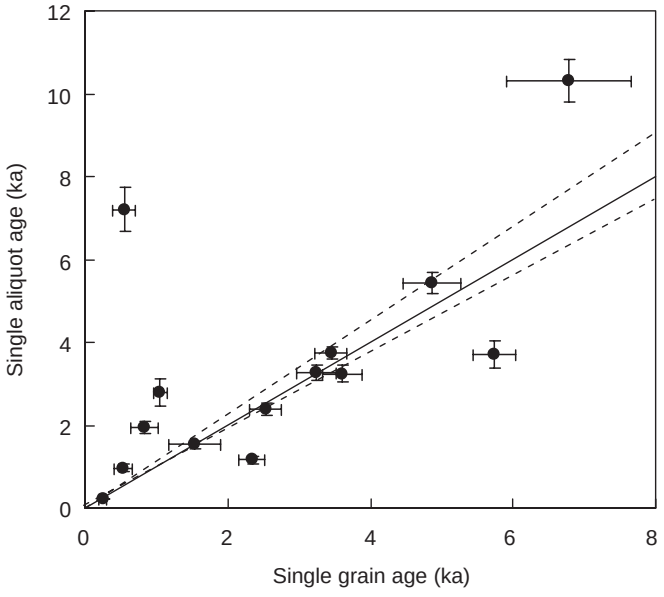

Fig. 2. Regression plot comparing the decision procedure age estimates for the 14 samples with replicate single-grain and single-aliquot D_e measurements. The 1:1 trendline is shown as a solid line, dashed lines represent $\pm 10\%$ of unity.

5. Final age estimates

The final OSL ages for these 50 samples are based on the single-grain D_e estimates where available (i.e. for the subset of 14 samples) and the single-aliquot D_e estimates in all other cases (Table S1). This combined OSL chronology displays a high degree of stratigraphic consistency between related samples, as reflected in the age–depth profiles shown in Fig. 3. Out of these 50 samples there are only 3 samples (02/11/16, 02/09/02 and 03/04/02) for which the decision procedure age estimates are not consistent with (i.e. 'bracketed' by) surrounding sample ages within their 1σ errors. The first of these samples is consistent with its surrounding sample ages within the 2σ error range. The other two samples display the complex *Type* 3 D_e distributions and are each assigned the CAM by the single-aliquot decision procedure. As Table S2 shows, use of the MAM-3 with these two samples would actually provide more consistent ages with their surrounding samples. Overall, however, the single-grain and single-aliquot decision procedures provide combined age estimates with good down-profile correspondence in 94% of these fluvial samples. This is particularly encouraging given that a relatively small number of grains and aliquots were accepted in the D_e analysis of some of these samples (e.g. $n_1 = <20$ for eight of the single-aliquot samples and four of the single-grain samples; Tables S2–S3).

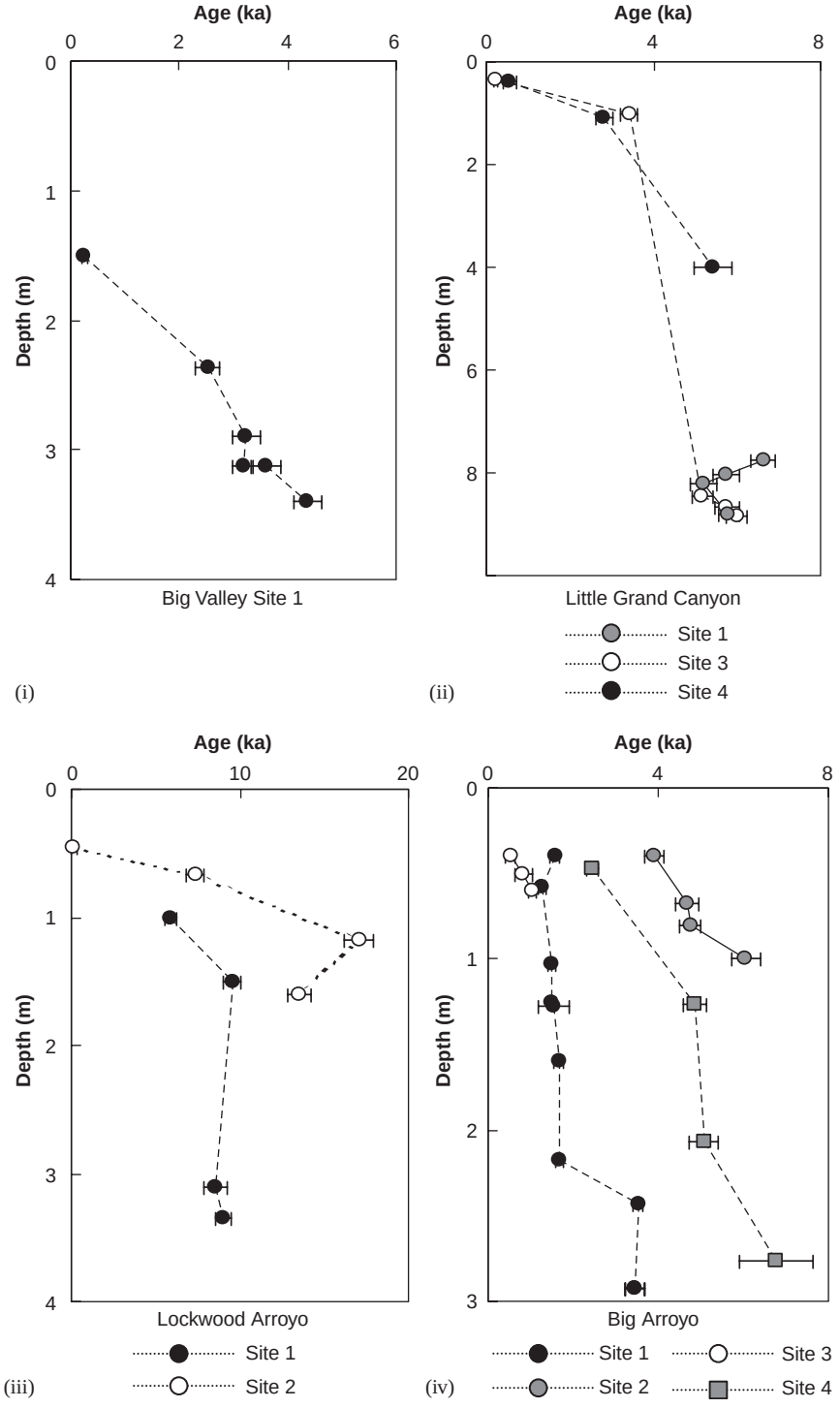

Fig. 3. Age–depth profiles obtained for various sites within four southern Colorado arroyo systems. Age–depth profiles are shown for all the stratigraphic sections that contain more than one OSL sample.

It is important to stress that this study is not a quantitative test of the suitability of the age model decision procedures (since these fluvial samples are devoid of independent age control). It merely represents an application of these previously generated decision procedures to an unrelated fluvial sample dataset. Had a single type of age model simply been applied universally to this fluvial sample dataset, the resultant final age estimates would have displayed greater down-profile discordance. For instance use of the CAM throughout would have resulted in twice as many samples having stratigraphically inconsistent final age estimates (i.e. 6 of the 50 samples). Alternatively, universal use of the MAM-3 would have resulted in 5 inconsistent final sample ages (cf. Tables S2–S3). The decision procedures used in this research do not offer a definitive solution, but are successful in providing a

transparent and systematic means of assessing age model suitability on a sample-by-sample basis. The real solution to the problem of dating partially bleached samples ultimately lies with the development of more sophisticated age models that can capture the true complexity and diversity of fluvial dose distributions. In the meantime, these multi-faceted decision criteria offer a more objective means of selecting appropriate age models based on firm theoretical and empirical evidence.

The OSL ages presented here represent the first detailed absolute age control on arroyo-system evolution in the southern Colorado piedmont region. It is apparent from the age–depth profiles (Fig. 3) that aggradation has not occurred in a continuous or linear fashion during the Holocene. Protracted periods of aggradation have often been interrupted by relatively short lived, intermittent arroyo incision episodes, as indicated by hiatuses in sediment accumulation (e.g. 3.6–3.2 ka on Fig. 3i) or abrupt reductions in sedimentation rates (e.g. 3.5–1.7 ka on Fig. 3iv). These patterns are consistent with sedimentological evidence that also suggests multiple cut-fill arroyo epicycles have taken place within these basins during the Holocene. The basal fill ages obtained from the four separate palaeochannels in the Little Grand Canyon are particularly interesting (Table S1). These samples reveal that a synchronous, basin wide arroyo-filling epicycle was initiated at the terminus of the Altithermal period ca.6–5.4 ka, as has been witnessed in other small valleys of the Arkansas River basin (e.g. Bettis and Mandel, 2002).

6. Conclusions

1. This study is amongst the first to apply a systematic, multi-dimensional method for D_e 'age model' selection. The age model selection procedures employed here were developed from independent analyses of simulated single-grain D_e populations (Bailey and Arnold, in press) and known-age empirical single-aliquot D_e datasets (Arnold, 2006).
2. Application of these predetermined decision procedures to a suite of 50 unrelated ephemeral fluvial samples yields final age estimates that are stratigraphically consistent in 94% of the cases tested.
3. Comparison of replicate single-grain and single-aliquot dates reveals statistically indistinguishable age estimates for 50% of the samples tested. Out of the remaining seven samples, five have single-aliquot ages, which systematically overestimate their single-grain counterparts. These disparities highlight the potential limitations of the single-aliquot technique when dealing with particularly poorly bleached samples (despite 'appropriate' age model selection).
4. Using this age model decision approach it has been possible to provide the first detailed absolute chronology of arroyo-system evolution in the southern Colorado piedmont region. The results qualitatively demonstrate that optical dating can offer a valuable chronological tool for investigating arroyo dynamics and causality when appropriate D_e statistical treatments are employed.

Acknowledgements

This research was funded by US Army Research Office grant DAAD19-01-1-0615. L.A. acknowledges the BGRG and LED2005 organisers for their kind financial support towards conference attendance.

Editorial handling by: R. Roberts

Appendix A. Supplementary materials

Supplementary data associated with this article can be found in the online version at doi:10.1016/j.quageo.2006.05.003

References

Aitken, M.J., 1998. An Introduction to Optical Dating: The Dating of Quaternary Sediments by the Use of Photon-stimulated Luminescence. Oxford University Press, Oxford.

Armitage, S.J., 2003. Testing and application of luminescence techniques using sediment from the southeast African coast. Ph.D. Thesis, University of Wales Aberystwyth, unpublished.

Arnold, L.J., 2006. Optical dating and computer modelling of arroyo epicycles in the American southwest. D.Phil. Thesis, University of Oxford, unpublished.

Bailey, R.M., Arnold, L.J., Statistical modelling of single grain quartz D_e distributions and an assessment of procedures for estimating burial dose. Quaternary Science Reviews, in press.

Bettis, E.A., Mandel, R.D., 2002. The effects of temporal and spatial patterns of Holocene erosion and alluviation on the archaeological record of the Central and Eastern Great Plains, USA. Geoarchaeology 17, 141–154.

Duller, G.A.T., 2003. Distinguishing quartz and feldspar in single grain luminescence measurements. Radiation Measurements 37, 161–165.

Galbraith, R.F., Roberts, R.G., Laslett, G.M., Yoshida, H., Olley, J.M., 1999. Optical dating of single and multiple grains of quartz from Jinmium rock shelter, northern Australia: Part I. Archaeometry 41, 339–364.

Lepper, K., Agersnap-Larsen, N., McKeever, S., 2000. Equivalent dose distribution analysis of Holocene aeolian and fluvial quartz sands from central Oklahoma. Radiation Measurements 32, 603–608.

Murray, A.S., Wintle, A.G., 2000. Luminescence dating of quartz using an improved single-aliquot regenerative-dose procedure. Radiation Measurements 32, 57–73.

Olley, J.M., Caitcheon, G., Murray, A.S., 1998. The distribution of apparent dose as determined by optically stimulated luminescence in small aliquots of fluvial quartz: Implications for dating young sediments. Quaternary Geochronology 17, 1033–1040.

Prescott, J.R., Hutton, J.T., 1994. Cosmic ray contributions to dose rates for luminescence and ESR dating: large depths and long-term time variations. Radiation Measurements 23, 497–500.

Thomsen, K.J., Murray, A.S., Bøtter-Jensen, L., 2005. Sources of variability in OSL dose measurements using single grains of quartz. Radiation Measurements 39, 47–61.

Appendix D

Reprint: Self-formed bedrock channels

Reference: Wobus, C.W., Tucker, G.E., and Anderson, R.S. (2006) Self-formed bedrock channels. Geophysical Research Letters, v. 33, L18408, doi: 10.1029/2006GL027182.

GEOPHYSICAL RESEARCH LETTERS, VOL. 33, L18408, doi:10.1029/2006GL027182, 2006

Self-formed bedrock channels

Cameron W. Wobus,[1] Gregory E. Tucker,[2] and Robert S. Anderson[3]

Received 9 June 2006; revised 8 August 2006; accepted 14 August 2006; published 28 September 2006.

[1] An effective physics-based rule for the evolution of bedrock channel cross sections is required for quantitative modeling of the roles of climate, tectonics, and sediment supply in setting bedrock longitudinal profiles and landscape form. Here we propose a modeling strategy in which the spatial pattern of erosion rates in a channel cross section is calculated, allowing exploration of the origin of the channel cross-sectional profile, and of the dependence of channel width on flow discharge and channel slope. Our approach reproduces many of the scaling relationships observed in natural systems, including power-law width-discharge ($W \sim Q^{0.4}$) and width-slope ($W \sim S^{-0.2}$) relationships. Models of channel cross-sections linked in series and subject to varying rock uplift (baselevel lowering) rates produce concave-up longitudinal profiles with power-law slope-uplift ($S \sim B^{1.31}$) and width-uplift ($W \sim B^{-0.24}$) relationships. Our modeling strategy can easily be adapted to handle i) better representations of erosional processes, ii) better approximations of the flow structure, and iii) the role of non-uniform sediment mantling of the bed. **Citation:** Wobus, C. W., G. E. Tucker, and R. S. Anderson (2006), Self-formed bedrock channels, *Geophys. Res. Lett.*, *33*, L18408, doi:10.1029/2006GL027182.

1. Introduction

[2] Models of mountain landscape response to changes in climate or rock uplift require a description of bedrock channel erosion, since bedrock-incising channels set the boundary condition for the rest of the landscape. In turn, a description of bedrock channels requires understanding how the erosion pattern depends on water and sediment discharge, local channel gradient, and bed roughness. While we have made considerable progress in modeling the evolution of longitudinal profiles of bedrock channels using simplified fluid mechanics and empirically-based scaling laws [e.g., *Howard*, 1994; *Whipple*, 2004], we have yet to develop a physics-based description of what sets bedrock channel geometry – the cross-sectional form and width-to-depth ratio of bedrock channels – or how this geometry responds to changes in climate, baselevel, or channel-bed lithology. Such a description is crucial to our understanding of landscape evolution, since channel cross-sectional geometry strongly influences fluid stresses and rates of erosion in natural systems.

[3] Here we describe a model for the evolution of the bedrock channel cross section based on the assumption that the incision rate at each point along the wetted perimeter of a channel scales with the local shear stress. By explicitly modeling the distribution of stresses along the channel perimeter, our model allows the bedrock channel to evolve to a steady-state geometry, without prescribing either channel shape or aspect ratio. The model reproduces many features observed in natural bedrock channels, including a positive power-law relationship between channel width and water discharge and an inverse power-law relationship between channel width and local gradient.

2. Background

[4] Most of the constraints for the hydraulic geometry of natural channels have come from alluvial rivers. These data suggest a nearly universal scaling for channel width, W, as a power-law function of water discharge, Q, with an exponent between 0.3–0.5 [e.g., *Leopold and Maddock*, 1953; *Parker*, 1979; *Whipple*, 2004]. In comparison to alluvial rivers, studies of hydraulic geometry of bedrock channels are relatively scarce. However, available data suggest that the width-discharge scaling for bedrock channels is similar to that for alluvial rivers [*Duvall et al.*, 2004; *Whipple*, 2004].

[5] Two recent models have sought to describe controls on the characteristic width of bedrock channels. In the first, *Finnegan et al.* [2005] combine the Manning equation and conservation of water to describe the relationships among width, discharge and channel gradient. The authors derive a width-discharge scaling of $W \sim Q^{3/8}$, and a width-gradient scaling of $W \sim S^{-3/16}$, both of which compare favorably with empirical data from field sites with both uniform and spatially variable uplift rates. However, this model requires an assumption of a constant width-to-depth ratio in order to obtain closure of the system of equations employed. While this assumption appears to be consistent with observations from natural rivers, we are left with no explanation of how or why a channel evolves to an equilibrium hydraulic geometry.

[6] In a second recent contribution, *Stark* [2006] models bedrock channels by dividing the cross-sectional geometry into four segments: two on the channel floor divided at the channel midpoint, and one on each channel wall, with a fixed angle between the floor and wall. The average shear stress is modeled for each segment of the channel cross-section by balancing the integrated shear on the bed with the downstream component of the weight of the water. This model also describes the evolution of channel geometry in response to changes in external forcing, and includes probability distribution functions (PDFs) of discharges, which our model does not yet do. However, in order to link channels to hillslopes, the *Stark* [2006] model assumes

[1] Cooperative Institute for Research in Environmental Sciences, University of Colorado, Boulder, Colorado, USA.
[2] Department of Geological Sciences and Cooperative Institute for Research in Environmental Sciences, University of Colorado, Boulder, Colorado, USA.
[3] Department of Geological Sciences and Institute for Arctic and Alpine Research, University of Colorado, Boulder, Colorado, USA.

0094-8276/06/2006GL027182$05.00

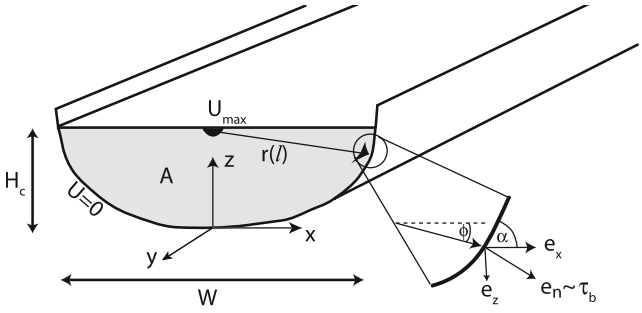

Figure 1. Schematic showing model setup. Shear stress (τ_b) is a function of the maximum velocity $U_{\max}$ and the distance from the high velocity core, r, where the maximum velocity is assumed to be at the center-top of the flow. Bed-normal erosion rate (e_n) is assumed to be linearly related to shear stress, and is decomposed into lateral (e_x) and vertical (e_z) components using the horizontal bed inclination, α, and the angle between the centerline vector and the horizontal, ϕ. Centerline depth, H_c and channel width, W evolve through the model run.

a fixed bank slope and therefore does not allow the channel cross-section to freely form its own shape.

3. Model Setup

[7] While our formulation is similar in principle to the work of *Finnegan et al.* [2005] and *Stark* [2006], we take two important steps beyond these and other previous studies by 1) explicitly modeling the erosion rate at each point along the wetted perimeter of a channel (Figure 1), and 2) allowing the channel cross section to evolve from any arbitrary geometry. The model channels are therefore "self-formed" in that the cross-sectional shape co-evolves with the erosion rate distribution until a stable form is achieved.

[8] We begin by prescribing the water discharge, local gradient, median grain size (D_{50}), and an initial (arbitrary) channel geometry. These prescribed parameters allow us to calculate a Chezy smoothness coefficient using a 1D logarithmic approximation for bed roughness [*Julien*, 1998, table 6.1], and a mean velocity (equation (1)), and discharge (equation (2)) for any value of water depth:

$$\overline{u}_h = C_h\sqrt{R_h S} \tag{1}$$

$$Q_h = \overline{u}_h A_h \tag{2}$$

Here C_h is the Chezy coefficient describing bed smoothness, R is the hydraulic radius (cross sectional area divided by the wetted perimeter), S is the local energy gradient (here assumed equal to the water surface gradient), $\overline{u}$ is the mean water velocity, Q is the water discharge, A is the cross-sectional area, and the subscript h denotes dependence of a parameter on water depth. By minimizing the misfit between calculated values of Q_h and the prescribed discharge for any estimated water depth, we obtain a best-fit hydraulic radius and corresponding mean velocity.

[9] The maximum velocity, $U_{\max}$, is taken to lie at the water surface in the channel center, and is obtained from the mean velocity found in equation (2) using the law of the wall. The mean velocity gradient at any point $l(x,z)$ along the channel perimeter is then $U_{\max}/r(l)$, where $r(l)$ is the radial distance from the channel centerline to the channel bed at position l (Figure 1). We can then calculate the bed-normal component of the velocity gradient at a characteristic roughness height z_o:

$$\left.\frac{du}{dr(l)}\right|_{z_o} = \frac{u_*}{\kappa z_o}\cdot\sin(\phi-\alpha) = \frac{U_{\max}}{z_o}\cdot\frac{1}{\ln\left(r(l)\Big/z_o\right)}\cdot\sin(\phi-\alpha) \tag{3}$$

where z_o is a roughness height (= $6.8D_{50}$), κ is von Kármán's constant, u is the shear velocity, and all other variables are as defined previously. Following Prandtl, we then scale the shear stress at each point on the bed with the square of this bed-normal velocity gradient [e.g., *Furbish*, 1997]:

$$\tau(l) = \varphi\rho A_h\left(\left.\frac{du}{dr(l)}\right|_{z_o}\right)^2 \tag{4}$$

Here ρ is the density of water, and φ is a dimensionless scale factor that ensures a force balance by dictating that the average shear stress along the perimeter is equal to the downstream component of the weight of water [e.g., *Parker*, 1979; *Stark*, 2006]:

$$\varphi = \frac{gS}{\sum_{i=1}^{N}\left(\left.\frac{du}{dr(l)}\right|_{z=z_o}\right)^2 dl(i)} \tag{5}$$

where g is the acceleration due to gravity, the summation is over $i = 1$ to N points along the channel perimeter, and $dl(i)$ is the length of a channel perimeter element at position i. The system of equations (1)–(5) is solved numerically by discretizing the channel perimeter into a set of (x,z) points, and calculating the shear stress at each point using equations (4) and (5). We then make the assumption that the bed-normal incision rate at each point scales linearly with the shear stress at that point:

$$e_n(l) = K\tau(l) = K\varphi\rho A\left(\left.\frac{du}{dr(l)}\right|_{z_o}\right)^2 \tag{6}$$

This assumption, which represents the simplest form of wear law one might reasonably adopt, is frequently used in erosion models [e.g., *Howard and Kerby*, 1983]. It is most applicable to fine-grained cohesive materials that respond to fluid stresses by detachment of small, easily suspended grains or aggregates. Equation (6) is used to calculate the x- and z- components of the erosion rate from the slope of the channel bed, and iteratively update channel shape, velocity, and wall shear using a simple forward-difference scheme.

4. Results

4.1. Channel Geometry

[10] Beginning with either a flat-floored "GS-type" channel [e.g., *Parker*, 1979], or a simple "V" shaped

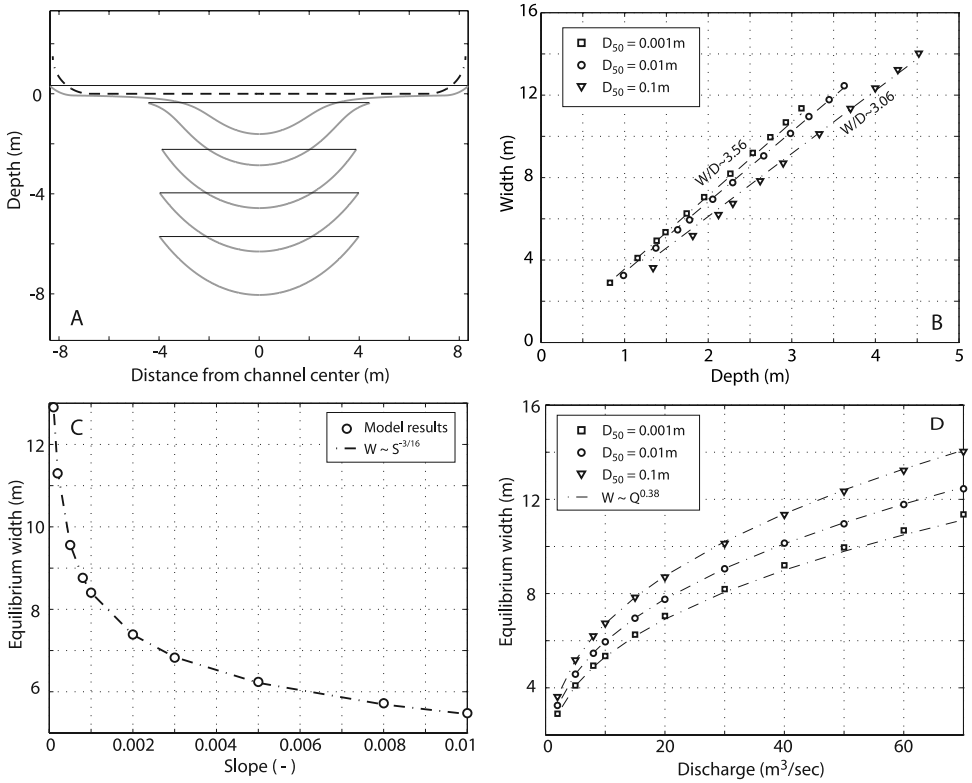

Figure 2. Response of hydraulic geometry to changes in imposed conditions. (a) Acquisition of stable cross-sectional form from an arbitrary initial condition. Grey lines represent the channel bed, and black lines represent the water level at five successive timesteps. (b) Plot of width versus depth for all model runs. Note nearly constant width-to-depth ratio for each value of D_{50}. (c) Plot of equilibrium width versus imposed channel gradient, which was varied from 10^{-3} to 10^{-1}. Dashed line shows scaling of $W \sim S^{-3/16}$ [e.g., *Finnegan et al.*, 2005]. (d) Plot of equilibrium width versus discharge, which was varied from 2 to 70 m^3/sec. Lines show width-discharge scaling of $W \sim Q^{0.38}$ for three values of median grain size, D_{50}.

channel, model runs for single channel cross-sections with prescribed discharge and gradient quickly converge to a stable, concave-up cross-sectional geometry (e.g., Figure 2a). This stable geometry arises from an inherent self-regulating mechanism described by equations (3)–(4): as the radial distance from a point on the bed to the high velocity core increases, the bed-normal incision rate at that point decreases, and vice-versa. As channels widen, the ratio of lateral to vertical incision rates should therefore decrease; conversely, as channels deepen, this ratio should increase.

[11] The equilibrium geometry is adjusted so that each point on the channel lowers at a uniform vertical rate. At any point on the cross section, this lowering rate is related to the bed-normal incision rate through:

$$e_n = \frac{d\eta}{dt} \cdot \cos\alpha \tag{7}$$

Where e_n is the bed-normal incision rate, η is the absolute elevation of a point on the profile, and α is the local sidewall gradient (see Figure 1). At the channel midpoint, the vertical lowering rate is equal to the bed-normal incision rate and we can replace $r(l)$ in equations (5)–(6) with the channel depth H. Substituting into equation (7) and rearranging, we find:

$$\left[\frac{\ln\left(\frac{H}{z_o}\right)}{\ln\left(\frac{r}{z_o}\right)}\right]^2 = \frac{\cos\alpha}{\sin(\phi-\alpha)} \tag{8}$$

While there is no apparent analytical solution to equation (8) for channel shape $z(x)$, numerical results verify that this relationship is satisfied by the equilibrium cross-channel geometry.

[12] Model channels subject to varying discharges each evolve to a nearly constant width-to-depth ratio (W/D) for a given bed material (Figure 2b). To a first approximation, this model result verifies the constant W/D assumption on which the analytical formulation of *Finnegan et al.* [2005] rests. As demonstrated in that paper, a constant W/D ratio allows the scaling relationships among channel width, slope, and discharge to be derived analytically.

[13] Holding discharge constant at 20 m^3/sec, we varied channel slope over two orders of magnitude to evaluate the response of channel width. These model runs produce a width-slope scaling of $W \sim S^{-0.2}$ (Figure 2c), consistent with

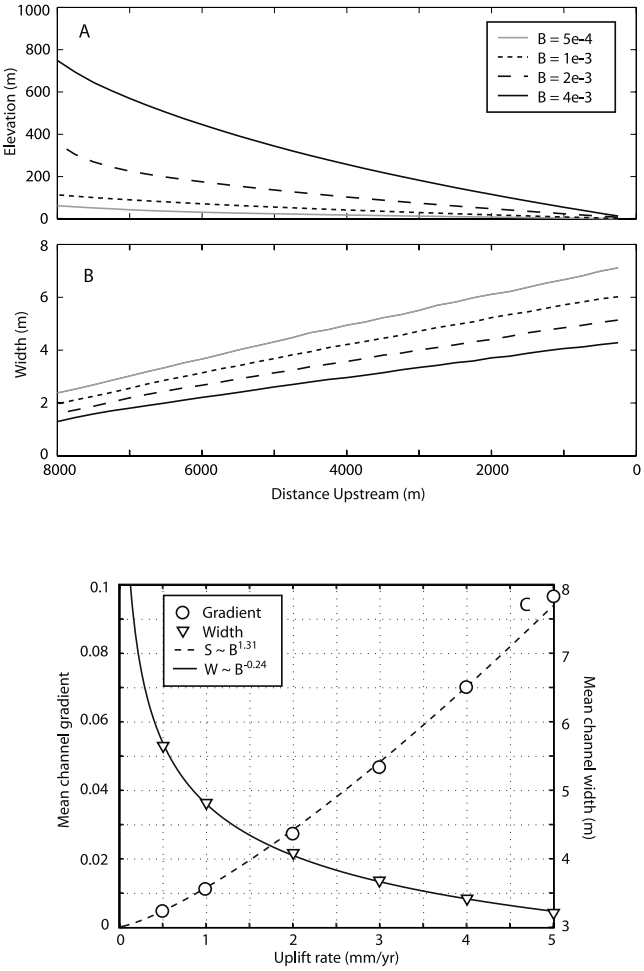

Figure 3. Plots of channel response to changes in rock uplift rate. (a) Longitudinal profiles for four model runs with rock uplift rates varying from 0.5 mm/yr to 4 mm/yr. (b) Channel width as a function of distance upstream for uplift rates varying from 0.5 mm/yr to 4 mm/yr. (c) Average channel gradient (triangles) and channel width (circles) for profiles adjusted to rock uplift rates varying from 0.5 mm/yr to 5 mm/yr.

analytical predictions [e.g., *Finnegan et al.*, 2005]. Similarly, holding gradient constant at 10^{-3}, we examined the response of channel width to changes in discharge. These model runs yield a width-discharge relationship of $W \sim Q^{0.38}$ (Figure 2d). This result is consistent with empirical data from alluvial channels [e.g., *Leopold and Maddock*, 1953], as well as the limited data compiled for bedrock channels [*Whipple*, 2004]. In all model runs, channels with coarse bed material (high D_{50}) are systematically wider and have lower W/D ratios than channels with finer bed material (Figures 2b and 2d). This reflects the fact that rougher channels yield lower mean velocities (equation (2)), thereby increasing the cross-sectional area needed to accommodate a given discharge and increasing the wetted perimeter along which erosion can occur.

4.2. Long Profile Evolution

[14] Our initial condition for modeling the co-evolution of channel width and gradient is a series of forty "V"-shaped channels aligned on a linear ramp with a gradient of 10^{-2}. We prescribe a downstream distribution of discharge of $Q \sim y^{1.7}$ [e.g., *Whipple and Tucker*, 1999], and a spatially uniform rock uplift rate (or baselevel lowering rate) B. The width and gradient then co-evolve in response to the imposed tectonic forcing.

[15] Varying B from 0.5 mm/yr to 4 mm/yr, all model channels reach an equilibrium channel width and longitudinal profile form, in which the channel width and gradient have each responded to changes in rock uplift rate (Figure 3). The dependence of channel gradient on rock uplift rate ($S \sim B^{1.31}$) is slightly weaker than that predicted from previous theoretical studies that do not incorporate a dynamic width adjustment ($S \sim B^{1.5}$ assuming a shear stress erosion rule [e.g., *Whipple and Tucker*, 1999]). This result underscores the importance of width adjustment as an additional degree of freedom for channel response. While the width response is less pronounced ($W \sim B^{-0.24}$), the inverse relationship between width and rock uplift rate is also consistent with the observation that natural channels are commonly narrower in regions with higher rock uplift rates [e.g., *Duvall et al.*, 2004; *Whittaker et al.*, 1996].

[16] In model runs in which the rock uplift rate is changed instantaneously, the transient response of an initial steady-state bedrock channel proceeds as an upstream-migrating wave of incision (Figure 4), consistent with previous modeling and field studies of bedrock channels [*Whipple and Tucker*, 1999; *Crosby and Whipple*, 2006]. This wave of incision is characterized by a simultaneous steepening and narrowing of the bedrock channel [e.g., *Whittaker et al.*, 1996]. Log-log plots of slope vs. discharge (Figure 4b) are consistent with previous studies of bedrock channels [e.g., *Whipple and Tucker*, 1999; *Wobus et al.*, 2006] which suggest that the steepness index (the y-intercept of the log-log relationship) is sensitive to the rock uplift rate, while the concavity index (the slope of the log-log relationship) is not.

5. Discussion

[17] Our simple model for the evolution of bedrock channel geometry creates smooth, concave channel cross-sections with width-discharge and width-slope scaling relationships similar to those found in natural systems (Figure 2). The model takes at least two important steps beyond previous studies by explicitly describing the spatial distribution of stresses on the channel bed, and eliminating the need for *a priori* constraints on channel geometry. This formulation also creates a natural feedback mechanism between the erosion rate and the distance from the high-velocity core of the flow, which drives self-organization of the channel cross-section. The consistency of our results with empirical observations suggests that this simple formulation may capture the essential physics controlling the evolution of bedrock channels. However, a number of complicating factors have been omitted from our analysis which should be explored in future studies.

[18] First, we have neglected the role of cross-channel variations in sediment cover and erosive process. Sediment plays the dual role of protecting the bed from erosion and providing tools for abrasion [e.g., *Gilbert*, 1877; *Sklar and*

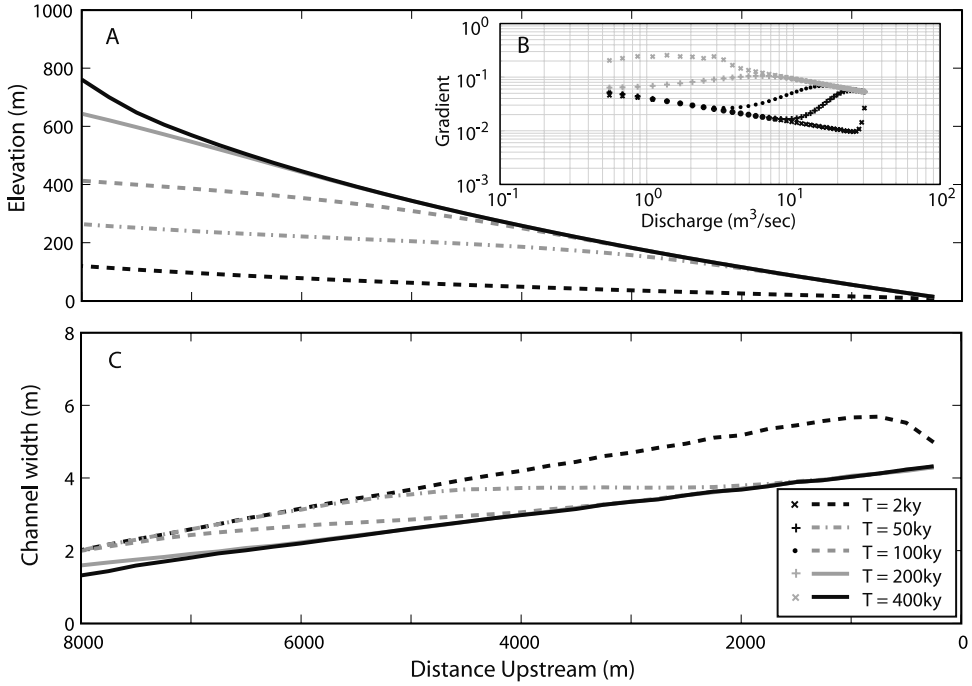

Figure 4. Transient response of model channels. (a) Elevation vs. upstream distance for initial (B = 1 mm/yr, dashed black line) and final (B = 4 mm/yr, solid black line) rock uplift conditions and three intermediate conditions during adjustment. (b) Log-log plot of slope vs. discharge for initial, final, and intermediate states shown in Figure 4a. (c) Transient adjustment of channel width to change in baselevel rate.

Dietrich, 2004]. In natural channels, we might expect the sediment mantle to be thickest near the channel center, primarily protecting the bed, and thinner near the channel walls, primarily providing tools for abrasion. Explicit consideration of the spatial distribution of sediment cover in our model channels might therefore be expected to enhance erosion at the channel walls and limit erosion near the channel center, increasing the width-to-depth ratio at equilibrium [*Hancock and Anderson*, 2002]. By assuming that erosion rate scales linearly with local shear stress, we have also not acknowledged the likely variation of erosional process and process efficiencies with position in the channel cross-section (for example, bedload abrasion on the bed vs. suspended load abrasion on the channel walls). Our formulation also assumes that the maximum flow velocity is restricted to the channel midpoint. In natural channels, maximum velocities should instead be found in a high velocity core that might extend across much of the middle part of the channel [e.g., *Knight and Sterling*, 2000], which would also increase their width-to-depth ratio at equilibrium. Further exploration of cross-channel velocity structure and other erosive processes would broaden the applicability of the model to natural systems.

[19] Channel geometry in the model equilibrates to a constant discharge, rather than to a probability distribution of discharge events. As shown by *Stark* [2006], this simplification might have important implications for the equilibrium shape of the channel cross-section if threshold effects are important in the dominant erosive process [e.g., *Snyder et al.*, 2003; *Tucker*, 2004]. Future work will incorporate both a threshold shear-stress erosion model and a PDF of discharge events into our model framework to evaluate the impacts of these natural complexities.

[20] The model's behavior is consistent with the hypothesis that bedrock channels will respond to a change in rock uplift rate by adjusting both their width and their gradient. However, in comparison to recent work by *Duvall et al.* [2004], in which channel width decreases by a factor of three for a seven-fold increase in rock uplift rate, our model suggests considerably less adjustment of channel width ($\sim$1.5–2 fold decrease; see Figure 3). This discrepancy might reflect temporal and spatial changes in bed material in natural systems, which we have kept steady in each of the model runs. For example, most of the low uplift zone channels described in *Duvall et al.* [2004] have headwaters dominated by considerably stronger lithologies than those in the high uplift zone channels. Such a configuration is likely to correlate with relatively higher roughness values in the low-uplift rate streams. As described above and illustrated in Figure 2c, this would drive the low uplift zone channels towards a larger equilibrium width than would be expected with a finer sediment load.

[21] Finally, our model suggests that channel width can adjust to changes in discharge or sediment composition in the absence of tectonic forcing (e.g., Figure 2d). The timescale for the adjustment of channel shape to a change in climatic forcing (I.E., discharge) should scale simply as the ratio of channel depth to the vertical incision rate. That this timescale might be as short as 10^3–10^4 years in natural systems suggests that a stable cross-sectional geometry might be more commonly achieved than a stable longitudinal profile form [e.g., *Whipple*, 2004]. Because cross-sectional geometry can adjust locally to changes in water

and sediment flux, channel widening might actually prolong the adjustment of the long profile by providing an additional mechanism for channels to partition their erosional work.

6. Conclusions

[22] The geometry of a bedrock channel co-evolves with its flow field, which ultimately drives the system to a stable cross-sectional form. Our formulation, in which these feedbacks are enacted, reproduces many features of natural channels, including a power-law scaling between width and discharge with an exponent of $\sim$0.4, a power-law scaling between width and gradient with an exponent of ~ -0.2, and a nearly constant width-to-depth ratio for a given bed material composition. These features emerge from the model without any *a priori* assumptions about channel shape or aspect ratio. Future work, guided by more detailed observations from natural channels, should explore the effects of sediment cover, erosion thresholds, and changes in erosive process on the geometry of bedrock channels. Ultimately, these studies will elucidate our understanding of how sediment size and flux influence bedrock incision rates, how strath terraces are formed, and how drainage networks respond to changes in climatic or tectonic conditions.

[23] **Acknowledgments.** We thank Colin Stark and an anonymous reviewer for exceptional reviews, which helped to focus our thinking and improve our model formulation. Support for this research came from the National Science Foundation (EAR-0545537 to RSA and EAR-0510971 to GT), the U.S. Army Research Office (47033-EV to GT), and a CIRES postdoctoral fellowship to CWW.

References

Crosby, B. T., and K. X. Whipple (2006), Knickpoint initiation and distribution within fluvial networks: 236 waterfalls in the Waipaoa River, North Island, New Zealand, *Geomorphology*, in press.

Duvall, A., E. Kirby, and D. Burbank (2004), Tectonic and lithologic controls on bedrock channel profiles and processes in coastal California, *J. Geophys. Res.*, *109*, F03002, doi:10.1029/2003JF000086.

Finnegan, N. J., G. Roe, D. R. Montgomery, and B. Hallet (2005), Controls on the channel width of rivers: Implications for modeling fluvial incision of bedrock, *Geology*, *33*, 229–232.

Furbish, D. J. (1997), *Fluid Physics in Geology: An Introduction to Fluid Motions on Earth's Surface and Within its Crust*, Oxford Univ. Press, New York.

Gilbert, G. K. (1877), *Report of the Geology of the Henry Mountains: Geographical and Geological Survey of the Rocky Mountain Region*, 160 pp., Gov. Print. Off., Washington, D. C.

Hancock, G. S., and R. S. Anderson (2002), Numerical modeling of fluvial strath-terrace formation in response to oscillating climate, *GSA Bull.*, *114*, 1131–1142.

Howard, A. D. (1994), A detachment-limited model of drainage basin evolution, *Water Resour. Res.*, *30*, 2261–2285.

Howard, A. D., and G. Kerby (1983), Channel changes in badlands, *Geol. Soc. Am. Bull.*, *94*, 739–752.

Julien, P. (1998), *Erosion and Sedimentation*, 280 pp., Cambridge Univ. Press, New York.

Knight, D. W., and M. Sterling (2000), Boundary shear in circular pipes running partially full, *J. Hydraul. Eng.*, *126*, 263–275.

Leopold, L., and T. Maddock (1953), The hydraulic geometry of stream channels and some physiographic implications, *U. S. Geol. Surv. Prof. Pap.*, *252*, 57 pp.

Parker, G. (1979), Hydraulic geometry of active gravel rivers, *J. Hydraul. Div. Am. Soc. Civ. Eng.*, *105*, 1185–1201.

Sklar, L. S., and W. E. Dietrich (2004), A mechanistic model for river incision into bedrock by saltating bed load, *Water Resour. Res.*, *40*, W06301, doi:10.1029/2003WR002496.

Snyder, N. P., K. X. Whipple, G. E. Tucker, and D. J. Merritts (2003), Importance of a stochastic distribution of floods and erosion thresholds in the bedrock river incision problem, *J. Geophys. Res.*, *108*(B2), 2117, doi:10.1029/2001JB001655.

Stark, C. P. (2006), A self-regulating model of bedrock river channel geometry, *Geophys. Res. Lett.*, *33*, L04402, doi:10.1029/2005GL023193.

Tucker, G. E. (2004), Drainage basin sensitivity to tectonic and climatic forcing: Implications of a stochastic model for the role of entrainment and erosion thresholds, *Earth Surf. Processes Landforms*, *29*, 185–205.

Whipple, K. (2004), Bedrock rivers and the geomorphology of active orogens, *Annu. Rev. Earth Planet. Sci.*, *32*, 151–185.

Whipple, K. X., and G. E. Tucker (1999), Dynamics of the stream-power river incision model: Implications for height limits of mountain ranges, landscape response timescales, and research needs, *J. Geophys. Res.*, *104*, 17,661–17,674.

Whittaker, A. C., P. A. Cowie, M. Attal, G. E. Tucker, and G. P. Roberts (1996), Bedrock channel adjustment to tectonic forcing: Implications for predicting river incision rates, *Geology*, in press.

Wobus, C., K. Whipple, E. Kirby, N. Snyder, J. Johnson, K. Spyropolou, B. T. Crosby, and D. Sheehan (2006), Tectonics from topography: Procedures, promise and pitfalls, in *Tectonics, Climate and Landscape Evolution*, edited by S. D. Willett, et al., *Geol. Soc. Am. Spec. Pap.*, *398*, 55–74.

R. S. Anderson, Department of Geological Sciences and Institute for Arctic and Alpine Research, University of Colorado, Boulder, CO 80309, USA.

G. E. Tucker and C. W. Wobus, Cooperative Institute for Research in Environmental Sciences, University of Colorado, Boulder, CO 80309, USA. (cameron.wobus@colorado.edu)

Appendix E

Reprint: Modeling the evolution of channel shape

Reference: Wobus, C.W., Kean, J.W., Tucker, G.E., and Anderson, R.S. (2008) Modeling the evolution of channel shape: balancing computational efficiency with hydraulic fidelity. Journal of Geophysical Research - Earth Surface, v. 113, F02004, doi:10.1029/2007JF000914.

JOURNAL OF GEOPHYSICAL RESEARCH, VOL. 113, F02004, doi:10.1029/2007JF000914, 2008

Modeling the evolution of channel shape: Balancing computational efficiency with hydraulic fidelity

Cameron W. Wobus,[1] Jason W. Kean,[2] Gregory E. Tucker,[1,3] and Robert S. Anderson[3,4]

Received 21 September 2007; revised 18 January 2008; accepted 21 February 2008; published 9 April 2008.

[1] The cross-sectional shape of a natural river channel controls the capacity of the system to carry water off a landscape, to convey sediment derived from hillslopes, and to erode its bed and banks. Numerical models that describe the response of a landscape to changes in climate or tectonics therefore require formulations that can accommodate evolution of channel cross-sectional geometry. However, fully two-dimensional (2-D) flow models are too computationally expensive to implement in large-scale landscape evolution models, while available simple empirical relationships between width and discharge do not adequately capture the dynamics of channel adjustment. We have developed a simplified 2-D numerical model of channel evolution in a cohesive, detachment-limited substrate subject to steady, unidirectional flow. Erosion is assumed to be proportional to boundary shear stress, which is calculated using an approximation of the flow field in which log-velocity profiles are assumed to apply along vectors that are perpendicular to the local channel bed. Model predictions of the velocity structure, peak boundary shear stress, and equilibrium channel shape compare well with predictions of a more sophisticated but more computationally demanding ray-isovel model. For example, the mean velocities computed by the two models are consistent to within ~3%, and the predicted peak shear stress is consistent to within ~7%. Furthermore, the shear stress distributions predicted by our model compare favorably with available laboratory measurements for prescribed channel shapes. A modification to our simplified code in which the flow includes a high-velocity core allows the model to be extended to estimate shear stress distributions in channels with large width-to-depth ratios. Our model is efficient enough to incorporate into large-scale landscape evolution codes and can be used to examine how channels adjust both cross-sectional shape and slope in response to tectonic and climatic forcing.

Citation: Wobus, C. W., J. W. Kean, G. E. Tucker, and R. S. Anderson (2008), Modeling the evolution of channel shape: Balancing computational efficiency with hydraulic fidelity, *J. Geophys. Res.*, *113*, F02004, doi:10.1029/2007JF000914.

1. Introduction

[2] Numerical models of landscape evolution have evolved to the point where they can now be used to understand how river systems transmit changes in base level through drainage networks [e.g., *Bishop et al.*, 2005; *Crosby and Whipple*, 2006; *Loget et al.*, 2006; *Berlin and Anderson*, 2007]; how landscapes respond to changes in climate [e.g., *Tucker and Slingerland*, 1997; *Whipple et al.*, 1999]; and how erosion and tectonics might interact at the orogen scale [*Beaumont et al.*, 1992; *Whipple and Meade*, 2004; *Simpson*, 2006]. While these modeling efforts have clearly bolstered our understanding of how landscapes function, in nearly all of them the assumption is made that bedrock channel width is a simple power law function of upstream drainage area. This is a particular problem for exploring the dynamics of landscapes, since recent work has shown that these power law relationships break down in exactly the settings we find most interesting from a tectonic perspective [e.g., *Harbor*, 1998; *Lave and Avouac*, 2001; *Montgomery and Gran*, 2001; *Finnegan et al.*, 2005; *Amos and Burbank*, 2007; *Whittaker et al.*, 2007]. Since the cross-sectional form of a bedrock river controls its ability to carry water off a landscape, to convey sediment derived from hillslopes, and to erode its bed and banks, unaccounted changes in channel shape through time could have important implications for landscape dynamics.

[3] In addition to providing better parameterizations of erosion that can feed into landscape evolution models, understanding the controls on channel geometry is an important research target in its own right. For example, dozens of geomorphic studies have relied on radiometric dates obtained from strath terraces (river terraces carved directly into bedrock) to reconstruct rates of fluvial erosion through time [e.g., *Merritts et al.*, 1994; *Hancock et al.*,

[1] Cooperative Institute for Research in Environmental Sciences, University of Colorado, Boulder, Colorado, USA.
[2] United States Geological Survey, Denver, Colorado, USA.
[3] Department of Geological Sciences, University of Colorado, Boulder, Colorado, USA.
[4] Institute of Arctic and Alpine Research, University of Colorado, Boulder, Colorado, USA.

0148-0227/08/2007JF000914$09.00

1999; *Lave and Avouac*, 2000; *Pazzaglia and Brandon*, 2001]. These strath terraces preserve information about the hydraulic conditions of a river system at some point in the past; however, these conditions are not always fully understood [e.g., *Montgomery*, 2004]. Physically based models describing how bedrock channels acquire their cross-sectional shape would improve our ability to interpret radiometric dates obtained from strath terraces.

[4] Ideally, models of fluvial erosion and drainage basin dynamics should therefore include a mechanism for rivers to adjust their cross-sectional form in response to natural or anthropogenic perturbations. This requires that we have a meaningful way of modeling the cross-sectional distribution of a physical quantity that can be used as a proxy for erosion rate, such as shear stress. However, models that explicitly describe the hydraulics of rivers generally require iterative solution schemes that are too computationally expensive to model shear stress distributions and evolve cross-sectional forms over long timescales [*Houjou et al.*, 1990; *Pizzuto*, 1991; *Naot et al.*, 1993; *Vigilar and Diplas*, 1997; *Lane et al.*, 1999; *Ma et al.*, 2002; *Kean and Smith*, 2004]. On the opposite end of the spectrum, the simplest possible formulation in which the shear stress is approximated by the local depth-slope product is both a misrepresentation of fluid physics and will inevitably lead to continually deepening and narrowing channel cross sections. The challenge, then, is to develop models that remain as faithful as possible to the physics of fluid flow without requiring iterative solutions to the equations for turbulence, momentum, and velocity structures.

[5] Toward this end, *Wobus et al.* [2006b] developed a simple model for bedrock channel evolution that used a "shortcut" to reconstructing the flow field by assuming that radial logarithmic velocity profiles connect the bed and banks with the channel centerline. While this model (hereafter Wobus, Tucker, and Anderson Model (WTA)) has been shown to reproduce many of the scaling relationships observed in natural channels, it has not yet been tested against more complete parameterizations of river hydraulics to ensure that there are no systematic biases introduced by the simplifications used. In this contribution we take a step back, and test the model against independently derived calculations of the velocity structure and shear stress distributions in natural channels. Where available, we also test the model against experimental data from laboratory flumes. These comparisons allow us to evaluate the sources of errors that might be introduced by the WTA model, and motivate some simple refinements that can be implemented to improve its approximation of the flow field in symmetrical channels with a wide range of aspect ratios.

2. Model Descriptions

2.1. Wobus, Tucker, and Anderson Model

[6] The goal of the model presented by *Wobus et al.* [2006b] is to allow channels to adjust both their cross-sectional shape and their longitudinal profile form in response to tectonic or climatic perturbations. Such perturbations are expected to occur over timescales on the order of 10^4-10^6 years. As such, the formulation requires tradeoffs to be made between computational efficiency and faithful implementation of fluid physics in open channel flow. The details of the model formulation are given by *Wobus et al.* [2006b]; a brief summary is provided here.

[7] The flow structure in the Wobus, Tucker, and Anderson model is calculated by the simultaneous solution of four equations describing the mean velocity, hydraulic roughness, and momentum balance in the model channels. First, the requirement that the channel must convey the prescribed discharge is combined with a modified Chézy formulation to determine the cross-sectional area and mean velocity of the flow for a given cross section (equations (1) and (2))

$$Q = \overline{u}A \tag{1}$$

$$\overline{u} = C\sqrt{RS} \tag{2a}$$

$$C = 2.5\sqrt{g}\ln\left(\frac{0.37R}{l_0}\right) \tag{2b}$$

where Q is the water discharge, $\overline{u}$ is the mean flow velocity, C is the Chézy smoothness coefficient, A is the cross-sectional area of the flow, R is the hydraulic radius (cross-sectional area divided by wetted perimeter), and S is the channel gradient. The Chézy coefficient C is a function of both the bed roughness and the hydraulic radius, and is calculated in equation (2b) using an empirical relationship described by *Julien* [1998]. Here l_0 represents an effective roughness length from the bed at which the velocity goes to zero, and is measured perpendicular to the channel boundary; g is the acceleration due to gravity at the Earth's surface.

[8] Conservation of momentum requires that the integrated shear stress on the bed is balanced by the downslope component of the weight of water [e.g., *Parker*, 1979; *Stark*, 2006]

$$\int_0^P \tau_b dp_b = \rho g A S \tag{3}$$

where P is the total distance along the wetted perimeter of the channel, τ_b is the local boundary shear stress, dp_b is an increment of distance along the channel's wetted perimeter, and ρ is the density of water. Once the flow depth and velocity are determined, the task that remains is to determine how the shear stress is distributed along the wetted perimeter of the channel in a manner that satisfies equations (1)–(3). For simplicity, the formulation follows Prandtl's mixing length hypothesis, which states that the bed shear stress at each point along the wetted perimeter of the channel is proportional to the square of the near-bed velocity gradient [e.g., *Furbish*, 1997]

$$\tau_b = \rho L^2 \left(\left.\frac{du}{dr}\right|_{r=l_0}\right)^2 \tag{4}$$

where L is the mixing length, r is a coordinate measured between the wall of the channel and the channel midpoint, and l_0 is the effective roughness length scale as above.

[9] Here a series of assumptions is required in order to efficiently reproduce the flow structure and shear stress

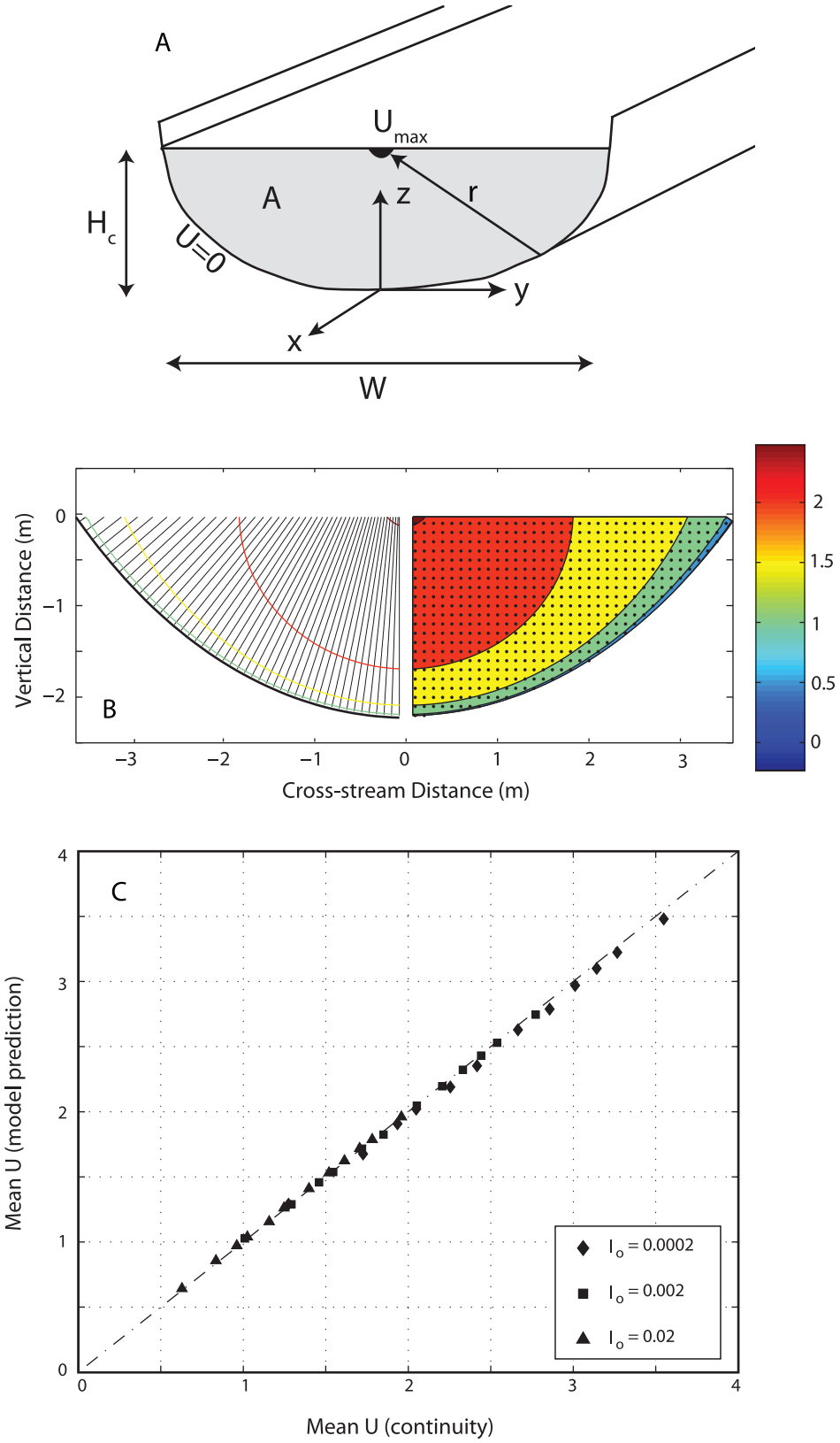
A
U max
A
z
r
H c
U=0
y
x
W
B
Vertical Distance (m)
Cross-stream Distance (m)
C
Mean U (model prediction)
Mean U (continuity)
I o = 0.0002
I o = 0.002
I o = 0.02

Figure 1

distribution. First, the model assumes that the maximum velocity occurs in the center of the channel at the top of the flow (Figure 1a). This assumption is broadly consistent with measurements from natural and experimental channels, in which the maximum velocity is typically found near the center of the channel and slightly below the surface [e.g., *Knight and Sterling*, 2000; *Ma et al.*, 2002]. Placing the maximum velocity at the water surface simplifies the model without substantial departure from this observation. Second, the velocity gradient near the bed is assumed to scale with the mean velocity gradient between wall and centerline by employing the law of the wall along "rays," r, drawn from the channel centerline to the bed

$$\left.\frac{du}{dr}\right|_{r=l_0} = \frac{U_{\max}}{l_0} \cdot \frac{1}{\ln(r/l_0)} \tag{5}$$

where r is a radial coordinate measuring distance from the channel wall to the centerline. Third, the formulation resolves the "total" velocity gradient onto a bed-normal vector in order to determine the shear stress. And finally, the mixing length scale L is assumed to be invariant along the wetted perimeter of the channel. The magnitude of L is found by combining equations (3) and (4) [e.g., *Wobus et al.*, 2006b].

[10] It is important to note that the approach outlined above does not require calculation of the full velocity structure of the flow. However, once the distribution of bed shear stresses has been estimated, it can be used to reconstruct the velocity field by calculating the shear velocity at each point ($u_* = \sqrt{\tau_b/\rho}$), and applying the law of the wall along bed-normal vectors. Note that because Prandtl's mixing theory is built upon momentum exchange and turbulent stresses across velocity gradients, the orientation of these vectors with respect to gravity does not enter into the formulation. Local flow depth is therefore only important as it relates to the length scale that determines the velocity gradient in equation (4). As a test of the degree to which the resulting flow structure is reasonable, the cross-sectionally averaged velocity can then be recalculated by projecting the velocities from these bed-normal vectors onto a Cartesian grid and finding the mean value of the gridded velocity structure (Figure 1b). This exercise typically yields a mean flow velocity that is within 1–3% of that required to satisfy equation (1) (Figure 1c), suggesting that the approximation of the flow structure is reasonable to first order, and obeys this integral constraint.

[11] The result of the assumptions made by the WTA model is an efficient approximation of the flow structure and the distribution of shear stress along the bed and banks. By assuming that the erosion rate depends on the local shear stress, the formulation can then be used to evolve channel cross sections quickly enough that both cross-sectional forms and longitudinal profiles can be modeled over geologically relevant timescales [e.g., *Wobus et al.*, 2006b]. The original WTA model makes the assumption that erosion rate scales linearly with shear stress [e.g., *Howard and Kerby*, 1983]; however, any erosion rule that depends on the local shear stress could also be used.

2.2. Ray-Isovel Model

[12] *Kean and Smith* [2004] developed a method for determining the distribution of velocity and boundary shear stress across the entire cross section of a straight channel. Their method, which is a generalization of the approach of *Houjou et al.* [1990], numerically solves the momentum equation for steady, uniform flow using a ray-isovel turbulence closure. The approach provides a foundation for making sediment transport and geomorphic adjustment calculations, because it accurately resolves the relative distribution of stress between the bed and the banks of channels of arbitrary cross section. A brief overview of the method is given below. The reader is referred to *Kean and Smith* [2004] for a complete description of the approach, as well as descriptions of the additional steps required to incorporate the effects of form drag on roughness elements such as the stems of rigid vegetation, which will be neglected within the analysis of this paper.

[13] The ray-isovel model calculates fluid stress along curves (rays) that run perpendicular to lines of constant velocity (isovels) (Figure 2). The rays begin perpendicular to the channel boundary and end at the surface. *Leighly* [1932] first used this approach empirically to determine the stress distribution in natural channels from measured velocity fields. Simultaneous determination of both the velocity and boundary shear stress fields, however, requires numerical integration. The procedure involves alternately solving for the velocity field, defined in a Cartesian coordinate system, and for the fluid stress and eddy viscosity fields, which are defined more easily in the orthogonal ray-isovel coordinate system. The momentum equation for steady, stream-wise uniform flow in a channel is given by

$$0 = \rho g S + \frac{\partial}{\partial y}\left(\rho K \frac{\partial u}{\partial y}\right) + \frac{\partial}{\partial z}\left(\rho K \frac{\partial u}{\partial z}\right) \tag{6}$$

[14] In this equation, K is the kinematic eddy viscosity and u is the velocity in the downstream (x) direction. The variables y and z represent the cross-stream and vertical directions, respectively. The boundary conditions for equa-

Figure 1. Wobus, Tucker and Anderson model summary. (a) Schematic showing channel cross section and coordinate system. Coordinate r is measured along radii from the bed to the channel midpoint; total distance along each radius is R. Boundary shear stress at each point on the wetted perimeter is calculated from the mean velocity gradient, $U_{\max}/R$. Velocity is assumed to be zero near the margin of the channel at a roughness length l_0 along these radii. (b) Calculation of mean velocity from boundary shear stress. (left) Isovels constructed by employing the law of the wall along bed-normal rays drawn from the channel bed to the water surface. (right) Cartesian regridding of the resulting two-dimensional velocities to calculate a cross-sectionally averaged mean velocity. (c) Comparison of cross-sectionally averaged mean velocity resulting from Figure 1b with the mean velocity required to satisfy conservation of mass. Agreement in all model runs is within 1–3%.

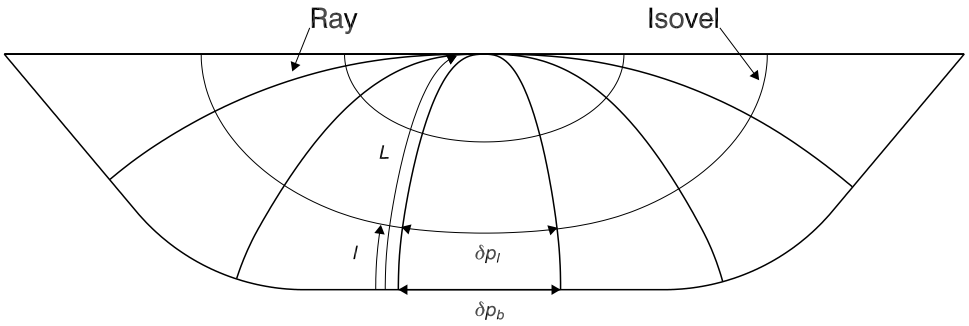

Figure 2. Ray-isovel model setup. Rays begin orthogonal to the channel bed and are everywhere perpendicular to the lines of constant velocity (isovels). Here δp_b is the perimeter distance along channel bed and δp_l is the distance between rays at a distance l from the bed as measured along a ray. See text for model description.

tion (6) are that $\partial u/\partial z = 0$ at the water surface and $u = 0$ at a roughness length perpendicular to the boundary, $l = l_0$.

[15] The two terms in parentheses in equation (6) represent the deviatoric stress components τ_{yx} and τ_{zx}. Stress throughout the channel also can be specified by the rays, which define the direction of shear along which mixing occurs. The boundary shear stress (τ_b) between any two rays is simply equal to the downstream component of the weight of water between the rays divided by the length of wetted perimeter that separates them. Similarly, the interior shear stress along a ray a distance l from the boundary (τ_{lx}) is equal to the downstream component of the weight of water between two rays from l to the surface, divided by length along the isovel between the two rays. The ray-isovel coordinate system also is used to define a scalar eddy viscosity that relates τ_{lx} to the velocity gradient along a ray

$$\tau_{lx} = \rho K(\partial u/\partial l) \tag{7}$$

[16] The functional form of K near the boundary used by *Kean and Smith* [2004] is

$$K = \kappa u_* l(\tau_{lx}/\tau_b) \tag{8}$$

where κ is von Karman's constant, and u_* is the shear velocity. The eddy viscosity is assumed to increase linearly along each ray until it reaches the channel-scale eddy viscosity, K_o, defined as

$$K_o = \kappa(gSR)^{1/2} H_c/\beta \tag{9}$$

where H_c is the flow depth, R is the hydraulic radius, and β is a constant equal to 6.24. In an infinitely wide channel, the value of $\beta = 6.24$ is that required to match the eddy viscosity profile in the linearly increasing portion of the profile (i.e., $z/H < 0.2$) with the channel-scale eddy viscosity defined in equation (9) (see *Kean and Smith* [2004] for a complete discussion). This algebraic form for the eddy viscosity has previously been shown to give good agreement with experimental results [e.g., *Shimizu*, 1989].

[17] Having defined K for the entire cross section it is possible to solve equation (6) iteratively for u. The procedure starts with an initial guess of the boundary shear stress distribution and the velocity in the interior. Then the computation alternately solves the momentum equation (6) for u and equations for τ_b, τ_{lx}, and K until the flow solution converges. To reduce the number of grid points required in the calculation, the velocity within a short distance of the boundary is computed using the law of the wall

$$u = \frac{u_*}{\kappa} \ln\left(\frac{l}{l_o}\right) \tag{10}$$

[18] To date, the ray-isovel method described above has been applied only to laboratory flumes and natural channels with fixed cross-sectional geometries [*Griffin et al.*, 2005; *Kean and Smith*, 2005]. In this paper, a simple erosion component is added to the modeling framework in order to permit the channel to change shape with time on the basis of the flow and sediment transport conditions. The erosion model used here is identical to the one used by *Wobus et al.* [2006b] and assumes that the bed-normal erosion rate scales linearly with the local boundary shear stress. Equilibrium channel geometries using this erosion model are computed for a constant discharge, channel slope, and channel roughness. The calculation begins with an initial cross section, the choice of which is arbitrary. Next, the stage corresponding to the specified discharge is determined iteratively. This phase of the computation typically requires three trials and is necessary because the discharge is not specified a priori in the ray-isovel calculation (i.e., it is an output of the calculation). After the flow and boundary shear stress fields for the specified discharge are determined, the y and z components of the erosion rate are determined from the bed slope and local boundary shear stress, and a new cross section is computed. The calculation is repeated in this manner until the channel geometry reaches an equilibrium shape. Despite being computationally less intensive than fully three-dimensional (3-D) numerical flow and geomorphic adjustment models, the ray-isovel approach requires approximately 2 orders of magnitude more time to compute equilibrium geometries relative to the semianalytical WTA method described in the previous section.

2.3. Depth-Slope Product

[19] An assumption that is commonly employed in modeling the long-term evolution of bedrock channels is that the

cross-sectionally averaged shear stress is proportional to the depth-slope product

$$\bar{\tau} = \rho g H S \tag{11}$$

where $\bar{\tau}$ is the average shear stress and H is the average depth of the flow. This expression can be derived from equation (3) for channels with a large width-to-depth ratio, where the width is approximately equal to the wetted perimeter and the wall stresses can be neglected. By extension, one might expect that a momentum balance could be applied locally, such that the local shear stress can be approximated by the local depth-slope product [e.g., *Li et al.*, 1976; *Parker*, 1979]:

$$\tau(y) = \alpha_n \rho g H(y) S \tag{12}$$

where $\tau(y)$ and $H(y)$ are the shear stress and depth evaluated at position y along the cross section, and α_n is a constant coefficient that ensures the momentum balance in (3) is satisfied.

[20] While it is appealing in its simplicity, there are at least two problems with this approximation of the shear stress distribution that make it unsuitable for modeling the dynamics of bedrock rivers. First, this formulation is inappropriate for channels with small width-to-depth ratios, since wall stresses represent an important component of energy dissipation and cannot be neglected to arrive at equation (11). Second, even in a wide channel, the depth-slope product gives a poor approximation to local stress close to the banks. For these reasons, such a model cannot be used to evolve cross sections through time, since the formulation would inevitably lead to a runaway feedback in which depth and local shear stress grow indefinitely in the deepest portions of the channel. The inadequacy of the depth-slope product for expressing local stress along a complete channel perimeter may at first seem startling. To demonstrate how and where the depth-slope product deviates from boundary stress even under unidirectional flow, several of the illustrations below compare boundary shear stress distribution with the stresses one would estimate using $\tau(y) = \alpha_n \rho g H(y) S$.

3. Intermodel Comparisons

[21] Although the details of the two hydraulic models are different, the essence of the WTA and ray-isovel model (RIM) models is quite similar. Both models reconstruct the flow field by assembling a series of rays through the flow, and calculating a 1-D velocity structure along each ray. These 1-D velocity structures are then used to construct the full two-dimensional structure of the flow. The main differences between the two formulations lie in the orientation of these rays within the flow, and in the parameterization of the kinematic eddy viscosity. The WTA model uses a simplification in which the rays are straight line segments drawn normal to the bed, while the RIM model ensures that the rays are constructed so that they are everywhere normal to lines of constant velocity. In addition, the RIM model uses a two-part eddy viscosity formulation, while the WTA model does not.

[22] To facilitate intermodel comparisons, the RIM and WTA models were each run to steady state under a series of identical discharge, slope, and roughness conditions. In all cases, model cross sections were started from a simple "V-shaped" geometry, and were allowed to evolve until both the channel geometry and the flow field stabilized. Below we compare the models' representations of channel cross-sectional shape, velocity structure, and boundary shear stress distributions at steady state, along with the shear stress predictions of the depth-slope product rule for our equilibrium geometry (section 3.1). We then briefly explore the scaling relationships among width, depth, slope, discharge, and roughness for the WTA and RIM models (section 3.2). In all cases, we find that the WTA and RIM models behave similarly, suggesting that the simplified WTA model captures the essence of the more computationally expensive RIM hydraulic formulation.

[23] We next compare the WTA model to the predictions from other available models and laboratory measurements for channels with both straight and gently curving cross-sectional profiles (section 3.3). Finally, we compare the shear stress distributions predicted by the RIM and WTA models for a set of prescribed cross-sectional shapes with varying aspect ratios. This inspires improvements to the WTA model that allow better representation of the flow structure in wide channels (section 3.4).

3.1. Flow Structure

[24] The channel form in both models must evolve to a steady state geometry in which (1) the cross-sectional shape and velocity structure are adjusted to convey the prescribed discharge; (2) the momentum balance in equation (3) is satisfied; and (3) the shear stress distribution at steady state (and therefore the erosion rate) is adjusted such that the channel will maintain its cross-sectional shape as it incises. The model comparisons described below are based on a prescribed discharge of 20 m^3/s, a gradient of 0.0015, and a roughness length (l_0) of $\sim$0.002 m. Note that intermodel comparisons using other combinations of discharge, gradient, and roughness length scales yield similar results.

[25] The steady state cross-sectional form and isovel structures predicted by the two models are shown in Figures 3a–3c. Both cross sections are quasi parabolic, with width-to-depth ratios of $\sim$3.3 for the WTA model and $\sim$3.9 for the RIM model. The steady state cross-sectional areas for the two models are $\sim$10.9 and $\sim$10.6 m^2, respectively. The RIM has a slightly higher-mean velocity ($\sim$3%), as required to compensate for its smaller cross-sectional area.

[26] The most important difference in the flow structure between the two models is the velocity structure in the upper portion of the flow (Figure 3d). This difference is primarily a result of the differences in the way the two models treat the eddy viscosity: to boost computational efficiency, the WTA model extends the law of the wall all the way to the free surface, which builds in an assumption that Prandtl's eddy length scale (L in equation (4)) grows with the flow depth throughout the water column. In contrast, the RIM model assumes a two-part eddy viscosity, in which the eddy length scale reaches the constant channel-scale value at about 20% of the distance along a ray from the boundary to the surface. As a result, the modeled flow

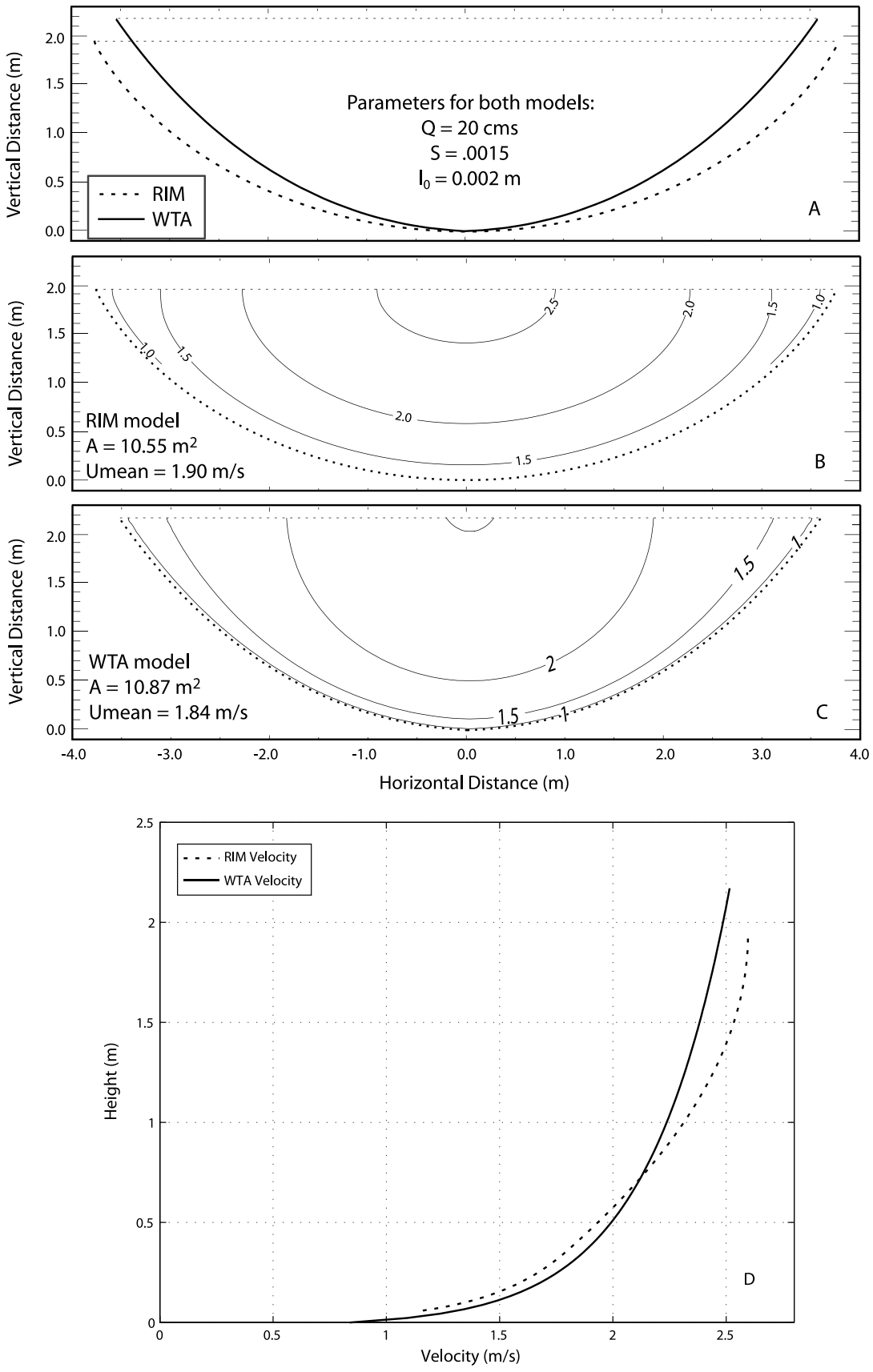

Figure 3. RIM and WTA model comparisons. In all cases $Q = 20$ m^3/s, $S = 1.5e - 3$ and $l_0 = 0.002$. (a) Steady state cross-sectional geometry. (b and c) Isovel structure for steady state RIM and WTA models, respectively. (d) Vertical profiles of velocity along channel midline.

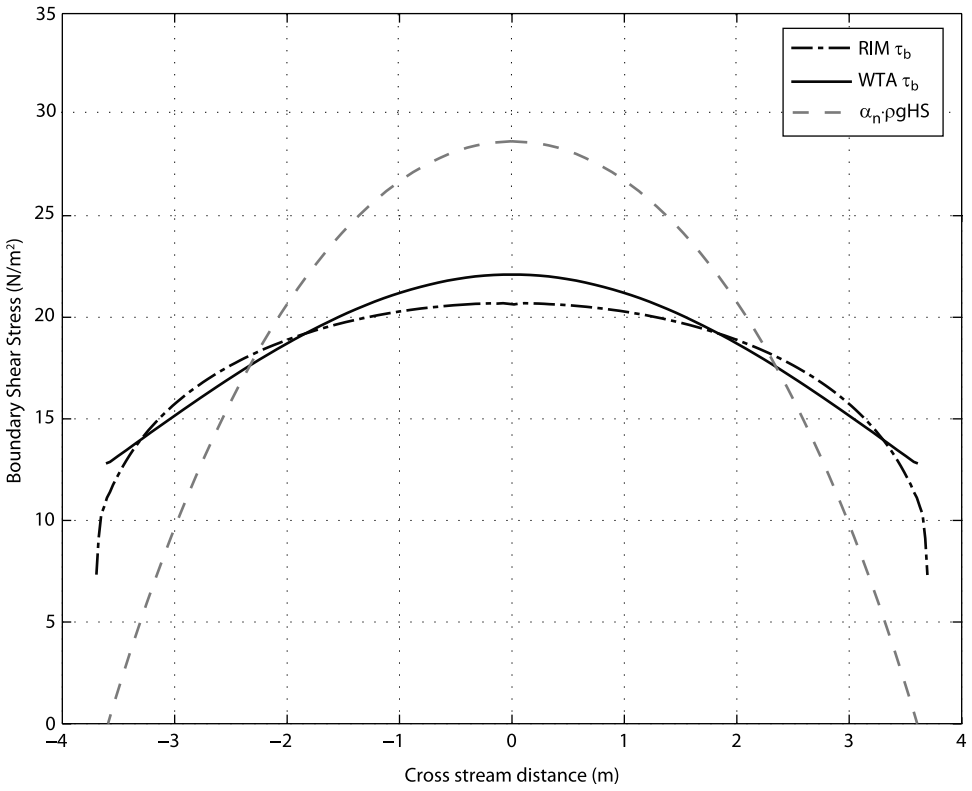

Figure 4. Steady state bed shear stress distributions for RIM and WTA models for steady state geometries shown in Figure 3. Shear stress distribution using local depth-slope product rule, normalized to ensure momentum conservation, is shown for comparison.

velocities are higher for the RIM in the upper portion of the flow.

[27] Also as a result of these differences in the treatment of the flow hydraulics, the near-bed velocity gradient is higher for the WTA model. This leads to a peak shear stress at the channel midpoint that is approximately 7% higher for the WTA model than it is for the RIM model (Figure 4). To satisfy the integral constraint imposed by conservation of momentum (i.e., equation (3)), the boundary shear stress in the WTA model is commensurately lower along the margins of the flow. As noted by *Wobus et al.* [2006b] (equations (7) and (8)), the shape of the shear stress distribution can be related to the vertical lowering rate and the shape of the channel at steady state. The higher-peak shear stress implies that the rate of vertical translation will be slightly faster for the WTA model than for the RIM model for a given erosion law.

[28] For comparison, we also include in Figure 4 the shear stress distribution predicted by the depth-slope product rule for the steady state geometry shown in Figure 3c. Note that this formulation substantially overpredicts the shear stress at the channel midpoint, and substantially underpredicts the stress along the channel margins, relative to both the WTA and RIM models. This shortcoming arises because wall stresses are neglected by this simplification of the flow hydraulics, so that the shear stress distribution is artificially weighted toward the channel midpoint. This also underscores the inherent problem with a depth-slope product rule in capturing the dynamics of bedrock channel adjustment: since boundary shear stress in such a formulation is always concentrated in the deepest portions of the channel, the implementation of any erosion rule that depends on shear stress will generate runaway deepening. As a result, wall stresses must be incorporated into our models if we hope to capture the dynamics of bedrock channel adjustment.

3.2. Scaling Relationships

[29] Even with the simplifications to the hydraulics such as those used by the WTA model, large-scale landscape evolution models typically cannot afford the computational expense of reconstructing the flow field at every individual channel cross section. In order to "scale up" the fluvial hydraulics to make predictions about landscape evolution, it is therefore useful to distill the predictions of our models into simple scaling relationships. To do this, we ran the WTA and RIM models to steady state under a variety of discharge, slope, and bed roughness conditions to evaluate their predictions for these scaling coefficients.

[30] Figure 5a shows the scaling of equilibrium width as a function of discharge. For the range of roughness values used in both model formulations, power law regressions on the width-discharge relationships yield exponents between 0.36 and 0.38. Figure 5b shows the scaling of equilibrium width as a function of slope. Regressions on the width-slope relationship yield exponents between −0.18 and −0.19. Finally, Figure 5c shows the relationship between width and depth for bed roughness values (l_0) ranging from 0.2–

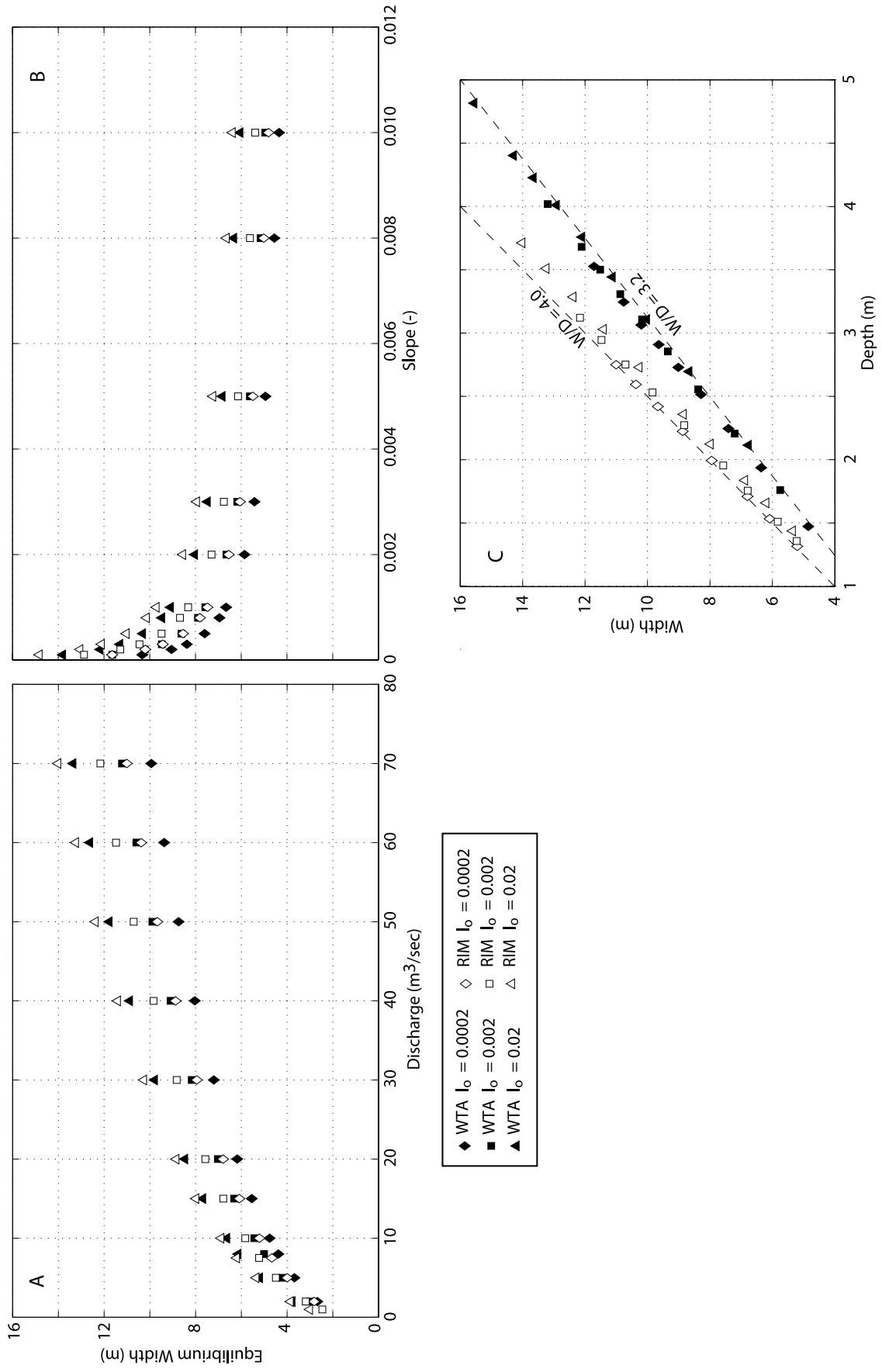

Figure 5. Scaling relationships for steady state channel width as a function of (a) discharge and (b) gradient for WTA and RIM models. Both models predict scaling relationships close to $W \sim Q^{0.4}$ and $W \sim S^{-0.2}$. (c) Width versus depth for WTA and RIM models. Both models predict an approximately constant width-to-depth ratio for a given roughness length scale.

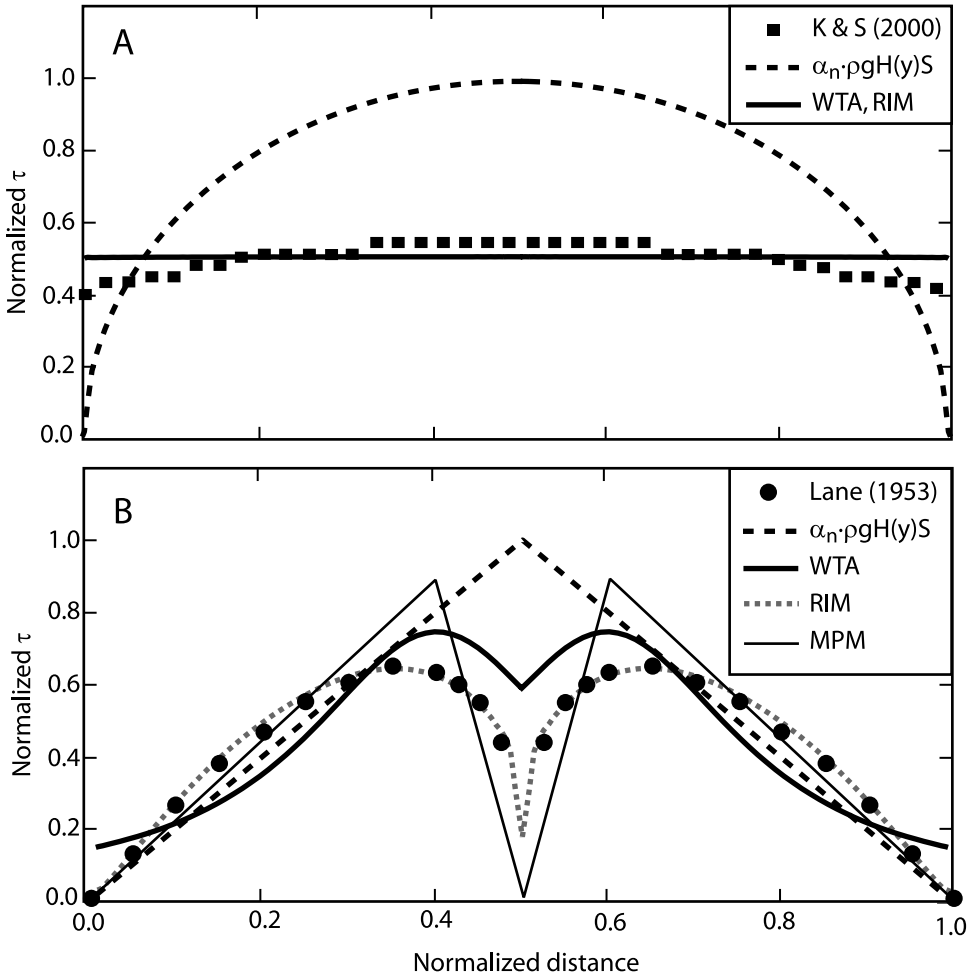

Figure 6. Comparisons between WTA and RIM models, depth-slope product, and independently derived experimental data for half-pipe and V-shaped channel geometries. (a) Comparisons with *Knight and Sterling*'s [2000] experimental Preston tube measurements of shear stress for a half pipe. (b) Comparisons with *Lane*'s [1953] membrane-analogy experiments for a V-shaped geometry. Results of *Khodashenas and Paquier* [1999] Merged Perpendicular Method (MPM) shown for comparison.

20 mm. In all cases, the width-to-depth ratio for smoother channels is slightly larger than that for rougher channels for a given discharge and slope. However, both models predict nearly constant width-to-depth ratios at steady state, ranging from ~3.2 for the roughest WTA channels to ~4.0 for the smoothest RIM channels. Note that the dependence of *W*/*D* on roughness is slightly weaker than that reported by *Wobus et al.* [2006b], reflecting an improved discharge matching scheme that imposes a tighter constraint (1%) on mass balance.

[31] The result of either the WTA or the RIM formulation is therefore a model that predicts channels with (1) a nearly constant width-to-depth ratio at steady state; (2) a power law relationship between width and discharge with an exponent near 2/5 (holding slope constant); and (3) a power law relationship between width and slope with an exponent near −1/5. For all parameters examined, the agreement between the two models is within ~10%. To the extent that the RIM model is an accurate representation of the hydraulics of natural channels [e.g., *Kean and Smith*, 2005], this implies that the WTA model should be able to capture the dynamics of channel adjustment to a similar level of accuracy.

3.3. Comparisons With Other Data Sets

[32] In addition to the intermodel comparisons outlined above, it is instructive to compare the predictions of the WTA model with experimental data from laboratory flumes, and with the results of other numerical schemes for approximating shear stress distributions. For brevity, we limit our comparisons to two of the simplest end-member geometries: a half-pipe geometry such as that used by *Knight and Sterling* [2000] in their experiments; and a V-shaped geometry for comparison with the work of *Lane* [1953] as described by *Khodashenas and Paquier* [1999] in their evaluation of the geometrical "Merged Perpendicular Method." To facilitate comparisons, we normalize all shear stress values by the depth-slope product at the channel midpoint.

[33] Figure 6a shows the results of our comparison with the experimental data of *Knight and Sterling* [2000]. The WTA model predicts a constant shear stress across the

channel, with a magnitude equal to half the midpoint depth-slope product. (The factor 1/2 arises because the hydraulic radius R is equal to $H_c/2$ for a half pipe; the shear stress is everywhere equal to ρgRS). The prediction of the WTA model agrees favorably with the experimental results, except that the latter indicate a slightly higher shear stress at the channel midpoint ($1.1\rho gHS$) and a slightly reduced shear stress along the channel margins ($0.8\rho gHS$). As noted by *Knight and Sterling* [2000], this modest redistribution of shear stress toward the channel midline is most likely a result of secondary flows generated near the margins of the flow. Note that explicit modeling of these secondary currents requires a substantial increase in computation time, and will not be considered further here [*Naot et al.*, 1993; *Ma et al.*, 2002; *Knight et al.*, 2007].

[34] The second data set we use for comparison, shown in Figure 6b, is the shear stress distribution in a V-shaped geometry as described by *Lane* [1953]. Note that these data were derived using a "membrane analogy," in which an elastic membrane is stretched over the channel form of interest and the local curvature is used as a proxy for shear stress [e.g., *Olsen and Florey*, 1952]. The measurements therefore differ from the direct Preston tube measurements used by *Knight and Sterling* [2000]. Nonetheless, this data set provides another experimentally derived estimate of the shear stress distribution for a well-constrained geometry. In this case, both the shear stress distribution described by *Lane* [1953] and the distribution predicted by the WTA model have a pronounced trough near the channel midpoint. In the WTA model, this trough arises because the center of the channel is actually further from the point of maximum velocity than the sloping channel sidewalls. Since the mean velocity gradient between the channel midline and the bed dictates the shear stress distribution in the WTA model, this results in a redistribution of maximum shear stress toward the portions of the channel with the shortest distance to the high-velocity midpoint. The same pattern is seen in the RIM model (Figure 6b). Note that both the RIM and WTA models are an improvement over the Merged Perpendicular Method described by *Khodashenas and Paquier* [1999], which is a purely geometrical method for distributing shear stress across irregular channels.

[35] Notably, the depth-slope product rule does poorly in estimating the shear stress in both of the cases outlined here: in general, using a depth-slope product for a narrow channel will substantially overpredict the shear stress in the deepest portions of the channel, and substantially underpredict the shear stress along the channel margins where the depth goes to zero. Again, we stress that this shortcoming arises because wall shear stress cannot be neglected in modeling narrow bedrock channels.

3.4. Prescribed Geometries

[36] On the basis of the comparisons outlined above, the WTA model appears to strike a reasonable balance between computational efficiency and hydraulic fidelity for a range of channel geometries with relatively low width-to-depth ratios. But what about channels that have evolved to a larger width-to-depth ratio, due to the bed becoming protected by a mantle of coarse sediment [e.g., *Hancock and Anderson*, 2002; *Wobus et al.*, 2006a; *Turowski et al.*, 2008a], or the banks becoming weakened by subaerial weathering [e.g., *Montgomery*, 2004]? In this case, the assumption that the velocity gradient at the bed scales with the distance from the channel midpoint may be problematic since wider channels appear to be characterized by a high-velocity "core" of finite width [e.g., *Knight and Sterling*, 2000; *Kean and Smith*, 2005].

[37] To improve model flexibility in such situations, we modified the original WTA formulation to better approximate the flow structure in wider channels. Our model adjustments included the following:

[38] 1. Rather than assuming the maximum velocity occurs at a single point, the flow is assumed to be characterized by a "high-velocity core" in which the surface velocity is approximately constant. The width of this high-velocity core is defined as the portion of the channel over which the bed-normal distance to the water surface remains approximately constant (e.g., Figure 7a).

[39] 2. The surface velocity within the high-velocity core is first approximated by assuming the shear stress along the bed below it is equal to ρgHS (as must be the case in infinitely wide channels). The shear velocity u is then $\sqrt{gHS}$ and the surface velocity is calculated by employing the law of the wall

$$U_{\mathrm{surf}} = \frac{u_*}{\kappa} \ln\left(\frac{H}{l_0}\right) \tag{13}$$

[40] 3. The distribution of surface velocities between the edge of the high-velocity core and the channel wall is assumed to be logarithmic, reaching zero at a roughness length l_0 from the channel wall.

[41] 4. The distance $\Re$ used to calculate the near-bed velocity gradient beyond the high-velocity core is assumed to be the length of a bed-normal vector from the channel bed to the surface, rather than the distance from the bed to the channel midpoint.

[42] 5. The near-bed velocity gradient is calculated using the above approximations for surface velocities and bed-normal distances, and equation (3) is used to ensure a momentum balance.

[43] This set of assumptions allows us to relax the assumption of a maximum velocity "point" at the channel midline, and to reconstruct the velocity field and the distribution of shear stresses for channels with larger width-to-depth ratios. The predictions of this modified WTA model and the depth-slope product rule are compared with the RIM model in Figure 7, for prescribed channels with width-to-depth ratios ranging from 5 to 15.

[44] This modified WTA model predicts a shear stress distribution that is very similar to the RIM model for large width-to-depth ratios. For wide channels, the shear stress distributions predicted by the RIM and modified WTA models diverge most substantially in the corners of the flow where the horizontal bed merges with the bank (Figure 7c). Note that these corners are also the locations where secondary currents are likely to be most important in modifying the flow structure of natural channels [e.g., *Naot et al.*, 1993; *Knight and Sterling*, 2000; *Knight et al.*, 2007]. Experimental work indicates that these secondary currents

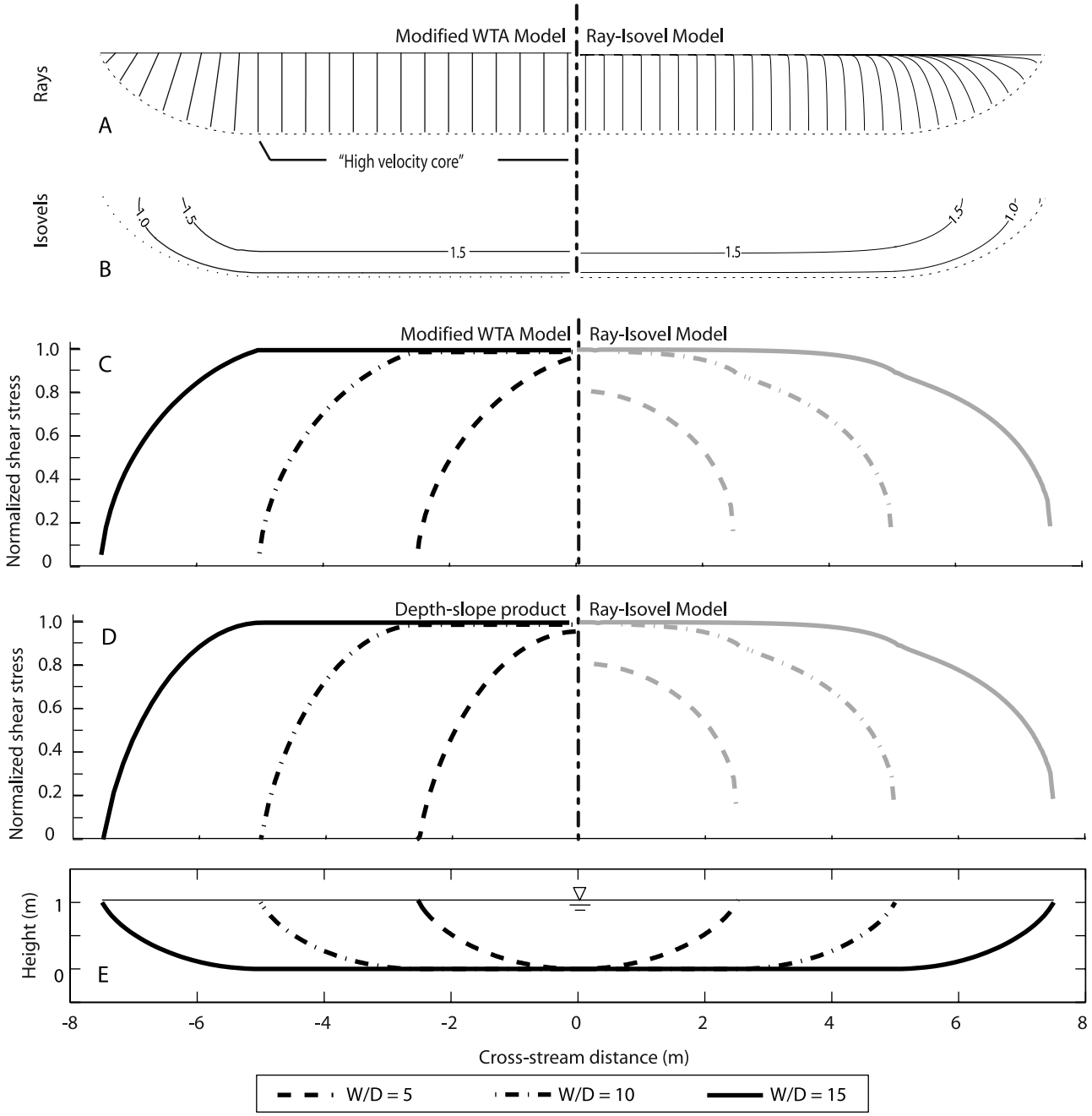

Figure 7. Model comparisons for varying width-to-depth ratios. (a–d) (right) Predictions for RIM model. (left) Predictions for modified WTA model (Figures 7a–7c) and predictions for depth-slope product (Figure 7d). Model-generated rays (Figure 7a) and isovels (Figure 7b) for WTA and RIM models for *W*/*D* of 15. Shear stress distributions for WTA (Figure 7c) and depth-slope product (Figure 7d) compared to RIM model for *W*/*D* values between 5 and 15. (e) Prescribed channel geometries for all models.

can influence the shear stress distribution in this region, particularly as these corners become more angular [*Knight and Sterling*, 2000; *Knight et al.*, 2007], but modeling the effects of these secondary currents would take us yet another step further from the computational efficiency we seek. As a result, we suggest that the general agreement between the modified WTA and RIM models is reasonable for our purposes.

[45] Note that for channels with large width-to-depth ratios, the depth-slope product rule does a reasonable job of replicating the shear stress distributions predicted by the RIM model (Figure 7d). In wider channels, wall stresses become less important so that calculating the center shear stress via the depth-slope product is reasonable. However, we emphasize that there is no physical basis for applying a

depth-slope product rule locally to calculate the wall stresses along the banks of a wide channel.

[46] Figure 7 indicates that the predictive capacity of both the modified WTA model and the depth-slope product rule become limited as width-to-depth ratios decrease from 10 to 5. Compared to the RIM model, both of these formulations accurately predict the peak shear stress for $W/D = 10$, but overpredict the peak shear stress by ~20% for a width-to-depth ratio of 5 (Figures 7c and 7d). Notably, early use of the ray-isovel model by *Shimizu* [1989] is consistent with this observation: a summary of their numerical simulations finds that the depth-slope product becomes a good predictor of the shear stress in the center of the channel only as the width-to-depth ratio increases to ~10. This is also consistent with a range of experimental work summarized by *Khodashenas and Paquier* [1999] all of which suggests that wall stresses rapidly become important in the center of the channel as width-to-depth ratios drop below ~5. At higher width-to-depth ratios, wall stresses account for less than ~10% of total stress, at which time the depth-slope product should predict the peak shear stress to within the same order. However, even in these wide channels, wall stresses remain locally important in affecting the near-bank bed stress, and must be considered if we hope to model lateral erosion of natural channels.

[47] The comparisons outlined above suggest that wall stresses, which are inherently incorporated in both the WTA and RIM models, need to be modeled for channels with low width-to-depth ratios. Although field studies that explicitly describe the geometry of bedrock channels are rare, available data suggest that width-to-depth ratios less than ~5 are not uncommon in natural systems [e.g., *Finnegan et al.*, 2005; *Whittaker et al.*, 2007]. It follows that a model developed to understand the evolution of bedrock channels must include wall stresses. Further, it must be flexible enough to incorporate a high-velocity core to the flow as width-to-depth ratios increase. We suggest that the combination of the original WTA model with the modified formulation outlined above strikes this balance. Future dynamic models of channel evolution in which changes in bed state might drive extreme widening or narrowing (e.g., because of large sediment influxes from landsliding) will implement changes between these end-members, guided by empirical observations of shear stress distributions in natural and experimental channels [e.g., *Shimizu*, 1989; *Knight et al.*, 1994].

4. Discussion

[48] The WTA model originally formulated by *Wobus et al.* [2006b] is based on a number of approximations that allow the model to be efficient enough to examine channel evolution over large spatial and temporal scales. On the basis of our comparisons with the ray-isovel formulation [e.g., *Leighly*, 1932; *Shimizu*, 1989; *Houjou et al.*, 1990; *Kean and Smith*, 2004], and with other available data from the literature [*Olsen and Florey*, 1952; *Lane*, 1953; *Khodashenas and Paquier*, 1999; *Knight and Sterling*, 2000] these approximations appear to capture the essence of velocity and boundary shear stress distributions driven by stream-wise flow in natural channels. In particular, the shape of the channels at equilibrium, the isovel structure, the shear stress distributions, and the scaling of width with slope and discharge are all within reasonable agreement between the two formulations, and between the model predictions and experimental results. Merging our original WTA model with a formulation that explicitly considers a widening high-velocity core as W/D ratios increase provides us with a model that can efficiently describe boundary shear stress distributions across the spectrum of concave up channel shapes.

4.1. A Constant Width-to-Depth Ratio?

[49] One of the intriguing findings of both the WTA and RIM models is that the steady state width-to-depth ratio is approximately constant, regardless of slope or discharge (Figure 5c). This finding is consistent with the assumption built into *Finnegan et al.*'s [2005] analytical model for the scaling of bedrock channel width with slope and discharge. However, as acknowledged both by *Finnegan et al.* [2005] and by *Turowski et al.* [2007] there is very limited field data to support the finding that width-to-depth ratios should be constant in nature. In fact, models that explicitly consider the effects of sediment in bedrock channels suggest that W/D may be highly variable due to downstream variations in sediment cover [*Wobus et al.*, 2006a; *Turowski et al.*, 2007].

[50] Despite these findings for models that explicitly consider sediment cover, *Whittaker et al.*'s [2007] data from the Fiamignano gorge in Italy suggests that width-to-depth ratios might actually approach a constant value when sediment cover is limited. Width-to-depth ratios from the Fiamignano exhibit a strongly nonlinear inverse relationship with channel gradient, which at first glance appears inconsistent with our findings. However, the channels with the highest W/D ratios are also those reported to have significant sediment cover, whereas the W/D ratios of high-gradient, cover-free channels asymptote to a value of ~3. These high-gradient channels with a nearly constant W/D ratio may in fact be the best natural analog for our model, since we do not explicitly consider the role of sediment in controlling channel incision. It is therefore instructive to consider the potential origin of a constant width-to-depth ratio for channels with limited sediment cover.

[51] As a way of gaining physical insight, we can manipulate the equations used in the WTA model to explore the origin of this constant width-to-depth ratio. For example, if we simplify equations (4) and (5) to express the rate of channel wall erosion as a function of the mean velocity gradient rather than the near-bed velocity gradient, we can write

$$\frac{d\Re}{dt} = B\left(\frac{U_{\max}}{\Re}\right)^2 \tag{14}$$

where B is a coefficient that includes the mixing length scale L and the erodibility of the substrate. At the channel midpoint, the radial distance is equivalent to the flow depth H_c, and the incision is purely vertical

$$\left.\frac{d\Re}{dt}\right|_{y=0} = \frac{dz}{dt} = B\left(\frac{U_{\max}}{H_c}\right)^2 \tag{15}$$

where z is the height of the bed relative to a datum in the underlying rock. Noting that at steady state the rate of vertical translation must everywhere be the same, and using the chain rule, equations (14) and (15) can be related as

$$B\left(\frac{U_{\max}}{\Re}\right)^2 = \frac{d\Re}{dz} \cdot B\left(\frac{U_{\max}}{H_c}\right)^2 \tag{16}$$

which can be simplified to yield

$$\int_0^{H_c} H_c^2 dz = \int_{H_c}^{W/2} \Re^2 d\Re \tag{17}$$

Here we can define the integration limits as follows for a steady state geometry: at the channel midpoint, $z = 0$ and $\Re = H_c$; where the water surface touches the bank $z = H_c$ and $\Re = W/2$. Evaluating the resulting expression, we find that $W = \sqrt{[3]}32\ H_c = 3.17H_c$ at steady state. Note that this is only an approximation since the near-bed velocity gradient used in the model is also a weak function of the ratio $\Re/l_o$ (see equation (5)). However, this manipulation of the governing equations yields insight into why the width-to-depth ratio should be constant, and what that constant should be, given our model formulation.

[52] Similar arguments could be made to suggest that W/D ratios should tend toward a constant value in natural bedrock channels, as long as three conditions are met: (1) the erosion rate is related to the local shear stress; (2) the local shear stress is related to the mean velocity gradient; and (3) the highest velocities occur near the center of the flow. To the extent that incision in natural channels adheres to these three first-order criteria, we might expect a tendency for channels to seek a constant W/D ratio [e.g., *Finnegan et al.*, 2005]. However, we again stress that this prediction is based on a simplified model that neglects sediment cover effects [*Wobus et al.*, 2006a; *Turowski et al.*, 2007, 2008a].

4.2. Origin of Scaling Relationships

[53] As shown by *Finnegan et al.* [2005], if the width-to-depth ratio is constant for a given channel, the power law scaling of width with discharge and slope can be derived analytically using a roughness equation for average velocity combined with mass balance. Using the Manning equation, this leads to

$$W \propto Q^{3/8} S^{-3/16} \tag{18}$$

while using the Chézy formulation employed by the WTA model (equation (1)) this gives

$$W \propto \sqrt{Q/u} \sim Q^{2/5} S^{-1/5} \tag{19}$$

Equation (19) is consistent with the scaling computed by the WTA model, as one would expect [*Wobus et al.*, 2006b]. Note that scaling relationships such as these are not as easily derived for the RIM model, since that formulation does not include closed form expressions for velocity or discharge as a function of width or slope.

4.3. Limitations of the Model

[54] As described in section 4.1, sediment cover appears to exert a strong influence on the shape of bedrock channels. A variety of experimental studies also underscore the importance of sediment for bedrock incision and channel shape. For example, *Shepherd* [1972], *Wohl and Ikeda* [1997], *Finnegan et al.* [2007], and *Johnson and Whipple* [2007] each describe controlled laboratory experiments in which sediment and water were passed across cohesive, eroding substrates. In all cases, channel shape evolves as a complex function of water discharge, local gradient, and importantly, sediment flux. The latter creates a feedback mechanism by which sediment is preferentially transported through topographic lows, enhancing incision of the substrate when sediment flux is low. However, consistent with the predictions of *Gilbert* [1877] and *Sklar and Dietrich* [2004], both experiments also uncover a negative feedback wherein an alluvial cover is formed on the bed that ultimately inhibits further incision. Sediment is not explicitly considered in either the WTA or RIM model, an obvious shortcoming of the formulations used here. However, preliminary modeling which accounts for the effects of sediment corroborates its importance in determining bedrock channel shape [*Wobus et al.*, 2006a].

[55] An additional complexity that needs to be addressed is the influence of variable water and sediment discharges on channel evolution [e.g., *Lague et al.*, 2005; *Stark*, 2006]. In natural channels, such variability in discharges will influence both the time-averaged thickness of alluvial cover and the velocity structure of the flow, such that single realizations of these parameters might not capture the hydraulics of the most important flow events. For example, alternating periods of high and low sediment flux might influence the relative importance of widening versus deepening in channel evolution [*Hancock and Anderson*, 2002; *Hartshorn et al.*, 2002; *Turowski et al.*, 2008a, 2008b], and wetting and drying of channel banks might lead to important changes in cross-channel erodibility that could strongly control the hydraulic geometry of natural channels [e.g., *Montgomery*, 2004].

[56] Finally, both the WTA and RIM models neglect the effects of secondary currents. As illustrated by our comparisons with experimental data, these currents can have the effect of redistributing boundary shear stresses, even for smooth channel forms (Figure 6). Furthermore, secondary currents are likely to become increasingly important as channel shapes become more angular and turbulence is enhanced. Models that explicitly account for the effects of secondary flows have been developed, but these models also increase model runtimes.

4.4. Numerical Approximations

[57] Both the WTA and RIM formulations make a series of numerical approximations in order to efficiently reproduce the flow structure in model channels. The effects of these approximations are likely to be of second order compared to the omission of sediment cover, secondary currents, and variable discharge as discussed above. Nonetheless, for completeness we briefly discuss here some of these numerical approximations.

[58] In finding the flow depth required to match the prescribed discharge (equations (1) and (2)), the WTA

model approximates the cross-sectional area of the flow by summing the areas of individual rectangles. As the node spacing decreases, this rectilinear approximation more closely approaches the area enclosed by the curvilinear cross section. However, this formulation is likely to introduce small errors into the calculation of cross-sectional area. In addition, the discharge-matching routine adds nodes to the upper portion of the cross section until the prescribed and modeled discharges match to within 1%. A better match to the discharge could be forced; however, since this scheme is already computationally intensive, a 1% match was deemed appropriate. Finally, as shown in Figure 1c, the mean velocity calculated from the boundary shear stress distribution does not always perfectly match the mean velocity required to convey the prescribed discharge (equation (1)). Again, in light of the close fit between models and the need for efficiency, iterative schemes that would improve this fit were not deemed appropriate.

[59] The numerical implementation of the RIM model also requires approximations that may influence its predictions of the flow structure. The model solves equation (6) using a boundary-fitted rectangular grid and the solution scheme of *Patankar* [1980]. A separate curvilinear grid following rays is used to solve the equations for shear stress and eddy viscosity. These computational grids must be constructed such that they minimize any systematic numerical errors in the calculations of velocity and boundary shear stress, which, in turn, produce artificial effects on the predictions of channel geometry. The number and spacing of the nodes for the computational grids was optimized by comparing model-calculated patterns of velocity and boundary shear stress to analytic solutions available for (1) an infinitely wide channel, and (2) a semicircular channel (half pipe). The semicircular channel comparison provides the strongest test of the numerics because it has geometric characteristics similar to the narrow channels that are the focus of this paper. On the basis of these comparisons, a mean cross-stream and vertical node spacing of about $H/50$ was used for the rectangular grid. This spacing corresponds to approximately 3000 active computational nodes for a channel having the geometry shown in Figure 3b. About twice as many nodes are used to define the curvilinear grid along rays in order to better resolve the near-surface ray structure and to reduce errors in interpolating the eddy viscosity field from the curvilinear grid to the rectangular grid, which is required to solve (6). It is likely that the desired computational accuracy could be achieved with fewer nodes using a numerical discretization of equation (6) on the basis of nonrectangular elements (which are better suited for fitting curved boundaries). Such a scheme, however, has not yet been implemented.

5. Conclusions

[60] In order to understand the response of landscapes to changes in climatic or tectonic conditions, landscape evolution models must accommodate the simultaneous evolution of channel width and gradient to these environmental controls. While there have been a number of notable recent advances in understanding the width response of natural channels [*Finnegan et al.*, 2005; *Stark*, 2006; *Whittaker et al.*, 2007], fully dynamic models have remained elusive due in part to the computational expense of modeling the full flow field in these channels. The model proposed by *Wobus et al.* [2006b] requires a number of approximations to the flow field in order to boost computational efficiency and achieve the goal of fully flexible channels. Despite these approximations, however, we have shown here that the first-order predictions of the model match well those derived from more sophisticated parameterizations of fluvial hydraulics and with available experimental data from laboratory flumes. Our modeling framework will in the future be used to investigate how sediment cover influences the shape of natural channels, how strath terraces are formed, and how a dynamic width response modulates the tempo of landscape response.

Notation

A cross-sectional area of flow [L^2].
B coefficient relating erosion rate to mean velocity gradient [LT].
C Chezy smoothness coefficient [$L^{0.5}T^{-1}$].
K kinematic eddy viscosity [L^2T^{-1}].
H_c centerline flow depth [L].
r coordinate measured along radii to channel midpoint [L].
R hydraulic radius [L].
S gradient [dimensionless].
$\overline{u}$ mean velocity [LT^{-1}].
U velocity at a point [LT^{-1}].
l_0 roughness length scale [L].
L Prandtl's mixing length scale [L].
dp length of an element along channel perimeter [L].
P total wetted perimeter length [L].
u_* shear velocity [LT^{-1}].
κ von Karman's constant [dimensionless].
β constant needed to match upper and lower eddy viscosity profiles in RIM.
τ_b boundary shear stress [$ML^{-1}T^{-2}$].
τ_{lx} interior shear stress along rays [$ML^{-1}T^{-2}$].
α_n normalization factor used in depth-slope product rule.
$\Re$ total radial distance from channel margin to midpoint [L].

[61] **Acknowledgments.** We thank Jens Turowski, Dimitri Lague, Rob Ferguson, and an anonymous reviewer for their extremely thorough and constructive reviews. This work was funded by a CIRES postdoctoral fellowship to C.W.W., by a NSF grant EAR-062199 and ARO grant 47033-EV awarded to G.E.T., and by a NSF grant EAR-0724960 to Suzanne P. Anderson.

References

Amos, C. B., and D. W. Burbank (2007), Channel width response to differential uplift, *J. Geophys. Res.*, *112*, F02010, doi:10.1029/2006JF000672.

Beaumont, C., P. Fullsack, J. Hamilton, and K. R. E. McClay (1992), Erosional control of active compressional orogens, in *Thrust Tectonics*, edited by K. McClay, pp. 1–18, Routledge, Boca Ranton, Fla.

Berlin, M. M., and R. S. Anderson (2007), Modeling of knickpoint retreat on the Roan Plateau, western Colorado, *J. Geophys. Res.*, *112*, F03S06, doi:10.1029/2006JF000553.

Bishop, P., T. B. Hoey, J. D. Jansen, and I. L. Artza (2005), Knickpoint recession rate and catchment area: The case of uplifted rivers in eastern Scotland, *Earth Surf. Process. Landf.*, *30*, 767–778, doi:10.1002/esp.1191.

Crosby, B. T., and K. X. Whipple (2006), Knickpoint initiation and distribution within fluvial networks: 236 waterfalls in the Waipaoa River,

North Island, New Zealand, *Geomorphology*, *82*, 16–38, doi:10.1016/j.geomorph.2005.08.023.

Finnegan, N. J., G. Roe, D. R. Montgomery, and B. Hallet (2005), Controls on the channel width of rivers: Implications for modeling fluvial incision of bedrock, *Geology*, *33*, 229–232, doi:10.1130/G21171.1.

Finnegan, N. J., L. S. Sklar, and T. K. Fuller (2007), Interplay of sediment supply, river incision, and channel morphology revealed by the transient evolution of an experimental bedrock channel, *J. Geophys. Res.*, *112*, F03S11, doi:10.1029/2006JF000569.

Furbish, D. J. (1997), *Fluid Physics in Geology: An Introduction to Fluid Motions on Earth's Surface and Within its Crust*, Oxford Univ. Press, New York.

Gilbert, G. K. (1877), *Report on the Geology of the Henry Mountains: Geographical and Geological Survey of the Rocky Mountain Region*, 160 pp., Gov. Print. Off., Washington, D. C.

Griffin, E. R., J. W. Kean, K. R. Vincent, J. D. Smith, and J. M. Friedman (2005), Modeling effects of bank friction and woody bank vegetation on channel flow and boundary shear stress in the Rio Puerco, New Mexico, *J. Geophys. Res.*, *110*, F04023, doi:10.1029/2005JF000322.

Hancock, G. S., and R. S. Anderson (2002), Numerical modeling of fluvial strath-terrace formation in response to oscillating climate, *Geol. Soc. Am. Bull.*, *114*, 1131–1142.

Hancock, G. S., R. S. Anderson, O. A. Chadwick, and R. C. Finkel (1999), Dating fluvial terraces with 10Be and 26Al profiles: application to the Wind River, Wyoming, *Geomorphology*, *27*, 41–60, doi:10.1016/S0169-555X(98)00089-0.

Harbor, D. J. (1998), Dynamic equilibrium between an active uplift and the Sevier River, *Utah, J. Geol.*, *106*, 181–198.

Hartshorn, K., N. Hovius, W. B. Dade, and R. L. Slingerland (2002), Climate-driven bedrock incision in an active mountain belt, *Science*, *297*, 2036–2038, doi:10.1126/science.1075078.

Houjou, K., Y. Shimizu, and C. Ishii (1990), Calculation of boundary shear stress in open channel flow, *J. Hydrosci. Hydraul. Eng.*, *8*, 21–37.

Howard, A. D., and G. Kerby (1983), Channel changes in badlands, *Geol. Soc. Am. Bull.*, *94*, 739–752, doi:10.1130/0016-7606(1983)94<739:CCIB>2.0.CO;2.

Johnson, J. P., and K. X. Whipple (2007), Feedbacks between erosion and sediment transport in experimental bedrock channels, *Earth Surf. Process. Landf.*, *32*, 1048–1062, doi:10.1002/esp.1471.

Julien, P. (1998), *Erosion and Sedimentation*, 280 pp., Cambridge Univ. Press, Cambridge, U. K.

Kean, J. W., and J. D. Smith (2004), Flow and boundary shear stress in channels with woody bank vegetation, in *Riparian Vegetation and Fluvial Geomorphology, Water Sci. Appl. Ser.*, vol. 8, edited by S. J. Bennett and A. Simon, pp. 237–252, AGU, Washington, D. C.

Kean, J. W., and J. D. Smith (2005), Generation and verification of theoretical rating curves in the Whitewater River basin, Kansas, *J. Geophys. Res.*, *110*, F04012, doi:10.1029/2004JF000250.

Khodashenas, S. R., and A. Paquier (1999), A geometrical method for computing the distribution of boundary shear stress across irregular straight open channels, *J. Hydraul. Res.*, *37*, 381–388.

Knight, D. W., and M. Sterling (2000), Boundary shear in circular pipes running partially full, *J. Hydraul. Eng.*, *126*, 263–275, doi:10.1061/(ASCE)0733-9429(2000)126:4(263).

Knight, D. W., K. W. H. Yuen, and A. A. I. Al-Hamid (1994), Boundary shear stress distributions in open channel flow, in *Mixing and Transport in the Environment*, edited by K. J. Bevin et al., pp. 51–87, John Wiley, Hoboken, N. J.

Knight, D. W., M. Omran, and T. Xiaonan (2007), Modeling depth-averaged velocity and boundary shear in trapezoidal channels with secondary flows, *J. Hydraul. Eng.*, *133*, 39–47, doi:10.1061/(ASCE)0733-9429(2007)133:1 (39).

Lague, D., N. Hovius, and P. Davy (2005), Discharge, discharge variability, and the bedrock channel profile, *J. Geophys. Res.*, *110*, F04006, doi:10.1029/2004JF000259.

Lane, E. W. (1953), Progress report on studies on the design of stable channels by the Bureau of Reclamation, *Proc. Am. Soc. Civ. Eng.*, *79*, 1–31.

Lane, S. N., K. F. Bradbrook, K. S. Richards, P. A. Biron, and A. G. Roy (1999), The application of computational fluid dynamics to natural river channels: Three-dimensional versus two-dimensional approaches, *Geomorphology*, *29*, 1–20, doi:10.1016/S0169-555X(99)00003-3.

Lave, J., and J. P. Avouac (2000), Active folding of fluvial terraces across the Siwaliks Hills, Himalayas of central Nepal, *J. Geophys. Res.*, *105*, 5735–5770, doi:10.1029/1999JB900292.

Lave, J., and J. P. Avouac (2001), Fluvial incision and tectonic uplift across the Himalayas of central Nepal, *J. Geophys. Res.*, *106*, 26,561–26,591, doi:10.1029/2001JB000359.

Leighly, J. B. (1932), Toward a theory of the morphologic significance of turbulence in the flow of water in streams, *Univ. Calif. Publ. Geogr.*, *6*, 1–22.

Li, R., D. D. Simons, and M. A. Stevens (1976), Morphology of cobble streams in small watersheds, *J. Hydr. Div.*, *102*, 1101–1117.

Loget, N., P. Davy, and J. Van Den Driessche (2006), Mesoscale fluvial erosion parameters deduced from modeling the Mediterranean Sea level drop during the Messinian (late Miocene), *J. Geophys. Res.*, *111*, F03005, doi:10.1029/2005JF000387.

Ma, L., P. J. Ashworth, J. L. Best, L. Elliott, D. B. Ingham, and L. J. Whitcombe (2002), Computational fluid dynamics and the physical modelling of an upland urban river, *Geomorphology*, *44*, 375–391, doi:10.1016/S0169-555X(01)00184-2.

Merritts, D., K. R. Vincent, and E. E. Wohl (1994), Long river profiles, tectonism, and eustasy: A guide to interpreting fluvial terraces, *J. Geophys. Res.*, *99*, 14,031–14,050, doi:10.1029/94JB00857.

Montgomery, D. R. (2004), Observations on the role of lithology in strath terrace formation and bedrock channel width, *Am. J. Sci.*, *304*, 454–476, doi:10.2475/ajs.304.5.454.

Montgomery, D. R., and K. B. Gran (2001), Downstream variations in the width of bedrock channels, *Water Resour. Res.*, *37*, 1841–1846, doi:10.1029/2000WR900393.

Naot, D., I. Nezu, and H. Nakagawa (1993), Hydrodynamic behavior of compound rectangular open channels, *J. Hydraul. Eng.*, *119*, 390–408, doi:10.1061/(ASCE)0733-9429(1993)119:3(390).

Olsen, O. J., and Q. L. Florey (1952), Sedimentation studies in open channels: Boundary shear and velocity distribution by membrane analogy, analytical and finite difference methods, *Lab. Rep. Sp-34*, U. S. Bur. of Reclam., Denver, Colo.

Parker, G. (1979), Hydraulic geometry of active gravel rivers, *J. Hydr. Div.*, *105*, 1185–1201.

Patankar, S. V. (1980), *Numerical Heat Transfer and Fluid Flow*, 197 pp., Hemisphere, Washington, D. C.

Pazzaglia, F. J., and M. T. Brandon (2001), A fluvial record of long-term steady-state uplift and erosion across the Cascadia forearc high, western Washington state, *Am. J. Sci.*, *301*, 385–431, doi:10.2475/ajs.301.4-5.385.

Pizzuto, J. E. (1991), A numerical model for calculating the distribution of velocity and boundary shear stress across irregular straight open channels, *Water Resour. Res.*, *27*, 2457–2466, doi:10.1029/91WR01469.

Shepherd, R. G. (1972), Incised river meanders: Evolution in simulated bedrock, *Science*, *178*, 409–411, doi:10.1126/science.178.4059.409.

Shimizu, Y. (1989), Effects of lateral shear stress in open channel flow, *Tech. Publ. 439*, 22 pp., Inst. of Civ. Eng. and Dev., Hokkaido, Japan.

Simpson, G. D. H. (2006), Modeling interactions between fold-thrust belt deformation, foreland flexure and surface mass transport, *Basin Res.*, *18*, 125–143, doi:10.1111/j.1365-2117.2006.00287.x.

Sklar, L. S., and W. E. Dietrich (2004), A mechanistic model for river incision into bedrock by saltating bed load, *Water Resour. Res.*, *40*, W06301, doi:10.1029/2003WR002496.

Stark, C. P. (2006), A self-regulating model of bedrock river channel geometry, *Geophys. Res. Lett.*, *33*, L04402, doi:10.1029/2005GL023193.

Tucker, G. E., and R. Slingerland (1997), Drainage basin responses to climate change, *Water Resour. Res.*, *33*, 2031–2047, doi:10.1029/97WR00409.

Turowski, J. M., D. Lague, and N. Hovius (2007), Cover effect in bedrock abrasion: A new derivation and its implications for the modeling of bedrock channel morphology, *J. Geophys. Res.*, *112*, F04006, doi:10.1029/2006JF000697.

Turowski, J. M., N. Hovius, M.-L. Hsieh, D. Lague, and M.-C. Chen (2008a), Distribution of erosion across bedrock channels, *Earth Surf. Process. Landf.*, *33*, 353–363, doi:10.1002/esp.1559.

Turowski, J. M., N. Hovius, A. Wilson, and M.-J. Horng (2008b), Hydraulic geometry, river sediment and the definition of bedrock channels, *Geomorphology*, doi:10.1016/j.geomorph.2007.1010.1001, in press.

Vigilar, G. G., Jr., and P. Diplas (1997), Stable channels with mobile bed: Formulation and numerical simulation, *J. Hydraul. Eng.*, *123*, 189–199, doi:10.1061/(ASCE)0733-9429(1997)123:3(189).

Whipple, K. X., and B. J. Meade (2004), Controls on the strength of coupling among climate, tectonics and deformation in two-sided, frictional orogenic wedges at steady state, *J. Geophys. Res.*, *109*, F01011, doi:10.1029/2003JF000019.

Whipple, K. X., E. Kirby, and S. H. Brocklehurst (1999), Geomorphic limits to climate-induced increases in topographic relief, *Nature*, *401*, 39–43, doi:10.1038/43375.

Whittaker, A. C., P. A. Cowie, M. Attal, G. E. Tucker, and G. P. Roberts (2007), Bedrock channel adjustment to tectonic forcing: Implications for predicting river incision rates, *Geology*, *35*, 103–106, doi:10.1130/G23106A.1.

Wobus, C. W., G. E. Tucker, and R. S. Anderson (2006a), Modeling the geometry of bedrock river channels, *EOS Trans. AGU*, *87*(52), Fall Meet. Suppl., Abstract H51G-0565.

Wobus, C. W., G. E. Tucker, and R. S. Anderson (2006b), Self-formed bedrock channels, *Geophys. Res. Lett.*, *33*, L18408, doi:10.1029/2006GL027182.

Wohl, E., and H. Ikeda (1997), Experimental simulation of channel incision into a cohesive substrate at varying gradients, *Geology*, *25*, 295–298, doi:10.1130/0091-7613(1997)025<0295:ESOCII>2.3.CO;2.

R. S. Anderson, Department of Geological Sciences and Institute of Arctic and Alpine Research, University of Colorado, Campus Box 399, 2200 Colorado Ave., Boulder, CO 80309, USA.

J. W. Kean, U.S. Geological Survey, M.S. 966, P.O. Box 25046, Denver, CO 80225, USA.

G. E. Tucker, Department of Geological Sciences and Cooperative Institute for Research in Environmental Sciences, University of Colorado, Campus Box 216, Boulder, CO 80309, USA.

C. W. Wobus, Cooperative Institute for Research in Environmental Sciences, University of Colorado, Boulder, CO 80309, USA. (cameron.wobus@colorado.edu)